Strain effects in semiconductor quantum wells

A.C.G. Wood

Wood, A.C.G. (1990) Strain effects in semiconductor quantum wells. Doctoral thesis, Durham University.

STRAIN EFFECTS IN SEMICONDUCTOR QUANTUM WELLS

by

A.C.G. Wood, B.Sc.

A thesis submitted for
the Degree of Doctor of Philosophy
at the University of Durham
September 1990

DECLARATION.

I hereby declare that the work reported in this thesis has not previously been submitted for any degree and is not being currently submitted in candidature for any other degree.

The work reported in this thesis was carried out by the candidate.

ABSTRACT

In this thesis the effect of the strain which is present in a lattice mismatched quantum well (QW) on the properties of the device is investigated. The **k.p** method is used within the envelope function framework to obtain the bandstructure and the wave functions of bound and unbound states in both lattice matched and strained quantum wells. The model includes spin and interband mixing effects. We show that the mixing of wave function character between adjacent subbands which occurs in a QW can be reduced in a strained structure, and that this can result in the ground state subband having a reduced effective mass. The effect of the reduction in mixing on the optical matrix elements for transitions between the conduction and valence bands is also investigated.

A model is developed which enables the calculation of the gain and spontaneous emission spectra and threshold properties of a multiple quantum well (MQW) laser device. The model includes a full description of the non-parabolic subband dispersion and the variation of the optical matrix elements along the subbands, together with an energy dependent lifetime broadening of the spectrum. The model is used to compare the performance of strained and unstrained InGaAs/InP MQW devices operating at 1.3μm and 1.55μm. The reduced valence band edge effective mass of the strained devices is shown to lead to a reduced threshold current, temperature dependence and linewidth enhancement factor and an enhanced gainslope.

The unbound states of the well are used to investigate the bound-unbound intervalence band absorption rate in the above devices. The absorption coefficient for this process is found to be small ($< 2\text{cm}^{-1}$) in all the cases considered.

ACKNOWLEDGEMENTS

I am indebted to the numerous friends and colleagues who have made this work possible and have contributed towards my enjoyment of the time spent at Durham. Particular thanks must go to my supervisor, Dick Abram, for his endless patience and encouragement, for sharing his great understanding of and insight into the problems that have confronted me during my research, and for his comments on the first draft of this thesis. I am grateful to my industrial supervisor, David Robbins, for suggesting that I investigate strained QW lasers, and for sharing his depth of knowledge on the subject. Thanks are also due for his assistance during the time I spent at Caswell, and for making available various computer programs. I would like to thank those who have spent time discussing difficult or contentious issues and debating the results I have obtained, especially Stuart Brand, John French, David Hall, David Hughes, Robert Kelsall, Graham Rees, Ian Taylor and Graham Warren. I also appreciate the patience of Anthony O'Neill in awaiting the completion of this thesis.

I would also like to thank my parents for their encouragement, and my fiancée Nicola Hoey for her constant support, especially during the time spent writing this thesis. I am grateful to Stephen Rayner and others for helping me to take regular breaks from my work to play bridge.

I gratefully acknowledge financial support for the period of this work from the Science and Engineering Research Council and Plessey Research (Caswell).

To Nicky

CONTENTS

Appendix A Parameters used in the Calculations

Appendix B Bandstructure Fitting Procedure

CHAPTER ONE

INTRODUCTION

In the last twenty years the techniques of molecular beam epitaxy (MBE) and metal-organic chemical vapour deposition (MOCVD), both of which make possible the reproduceable deposition of layers of semiconducting material with thicknesses on the nanometre scale, have been used to produce a wide variety of novel structures and devices. A recent exciting development has been the ability to grow epitaxial layers of one semiconductor on a substrate of a second material with a different lattice constant and maintain very low defect densities. Provided the epitaxial layer is sufficiently thin, it will be elastically strained by the substrate, experiencing either a biaxial tension or compression depending on the relative sizes of the substrate and layer lattice constants. Such strained layers have been successfully incorporated into quantum well and superlattice structures in the Si-Ge, III-V and II-VI material systems. The strain field experienced by the well material in such a structure affects the electronic states, and can result in radically different optical and electronic properties from those observed in lattice matched devices. The relaxation of the requirement that heterostructures be grown from lattice matched materials also allows greater freedom to tailor the structure to the required device properties.

In this thesis the way in which the strain modifies the bandstructure of a lattice mismatched semiconductor quantum well is investigated, and the results obtained are used to investigate the optical properties of these structures. In particular, the properties of strained layer quantum well lasers in the InGaAs/InP materials system are investigated.

In chapter 2 we describe how the **k.p** method in the envelope function formalism can be used to calculate the bandstructure and the wave functions of both bound and unbound states in a quantum well. The model developed is illustrated by applying it to a study of an $\mathrm{In_{0.53}Ga_{0.47}As/InP}$ quantum well. Chapter 3 describes how the effect of strain is incorporated into this model, and demonstrates the influence of the strain on the bandstructure of the quantum well. In chapter 4 the optical matrix elements between bound conduction and valence band states in the quantum well are investigated. The way in which the strain present in a mismatched structure reduces mixing effects between adjacent subbands is illustrated and discussed.

In chapter 5 we describe how the bandstructure details and optical matrix elements obtained from the **k.p** model can be used to investigate the performance of strained (and unstrained) quantum well lasers. The way in which gain and spontaneous emission spectra are calculated is discussed, together with the means of obtaining the threshold properties of the laser. The model is applied to an unstrained $\mathrm{In_{0.53}Ga_{0.47}As/InP}$ laser. In chapter 6 the laser model described in the previous chapter is used to calculate the properties of strained InGaAs/InP devices suitable for operation at 1.3μm and 1.55μm, and comparison is made with the corresponding unstrained structures. The strained devices are shown to offer a variety of advantages over the unstrained structures, and the calculations give a reliable, quantitative measure to these device advantages. The results confirm previous predictions obtained by less sophisticated models.

The intervalence band absorption (IVBA) process is thought to be a significant loss mechanism in long wavelength lasers. In chapter 7 we show how the states of the quantum well obtained from the **k.p** model can be used to obtain the IVBA rate in the lasers considered in chapter 6.

The results obtained are summarised in chapter 8, together with a discussion of the conclusions reached and suggestions for further work.

CHAPTER TWO

QUANTUM WELL BANDSTRUCTURE

2.1 Introduction

In this chapter we describe in detail how the electronic states of a semiconductor quantum well (QW) may be calculated. Our method allows us to obtain the energy levels of quantum confined ('bound') states and the wave functions of both bound and unbound (continuum) states.

A quantum well is a semiconductor 'sandwich' (see figure 2.1), consisting of a thin slice (typically $\sim$ 100Å) of one semiconductor material surrounded on both sides by semi-infinite (in practice $\sim$ 1μm) slabs of a second semiconductor material. We shall only consider type I QWs, in which both electrons and holes are confined in region B by a potential well (clearly such a structure can only occur when material II has a smaller bandgap than material I). Henceforth we shall refer to regions A and C as the barriers and region B as the well.

In essence, the quantum well is a physical realisation of the classic undergraduate quantum mechanical 'particle in a box' problem [1]. Electrons and holes are confined in the growth direction (which we shall label as the z direction), but are free to move in a constant potential in the (x, y) directions, i.e. parallel to the interface planes (in future we shall refer to a

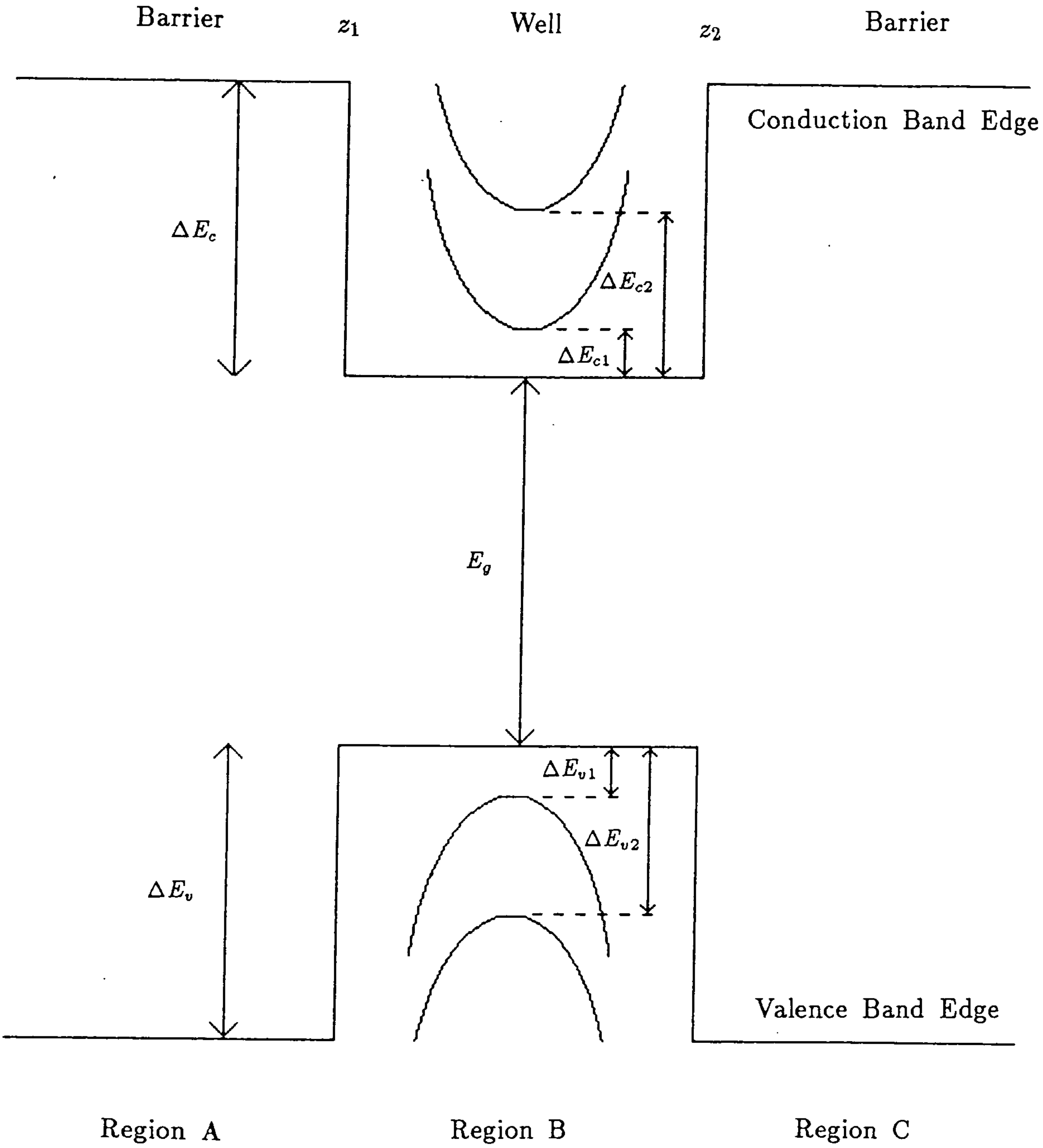

Figure 2.1

Schematic diagram of a quantum well.

direction in the (x, y) plane as 'in-plane'). This leads to a set of discrete energy subbands for both the electrons and holes, given by

$$E_n(\mathbf{k}) = \Delta E_n + E_{\|}(k_{\|}) \tag{2.1}$$

where ΔE_n is the energy of the nth subband at $k_{\|} = 0$ and $E_{\|}$ is the kinetic energy due to the particle's motion in the (x, y) plane, characterised by its in-plane wave vector $k_{\|}$. In the following sections we shall show how the precise form of $E_n(\mathbf{k})$ and the associated wave functions can be calculated.

2.2 Method of Solution

The wave function of a carrier at a given energy in any of the regions A, B or C of the quantum well can be expressed as a linear combination of the allowed bulk states in that region at the appropriate energy. By applying appropriate boundary conditions to match up these wave functions and their derivatives at the interfaces, and by requiring physically sensible behaviour as $z \rightarrow \pm\infty$, we can obtain the allowed states of the QW and the associated wave functions.

Many methods have been put forward to calculate the bulk bandstructure of a semiconductor, those most commonly used being the effective mass [2], **k.p** [3], tight-binding [4] and pseudopotential methods [5]. We have elected to use an 8 band **k.p** model, with the effect of lower and higher-lying energy bands included as a perturbation, which maintains computational speed (using 8 × 8 matrices (for bulk materials) compared with 130 × 130 for a 65 plane wave pseudopotential approach) whilst including the effects of spin and mixing between the different subbands. An additional advantage of this approach is the ease with which it can be extended to study strained systems (see chapter 3). Obviously the use of only 8 basis states leads to a loss of accuracy in the bandstructure, but we expect the lowest subbands to be well represented near to the centre of the Brillouin zone [6]. (It should be pointed out that this approach is not suitable for a study of states derived from different points in the Brillouin zone, such as $\Gamma - X$ mixing).

2.3 Development of the k.p Method

In the last four decades, the **k.p** method has been widely used to study a range of materials and devices within the field of semiconductor physics. Most of the early application of **k.p** theory to bulk semiconductor materials was carried out in the mid 1950's by Kane [7], Luttinger [8] and Dresselhaus [9], together with various coworkers. In the early 1970's Nedorezov [10] showed how the method could be applied to heterostructures, and investigated the valence band states in infinitely deep quantum wells. More recently the method has frequently been used to calculate the bandstructure of quantum wells and superlattices, the current popularity of the method being largely due to the work of Bastard [11] and Altarelli [12] who brought an awareness of the virtues of the method to a much wider audience in the early 1980's. These authors, however, neglected the effect of spin, and hence did not include the spin-orbit split Γ_7 states. In the last few years further work has been done by Schuurmans, 't Hooft, Eppenga and Colak [6,13], who have included the Γ_7 states, and have shown their results to agree well with the more sophisticated tight binding work of Schulman and Chang [14]. Recently the method has also been applied to strained systems by Smith and Mailhiot [15] and O'Reilly [16].

2.4 Bulk Bandstructure in the k.p Method

To calculate the bulk bandstructure of a semiconductor we expand the wave function in terms of our chosen basis set, and substitute this into the Schrödinger equation. Obviously we need to know the form of the Hamiltonian relevant to our chosen basis. We shall mainly be interested in states which lie close to the band edges, so since the valence band maximum of a tetrahedral semiconductor always lies at the Γ point ($\mathbf{k} = 0$), and the conduction band minimum is also at the Γ point in direct gap materials (to which we shall confine our investigations), it is logical to use the zone centre (Γ) Bloch functions as the basis set.

The valence band maximum in such a semiconductor is derived from atomic p orbitals, and is split by the spin-orbit interaction into an upper fourfold-degenerate Γ_8 level with $j = 3/2$ character (j being the total angular momentum quantum number) and a lower twofold-degenerate Γ_7 level with $j = 1/2$ character. The conduction band minimum lies at the Γ_6 point, where the wave function is derived from atomic s orbitals. Obviously there is a trade off to be made between the accuracy of the bandstructure obtained and the speed of calculation, and we thus restrict our basis to the eight zone centre states (Γ_6, Γ_7, Γ_8) shown in table 2.1, which will represent the bandstructure realistically near to the band edges without being too demanding on computer time.

Diamond semiconductors (Si and Ge) possess inversion symmetry, and so each state is doubly degenerate (so-called Kramers degeneracy). All the semiconductors we shall study will be III-V compounds with the zinc-blende structure, and hence this degeneracy will be lifted. This effect is small, however, and we shall assume all inversion asymmetry terms to be neglible. As a result, all the bandstructure obtained from our model will be at least doubly degenerate. Indeed, it can be seen that the states $|u_5\rangle \rightarrow |u_8\rangle$ are just the Kramers counterparts of $|u_1\rangle \rightarrow |u_4\rangle$. We should also point out that if the state with wave vector k exists, the states with wave vectors k^*, $-k$ and $-k^*$ will also.

The bulk wave functions are written as the product of a linear combination of the zone centre Bloch functions and a slowly varying envelope function, which we assume to take the form of a plane wave :

$$\psi = e^{i\mathbf{k}.\mathbf{r}} \sum_j F_j \left| u_j \right\rangle \tag{2.2}$$

		$\|j, m_j\rangle$	
u_1	$\|S\uparrow\rangle$	$\|\frac{1}{2}, \frac{1}{2}\rangle$	Conduction
u_2	$\sqrt{\frac{1}{2}}\,\|(X+iY)\uparrow\rangle$	$\|\frac{3}{2}, \frac{3}{2}\rangle$	Heavy hole
u_3	$\sqrt{\frac{1}{6}}\,\|(X+iY)\downarrow\rangle - \sqrt{\frac{2}{3}}\,\|Z\uparrow\rangle$	$\|\frac{3}{2}, \frac{1}{2}\rangle$	Light hole
u_4	$\sqrt{\frac{1}{3}}\,[\|(X+iY)\downarrow\rangle + \|Z\uparrow\rangle]$	$\|\frac{1}{2}, \frac{1}{2}\rangle$	Spin-orbit
u_5	$\|S\downarrow\rangle$	$\|\frac{1}{2}, -\frac{1}{2}\rangle$	Conduction
u_6	$\sqrt{\frac{1}{2}}\,\|(X-iY)\downarrow\rangle$	$\|\frac{3}{2}, -\frac{3}{2}\rangle$	Heavy hole
u_7	$-\sqrt{\frac{1}{6}}\,\|(X-iY)\uparrow\rangle - \sqrt{\frac{2}{3}}\,\|Z\downarrow\rangle$	$\|\frac{3}{2}, -\frac{1}{2}\rangle$	Light hole
u_8	$-\sqrt{\frac{1}{3}}\,[\|(X-iY)\uparrow\rangle - \|Z\downarrow\rangle]$	$\|\frac{1}{2}, -\frac{1}{2}\rangle$	Spin-orbit

Table 2.1

The basis set

The Hamiltonian is readily derived using **k.p** theory [3,7], and the effects of remote bands are included using Löwdin perturbation theory [17]. In our chosen basis, the Hamiltonian takes the form shown in table 2.2 [13] (where we have set $\hbar/2m$ equal to unity), with a list of symbols given in table 2.3. It should be noted that the Luttinger parameters (γ_1, γ_2, γ_3) are modified from those normally quoted due to the explicit inclusion of the conduction band in the basis. They are obtained from the true Luttinger parameters (γ_1^L,γ_2^L,γ_3^L) as follows :

$$\begin{aligned} \gamma_1 &= \gamma_1^L - \lambda/2 \\ \gamma_{2,3} &= \gamma_{2,3}^L - \lambda/4 \end{aligned} \tag{2.3}$$

where

$$\lambda = \frac{4mP^2}{3\hbar^2 E_g}. \tag{2.4}$$

(P is the momentum matrix element $|\langle s \mid \frac{\partial}{\partial z} \mid z \rangle|$ and E_g is the band gap). These modified Luttinger parameters are related to the effective masses of the bands by [13]

$$\frac{m}{m_{hh(001)}} = \gamma_1 - 2\gamma_2 \tag{2.5}$$

$$\frac{m}{m_{el(001)}} = s + \lambda(1 + 1/2r) \tag{2.6}$$

$$\frac{m}{m_{lh(001)}} = \gamma_1 + 2\gamma_2 + \lambda \tag{2.7}$$

$$\frac{m}{m_{so(001)}} = \gamma_1 + 1/2\lambda r \tag{2.8}$$

$$\frac{m}{m_{hh(111)}} = \gamma_1 - 2\gamma_3 \tag{2.9}$$

with

$$r = \frac{E_g}{E_g + \Delta}. \tag{2.10}$$

$$
\begin{pmatrix}
s\mathbf{k}^2+E_g & \sqrt{\tfrac{1}{2}}iP(k_x+ik_y) & -\sqrt{\tfrac{2}{3}}iPk_z & \sqrt{\tfrac{1}{3}}iPk_z & 0 & 0 & -\sqrt{\tfrac{1}{6}}iP(k_x-ik_y) & -\sqrt{\tfrac{1}{3}}iP(k_x-ik_y) \\
-\sqrt{\tfrac{1}{2}}iP(k_x-ik_y) & \begin{matrix}(2\gamma_2-\gamma_1)k_z^2\\-(\gamma_1+\gamma_2)k_\parallel^2\end{matrix} & 2\sqrt{3}\gamma_3(k_x-ik_y)k_z & -\sqrt{6}\gamma_3(k_x-ik_y)k_z & 0 & 0 & \begin{matrix}\sqrt{3}\gamma_2(k_x^2-k_y^2)\\-2\sqrt{3}i\gamma_3k_xk_y\end{matrix} & \begin{matrix}\sqrt{6}\gamma_2(k_x^2-k_y^2)\\-2\sqrt{6}i\gamma_3k_xk_y\end{matrix} \\
\sqrt{\tfrac{2}{3}}iPk_z & 2\sqrt{3}\gamma_3(k_x+ik_y)k_z & \begin{matrix}-(\gamma_1+2\gamma_2)k_z^2\\+(\gamma_2-\gamma_1)k_\parallel^2\end{matrix} & \begin{matrix}2\sqrt{2}\gamma_2k_z^2\\-\sqrt{2}\gamma_2k_\parallel^2\end{matrix} & -\sqrt{\tfrac{1}{6}}iP(k_x-ik_y) & \begin{matrix}-\sqrt{3}\gamma_2(k_x^2-k_y^2)\\+2\sqrt{3}i\gamma_3k_xk_y\end{matrix} & 0 & -3\sqrt{2}\gamma_3(k_x-ik_y)k_z \\
-\sqrt{\tfrac{1}{3}}iPk_z & -\sqrt{6}\gamma_3(k_x+ik_y)k_z & \begin{matrix}2\sqrt{2}\gamma_2k_z^2\\-\sqrt{2}\gamma_2k_\parallel^2\end{matrix} & \begin{matrix}-\gamma_1k_z^2-\gamma_1k_\parallel^2\\-\Delta\end{matrix} & -\sqrt{\tfrac{1}{3}}iP(k_x-ik_y) & \begin{matrix}-\sqrt{6}\gamma_2(k_x^2-k_y^2)\\+2\sqrt{6}i\gamma_3k_xk_y\end{matrix} & 3\sqrt{2}\gamma_3(k_x-ik_y)k_z & 0 \\
0 & 0 & \sqrt{\tfrac{1}{6}}iP(k_x+ik_y) & \sqrt{\tfrac{1}{3}}iP(k_x+ik_y) & s\mathbf{k}^2+E_g & \sqrt{\tfrac{1}{2}}iP(k_x-ik_y) & -\sqrt{\tfrac{2}{3}}iPk_z & \sqrt{\tfrac{1}{3}}iPk_z \\
0 & 0 & \begin{matrix}-\sqrt{3}\gamma_2(k_x^2-k_y^2)\\-2\sqrt{3}i\gamma_3k_xk_y\end{matrix} & \begin{matrix}-\sqrt{6}\gamma_2(k_x^2-k_y^2)\\-2\sqrt{6}i\gamma_3k_xk_y\end{matrix} & -\sqrt{\tfrac{1}{2}}iP(k_x+ik_y) & \begin{matrix}(2\gamma_2-\gamma_1)k_z^2\\-(\gamma_1+\gamma_2)k_\parallel^2\end{matrix} & 2\sqrt{3}\gamma_3(k_x+ik_y)k_z & -\sqrt{6}\gamma_3(k_x+ik_y)k_z \\
\sqrt{\tfrac{1}{6}}iP(k_x+ik_y) & \begin{matrix}\sqrt{3}\gamma_2(k_x^2-k_y^2)\\+2\sqrt{3}i\gamma_3k_xk_y\end{matrix} & 0 & 3\sqrt{2}\gamma_3(k_x+ik_y)k_z & \sqrt{\tfrac{2}{3}}iPk_z & 2\sqrt{3}\gamma_3(k_x-ik_y)k_z & \begin{matrix}-(\gamma_1+2\gamma_2)k_z^2\\+(\gamma_2-\gamma_1)k_\parallel^2\end{matrix} & \begin{matrix}2\sqrt{2}\gamma_2k_z^2\\-\sqrt{2}\gamma_2k_\parallel^2\end{matrix} \\
\sqrt{\tfrac{1}{3}}iP(k_x+ik_y) & \begin{matrix}\sqrt{6}\gamma_2(k_x^2-k_y^2)\\+2\sqrt{6}i\gamma_3k_xk_y\end{matrix} & -3\sqrt{2}\gamma_3(k_x+ik_y)k_z & 0 & -\sqrt{\tfrac{1}{3}}iPk_z & -\sqrt{6}\gamma_3(k_x-ik_y)k_z & \begin{matrix}2\sqrt{2}\gamma_2k_z^2\\-\sqrt{2}\gamma_2k_\parallel^2\end{matrix} & \begin{matrix}-\gamma_1k_z^2-\gamma_1k_\parallel^2\\-\Delta\end{matrix}
\end{pmatrix}
$$

Table 2.2

The Hamiltonian matrix

k_x, k_y, k_z	x, y, z component of wave vector
k^2	$= k_x^2 + k_y^2 + k_z^2$
$k_\parallel^2$	$= k_x^2 + k_y^2$ ($k_\parallel$ is the in-plane wave vector)
$\gamma_1, \gamma_2, \gamma_3$	modified Luttinger parameters
P	momentum matrix element $|\langle s \mid \frac{\partial}{\partial z} \mid z \rangle|$
E_g	band gap
Δ	spin orbit splitting
s	conduction band parameter

Table 2.3 List of Symbols used in Hamiltonian Matrix

Hence a knowledge of these five effective masses enables us to determine all the coupling parameters which occur in the Hamiltonian.

We can thus solve the Schrödinger equation

$$\mathbf{H}\psi = E\psi \tag{2.11}$$

to find the energy eigenvalues E and eigenvectors ψ for any given wave vector $\mathbf{k}$. However, to calculate states in a quantum well by the method described in section 2.2, it is necessary to obtain the wave vector $\mathbf{k}$ at a given energy E, which can be effected by a rearrangement of equation (2.11).

For any given in-plane wave vector $k_{||}$, we can rewrite equation (2.11) in the form

$$(\mathbf{H}_2 k_z^2 + \mathbf{H}_1 k_z + \mathbf{H}_0)\psi = 0 \tag{2.12}$$

where we have separated the Hamiltonian into terms $\mathbf{H}_0$, $\mathbf{H}_1$, $\mathbf{H}_2$, which are respectively independent of, linear in and quadratic in k_z, and have included the $E\psi$ term in $\mathbf{H}_0\psi$.

It is now possible to write an eigenvalue equation in k_z :

$$\begin{pmatrix} 0 & 1 \\ -\mathbf{H}_2^{-1}\mathbf{H}_0 & -\mathbf{H}_2^{-1}\mathbf{H}_1 \end{pmatrix} \begin{pmatrix} \psi \\ k_z\psi \end{pmatrix} = k_z \begin{pmatrix} \psi \\ k_z\psi \end{pmatrix} \tag{2.13}$$

with the top line being trivial and the bottom line derived from equation (2.12). The wave vectors of the bulk states at any given energy E can now be found by solving the eigenvalue equation.

2.5 The Form of the Complex Bandstructure

In general, the solution of the eigenvalue equation (2.13) will yield states with imaginary or general complex wave vectors in addition to the Bloch functions (which must have real wave vectors). Any complete description of the allowed states in a semiconductor must include all three (real, imaginary and complex) types of solution; the complete dispersion relation of these states is known as the complex bandstructure of the material.

The complex bandstructure of GaAs, obtained using the **k.p** method is illustrated in figure 2.2, for $k_{\|} = 0$. Note that for each point k_z on the bandstructure, states will exist with wave vector k_z, $-k_z$, k_z^* and $-k_z^*$. States with real wavevector k_z (propogating states) are shown on the right hand side of the energy axis, and states with imaginary k_z are shown on the left hand side of the energy axis. The latter solutions, which may lie within the forbidden energy gap of the semiconductor, correspond to states which decay or grow exponentially as they progress through the material. In an ideal bulk crystal, these states cannot manifest themselves due to the boundary condition that the wave function must remain finite in the approach to plus or minus infinity. However, these evanescent states become important in the region of a defect or interface, and hence in low dimensional structures, since evanescent wave functions defined in a semi-infinite half space or a layer of finite thickness can remain finite. Such states have been indirectly observed experimentally; for example they can give rise to tunnelling effects which

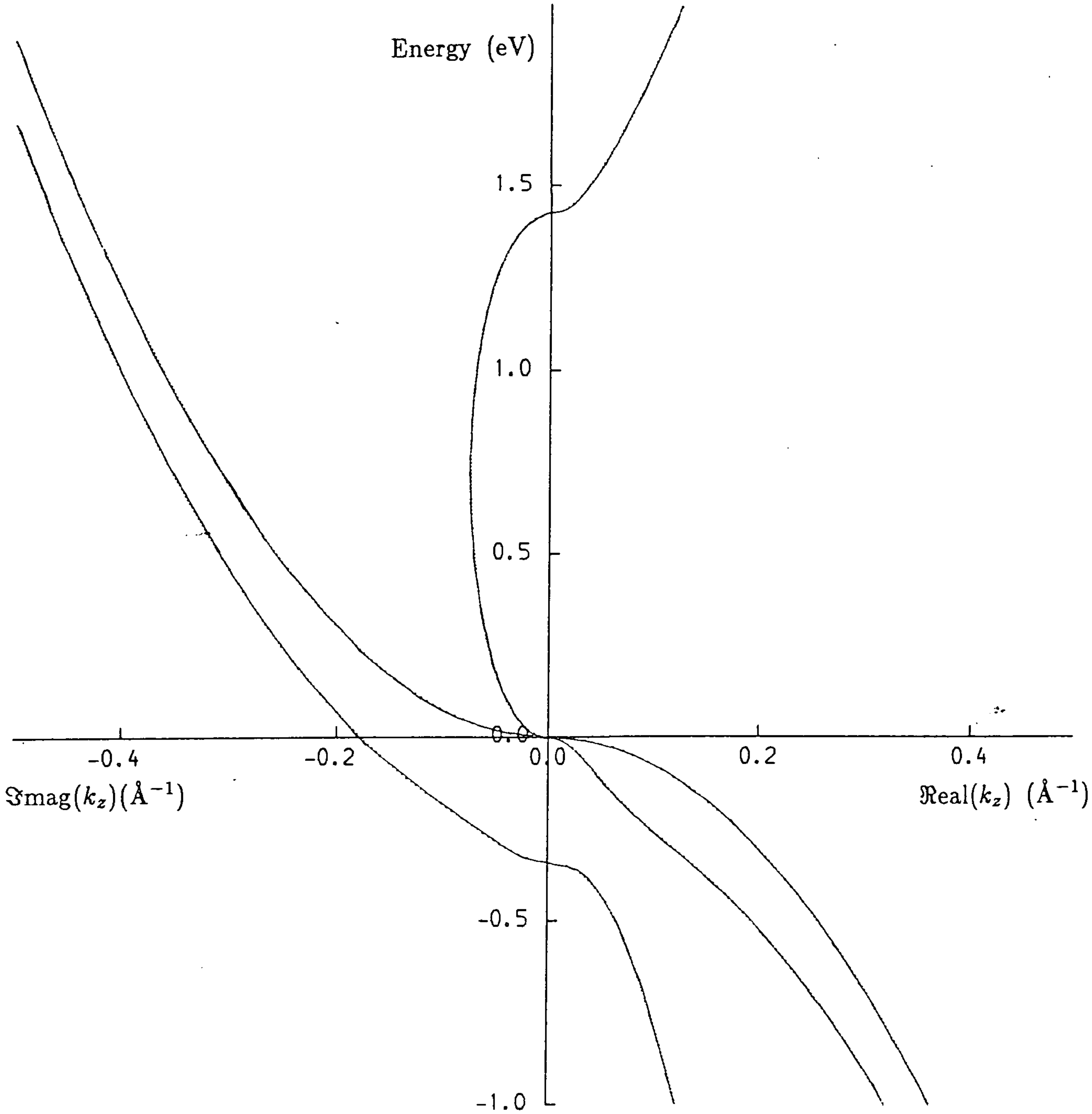

Figure 2.2 Complex Bandstructure of GaAs

$(k_x = k_y = 0)$.

cannot be explained by any other means (see for example the experiments of Parker and Mead [18]).

When $k_{\|} \neq 0$, as in figure 2.3, we also obtain general complex solutions, indicated by the dashed lines. These states are the product of an oscillatory wave function and a decaying wave function, and so appear as decaying waves. As with states with purely imaginary wave vector, these states can only occur in the region of interfaces or defects.

We should at this point note that there are only three distinct bands in the bandstructure shown in figure 2.2, since the conduction band and the light hole band are coupled by a band within the energy gap corresponding to evanescent wave functions. Thus at every energy there are only 12 eigenvalues of equation (2.13) (three sets of four as described above). Clearly this cannot be the case, since the matrix in equation (2.13) is a non-singular 16×16 matrix and so must have 16 eigenvalues. In fact, we do obtain four additional solutions. The Hamiltonian only contains matrix elements between the three bands shown in figure 2.2, and hence the additional solutions can have no physical significance. It is therefore desirable to ignore them when constructing the wave function. This turns out not to be a problem, since we can always ensure that these solutions are rapidly decaying (having a large imaginary wave vector), at the cost of a slight misrepresentation of one of the other bands, by careful choice of the bandstructure parameters. For example, for intervalence band absorption calculations (chapter 7) the conduction band plays no part, so we can safely

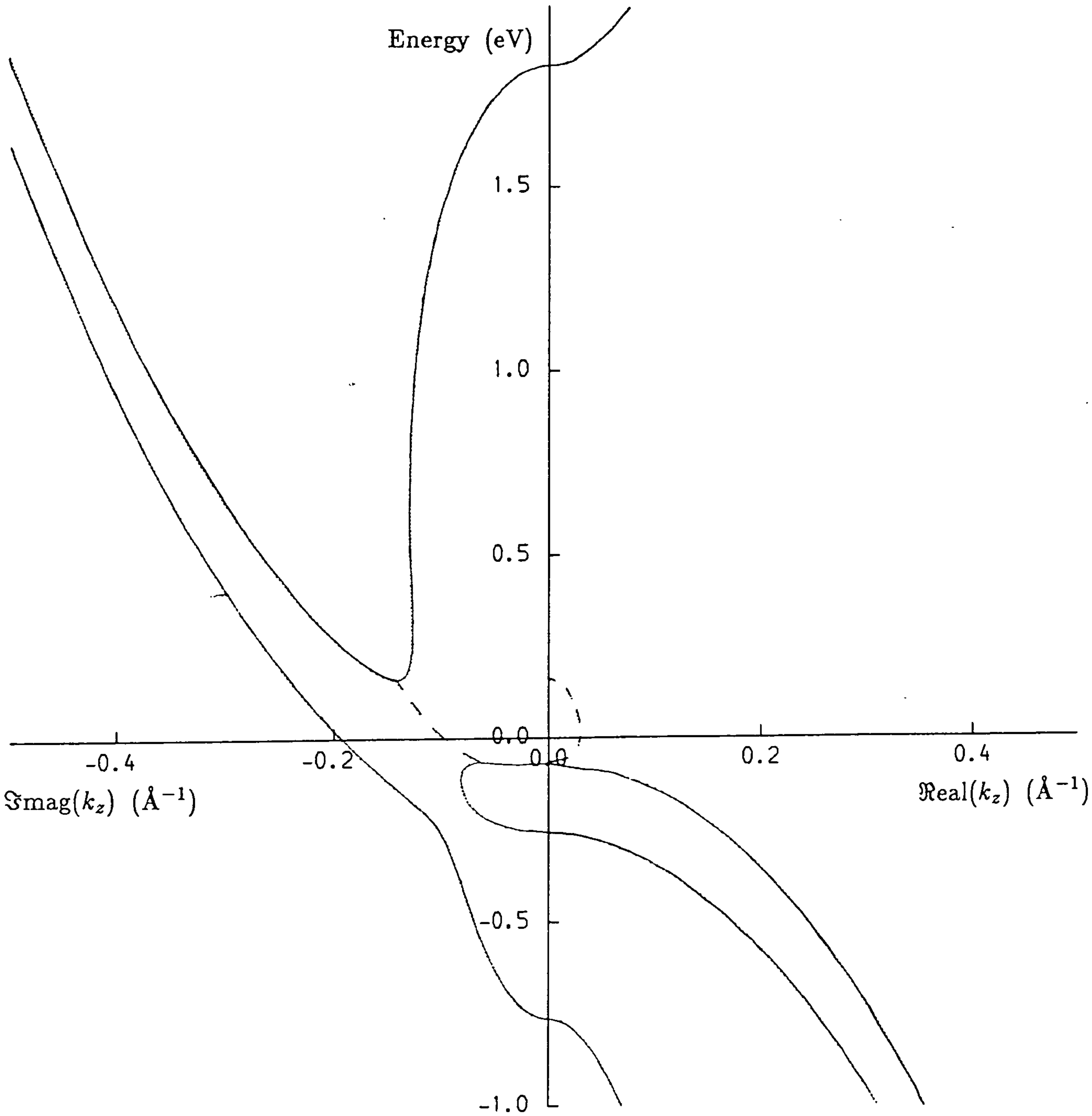

Figure 2.3 Complex Bandstructure of GaAs

($k_x = 0.1$Å^{-1}; $k_y = 0$).

adjust the parameters to ensure that the unphysical solutions have large imaginary k_z and m^*_{hh}, m^*_{lh} and m^*_{so} are well fitted, without worrying about the quality of the fit to m^*_{el}. Similarly, for gain calculations (chapters 5 and 6), we can sacrifice the accuracy of the fit to the spin-orbit split-off band.

These additional solutions have been commented on by several authors. Smith and Mailhiot [15] and White and Sham [19] (who referred to them as 'wing bands'), both found them to have large imaginary wave vector (and hence decay rapidly) for the materials they studied. These states have been discussed in detail by Eppenga *et al* [13], who found them to have a large real wave vector, and hence to be oscillatory in nature.

2.6 Boundary Conditions on the Quantum Well Wave Function

As we have mentioned in section 2.2, the quantum well wave function at a given energy can be expressed as a linear combination of bulk states in each region, i.e.

Region A :
$$\Psi^A = \sum_i \sum_j A_i^A F_{ij}^I e^{i\mathbf{k}_i^I.\mathbf{r}} \left|u_j^I\right\rangle \tag{2.14}$$

Region B :
$$\Psi^B = \sum_i \sum_j A_i^B F_{ij}^{II} e^{i\mathbf{k}_i^{II}.\mathbf{r}} \left|u_j^{II}\right\rangle \tag{2.14}$$

Region C :
$$\Psi^C = \sum_i \sum_j A_i^C F_{ij}^I e^{i\mathbf{k}_i^I.\mathbf{r}} \left|u_j^I\right\rangle \tag{2.15}$$

where I and II represent the barrier and well material respectively, and the wave vectors $\mathbf{k}_i$ are given by the bulk bandstructure of the relevant material. The z component of $\mathbf{k}_i$ may be imaginary or complex, giving growing or decaying states, as discussed in the previous section. The zero of energy is taken to lie at the bulk valence band edge in the well material; the energy relevant to a bulk barrier state is determined by the band offsets ΔE_c and ΔE_v (see figure 2.1).

By applying the relevant boundary conditions to this wave function the expansion coefficients A_i appropriate to a QW confinement state can be determined. Clearly the wave function Ψ must be continuous at the interfaces $(z = z_1, z_2)$ and remain finite in the limit $z \rightarrow \pm\infty$. We must also ensure that the derivative of the wave function in the epitaxial growth direction, $\frac{\partial \Psi}{\partial z}$ is continuous across the interface planes.

The requirement that the wave function remain finite in the approach to infinity is readily implemented for bound states by restricting the sum over the bulk states i in the barriers to those states which decay away from the interface. Since all bound states will have an energy within the band gap of the barrier material, the bulk barrier states used in the linear combination cannot have a real wave vector k_z, and will either decay or grow exponentially with distance from the interface plane. Thus we must include half of the bulk barrier states (those with $\Im mag(k_z) < 0$ — $i = 1 \rightarrow 8$, say) in Ψ^A and the other half (those with $\Im mag(k_z) > 0$ — $i = 9 \rightarrow 16$) in Ψ^C. All the bulk well states must be included in Ψ^B.

Since Ψ^A, Ψ^B and Ψ^C all contain the term $e^{i\mathbf{k}_i\cdot\mathbf{r}} = e^{ik_iz} \times e^{i\mathbf{k}_\| \cdot \mathbf{r}_\|}$ (where k_i is the z component of $\mathbf{k}_\mathrm{i}$), the wave function can only be continuous at all points $\mathbf{r}_\|$ on the interface if the in-plane wave vector $\mathbf{k}_\|$ is the same in all three regions of the QW.

In order to greatly simplify the form that the boundary conditions will take, we assume that the Bloch functions $|u_j>$ are the same in both materials, i.e.

$$\left|u_j^I\right\rangle = \left|u_j^{II}\right\rangle \qquad \text{for all } j. \tag{2.16}$$

Provided the well and barrier materials are isoelectronic, and have a similar structure, (2.16) will be a good approximation. Moreover we can tell how good the approximation is by comparing the matrix elements P (see below equation (2.4)) in the two materials. If (2.16) holds exactly, then $P^I = P^{II}$, and as the approximation gets worse the matrix elements will diverge.

Clearly it now follows from the requirement that Ψ be continuous that the coefficient of each $|u_j>$ (the 'envelopes') must be continuous, since the $|u_j>$'s are orthogonal. Thus Ψ is continuous when

$$\sum_{i=1}^{8} A_i^A F_{ij}^I e^{ik_i^I z_1} = \sum_{i=1}^{16} A_i^B F_{ij}^{II} e^{ik_i^{II} z_1} \tag{2.17}$$

$$\sum_{i=9}^{16} A_{i-8}^C F_{ij}^I e^{ik_i^I z_2} = \sum_{i=1}^{16} A_i^B F_{ij}^{II} e^{ik_i^{II} z_2} \tag{2.18}$$

or, in matrix form,

$$\mathbf{W}_{\mathbf{AL}}\mathbf{l} = \mathbf{W}_{\mathbf{BL}}\mathbf{w} \tag{2.19}$$

$$\mathbf{W}_{\mathbf{AR}}\mathbf{r} = \mathbf{W}_{\mathbf{BR}}\mathbf{w} \tag{2.20}$$

with

$$\mathbf{W}_{\mathbf{AL(R)}}(i,j) = F^{I}_{i'j} e^{ik^{I}_{i'} z_{1(2)}}$$

$$\mathbf{W}_{\mathbf{BL(R)}}(i,j) = F^{II}_{ij} e^{ik^{II}_{i} z_{1(2)}}$$

where $i' = i \;\; (i-8)$ and the column vectors $\mathbf{l}$, $\mathbf{r}$ and $\mathbf{w}$ represent the wave function in the left-hand barrier, right-hand barrier and well respectively, i.e. $\mathbf{l}(i) = A^A_i$, $\mathbf{w}(i) = A^B_i$, $\mathbf{r}(i) = A^C_i$.

This can be rewritten as

$$\begin{pmatrix} \mathbf{W}_{\mathbf{AL}} & 0 \\ 0 & \mathbf{W}_{\mathbf{AR}} \end{pmatrix} \mathbf{b} = \begin{pmatrix} \mathbf{W}_{\mathbf{BL}} \\ \mathbf{W}_{\mathbf{BR}} \end{pmatrix} \mathbf{w}$$

or

$$\mathbf{W}_{\mathbf{A}} \mathbf{b} = \mathbf{W}_{\mathbf{B}} \mathbf{w} \tag{2.21}$$

where

$$\mathbf{b} = \begin{pmatrix} \mathbf{l} \\ \mathbf{r} \end{pmatrix}.$$

The final boundary condition we have to apply is to ensure conservation of probability current, i.e. continuity of $\frac{\partial \Psi}{\partial z}$. It is far less obvious how this condition can be expressed in terms of the envelopes. If a complete basis set were being used, continuity of $\frac{\partial \Psi}{\partial z}$ could be ensured by requiring that $\frac{\partial \mathcal{F}_j}{\partial z}$ must be continuous for all j (which we will label condition (a)), where the envelope $\mathcal{F}_j = \sum_i A_i F_{ij} e^{ik_i z}$. Similarly, if we used only one basis function the appropriate condition would be that $\frac{1}{m^*(z)} \frac{\partial \mathcal{F}}{\partial z}$ must be continuous (condition (b)), where $m^*(z)$ is a position dependent effective mass. The latter boundary condition has been used by many authors, notably

Bastard [11] and Altarelli [12]. It has been suggested by Pötz and Ferry [20] that the conditions appropriate to an n band **k.p** model are that $\mathbf{B}\frac{\partial \mathcal{F}_j}{\partial z}$ must be continuous (condition (c)), where **B** is obtained by integrating the Hamiltonian across the interface, and this is the method used by Eppenga *et al* [13] (Indeed, this reduces to condition (b) in the limit $n \rightarrow 1$). Recently Burt [21] has discussed this issue in some depth and has pointed out that all three approaches should lead to the same result, since one of the assumptions made in deriving conditions (b) and (c) is that the effective masses of both regions are similar, and thus these conditions should reduce to condition (a).

We have adopted the procedure suggested by Pötz and Ferry (condition (c)), which involves integrating the Hamiltonian across the interfaces. This approach seems the most appropriate to an 8 band **k.p** model, since it guarantees the conservation of probability current. (In the next section the results obtained in this way will be compared with those obtained by simply requiring the derivatives of the envelopes to be continuous).

As mentioned previously, we can write the Hamiltonian as

$$\mathbf{H} = \mathbf{H}_2\frac{\partial^2}{\partial z^2} + \mathbf{H}_1\frac{\partial}{\partial z} + \mathbf{H}_0 \tag{2.22}$$

(where we have written k_z explicitly as the $\frac{\partial}{\partial z}$ operator).

In section 2.4 it was assumed implicitly that all the terms in the Hamiltonian are independent of z. When considering the matching of the wave function across an interface (lying in the (x, y) plane), however, the

Hamiltonian will not be independent of z, and we must rewrite equation (2.2) in the more general form

$$\mathbf{H} = \frac{\partial}{\partial z}\mathbf{H}_2\frac{\partial}{\partial z} + \frac{1}{2}\left[\mathbf{H}_1\frac{\partial}{\partial z} + \frac{\partial}{\partial z}\mathbf{H}_1\right] + \mathbf{H}_0 \tag{2.23}$$

Integrating this expression across an interface we obtain [13]

$$\sum_i A_i\left[\mathbf{H}_2\frac{\partial}{\partial z} + \frac{1}{2}\mathbf{H}_1\right]\mathbf{f}_i \quad \text{must be continuous} \tag{2.24}$$

where $\mathbf{f}_i = (F_{i1}, \ldots, F_{ij}, \ldots, F_{i8})e^{ik_iz}$. In deriving this boundary condition it is necessary to assume that the matrix functions are slowly varying on the scale of the lattice parameter.

Since $\frac{\partial}{\partial z}\mathbf{f}_i = ik_i\mathbf{f}_i$, we can express condition (2.24) as

$$\sum_{i=1}^{8} A_i^A \sum_{l=1}^{8} B_{jl}^{Ii}F_{il}^{I}e^{ik_i^Iz_1} = \sum_{i=1}^{16} A_i^B \sum_{l=1}^{8} B_{jl}^{IIi}F_{il}^{II}e^{ik_i^{II}z_1} \tag{2.25}$$

$$\sum_{i=9}^{16} A_{i-8}^C \sum_{l=1}^{8} B_{jl}^{Ii}F_{il}^{I}e^{ik_i^Iz_2} = \sum_{i=1}^{16} A_i^B \sum_{l=1}^{8} B_{jl}^{IIi}F_{il}^{II}e^{ik_i^{II}z_2} \tag{2.26}$$

where $\mathbf{B}^{Li}$ is the matrix $\left[\mathbf{H}_2^Lk_i^L + \frac{1}{2}\mathbf{H}_1^L\right]$. (In practice in turns out that the $\mathbf{H}_1^L$ term is very much smaller than the first term, and the inclusion of this term introduces numerical difficulties into the solution of the quantum well eigenvalue problem. For these reasons we neglect this term in our calculations).

Equations (2.25) and (2.26) can be expressed in matrix form :

$$\mathbf{D}_{\mathbf{AL}}\mathbf{l} = \mathbf{D}_{\mathbf{BL}}\mathbf{w}$$

$$\mathbf{D}_{\mathbf{AR}}\mathbf{r} = \mathbf{D}_{\mathbf{BR}}\mathbf{w}$$

where

$$\mathbf{D}_{\mathbf{AL(R)}}(i,j) = \sum_{l=1}^{8} B_{jl}^{Ii'} F_{i'l}^{I} e^{ik_{i'}^{I} z_{1(2)}}$$

$$\mathbf{D}_{\mathbf{BL(R)}}(i,j) = \sum_{l=1}^{8} B_{jl}^{IIi'} F_{i'l}^{II} e^{ik_{i}^{II} z_{1(2)}}$$

and i', $\mathbf{l}$, $\mathbf{r}$ and $\mathbf{w}$ are as previously defined. Alternatively, as with the first boundary condition, we can write

$$\mathbf{D}_{\mathbf{A}}\mathbf{b} = \mathbf{D}_{\mathbf{B}}\mathbf{w} \tag{2.27}$$

where $\mathbf{D}_{\mathbf{A}} = \begin{pmatrix} \mathbf{D}_{\mathbf{AL}} & 0 \\ 0 & \mathbf{D}_{\mathbf{AR}} \end{pmatrix}$ and $\mathbf{D}_{\mathbf{B}} = \begin{pmatrix} \mathbf{D}_{\mathbf{BL}} \\ \mathbf{D}_{\mathbf{BR}} \end{pmatrix}$. By simple rearrangement of (2.27) and (2.21) we have

$$\mathbf{b} = \mathbf{D}_{\mathbf{A}}^{-1}\mathbf{D}_{\mathbf{B}}\mathbf{w}$$

and

$$\mathbf{w} = \mathbf{W}_{\mathbf{B}}^{-1}\mathbf{W}_{\mathbf{A}}\mathbf{b}.$$

Hence

$$\mathbf{W}_{\mathbf{B}}^{-1}\mathbf{W}_{\mathbf{A}}\mathbf{D}_{\mathbf{A}}^{-1}\mathbf{D}_{\mathbf{B}}\mathbf{w} = \mathbf{w} \tag{2.28}$$

We thus need to locate the eigenvectors of $\mathbf{W}_{\mathbf{B}}^{-1}\mathbf{W}_{\mathbf{A}}\mathbf{D}_{\mathbf{A}}^{-1}\mathbf{D}_{\mathbf{B}}$ which have an eigenvalue of 1 to obtain the wave function of a quantum well bound state. Alternatively we can search for the points at which

$\det(\mathbf{W}_\mathrm{B}{}^{-1}\mathbf{W}_\mathrm{A}\mathbf{D}_\mathrm{A}{}^{-1}\mathbf{D}_\mathrm{B} - 1) = 0$. Such eigensolutions will only exist at discrete energies (for any given in-plane wave vector $k_\parallel$), corresponding to the energy levels of the bound states. These energies are located using a simple binary search.

2.7 Bandstructure of $\mathrm{In}_{0.53}\mathrm{Ga}_{0.47}\mathrm{As/InP}$ Quantum Wells

In recent years much interest has been shown in the InGaAsP/InP system, due to the scope it offers for optical devices. The alloy composition of the quaternary in such a device can be varied independently of the physical dimensions (e.g. quantum well width), which allows the device parameters to be tailored to some extent. By selecting the appropriate alloy composition, the band gap can be chosen to match the 1.3μm or 1.55μm optical fibre windows, the wavelengths at which transmission along optical fibres is most efficient. Indeed, it turns out that an $\mathrm{In}_x\mathrm{Ga}_{1-x}\mathrm{As}$ ternary alloy lattice matched to InP (this requires $x = 0.53$) has a band gap within the 1.55μm window.

We present in this section the results of a calculation of the energy levels and wave functions of the bound states of a $\mathrm{In}_{0.53}\mathrm{Ga}_{0.47}\mathrm{As/InP}$ quantum well. The bandstructure parameters used are given in Appendix A. Some of the effective masses of $\mathrm{In}_{0.53}\mathrm{Ga}_{0.47}\mathrm{As}$ are not well characterised, and where necessary we have interpolated linearly between the parameters of the InAs and GaAs binaries.

The in-plane bandstructure of a 50Å $In_{0.53}Ga_{0.47}As/InP$ quantum well is shown in figure 2.4. The full lines represent the [100] direction and the broken lines the [110] direction. Clearly the bandstructure is very nearly isotropic, and in our calculations on optical properties (see later chapters) we shall make this simplifying assumption.

The conduction band can be seen to be almost parabolic, which suggests that a simple effective mass approach will give a reasonable representation of this band. In the valence band, however, marked non-parabolic behaviour is evident. The valence bandstructure is strongly influenced by interactions between subbands, such as those seen between the 1st and 2nd subbands at $k_{\|} \simeq 0.03\text{Å}^{-1}$ and between the 3rd and 4th subbands at $k_{\|} \simeq 0.06\text{Å}^{-1}$. These effects arise because the symmetry of the valence band states and the quantum well are such that the subbands cannot cross and *anticrossing* structure occurs.

Figure 2.5 shows the form of the wave function for each of the subbands at $k_{\|} = 0$. The envelope $\mathcal{F}_j(z) = \sum_i A_i F_{ij} e^{ik_i z}$ (i.e. the coefficient of each zone centre Bloch function $|u_j>$) is plotted as a function of z for each j. The vertical lines indicate the limits of the quantum well. At $k_{\|} = 0$ the bulk heavy hole band is completely decoupled from the other subbands (see table 2.2), so for a heavy hole state only $\mathcal{F}_2$(hh) (or $\mathcal{F}_6$ for a spin down state) will be non-zero. The light hole states contain some components derived from bulk zone centre conduction band and spin split-off states, and so will in general have non-zero values of $\mathcal{F}_1$(el) and $\mathcal{F}_4$(so) in

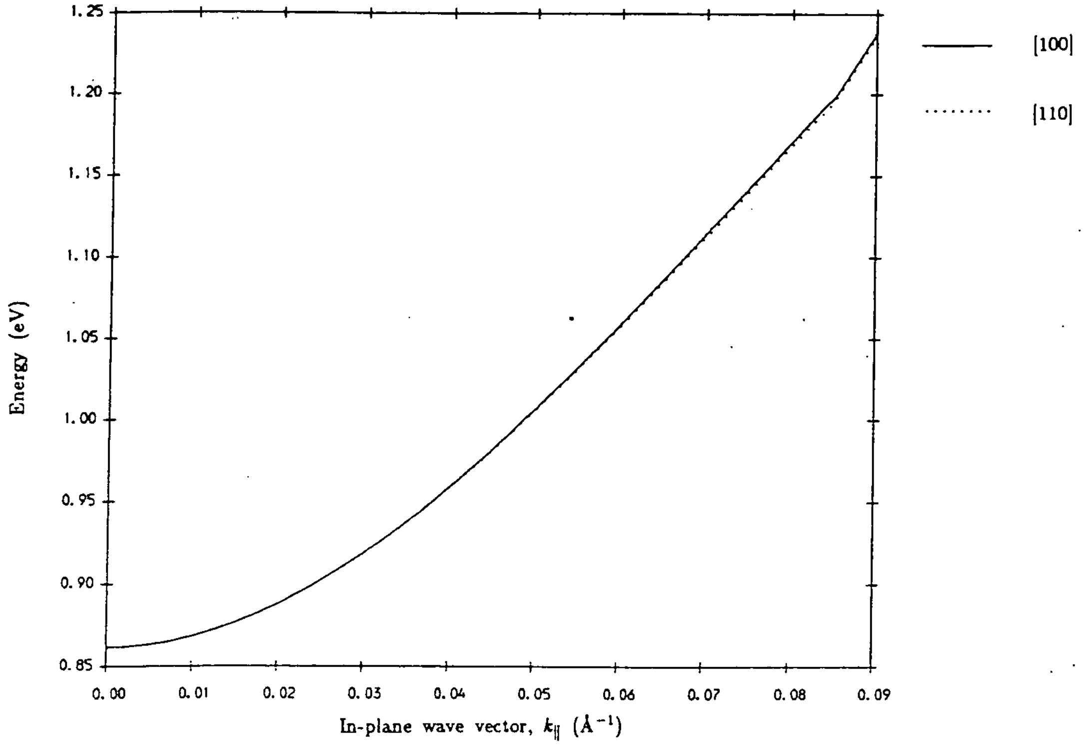

a) Conduction Band.

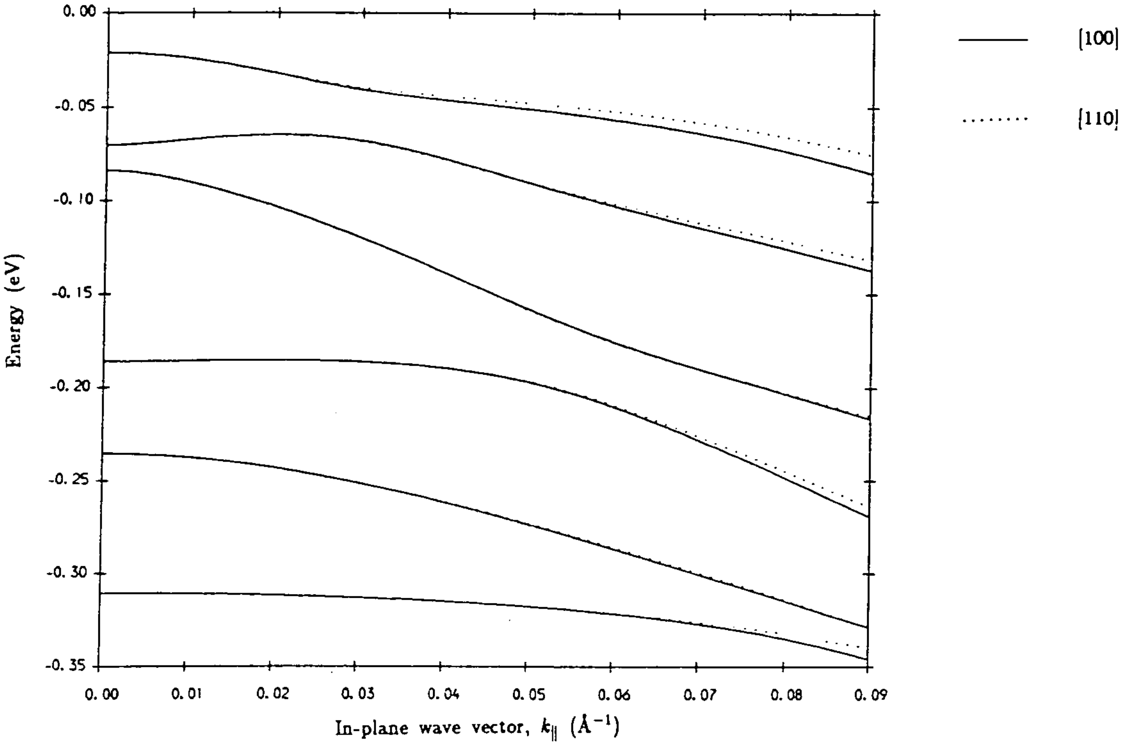

b) Valence Band.

Figure 2.4

In-plane bandstructure of a 50Å $In_{0.53}Ga_{0.47}As/InP$ quantum well.

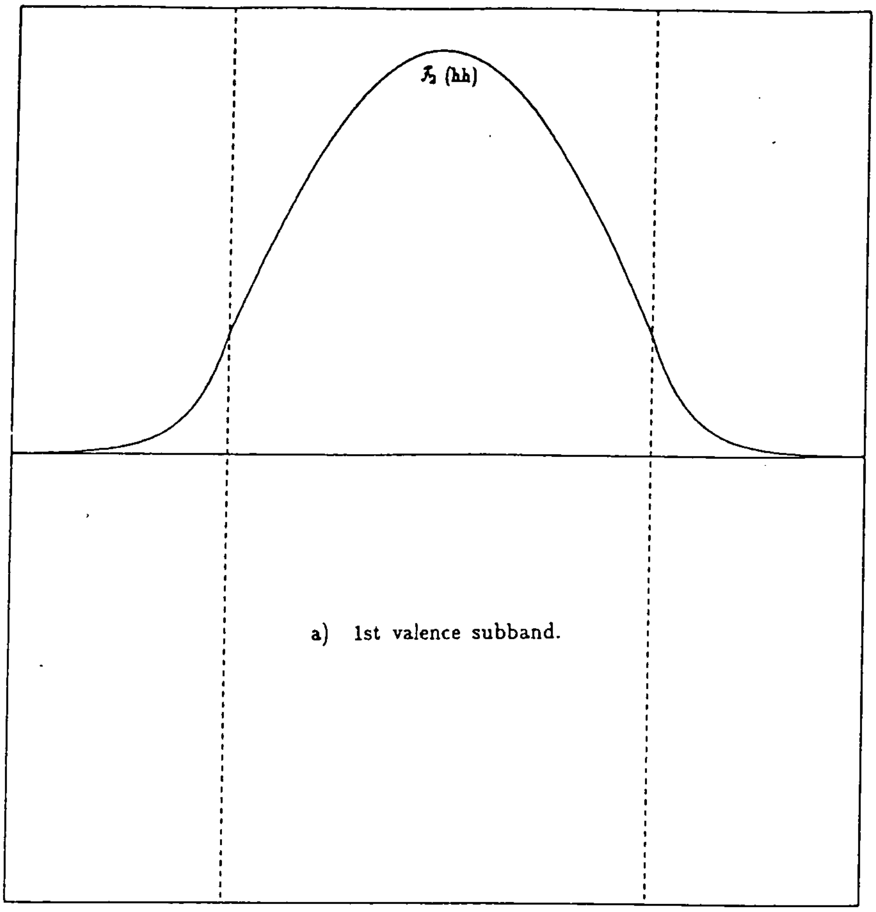

a) 1st valence subband.

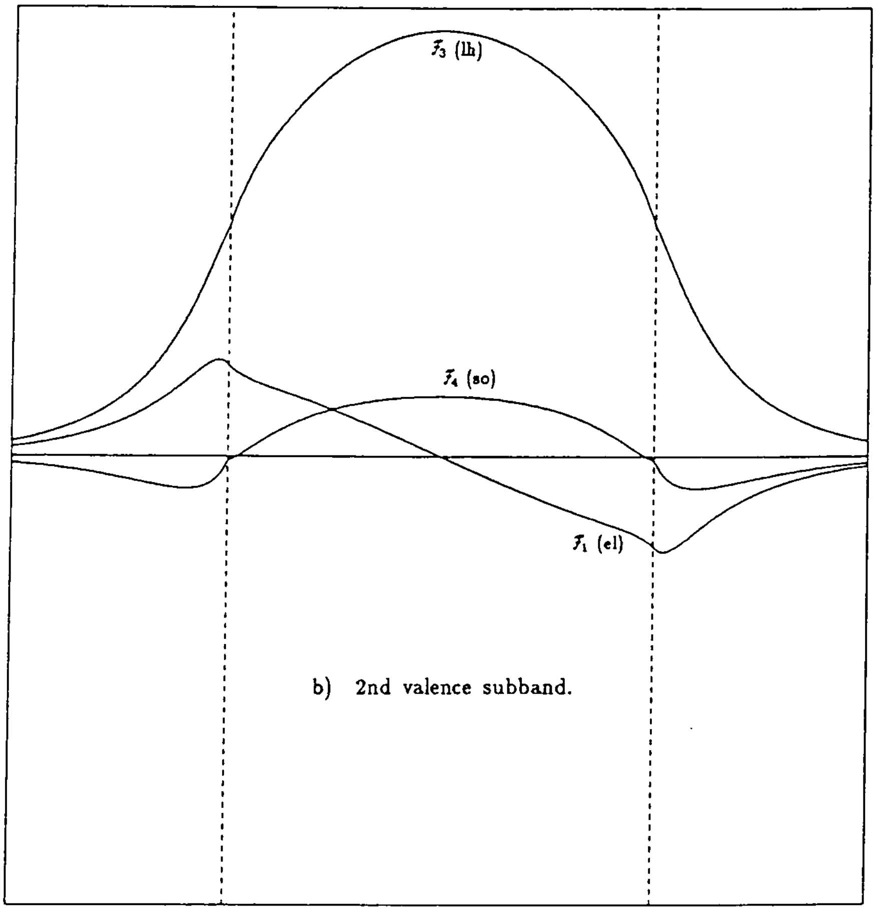

b) 2nd valence subband.

Figure 2.5

Subband edge wave functions.

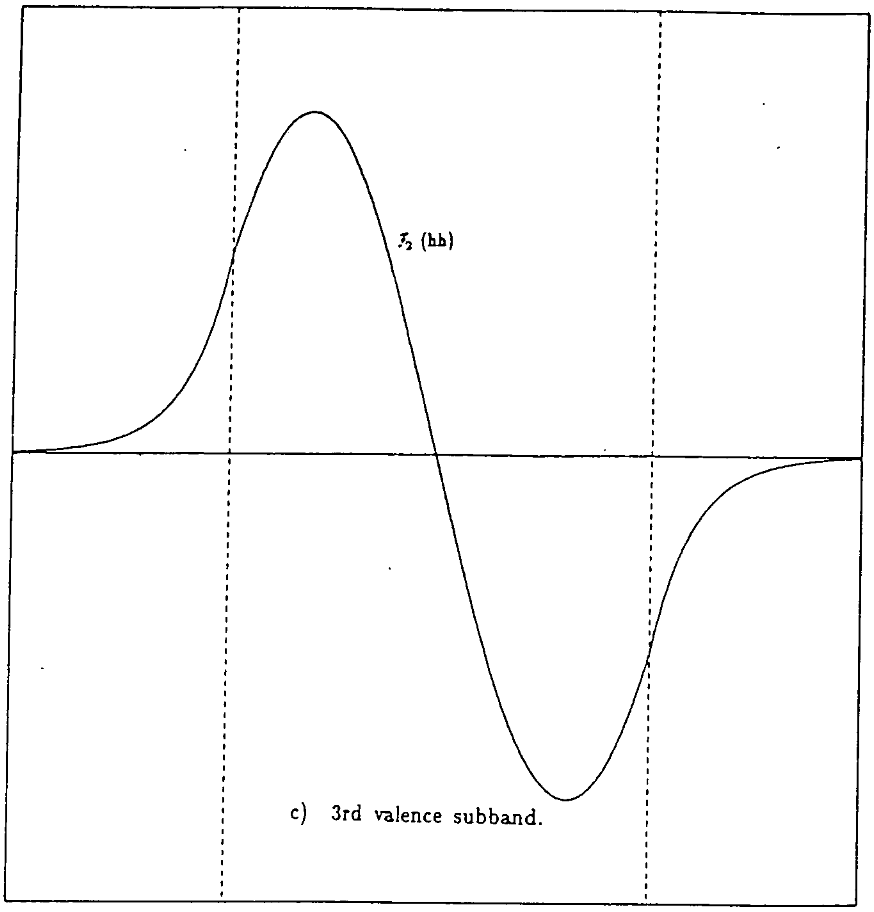

c) 3rd valence subband.

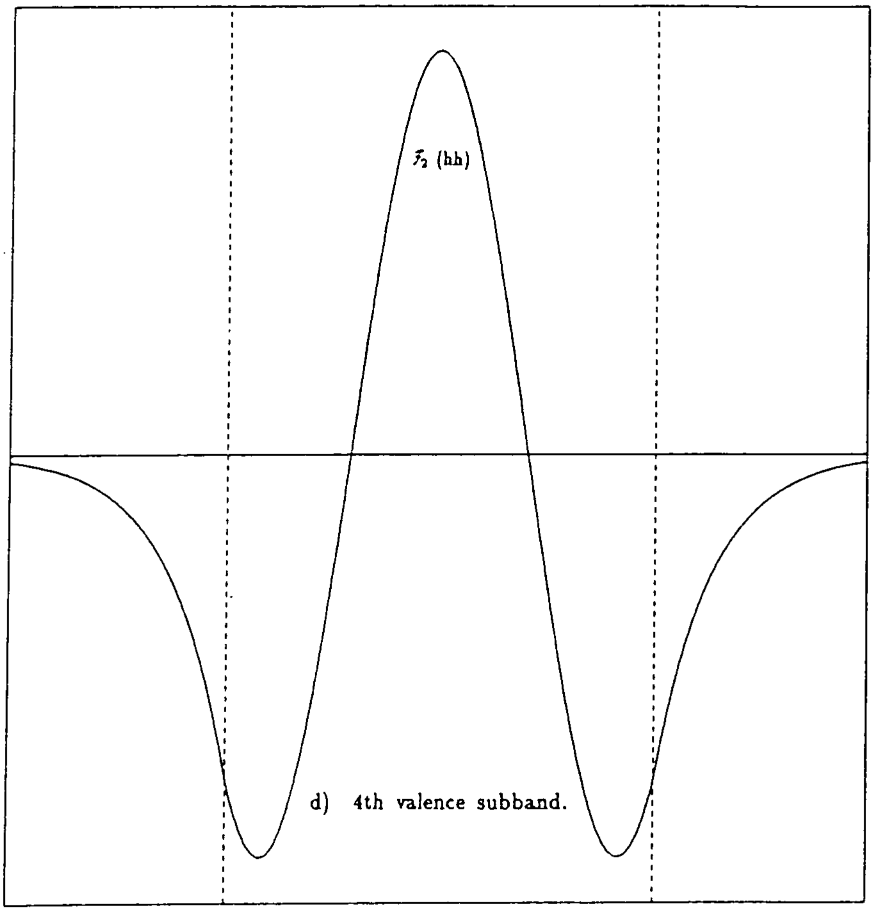

d) 4th valence subband.

Figure 2.5 (continued)

Subband edge wave functions.

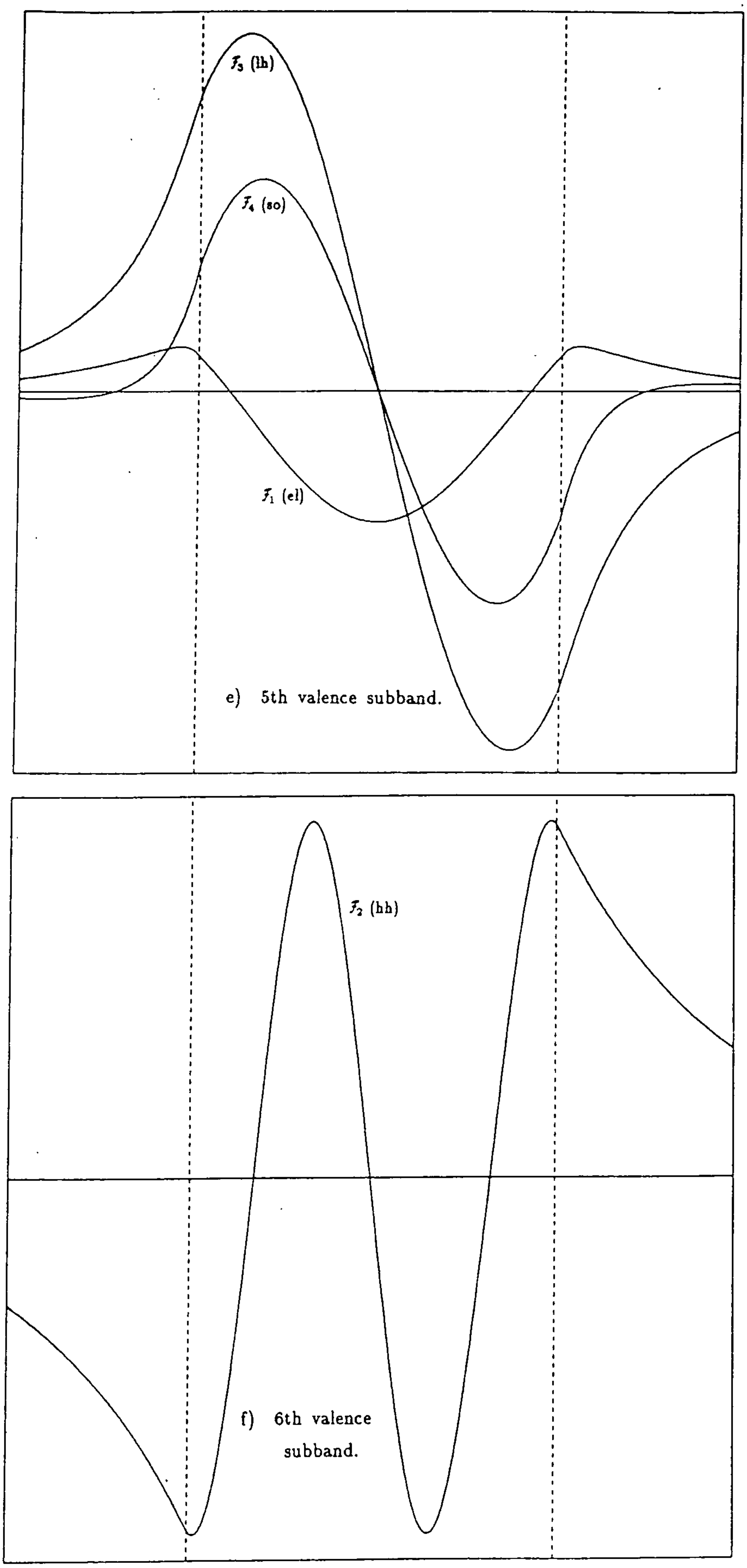

Figure 2.5 (continued)

Subband edge wave functions.

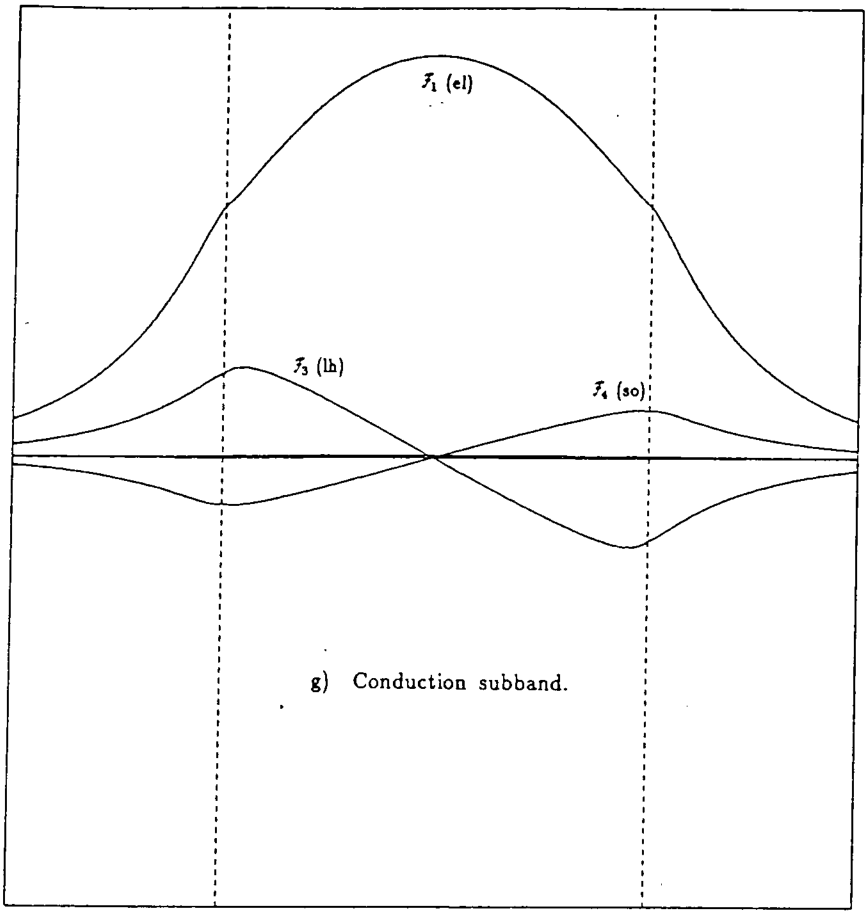

g) Conduction subband.

Figure 2.5 (continued)

Subband edge wave functions.

addition to $\mathcal{F}_3$(lh). At $k_{\|} \neq 0$ the bulk states are all coupled, so mixing between heavy holes and other states is possible.

The first, third, fourth and sixth valence band bound states (figures 2.5 a, c, d and f) respectively correspond to the first four heavy hole states, and the envelopes clearly correspond to the equivalent 'particle in a box' harmonics. Similarly, the second and fifth states (figures 2.5 b and e) are the so-called ground and first excited light hole states although, as discussed above, these states do contain a contribution from the bulk conduction and spin split-off Bloch states. In the same way, the conduction band bound state (figure 2.5 g) contains contributions from bulk light hole and spin split-off Bloch states. Note that in both of the light hole states and in the conduction band state the envelopes $\mathcal{F}_3$(lh) and $\mathcal{F}_4$(so) have the same parity (odd or even), and $\mathcal{F}_1$(el) has the opposite parity. In fact, the envelopes fall into two sets $\{\mathcal{F}_1, \mathcal{F}_2, \mathcal{F}_7, \mathcal{F}_8\}$ and $\{\mathcal{F}_3, \mathcal{F}_4, \mathcal{F}_5, \mathcal{F}_6\}$, with envelopes from the same set all having the same parity (within a given state) and envelopes from the other set having the opposite parity [14].

In the region of an anticrossing in the bandstructure, the wave functions of the states involved become very heavily mixed (see figure 2.6). It is no longer possible to describe the character of a state as the nth excited heavy or mth light hole level; rather it is an admixture of two such levels. In this case both of the first two subbands are admixtures of the ground heavy hole state with the ground light hole state. This is seen most clearly in figure 2.6a, which represents the wave function of the first

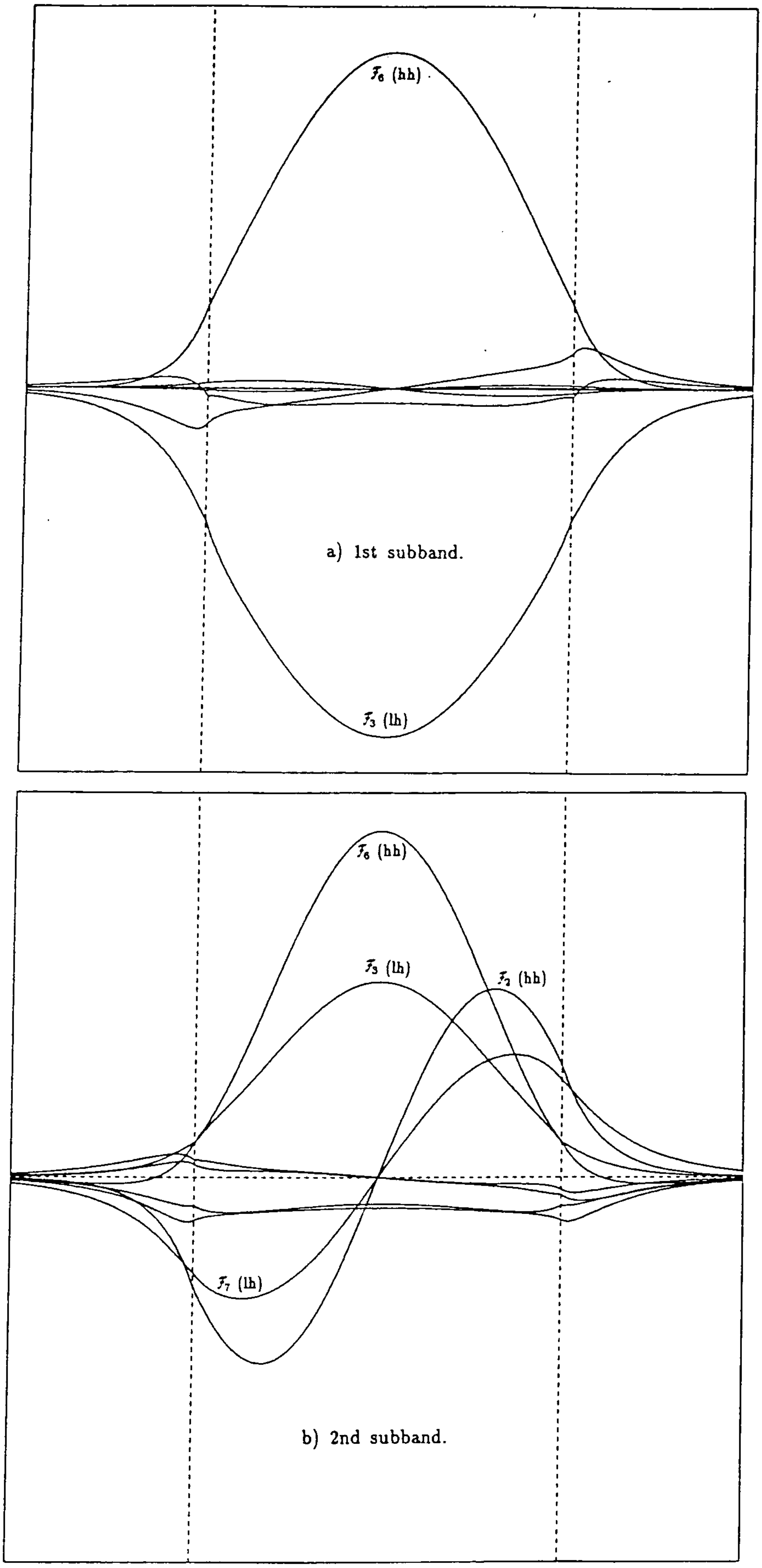

Figure 2.6

Wave functions in an anticrossing region
(1st and 2nd subbands at $k_{\|} = 0.05\text{Å}^{-1}$).

subband at $k_x = 0.05\text{Å}^{-1}$, $k_y = 0$.

Essentially what is happening in such a region is that the character of the states is behaving as though the subbands were actually crossing. Beyond the anticrossing region the first two subbands can be seen to have exchanged character — the first subband looks like a ground light hole state, and the second like a ground heavy hole state (see figure 2.7).

This anticrossing of the subbands and the mixing of their character can have a profound effect on the optical matrix elements between bound states, allowing transitions which would be expected to be forbidden by parity considerations applied to simple single band effective mass models. These effects will be discussed in detail in chapter 4.

In the previous section we discussed the form taken by the boundary conditions on the quantum well wave function, and pointed out that Burt [21] has suggested that the precise form of the boundary condition on the derivative of the wave function does not seriously affect the bandstructure. We have tested this assertion for a 50Å $\text{In}_{0.53}\text{Ga}_{0.47}\text{As/InP}$ quantum well (figure 2.8), and find discrepancies of up to around 10 meV in the positions of the subbands when the condition making $\frac{\partial \mathcal{F}_j}{\partial z}$ continuous is used, rather than requiring $\mathbf{B}\frac{\partial \mathcal{F}_j}{\partial z}$ to be continuous (where the symbols are as defined in the previous section). The shape of the subbands is essentially unaffected by the boundary conditions used, and so for most applications Burt's assertion would appear to be a reasonable one, especially considering how poorly characterised the bandstructure parameters of some materials (particularly

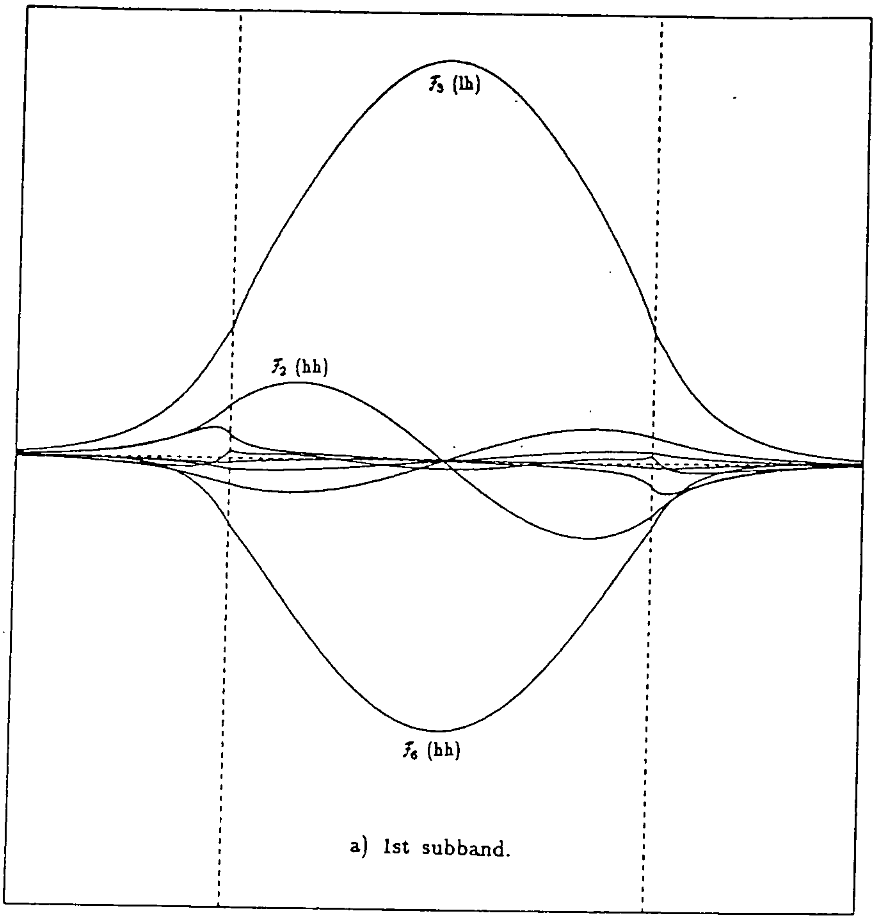

a) 1st subband.

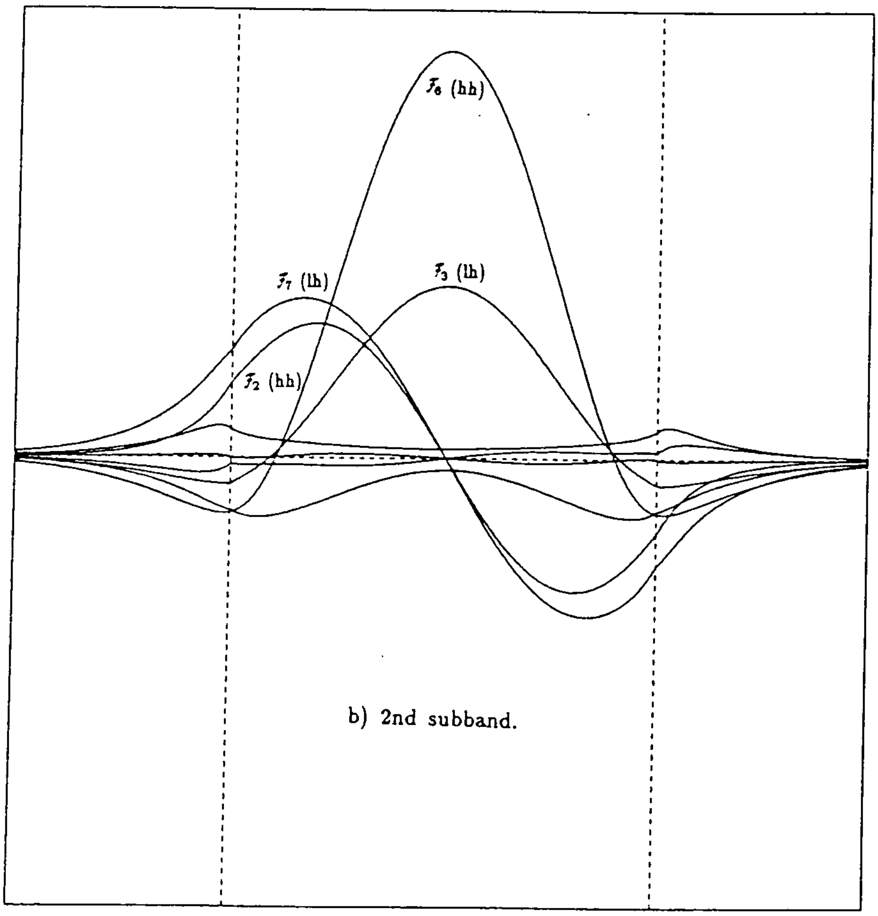

b) 2nd subband.

Figure 2.7

Wave functions at $k_{\|} = 0.09\text{Å}^{-1}$.

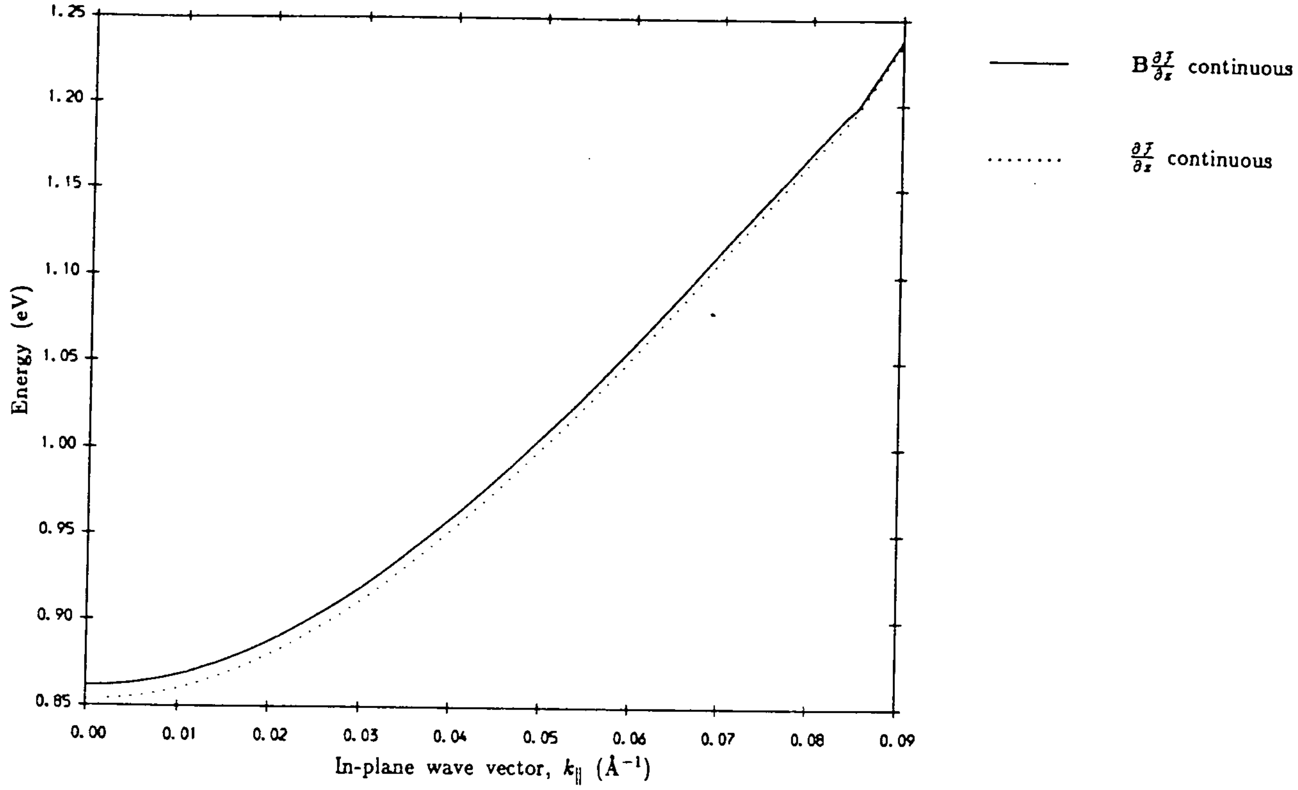

a) Conduction Band.

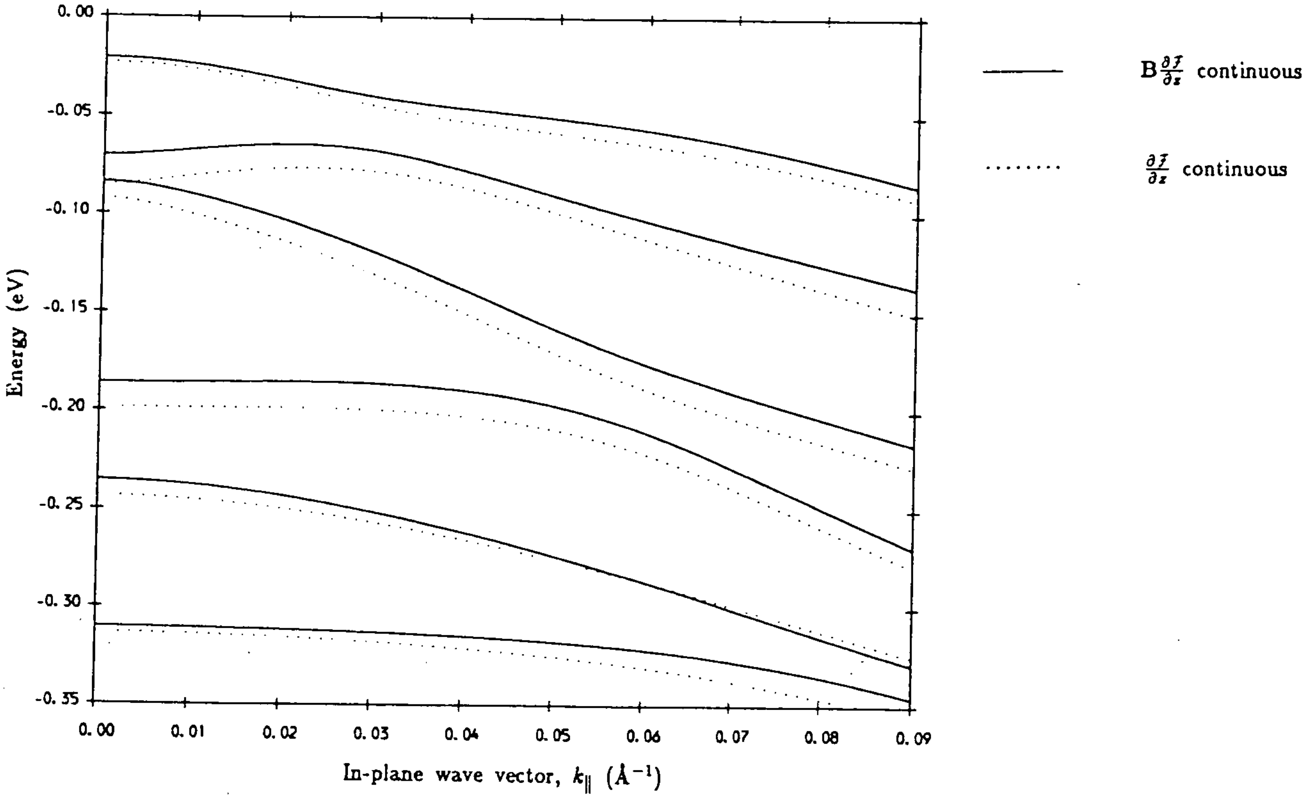

b) Valence Band.

Figure 2.8

Effect of boundary conditions on the bandstructure.

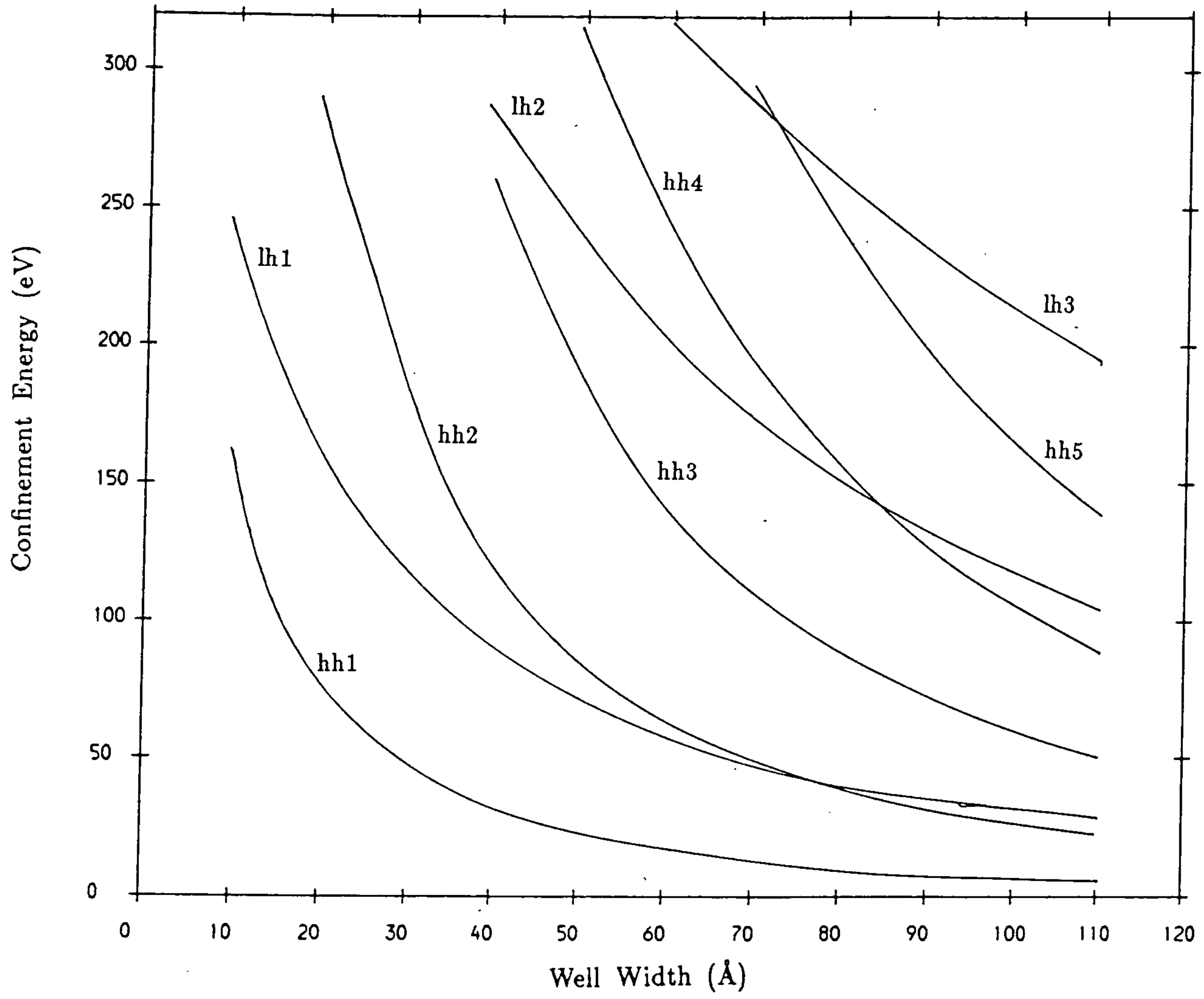

Figure 2.9

Variation of confinement energy with quantum well width in the $In_{0.53}Ga_{0.47}As/InP$ system.

2.8 Unbound States

In the preceding sections we have described how the energy levels and wave functions of the bound states of a quantum well can be calculated. We now turn our attention to those states which lie at an energy above the top of the barriers, in either the conduction band or the valence band. Unlike the bound states, these 'unbound' states are not restricted to discrete energy levels, but form a continuum.

Since the energy of an unbound state lies within the conduction or valence band of the barrier material, rather than in the band gap, its wave function will not, in general, decay away from the interfaces. Rather it will be oscillatory in the barriers, extending throughout all space. Whereas the nature of a bound state is largely determined by the properties of the well material, the nature of an unbound state will be intrinsically dependent on the form of this 'barrier wave'. The problem is essentially that of a free particle interacting with a potential well. We consider wave functions in the form of stationary waves. It would be perfectly possible to consider travelling waves in an alternative but essentially equivalent approach, but stationary waves are more convenient to deal with.

One interesting aspect to the continuum states is the resonance effect which occurs when the energy of the unbound state is such that a half-integral number of wavelengths of the wave function will fit exactly within the well. At this energy the probability of the particle (electron or hole) being found in the well reaches a maximum. These resonant states have been investigated theoretically by Brum and Bastard [23], who referred to them as 'virtual bound states'. These states are indeed a continuation of the set of bound states, and can in principle exist even if the wave function in the barriers decays to zero rather than taking the form of a standing wave. They occur at certain discrete energies which correspond to the energies at which bound states would exist were the well depth to be infinite.

Although the nature of the unbound state problem is somewhat different to the bound state calculation, the same techniques can be used to obtain the wave function. The boundary conditions on the wave function and its derivative at the interfaces take exactly the same form, and again the wave function must remain finite on approaching infinity, but now some of the bulk barrier states are oscillatory in nature. When calculating bound states all the bulk barrier states were restricted to either the left-hand or right-hand barrier, to ensure that the wave function remained finite, but these oscillatory states must be allowed to exist in both barrier regions. We thus have more bulk states to include in the linear combinations in regions A and C than was the case for a bound state, yet there are the same number of boundary conditions. The problem is now underspecified if only the interface matching conditions for the wave function are considered. It is necessary to specify the form of the barrier wave function to some extent before we can obtain the unbound state wave function.

Consider an unbound conduction band state. There will be four oscillatory conduction band bulk states in each of the barrier regions A and C — one 'ingoing' and one 'outgoing' wave of each spin state. The bulk valence band states are all evanescent and those which decay away from the interfaces are chosen for each region. In order to have 32 unknown expansion coefficients as before (16 in the well and 8 in each barrier) we must treat the coefficients of half of the oscillatory conduction band states in the barriers as 'unknowns' and specify the coefficients of the other half. Thus, for example, if we specify the coefficients of the ingoing wave of each spin state on both sides of the heterostructure we can determine the coefficients of the outgoing waves. Since one of the boundary conditions ($\frac{\partial \Psi}{\partial z}$ continuous) requires the conservation of probability current, if we set the coefficient of the ingoing waves of one spin state to zero, that spin state will be eliminated from the outgoing waves as well. We can specify the parity of the wave function (symmetric or antisymmetric) by choosing the coefficients of the ingoing waves of the required spin state on each side of the well to be equal or opposite (equal in magnitude but of opposite sign).

For an unbound valence band state the situation is essentially the same, but there will be more oscillatory states in the barriers, half of which will be light hole states and half heavy hole states (and at higher energies spin-orbit split-off hole states as well). We can follow a similar prescription to that described for the conduction band, and can eliminate one type of bulk hole state from the solution in the barrier by setting the coefficients of the appropriate ingoing waves to zero.

We can thus write the wave function of an unbound state as

$$\text{Region A}: \quad \Psi^A = \sum_i \sum_j A_i^A F_{ij}^I e^{i\mathbf{k}_i^I . \mathbf{r}} \left|u_j^I\right\rangle + \sum_c \sum_j U_c^A F_{cj}^I e^{i\mathbf{k}_c^I . \mathbf{r}} \left|u_j^I\right\rangle \tag{2.30}$$

$$\text{Region B}: \quad \Psi^B = \sum_i \sum_j A_i^B F_{ij}^{II} e^{i\mathbf{k}_i^{II} . \mathbf{r}} \left|u_j^{II}\right\rangle \tag{2.31}$$

$$\text{Region C}: \quad \Psi^C = \sum_i \sum_j A_i^C F_{ij}^I e^{i\mathbf{k}_i^I . \mathbf{r}} \left|u_j^I\right\rangle + \sum_c \sum_j U_c^C F_{cj}^I e^{i\mathbf{k}_c^I . \mathbf{r}} \left|u_j^I\right\rangle \tag{2.32}$$

where the first term $\left(\sum_i\right)$ in Ψ^A and Ψ^C includes all the evanescent bulk barrier states and the outgoing oscillatory states, and the second term $\left(\sum_c\right)$ includes all the ingoing oscillatory states. If we specify the U_c^A's and U_c^C's we can obtain the A_i's in each region by applying the same boundary conditions as for the bound states.

Continuity of the total wave function then requires

$$\sum_{i=1}^{8} A_i^A F_i^I j e^{ik_i^I z_1} + \sum_c U_c^A F_{cj}^I e^{ik_c^I z_1} = \sum_{i=1}^{16} A_i^B F_{ij}^{II} e^{ik_i^{II} z_1} \tag{2.33}$$

and

$$\sum_{i=9}^{16} A_i^C F_i^I j e^{ik_i^I z_2} + \sum_c U_c^C F_{cj}^I e^{ik_c^I z_2} = \sum_{i=1}^{16} A_i^B F_{ij}^{II} e^{ik_i^{II} z_2} \tag{2.34}$$

for all j.

Using the same notation as before, we can express the boundary conditions in matrix notation :

$$\mathbf{W_{AL}l} + \mathbf{u_L} = \mathbf{W_{BL}w}$$

$$\mathbf{W_{AR}r} + \mathbf{u_R} = \mathbf{W_{BR}w}$$

and, similarly, to ensure conservation of probabilty current

$$\mathbf{D_{AL}l} + \mathbf{d_L} = \mathbf{D_{BL}w}$$

$$\mathbf{D_{AR}r} + \mathbf{d_R} = \mathbf{D_{BR}w}$$

with the column vectors $\mathbf{u_L}$, $\mathbf{u_R}$, $\mathbf{d_L}$ and $\mathbf{d_R}$ given by

$$\mathbf{u_L}(j) = \sum_c U_c^A F_{cj}^I e^{ik_c^I z_1} \tag{2.35}$$

$$\mathbf{u_R}(j) = \sum_c U_c^C F_{cj}^I e^{ik_c^I z_2} \tag{2.36}$$

and

$$\mathbf{d_L} = \mathbf{B u_L} \tag{2.37}$$

$$\mathbf{d_R} = \mathbf{B u_R} \tag{2.38}$$

with

$$\mathbf{B} = \left[\mathbf{H_2}\frac{\partial}{\partial z} + \frac{1}{2}\mathbf{H_1}\right]$$

As before, we can combine the equations for the left and right hand interfaces together to obtain

$$\mathbf{W_A b} + \mathbf{u} = \mathbf{W_B w} \tag{2.39}$$

$$\mathbf{D_A b} + \mathbf{d} = \mathbf{D_B w} \tag{2.40}$$

where $\mathbf{u} = \begin{pmatrix} \mathbf{u_L} \\ \mathbf{u_R} \end{pmatrix}$ and $\mathbf{d} = \begin{pmatrix} \mathbf{d_L} \\ \mathbf{d_R} \end{pmatrix}$. Solving (2.39) and (2.40) gives

$$\mathbf{b} = \left(\mathbf{W_B^{-1} W_A} - \mathbf{D_B^{-1} D_A}\right)^{-1} \left(\mathbf{D_B^{-1} d} - \mathbf{W_B^{-1} u}\right) \tag{2.41}$$

$$\mathbf{w} = \left(\mathbf{W_A^{-1} W_B} - \mathbf{D_A^{-1} D_B}\right)^{-1} \left(\mathbf{W_A^{-1} u} - \mathbf{D_A^{-1} d}\right) \tag{2.42}$$

Since $\mathbf{u}$ and $\mathbf{d}$ are completely specified by our choice of ingoing barrier waves we can solve (2.41) and (2.42) to obtain the unbound wave function. Sample results are given in figure 2.10 for a 50Å $In_{0.53}Ga_{0.47}As$ quantum well. The wave functions are plotted in the same convention as for bound states, i.e. plotting the z dependence of the envelope of each zone centre Bloch function, and are shown for $k_{\|} = 0$. As discussed above, the nature and parity of the wave function is determined by the choice of 'barrier wave', and as with the bound states the heavy and light hole states are completely decoupled for $k_{\|} = 0$.

2.9 Summary and Applications of the Method

In this chapter we have described a method of obtaining the bandstructure and wave functions of both bound and unbound quantum well states. The method has the advantage of giving realistic bandstructure close to the Γ point without being too demanding on computer resources. Since the wave function is expressed as a linear combination of bulk states, each of which is expressed as the product a plane wave envelope and a zone centre Bloch function, the nature of a calculated state (whether it is a light or heavy hole, a ground or excited state, etc) is immediately apparent; this makes it easy to achieve a physical understanding of the problem under consideration. In particular, mixing effects between quantum well subbands can be easily discerned by inspection of the relevant wave functions. Although all the results we describe have been obtained by numerical calculations, the approach we have used enables us to gain the kind of insight associated

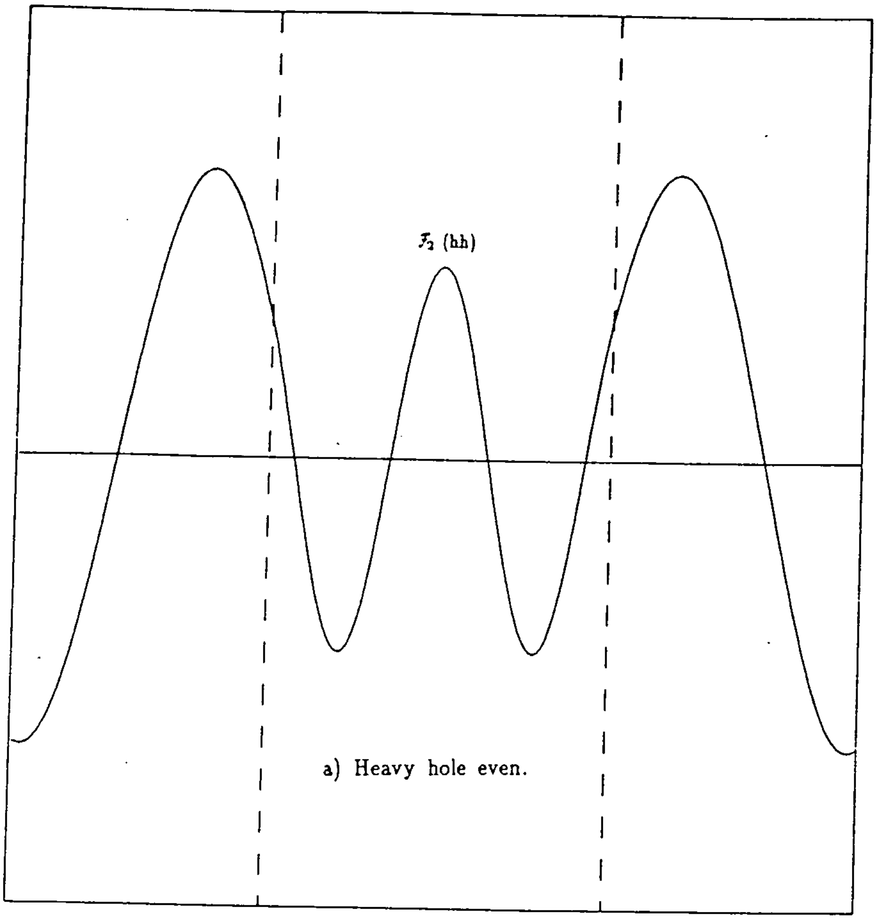

a) Heavy hole even.

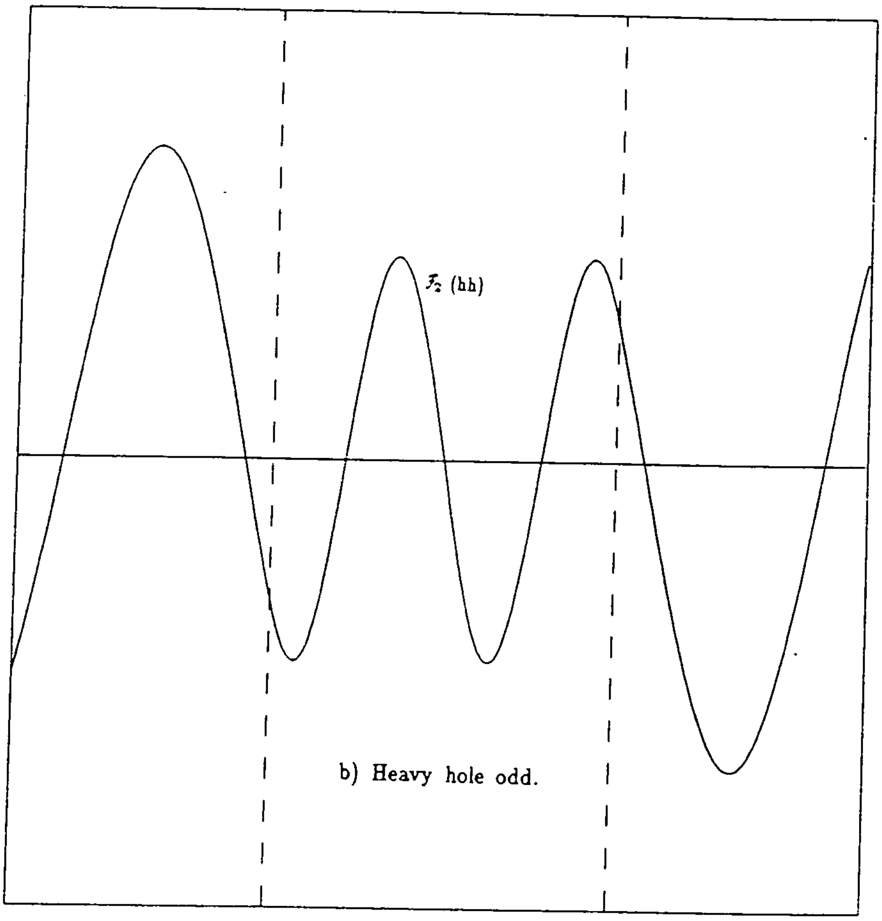

b) Heavy hole odd.

Figure 2.10

Wave functions of unbound states.

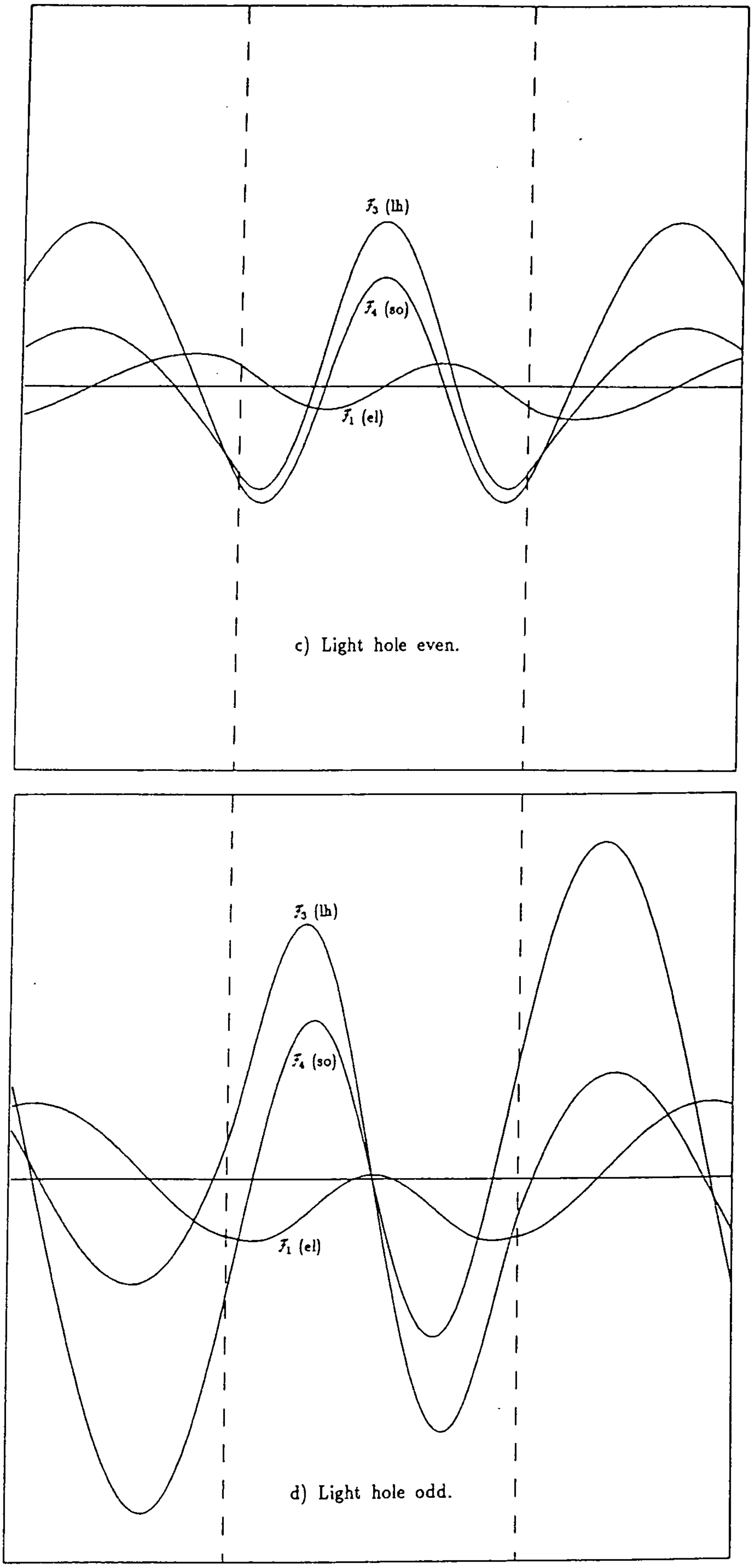

Figure 2.10 (continued)

Wave functions of unbound states.

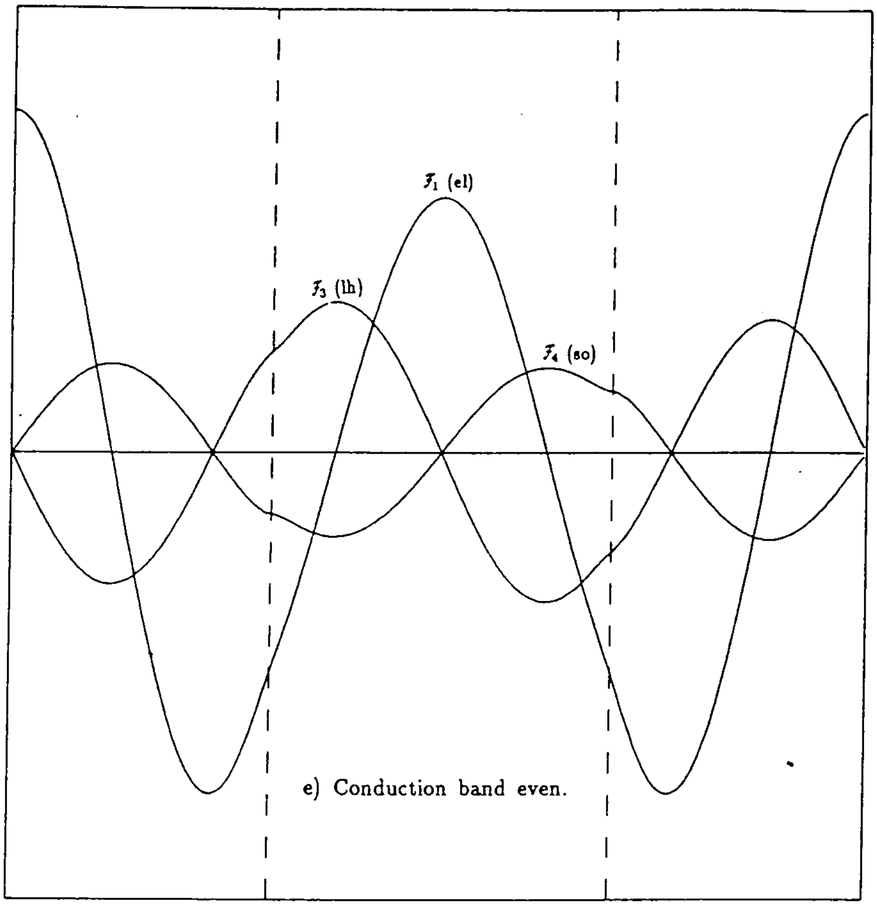

e) Conduction band even.

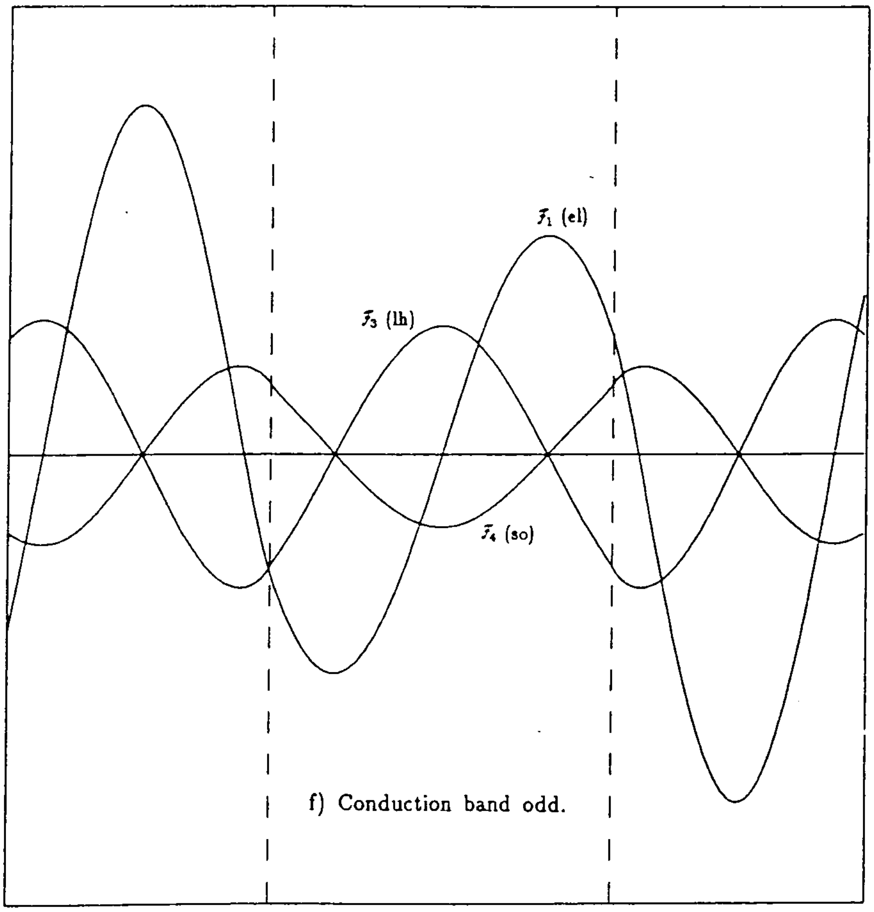

f) Conduction band odd.

Figure 2.10 (continued)

Wave functions of unbound states.

with algebraic theory because of the small dimensionality of the matrices involved and the physical significance of the basis functions.

Although the work in this thesis will be confined to studies of quantum wells, the approach we have described is equally applicable to superlattice structures — the only difference occurs in the boundary conditions. In the next chapter, we shall describe how the method can be extended to study strained layer systems — heterostructures in which materials with different lattice constants in the bulk are used for the well and barrier. One great advantage of our model is the ease with which such enhancements can be introduced.

The bandstructure calculations described in this chapter form the basis of all the work described in this thesis. In chapters 5 and 6 the method is applied to calculations of gain and spontaneous emission spectra in heterostructure lasers, and in chapter 7 the calculations of unbound states will be used to investigate intervalence band absorption, a significant loss mechanism in the same devices.

In addition, the model has been used to perform calculations of valence band states in GaAs/AlAs quantum wells [24]. The results of this work have been used as the foundation for a Monte Carlo study of hole transport in such a system [25,26]. Matrix elements were computed for deformation potential, non-polar optical, polar optical and piezoelectric phonon scattering processes from wave functions obtained using our **k**.**p** model. As will be shown to be the case in the optical processes described later in this thesis, the matrix elements show marked deviations from those derived using a simple one band effective mass approach, because of the strong subband mixing effects. The scattering rates for the various phonon scattering processes have been derived from the matrix elements and bandstructure using Fermi's Golden Rule, and have formed the basis of both steady state and ensemble Monte Carlo simulations. These simulations have been used to study hole transport and relaxation in a GaAs quantum well [25,26].

References for Chapter Two

[1] See any quantum mechanics text, e.g L.I. Schiff, *Quantum Mechanics*, 3rd edition, McGraw Hill, 1968, pp 37-44.

[2] R. Dingle, Festkorperprobleme **15**, 21 (1975).

[3] E.O. Kane, 'Energy band theory' in *Handbook on Semiconductors* vol. 1, ed. Moss, North-Holland, 1982, pp 193-217.

[4] J.N. Schulman and T.C. McGill, Phys. Rev. B **19**, 6341 (1979).

[5] M.L. Cohen and J.R. Chelikowsky, 'Pseudopotentials for semiconductors' in *Handbook on Semiconductors* vol. 1, ed. Moss, North-Holland, 1982, pp 219-255.

[6] M.F.H. Schuurmans and G.W. 't Hooft, Phys. Rev. B **31**, 8041 (1985).

[7] E.O. Kane, J. Phys. Chem. Solids **1**, 82 (1956); **1**, 249 (1957).

[8] J.M. Luttinger and W. Kohn, Phys. Rev. **97**, 869 (1955).

[9] G. Dresselhaus, A.F. Kip and C. Kittel, Phys. Rev. **98**, 368 (1955).

[10] S.S. Nedorezov, Sov. Phys. - Solid State **12**, 1814 (1971).

[11] G. Bastard, Phys. Rev. B **24**, 5693 (1981); **25**, 7584 (1982).

[12] M. Altarelli, Physica **117B** & **118B**, p.747 (1983) North Holland; Phys. Rev. B **28**, 842 (1983); M. Altarelli, U. Ekenberg and A. Fasolino, Phys. Rev. B **32**, 5138 (1985).

[13] R. Eppenga, M.F.H. Schuurmans and S. Colak, Phys. Rev. B **36**, 1554 (1987).

[14] J.N. Schulman and Y.C. Chang, Phys. Rev. B **31**, 2056 (1981); Y.C. Chang and J.N. Schulman, Phys. Rev. B **31**, 2069 (1981).

[15] D.C. Smith and C. Mailhiot, Phys. Rev. B **33**, 8345 (1986); **33**, 8360 (1986).

[16] E.P. O'Reilly, Semicond. Sci. Technol. **1**, 128 (1986).

[17] P. Löwdin, J. Chem. Phys. **19**, 1396 (1951).

[18] G.H. Parker and C.A. Mead, Phys. Rev. Lett. **21**, 605 (1968).

[19] S.R. White and L.J. Sham, Phys. Rev. Lett. **47**, 879 (1981).

[20] W. Pötz and D.K. Ferry, Superlattices and Microstructures **3**, 57 (1987).

[21] M.G. Burt in *Bandstructure Engineering in Semiconductor Microstructures* ed. R.A. Abram and M. Jaros, NATO ASI Series B Vol. 189, Plenum 1989 p 99.

[22] S. Brand and D.T. Hughes, Semicond. Sci. Technol. **2**, 607 (1987).

[23] J.A. Brum and G. Bastard, Phys. Rev. B **33**, 1420 (1986).

[24] A.C.G. Wood, University of Durham internal report, unpublished (1987).

[25] R.W. Kelsall, R.I. Taylor, A.C.G. Wood and R.A. Abram, Superlattices and Microstructures **5**, 207 (1989).

[26] R.W. Kelsall, R.I. Taylor, A.C.G. Wood and R.A. Abram, Semicond. Sci. Technol. **5**, 877 (1990).

CHAPTER THREE

STRAINED LAYER QUANTUM WELLS

3.1 Introduction

In the previous chapter we discussed the properties of quantum wells in which the lattice constant of both the well and barrier materials was the same. Much work has been carried out on such materials systems, especially in the GaAlAs and InGaAlAs/InP families. However, recent advances in epitaxial growth technology, especially the continuing development of molecular beam epitaxy (MBE) and metal organic chemical vapour deposition (MOCVD), have opened up the possibility of growing heterostructures in which there is a mismatch between the lattice parameters of the constituent materials. Provided the layers are thin ($\lesssim$100Å)[†], this lattice mismatch is accommodated via an elastic strain, which modifies the electronic properties of the device. In particular the highest valence band state in a strained device may have a reduced effective mass, promising faster complementary logic devices and more efficient long wavelength lasers. The ability to grow heterostructures in new material combinations, in particular Ga(Al)InAs/Ga(Al)As and Si/Ge, and the prospect of being able to tailor

---

[†] The thickness allowed depends on the degree of mismatch and on material and growth parameters. For most moderately ($\sim$ 1%) strained systems this thickness will be $\sim$ 100Å.

the properties of a device by varying the lattice constant and layer width have led to a great deal of interest being shown in strained layer structures in the last couple of years.

Another technologically important application of the ability to grow strained layers is the prospect of combining optical devices grown from III-V materials and conventional silicon devices on the same chip.

In this chapter, we shall show how the effect of strain can be included within the framework of our **k**.**p** quantum well model, and describe the effect that such a strain field has on a low dimensional device.

3.2 Growth and Critical Epilayer Size

We shall at this point consider the effect of attempting to grow an epilayer of a material with lattice constant a_e on a substrate with a different lattice constant a_s (see figure 3a). We confine our attention to growth along the [100] crystal axis. The lattice mismatch can be accomodated in one of two ways, depending on the size of the mismatch and the thickness of the layers.

One possibility (see figure 3.1b) is that the lattice of the epilayer can be elastically distorted such that its lattice constant in the plane parallel to the interface $a_{\|}$ matches that of the substrate a_s [1]. In this case, the epilayer relaxes in the growth direction by an amount determined by the

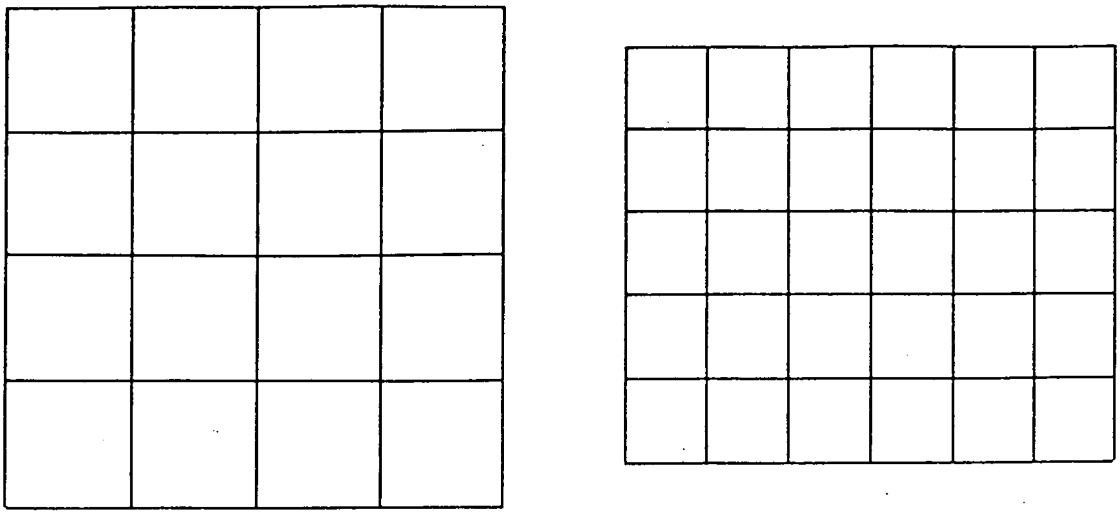

a) Free standing epilayer and substrate.

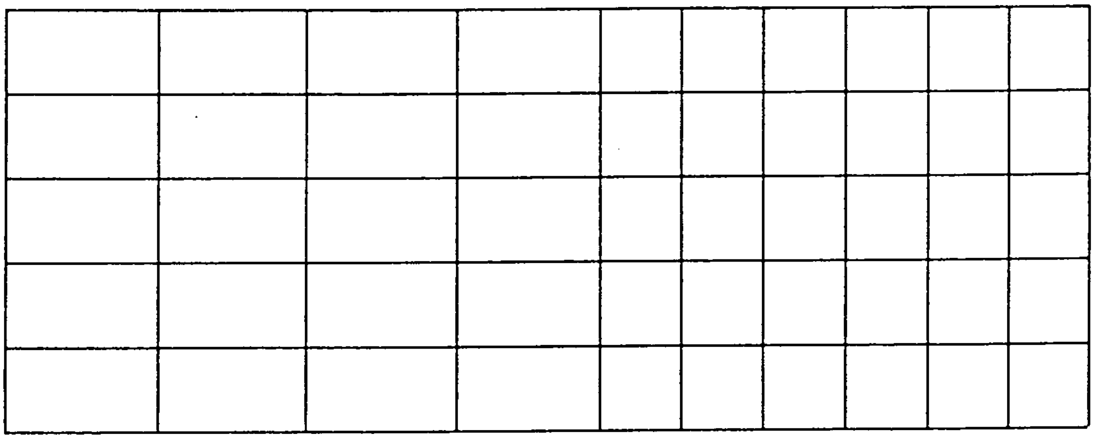

b) Strained layer regime.

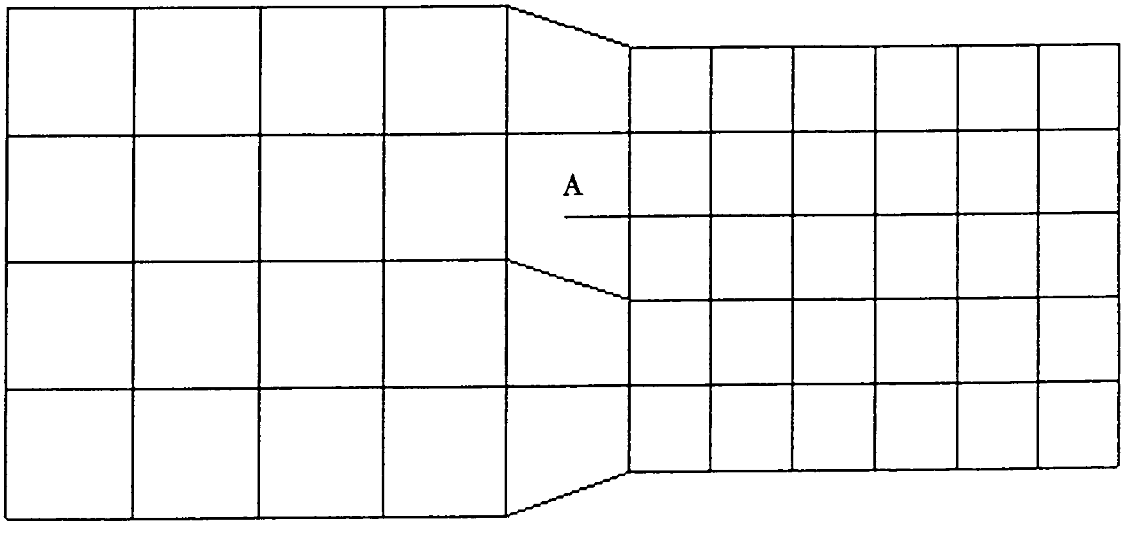

c) Relaxed regime, showing dangling bond (A).

Figure 3.1

Growth of a lattice mismatched epilayer.

two dimensional Poisson ratio

$$\Delta a_{\perp} = \Delta a_{\parallel} \left(\frac{-2\sigma}{1-\sigma} \right) \tag{3.1}$$

with $\Delta a_{\perp}$ the induced change in the lattice constant in the growth direction, and σ the one dimensional Poisson ratio. This is known as the *strained layer* regime, since the perturbation of the lattice creates a uniform elastic strain field throughout the epilayer. The deformation energy of the strained epilayer is clearly proportional to its height h, and is given by [2]

$$E_{st} = 2G \left(\frac{1+\sigma}{1-\sigma} \right) \varepsilon_{\parallel}^{2} h \tag{3.2}$$

where G is the shear modulus of the epilayer material, σ is Poisson's ratio in the epilayer, and $\varepsilon_{\parallel}$ is the net in-plane strain, $(a_s - a_e)/a_e$.

Alternatively, the epilayer may retain its natural lattice parameter and form as many chemical bonds as possible with the top atomic layer of the substrate (see figure 3.1c). In this *relaxed* regime the strain is accomodated by dangling bonds and other interface defects, some of which may propogate through the epilayer [3]. The deformation energy in this case is a property of the interface, and is largely independent of the height of the epilayer.

It is clear that for sufficiently thin epilayers, the strained layer regime will be energetically favourable. As the epilayer height is increased, a critical thickness will be reached at which the deformation energy is the same for the two regimes, and beyond this point dislocations start to form and the relaxed regime is entered (see figure 3.2). This critical thickness was investigated by Matthews and Blakeslee [1] in the mid 1970's, who showed it to be given by the equation

$$h_c = \left(\frac{1-\sigma/4}{4\pi(1+\sigma)}\right)\frac{b}{\varepsilon_{\|}}\left[\ln\left(\frac{h_c}{b}\right)+1\right] \tag{3.3}$$

where b is the dislocation Burgers vector (typically $\simeq$ 4Å). This equation has more recently been verified in the InGaAs/GaAs system by Andersson *et al* [4].

The Matthews - Blakeslee formula predicts $h_c \simeq$90Å for $\varepsilon_{\|} = 1\%$. In fact, it is possible to grow stable strained layers of widths greater than h_c under certain conditions [5] since the energy required to nucleate a dislocation is greater than that required to sustain one which is already present. However, growth of layers thicker than h_c is only possible if the growth process does not itself introduce too many defects, and hence the precise critical layer thickness depends upon the growth temperature and growth rate as well as on the interface quality [6,7].

3.3 Modelling Strained Layer Structures

It is clear that the presence of an elastic strain field arising from the tetragonal distortion of the crystal unit cell which occurs in lattice-mismatched structures will alter the electronic properties of a device. In this section we shall show how this effect can be described within the

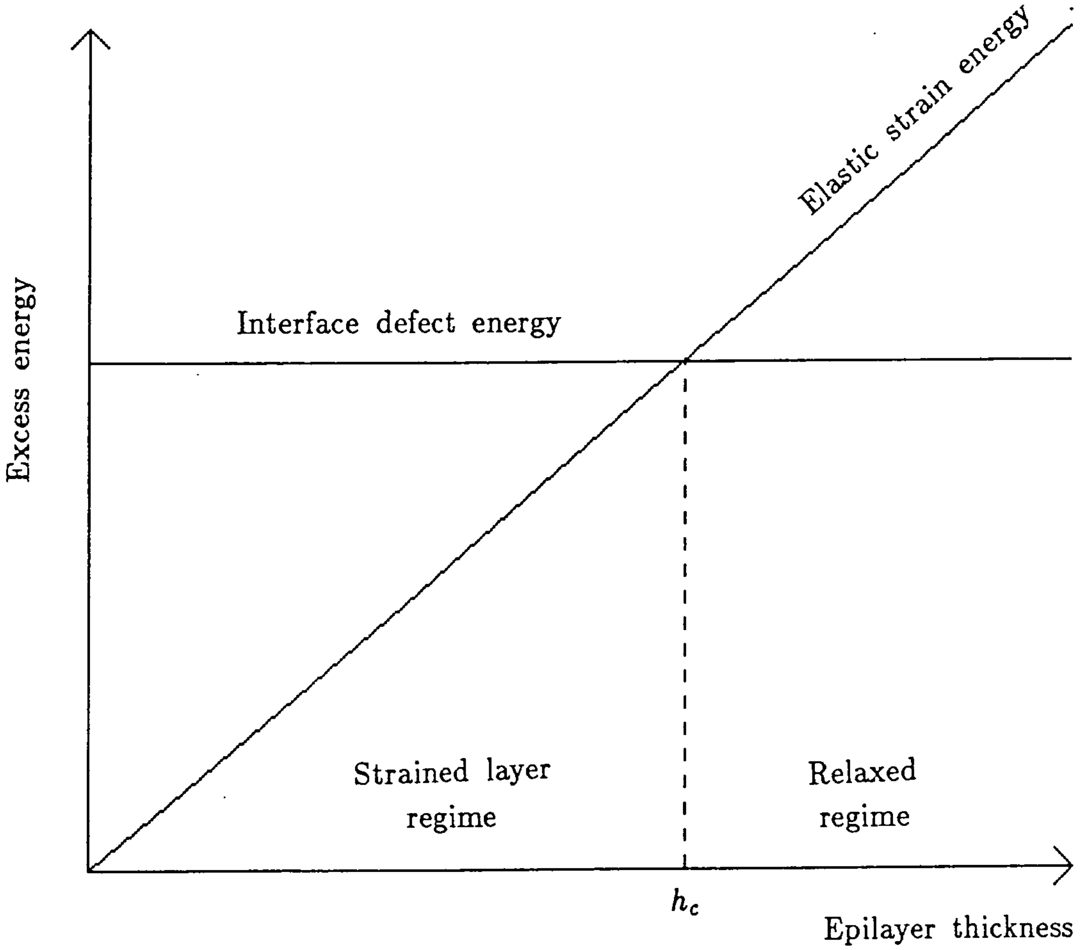
Elastic strain energy
Interface defect energy
Excess energy
Strained layer regime
Relaxed regime
h_c
Epilayer thickness

Figure 3.2

framework of our **k.p** model.

In a strained layer system, as we described in the previous section, the epilayer material is under a biaxial strain. In the case of the quantum well structures we shall study, the well material will be under a biaxial compression (or tension), and the barriers lattice matched to the substrate and hence unstrained. This biaxial compression (tension) is equivalent to a combination of a hydrostatic compression (tension) and a uniaxial tension (compression). The effects of both hydrostatic and uniaxial stresses on the electronic properties of semiconductors have been extensively studied experimentally [8,9,10] and theoretically [11,12].

For a strained-layer quantum well grown along the [100] axis, the strain tensor is diagonal, with the following non-zero components [12] (where the growth direction is taken to be the z axis) :

$$\varepsilon_{xx} = \varepsilon_{yy} = \frac{\Delta a_0}{a_0} \tag{3.4}$$

$$\varepsilon_{zz} = -2\frac{c_{12}}{c_{11}}\varepsilon_{xx} \tag{3.5}$$

where a_0 is the natural lattice constant of the well material and Δa_0 is the distortion of this lattice constant in the (x, y) plane resulting from the mismatched growth, i.e. $\Delta a_0 = a_s - a_0$ with a_s being the substrate lattice constant; c_{11} and c_{12} are the elastic moduli of the well material.

Since the terms introduced into the Hamiltonian by the strain turn out to induce much smaller splittings than the spin-orbit parameter Δ and the Kane matrix element E_P $(= 2m_0P^2/\hbar^2)$, as will be seen in the next section, the angular momentum quantum numbers j and m_j remain good quantum numbers in the strained system. Thus we may use the same basis functions as for the unstrained system. The strain terms which appear in the Hamiltonian are then obtained from the operation of the deformation potential tensor (which is spin independent and diagonal in the S,X,Y,Z basis) on the strain tensor. In the X,Y,Z basis the strain Hamiltonian is then diagonal, with each 4 × 4 spin block being [12]

$$\begin{pmatrix} c(\varepsilon_{xx}+\varepsilon_{yy}+\varepsilon_{zz}) & 0 & 0 & 0 \\ 0 & l\varepsilon_{xx}+m(\varepsilon_{yy}+\varepsilon_{zz}) & 0 & 0 \\ 0 & 0 & l\varepsilon_{yy}+m(\varepsilon_{xx}+\varepsilon_{zz}) & 0 \\ 0 & 0 & 0 & l\varepsilon_{zz}+m(\varepsilon_{xx}+\varepsilon_{yy}) \end{pmatrix} \tag{3.6}$$

where c, l, m and n are deformation potentials.

These terms are readily transformed into our chosen basis, giving the strain Hamiltonian shown in table 3.1.

We can then follow exactly the same procedure to obtain the quantum well bandstructure and wave functions as we outlined for unstrained wells in chapter 2, simply including the extra terms of table 3.1 in the Hamiltonian of table 2.2.

3.4 The Bulk Bandstructure of a Strained Semiconductor

Before going on to discuss the effect of an elastic strain on the bandstructure of a quantum well, it will be helpful to investigate how such a strain modifies the states of a bulk semiconductor. We shall imagine a bulk semiconductor which is somehow under a uniform biaxial strain, in the same way that the well material of a lattice mismatched quantum well is strained.

The material we shall study is $\mathrm{In}_{0.53}\mathrm{Ga}_{0.47}\mathrm{As}$, which is lattice matched to InP and is widely used in optoelectronic devices. The InGaAa alloy system forms the basis of many experimental investigations into the effects of strained layers because devices can be grown in which the alloy is either under a biaxial compression or a tension, by respectively increasing or decreasing the indium content from 53%.

The bulk complex bandstructure of unstrained $\mathrm{In}_{0.53}\mathrm{Ga}_{0.47}\mathrm{As}$ is illustrated in figure 3.3, following the conventions outlined in section 2.5. This material has a direct band gap of 0.75eV and a spin-orbit splitting of 0.356eV. The effective masses and bandstructure parameters used are given in Appendix A. The bandstructure is isotropic for the unstrained material, which is in fact a consequence of the degeneracy at the top of the valence band. When this degeneracy is broken, for example by a biaxial strain, the dispersion becomes anisotropic. This can be seen in figure 3.4, which shows the effect of a 1.5% biaxial compression on the bandstructure. The strain

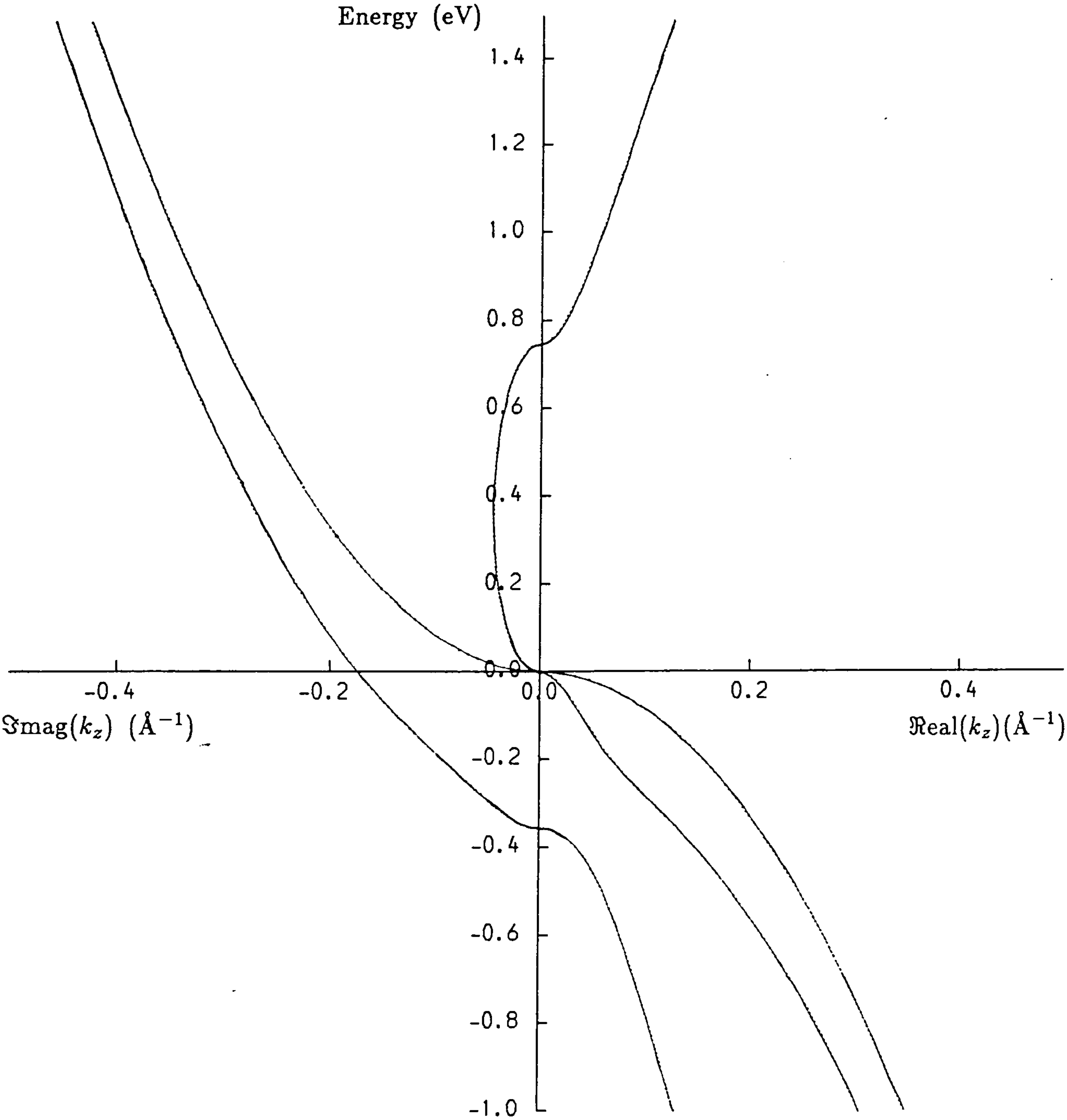

Figure 3.3

Bulk bandstructure of $In_{0.53}Ga_{0.47}As$ — unstrained.

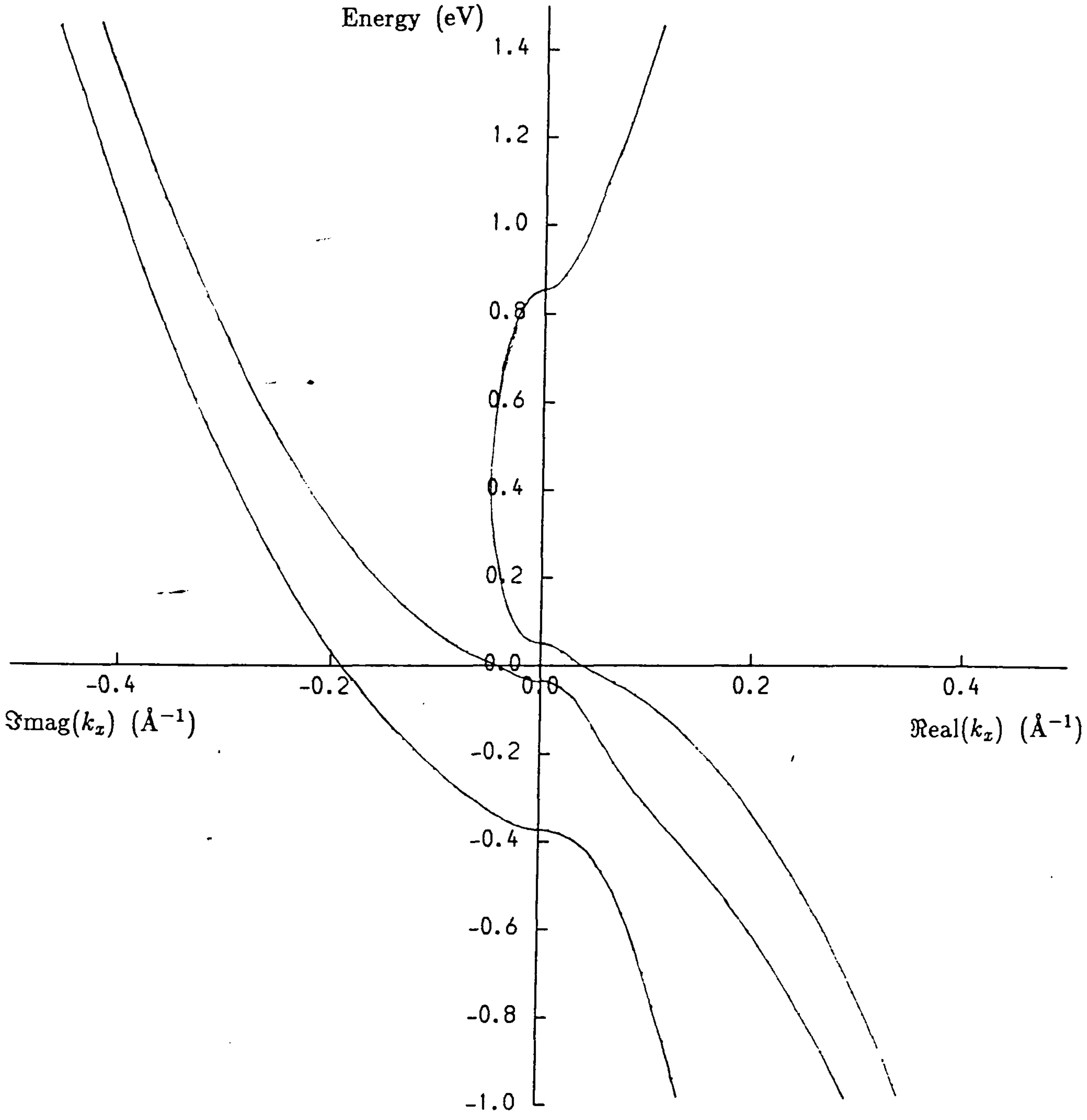

a) k_x direction.

Figure 3.4

Bulk bandstructure of $In_{0.53}Ga_{0.47}As$ — $1\frac{1}{2}$% biaxial compression.

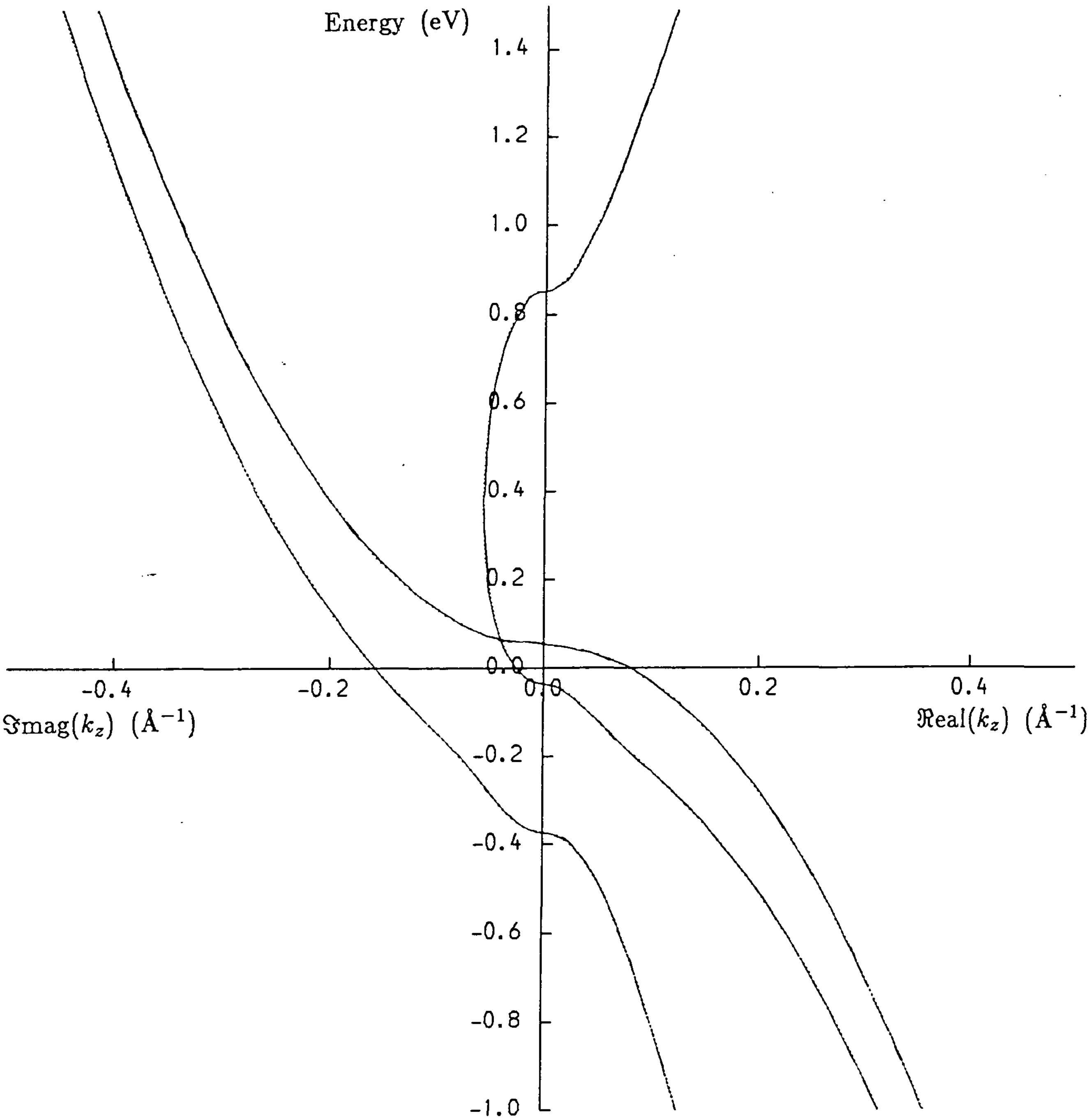

b) k_z direction.

Figure 3.4 (continued)

Bulk bandstructure of $In_{0.53}Ga_{0.47}As$ — $1\frac{1}{2}$% biaxial compression.

is applied in the (x,y) plane, with the unit cell relaxing in the z direction to compensate; figure 3.4a shows the dispersion in the k_x direction (the k_y direction being equivalent), figure 3.4b the k_z direction.

The effect of a biaxial compression is to raise the conduction and heavy ($m_j = \frac{3}{2}$) hole band edges, whilst lowering the light ($m_j = \frac{1}{2}$) hole (and to a much lesser extent the spin-orbit) band edge. The heavy ($m_j = \frac{3}{2}$) hole band is now visibly lighter in the k_x direction than in the k_z direction; this will have important consequences for quantum well devices, as we shall show in the next section.

Figure 3.5 shows the effect of a 1.5% biaxial tension. In this case, the conduction and heavy ($m_j = \frac{3}{2}$) hole band edges are lowered in energy, whilst the light ($m_j = \frac{1}{2}$) hole band is raised. The change in effective mass between the k_x and k_z directions is much clearer in this case — the 'light hole' band is in fact heavy and the 'heavy hole' band light in the k_x direction.

Clearly it is not meaningful to refer to 'heavy' and 'light' holes when discussing strained systems, and henceforth we shall refer to these states solely by their angular momentum quantum number m_j.

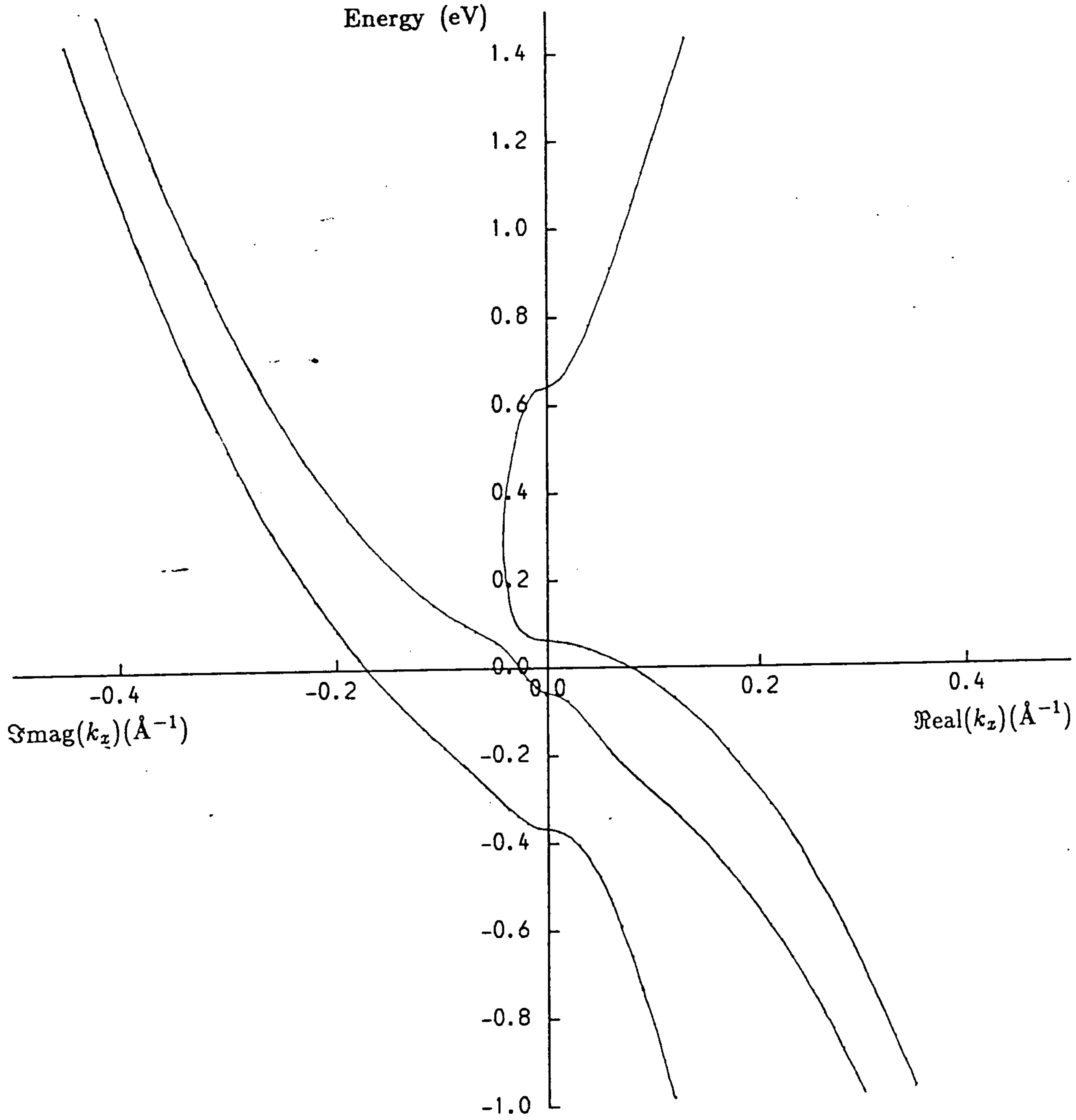

a) k_x direction.

Figure 3.5

Bulk bandstructure of $In_{0.53}Ga_{0.47}As$ — $1\frac{1}{2}$% biaxial tension.

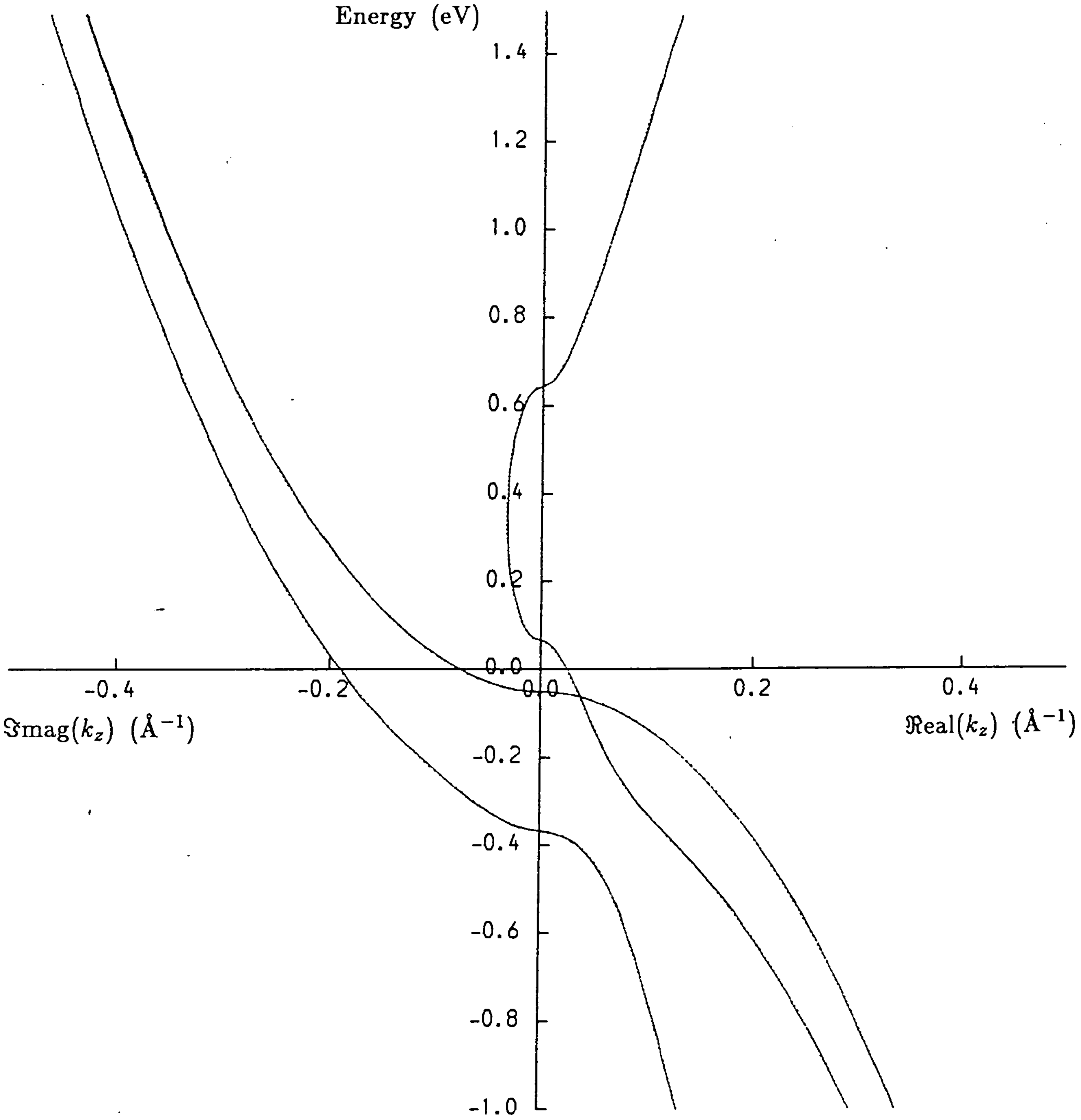

b) k_z direction.

Figure 3.5 (continued)

Bulk bandstructure of $In_{0.53}Ga_{0.47}As$ — $1\frac{1}{2}$% biaxial tension.

3.5 Quantum Well Bandstructure in the Strained Layer Regime

We now turn our attention to the way in which the quantum well bound states are affected by the elastic strain field which is present when the well and barrier materials have a different natural lattice constant. We only consider the strained layer regime. In order to compare results for a strained system with those of the corresponding unstrained case it is necessary to change either the well or the barrier material so that the materials are lattice mismatched. This of course also modifies the bulk band gaps and effective masses of one of the constituent materials, which makes it difficult to isolate the effect of the strain. For this reason, in this section we consider an imaginary device consisting of a 50Å $In_{0.53}Ga_{0.47}As$ quantum well lattice *mismatched* to unstrained InP barriers. That is we assume that the barriers are fabricated from an imaginary material which has the same electronic properties as InP but has a different lattice constant. We will in fact assume the existence of a whole set of such materials, with a range of lattice parameters. The only way in which these quantum well structures then differ from that investigated in section 2.7 is through the presence of an elastic strain field in the well region.

Figure 3.6 shows the dependence of the valence subband edges on strain. In this diagram Δa_0 is the amount by which the lattice constant of the barriers differs from that of InP. The states follow the pattern seen

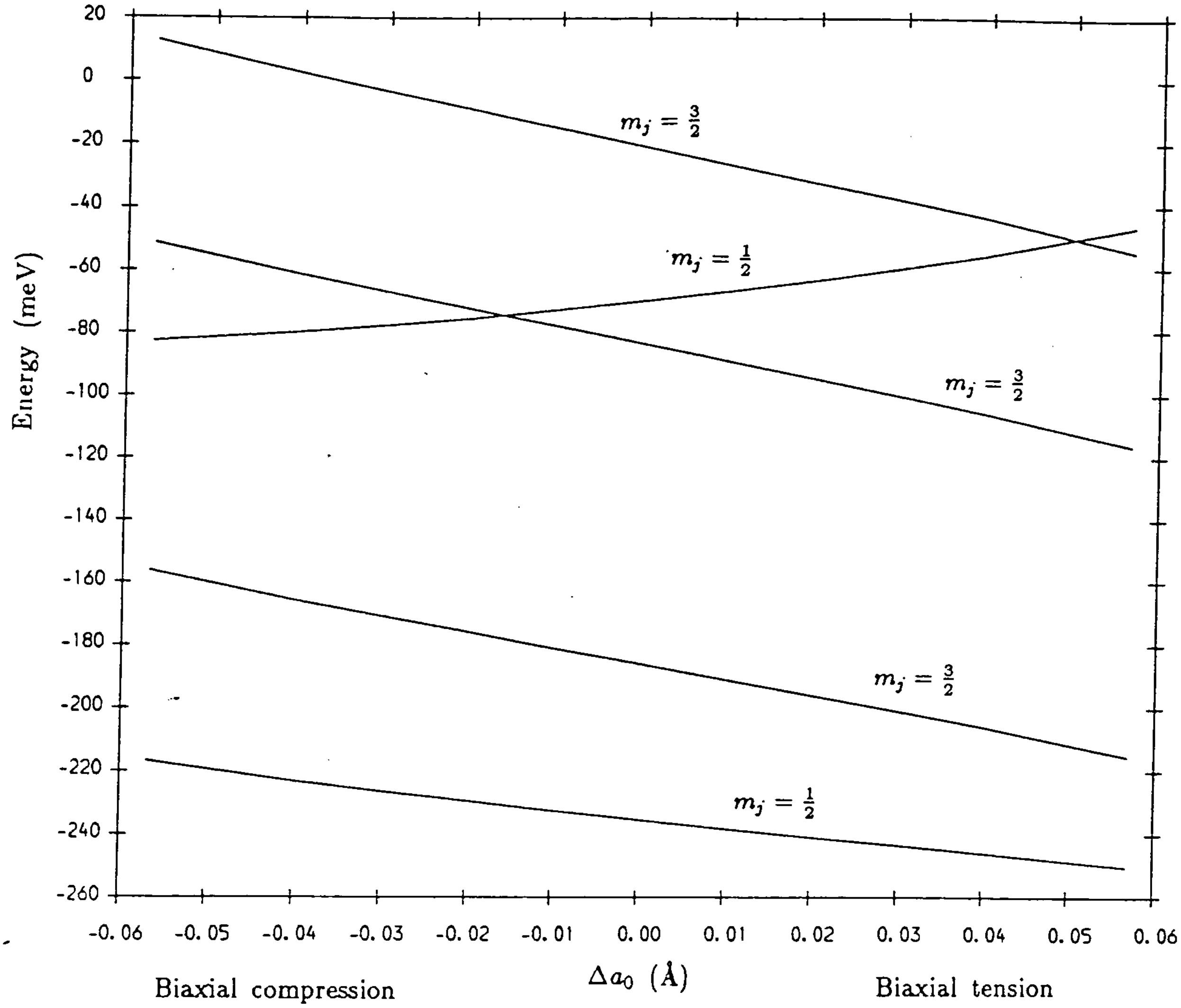

Figure 3.6

Variation of valence subband edges with strain.

for the bulk bandstructure — under biaxial compression the $m_j = \frac{3}{2}$ states are raised in energy and the $m_j = \frac{1}{2}$ states lowered; under biaxial tension the reverse is true. This effect is clearly seen for the first four subbands (i.e. the four with the lowest hole energy). The fifth subband appears to be something of an anomaly, showing the opposite behaviour to that which would be expected for a $m_j = \frac{1}{2}$ state. Close inspection of the wave function of this state (figure 2.5e), however, reveals that the state contains a large contribution from the $\left|\frac{1}{2}, \frac{1}{2}\right\rangle$ (spin split-off) and $|s\rangle$ (electron) Bloch functions. The presence of a large 'electron-like' component in the wave function will tend to cause the subband to move up under biaxial compression and down under biaxial tension, and this is what is observed.

This relative movement of the subband edges can have a dramatic effect on the in-plane bandstructure of the quantum well. In the last chapter it was shown that when an $m_j = \frac{1}{2}$ state and an $m_j = \frac{3}{2}$ state lie close in energy, the subbands can anticross, leading to marked non-parabolicity of the bandstructure, and mixing of the subband character. This is clearly seen in figure 3.7, which shows the bandstructure of a 50Å $\mathrm{In_{0.53}Ga_{0.47}As/InP}$ quantum well with an artificial biaxial tension of 1% ($\Delta a_0 = +0.05689$Å). The first two subbands have $m_j = \frac{1}{2}$ and $m_j = \frac{3}{2}$ character respectively at $k_{\|} = 0$, and at this point the subbands lie less than 10meV apart. This results in a substantial interaction between the subbands, and as a consequence the first subband has a negative (electron-like) hole effective mass for small $k_{\|}$, before turning over at $k_{\|} \simeq 0.04$Å^{-1}. This effect is seen

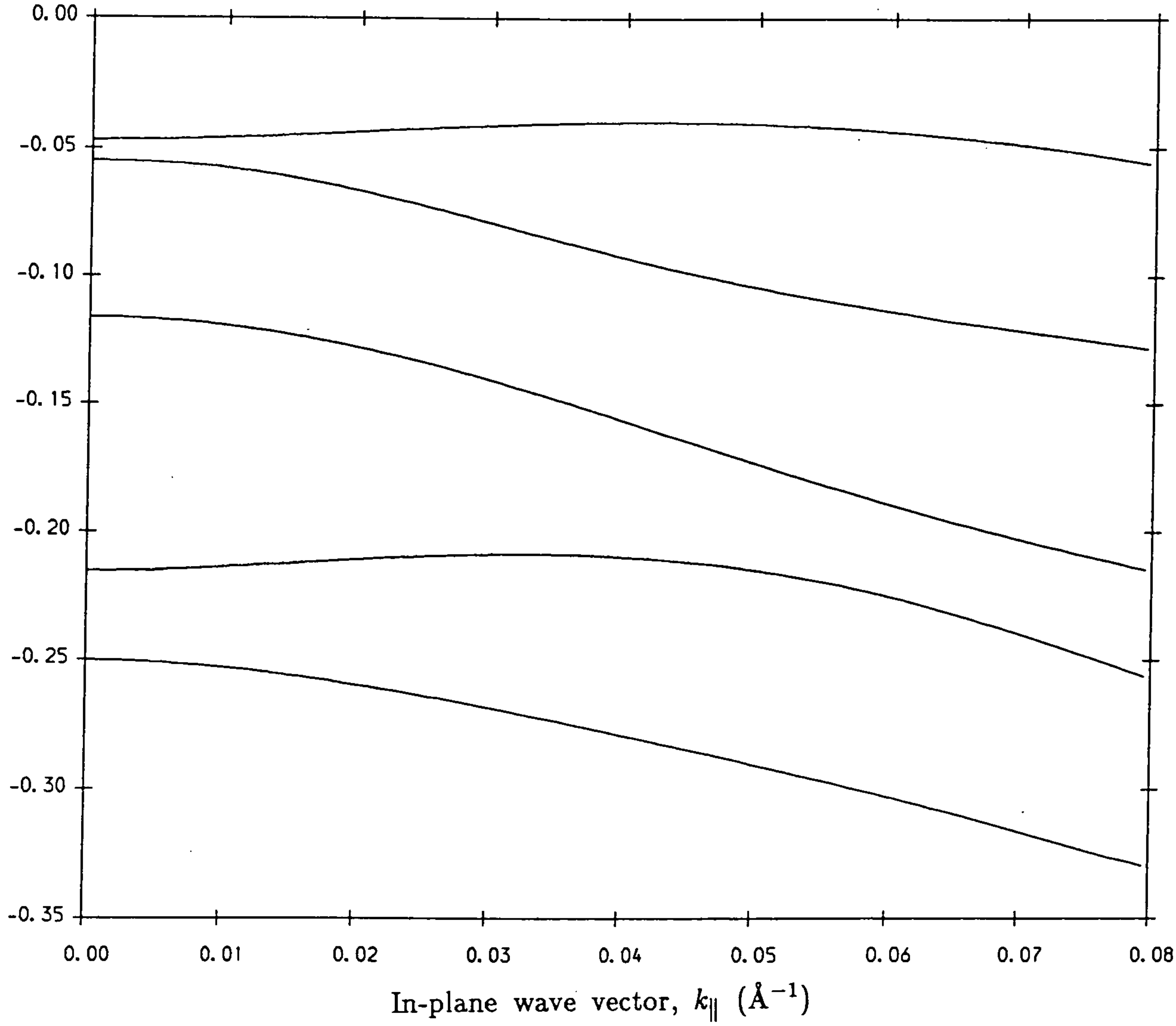

Figure 3.7

Bandstructure of 50Å $In_{0.53}Ga_{0.47}As/InP$ quantum well under a 1% artificial biaxial tension.

in unstrained quantum wells for higher subbands, but never at the top of the valence band because the difference in bulk effective masses of $m_j = \frac{3}{2}$ and $m_j = \frac{1}{2}$ states results in all the $m_j = \frac{1}{2}$ subbands lying well below the first $m_j = \frac{3}{2}$ subband.

Whilst undoubtedly an interesting phenomenon, this electron-like curvature of the first subband is of little use for the laser applications we consider in this thesis. For these devices it would be useful to make the top valence subband as light as possible, although the effect of a biaxial tension may be advantageous for optical amplifiers [13]. A close study of figure 3.6 suggests that the reduced effective mass required for more efficient lasers may be achievable using strain. Just as a biaxial tension tends to move the $m_j = \frac{3}{2}$ and $m_j = \frac{1}{2}$ states closer together, leading to stronger intersubband mixing and higher non-parabolicity, so a biaxial compression will tend to move the $m_j = \frac{1}{2}$ states deeper into the valence band and diminish their interactions with the lowest (in hole energy) lying $m_j = \frac{3}{2}$ states. Moreover, these $m_j = \frac{3}{2}$ subbands can be expected from the bulk behaviour in figure 3.4 to have an effective mass which is heavy in the growth direction but light in the in-plane direction.

Figure 3.8 shows the results of a valence bandstructure calculation for a 50Å $In_{0.53}Ga_{0.47}As/InP$ quantum well with an artificial biaxial compression of 1% ($\Delta a_0 = -0.05689$Å). In this case the first valence subband is indeed light over a wide range of $k_{\|}$, and is close to parabolic, especially over the first 30 or 40 meV (corresponding to $\sim \frac{3}{2}$kT at room temperature). Comparison

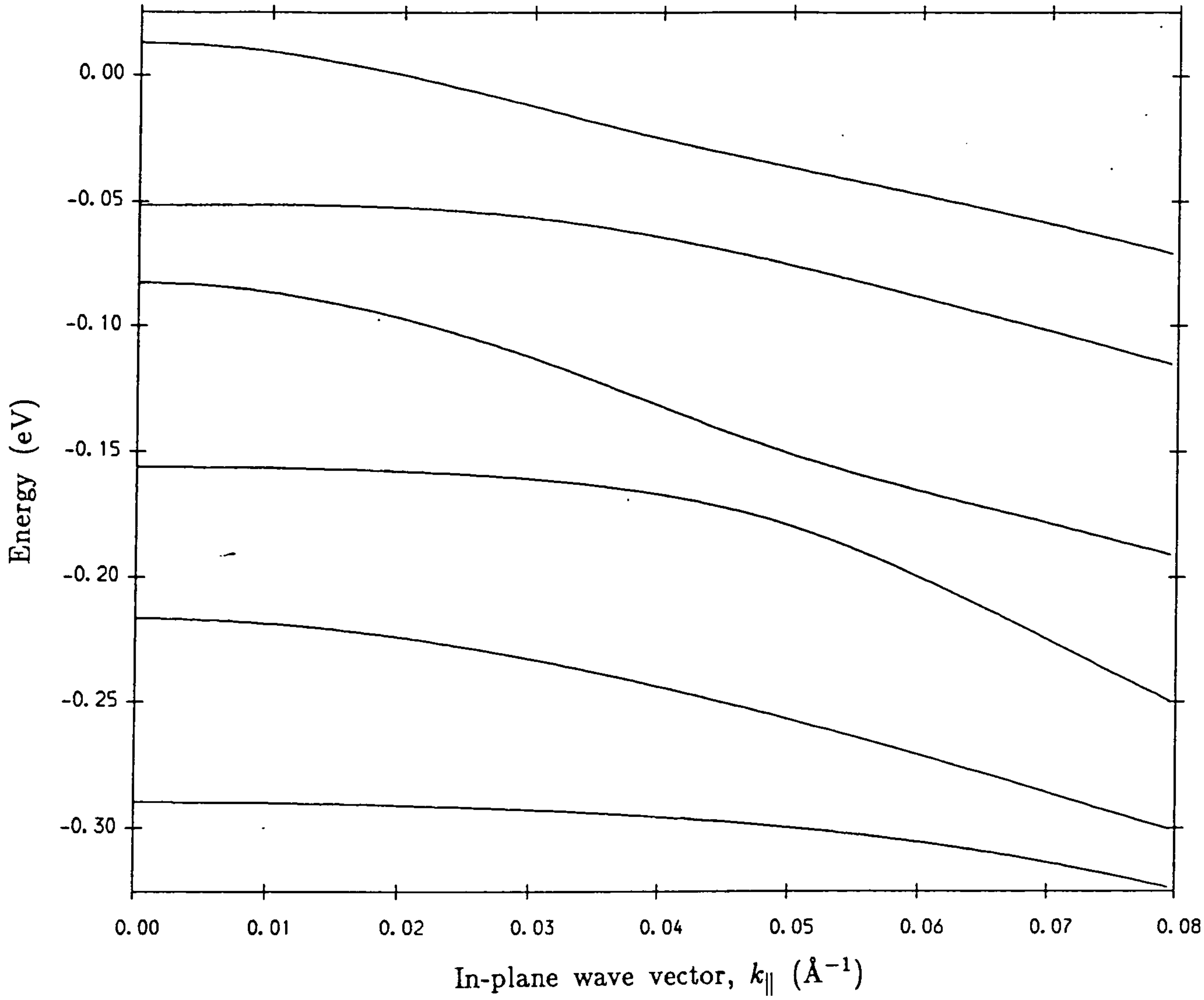

Figure 3.8

Bandstructure of 50Å $In_{0.53}Ga_{0.47}As/InP$ quantum well under a 1% artificial biaxial compression.

with figure 2.4b reveals that the effective mass of this subband is lower than in the equivalent unstrained system. The second subband is heavy close to the band edge, but lies more than 2kT (at room temperature) higher in energy than the first subband, and so should not affect the performance of a quantum well laser based on such a structure.

In order for a laser based on these effects to show enhanced performance it is obviously important that the conduction bandstructure is not adversely affected by the strain. Figure 3.9 shows how the quantum well conduction subband changes under the influence of strain in the 50Å $In_{0.53}Ga_{0.47}As/InP$ device under investigation. It is clear from this diagram that the main effect of the strain is to rigidly shift the subband in energy — a closer inspection shows that the effective mass is essentially unchanged and the subband remains virtually parabolic. This is an important result, since it suggests that strain can be freely used to engineer the valence bandstructure of a device without the risk of detrimentally affecting the conduction band.

3.6 Summary and Device Prospects

In this chapter we have shown how the **k.p** model described in chapter 2 can be applied to lattice mismatched quantum well structures, within the strained layer regime. We have discussed the way in which the in-plane bandstructure of such a device is modified by the strain, and have

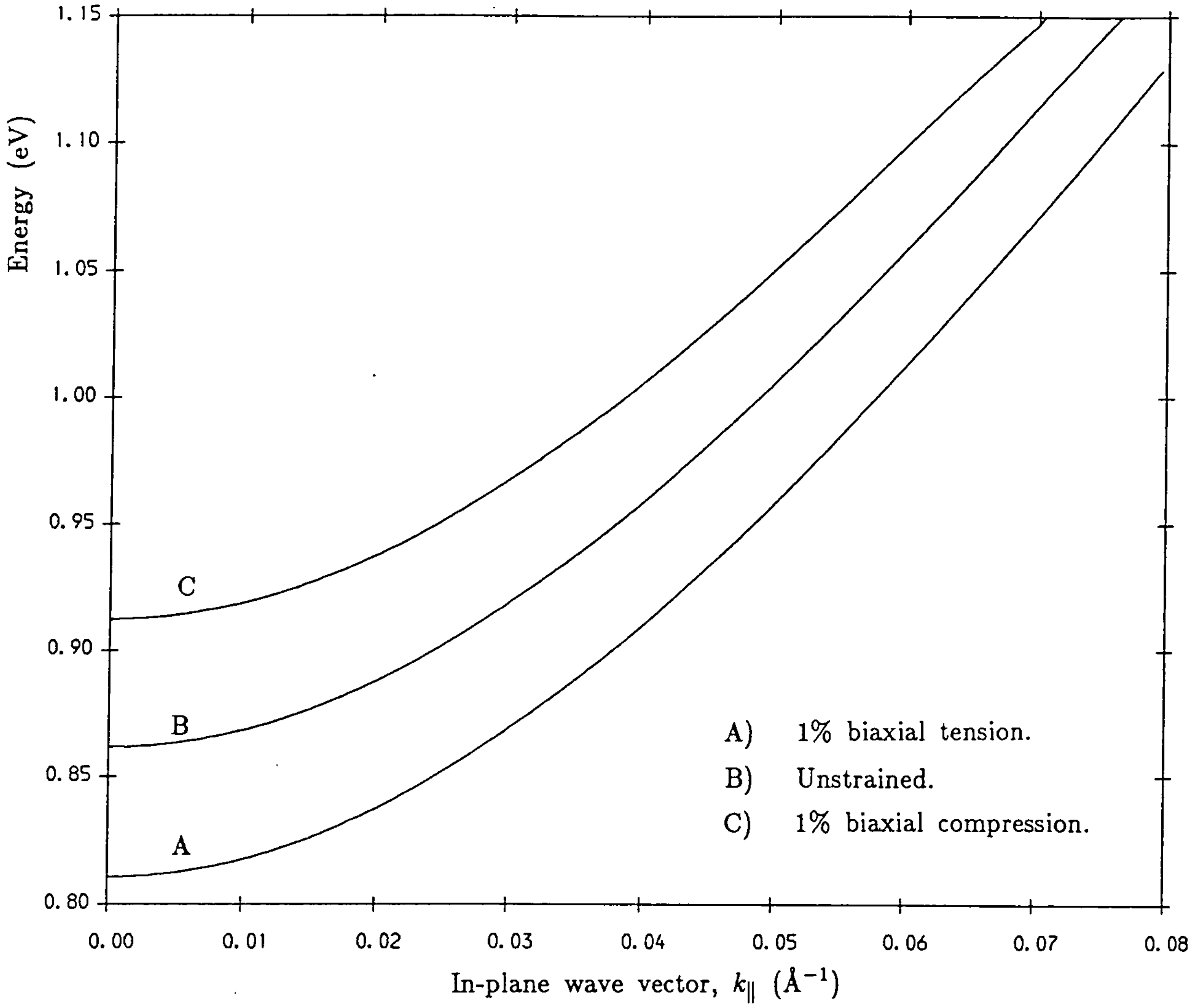

Figure 3.9

Effect of strain on the conduction band in a quantum well.

shown that in the case where the well region is under a biaxial compression this can lead to a reduction in the effective mass of the first valence subband as well as a reduction of non-parabolicity effects.

It was mentioned in the previous section that the prospect of reducing the effective mass of the lowest valence subband suggests the possibility of improving the performance of certain devices. In particular, it has been proposed that this effect could be used to achieve faster complementary logic devices [14] and more efficient long wavelength lasers [15,16]. Much of the remainder of this thesis will be concerned with the use of strain to enhance the performance of quantum well lasers.

It should be noted that all the calculations in this chapter have been based on an imaginary structure which utilises a fictitious barrier material. This was done in order to isolate the effect of strain from other effects such as differences in the band gaps and effective masses which are inevitable in any experimental comparison of strained and unstrained structures. In a physical device, the introduction of strain by changing the exact composition of one of the constituent materials may introduce undesirable effects which may outweigh the advantages gained by the strain. However these can often be compensated for by varying other device parameters. For example, a 1.55μm InGaAs/InP quantum well laser may show an enhanced performance when the indium content of the alloy is increased, and a biaxial compression exists in the well region. An unfortunate consequence of this is that the operating wavelength of the strained device will now be increased beyond

$1.55\mu m$. This undesirable effect can be compensated by using InAlGaAs, for example, as the well material and increasing the aluminium content as the indium content is reduced, or more simply by changing the well width.

In principle then, it is clear that strained layer structures offer the prospect of improved devices. The strain provides an additional variable parameter, which can be used to tailor the device parameters with the aim of enhanced performance. In chapter 6 we shall present a more detailed discussion of how this can be achieved in a $1.55\mu m$ multiple quantum well laser structure.

References for Chapter Three

[1] J.W. Matthews and A.E. Blakeslee, J. Cryst. Growth **27**,118 (1974); **29**, 273 (1975); **32**, 265 (1976).

[2] E.P. O'Reilly, Semicond. Sci. Technol. **4**, 121 (1989).

[3] W. Hagen and H.J. Queisser, Appl. Phys. Lett. **32**, 269 (1978).

[4] T.J. Andersson, Z.G. Chen, V.D. Kulakovski, A. Uddin and J.T. Vallin, Appl. Phys. Lett. **51**, 752 (1987).

[5] J.C. Bean, L.C. Feldman, A.T. Fiory, S. Nakahara and I.K. Robinson, J. Vac. Sci. Technol. A **2**, 436 (1984).

[6] R. People and J.C. Bean, Appl. Phys. Lett. **47**, 322 (1985).

[7] E. Kasper, Surface Science **174**, 630 (1986).

CHAPTER FOUR

OPTICAL MATRIX ELEMENTS IN QUANTUM WELLS

4.1 Introduction

In the remainder of this thesis, various optical properties of quantum well structures (gain and spontaneous emission in chapters 5 and 6 and intervalence band absorption in chapter 7) are investigated, and the way in which such properties are modified by the presence of strained layers is discussed. In all these processes the transition probabilities depend upon the optical (or dipole) matrix element between the wave functions of the initial and final states involved in the transition.

The values of optical matrix elements in quantum well devices have been calculated by a number of authors. Initially many of them used a simplified parabolic band approach [1,2,3], but more recently Colak *et al* [4] have shown that the quantum well matrix elements calculated from wave functions obtained using a **k**.**p** model can differ markedly from those predicted by the simpler approach due to subband mixing effects. The work of Colak's group agrees well with the more sophisticated tight-binding results of Chang and Schulman [5].

We thus need to calculate the optical matrix elements from the wave functions obtained from the **k**.**p** model described in chapter 2. In this chapter the method of obtaining these matrix elements is described, and the form of their dependence on the in-plane wave vector $k_{\|}$ is discussed for both unstrained and strained quantum wells.

4.2 Quantum Theory of Optical Transitions

The effect of an electromagnetic radiation field on the electronic states of a crystal can be obtained using standard non-relativistic quantum mechanical methods [6]. In the presence of an electromagnetic field, the Hamiltonian for an electron in a periodic potential $V(\mathbf{r})$ is given by

$$H_T = \frac{1}{2m}(\mathbf{p} + |e|\mathbf{A})^2 + V(\mathbf{r}) \tag{4.1}$$

The Lorentz condition implies $\nabla.\mathbf{A} = 0$, so neglecting non-linear effects (these arise from the terms in $\mathbf{A}^2$ and can be shown to be small [6]) equation (4.1) reduces to

$$H_T = H_0 + H'$$

with

$$H_0 = \text{unperturbed Hamiltonian}$$

$$H' = -\frac{i|e|\hbar}{m}\mathbf{A}.\nabla \tag{4.2}$$

The interaction term H' can then be treated using time dependent perturbation theory.

The vector potential $\mathbf{A}$ of an electromagnetic wave will take the form

$$\mathbf{A} = \frac{\mathbf{A_0}}{2} e^{-i(\mathbf{k}.\mathbf{r}-\omega t)} + \frac{\mathbf{A_0}}{2} e^{i(\mathbf{k}.\mathbf{r}-\omega t)} \tag{4.3}$$

and the electric and magnetic fields are obtained from

$$\mathbf{E} = -\frac{\partial \mathbf{A}}{\partial t}$$

$$\text{and} \qquad \mathbf{B} = \nabla \times \mathbf{A}.$$

The time dependent perturbation H' is then given by

$$H' = -\frac{i|e|\hbar}{2m}\left[e^{-i(\mathbf{k}.\mathbf{r}-\omega t)} + e^{i(\mathbf{k}.\mathbf{r}-\omega t)}\right]\mathbf{A}_0.\nabla \tag{4.4}$$

When compared with the typical wave vector of an electron or a hole the photon wave vector is very small, and we thus take $\mathbf{k} = 0$. H' then contains two terms : the first is proportional to $e^{i\omega t}$ and results in emission, and the second is proportional to $e^{-i\omega t}$ and results in absorption. Which term is dominant will depend on the initial and final states of the system; if the initial state is the ground state only absorption is possible, and similarly if the final state is the ground state only emission can have occurred. Both transition rates are determined by Fermi's Golden Rule, which states that the probability per unit time that a perturbation of the form $H'e^{\mp i\omega t}$ induces a transition from an intial state $|\Psi_i\rangle$ with energy E_i to a final state $|\Psi_f\rangle$ with energy E_f is

$$P_{i\rightarrow f} = \frac{2\pi}{\hbar}\left|\langle\Psi_f|H'|\Psi_i\rangle\right|^2 \delta(E_f - E_i \mp \hbar\omega) \tag{4.5}$$

where H' for an electromagnetic field is given by

$$H' = -\frac{i|e|\hbar}{2m}\mathbf{A}_0.\nabla$$

Since $\mathbf{E} = -\frac{\partial \mathbf{A}}{\partial t}$, $\mathbf{A}_0$ will lie in the direction of polarisation of the electric field, so $\mathbf{A}_0 = A_0\hat{\mathbf{E}}$, where $\hat{\mathbf{E}}$ is a unit vector in the direction of $\mathbf{E}$. To obtain the rate at which optical transitions occur in semiconductors, we shall thus need to obtain the matrix element

$$M^2 = \left|\langle\Psi_f|\hat{\mathbf{E}}.\nabla|\Psi_i\rangle\right|^2 \qquad (4.6)$$

This is sometimes referred to as the momentum matrix element since the ∇ operator is proportional to the momentum operator, and determines the rate of both absorption and emission processes.

4.3 Calculation of the Optical Matrix Elements

In chapter 2 we showed how the wave function of a quantum well state can be obtained using a **k.p** Hamiltonian in the envelope function formalism. We shall now show how the optical matrix element between two such states is calculated from these wave functions. Recall that the wave functions obtained took the form

$$\psi = \sum_i \sum_j A_i F_{ij} e^{i\mathbf{k}_i.\mathbf{r}} |u_j\rangle \qquad (4.7)$$

in each region of the heterostructure. We can write the total wave function of a given state as

$$\Psi = \psi_L + \psi_W + \psi_R \qquad (4.8)$$

where each ψ on the right hand side of equation (4.8) takes the form of equation (4.7) within one region (left-hand barrier, well, right-hand barrier for ψ_L, ψ_W, ψ_R respectively) and is zero outside of that region.

We wish to obtain the matrix element $\left|\langle\Psi_f|\hat{\mathbf{E}}.\nabla|\Psi_i\rangle\right|^2$ from two such wave functions Ψ_f,Ψ_i. We consider only so called vertical transitions (in the bandstructure diagram), so that the in-plane (x,y) components of the wave vectors $\mathbf{k}_\mathrm{f}$ and $\mathbf{k}_\mathrm{i}$ are equal.

The matrix element is given by

$$\begin{aligned}|M|^2 &= \left|\int \Psi_f^*\hat{\mathbf{E}}.\nabla\Psi_i d^3\mathbf{r}\right|^2 \\ &= \left|\int_{z=-\infty}^{z=z_1} \Psi_{fL}^*\hat{\mathbf{E}}.\nabla\Psi_{iL}d^3\mathbf{r} + \int_{z=z_1}^{z=z_2} \Psi_{fW}^*\hat{\mathbf{E}}.\nabla\Psi_{iW}d^3\mathbf{r} + \int_{z=z_2}^{z=\infty} \Psi_{fR}^*\hat{\mathbf{E}}.\nabla\Psi_{iR}d^3\mathbf{r}\right|^2\end{aligned} \tag{4.9}$$

Consider for the moment any one of these integrals :

$$\begin{aligned}I &= \int_{z=a}^{z=b} \Psi_f^*\hat{\mathbf{E}}.\nabla\Psi_i d^3\mathbf{r} \\ &= \int_{z=a}^{z=b} \sum_i\sum_j\sum_{i'}\sum_{j'} A_i^* F_{ij}^* e^{-i\mathbf{k}_\mathrm{i}^*.\mathbf{r}} u_j^*(\mathbf{r})\hat{\mathbf{E}}.\nabla A_{i'}F_{i'j'}e^{i\mathbf{k}_{\mathrm{i}'}.\mathbf{r}}u_{j'}(\mathbf{r})d^3\mathbf{r}\end{aligned}$$

The constant terms can be removed from the integral to give

$$I = \sum_{iji'j'} C_{iji'j'} \int_{z=a}^{z=b} e^{i(\mathbf{k}_{\mathrm{i}'}-\mathbf{k}_\mathrm{i}^*).\mathbf{r}} \left\{ik_{i'}^{\hat{\mathbf{E}}}u_j^*(\mathbf{r})u_{j'}(\mathbf{r}) + u_j^*(\mathbf{r})\hat{\mathbf{E}}.\nabla u_{j'}(\mathbf{r})\right\} d^3\mathbf{r} \tag{4.10}$$

where $C_{iji'j'} = A_i^*F_{ij}^*A_{i'}F_{i'j'}$, and $k_{i'}^{\hat{\mathbf{E}}}$ is the component of $\mathbf{k}_{\mathrm{i}'}$ along the electric field direction.

Since the in-plane components of $\mathbf{k}_{\mathrm{i}'}$ and $\mathbf{k}_\mathrm{i}$ are equal (and real), the integrand is independent of x and y, so equation (4.10) can be reduced to a one dimensional integral (the integration being performed in the growth direction):

$$I = \sum_{iji'j'} C_{iji'j'} \left\{ ik_{i'}^{\hat{\mathbf{E}}} \delta_{jj'} + \langle u_j | \hat{\mathbf{E}}.\nabla | u_{j'} \rangle \right\} \int_a^b e^{i(k_{i'} - k_i^*)z} dz$$

(where we have used the relation $\langle u_j | u_{j'} \rangle = \delta_{jj'}$).

We can write this in the form

$$I = \sum_{iji'j'} C_{iji'j'} \, Q_{i'jj'} \, {}_a^bL_{ii'} \tag{4.11}$$

where

$$Q_{i'jj'} = ik_{i'}^{\hat{\mathbf{E}}} \delta_{jj'} + \langle u_j | \hat{\mathbf{E}}.\nabla | u_{j'} \rangle \tag{4.12}$$

and

$${}_a^bL_{ii'} = \int_a^b e^{i(k_{i'} - k_i^*)z} dz \tag{4.13}$$

There are 3 L's to calculate :

$${}_{-\infty}^{z_1}L_{ii'} = \frac{\exp(-i(k_{i'} - k_i^*)L_z/2)}{i(k_{i'} - k_i^*)} \tag{4.14}$$

$${}_{z_1}^{z_2}L_{ii'} = L_z \mathrm{sinc}((k_{i'} - k_i^*)L_z/2) \tag{4.15}$$

$${}_{z_2}^{\infty}L_{ii'} = -\frac{\exp(i(k_{i'} - k_i^*)L_z/2)}{i(k_{i'} - k_i^*)} \tag{4.16}$$

where L_z is the quantum well width $(= z_2 - z_1)$. (Note that since the wave vectors in each barrier are equal in magnitude but of opposite sign the terms appearing in ${}_{-\infty}^{z_1}L_{ii'}$ and ${}_{z_2}^{\infty}L_{ii'}$ are in fact the same).

Clearly the $C_{iji'j'}$ and ${}_a^bL_{ii'}$ are easily calculated from the initial and final state wave functions. We just need to obtain the values of $Q_{i'jj'}$ (equation (4.12)). The first term $(ik_{i'}^{\hat{\mathbf{E}}} \delta_{jj'})$ is readily obtained from the wave function of the initial state, but to obtain the second term $(\left\langle u_j|\hat{\mathbf{E}}.\nabla|u_{j'}\right\rangle)$, it is necessary to know the momentum matrix element between each of the individual zone centre Bloch functions $|u_j\rangle$. These terms are well known, and in the $|S\rangle$, $|X\rangle$, $|Y\rangle$, $|Z\rangle$ basis are given by [7]

$$\langle S|p_x|X\rangle = \langle S|p_y|Y\rangle = \langle S|p_z|Z\rangle = \frac{imP}{\hbar} \tag{4.17}$$

if the states have the same spin; all other matrix elements are zero. p_x is the x component of the momentum operator and P is the Kane matrix element (as appears in the Hamiltonian in table 2.2). The appropriate values for our chosen basis are readily calculated from equation (4.17); the results are shown in table 4.1.

In fact, the first term in equation (4.12) turns out to be small compared with the second for most transitions. The contribution to $|M|^2$ from the first term is characterised by the wave vector associated with the in-plane kinetic energy of the state, which is typically ~ 10–100 meV, whilst the contribution of the second term is characterised by the wave vector associated with E_p (~ 20 eV). Also, for transitions between conduction band states (largely $|S\rangle$ like) and valence band states (largely $|X\rangle$, $|Y\rangle$, or $|Z\rangle$ like) the coefficients $C_{ii'jj'}$ are very much larger for values of j and j' with large $\langle u_j|\hat{\mathbf{E}}.\nabla|u_{j'}\rangle$ than for the case $j = j'$. Thus it is reasonable to neglect the first term in $Q_{i'jj'}$.

Up to this point we have implicitly assumed the wave functions Ψ_f and Ψ_i to be normalised. However, it is easy to ensure normalisation of

(Units of $-\frac{mP}{i\hbar}$)

$$\begin{array}{c c}
 & \begin{array}{cccccccc} u_1 & u_2 & u_3 & u_4 & u_5 & u_6 & u_7 & u_8 \end{array} \\
\begin{array}{c} u_1 \\ u_2 \\ u_3 \\ u_4 \\ u_5 \\ u_6 \\ u_7 \\ u_8 \end{array} &
\left(\begin{array}{cccccccc}
0 & \sqrt{\frac{1}{2}} & 0 & 0 & 0 & 0 & -\sqrt{\frac{1}{6}} & -\sqrt{\frac{1}{3}} \\
\sqrt{\frac{1}{2}} & 0 & 0 & 0 & 0 & 0 & 0 & 0 \\
0 & 0 & 0 & 0 & \sqrt{\frac{1}{6}} & 0 & 0 & 0 \\
0 & 0 & 0 & 0 & \sqrt{\frac{1}{3}} & 0 & 0 & 0 \\
0 & 0 & \sqrt{\frac{1}{6}} & \sqrt{\frac{1}{3}} & 0 & \sqrt{\frac{1}{2}} & 0 & 0 \\
0 & 0 & 0 & 0 & \sqrt{\frac{1}{2}} & 0 & 0 & 0 \\
-\sqrt{\frac{1}{6}} & 0 & 0 & 0 & 0 & 0 & 0 & 0 \\
-\sqrt{\frac{1}{3}} & 0 & 0 & 0 & 0 & 0 & 0 & 0
\end{array}\right)
\end{array}$$

a) TE mode

$$\begin{array}{c c}
 & \begin{array}{cccccccc} u_1 & u_2 & u_3 & u_4 & u_5 & u_6 & u_7 & u_8 \end{array} \\
\begin{array}{c} u_1 \\ u_2 \\ u_3 \\ u_4 \\ u_5 \\ u_6 \\ u_7 \\ u_8 \end{array} &
\left(\begin{array}{cccccccc}
0 & 0 & -\sqrt{\frac{2}{3}} & \sqrt{\frac{1}{3}} & 0 & 0 & 0 & 0 \\
0 & 0 & 0 & 0 & 0 & 0 & 0 & 0 \\
-\sqrt{\frac{2}{3}} & 0 & 0 & 0 & 0 & 0 & 0 & 0 \\
\sqrt{\frac{1}{3}} & 0 & 0 & 0 & 0 & 0 & 0 & 0 \\
0 & 0 & 0 & 0 & 0 & 0 & -\sqrt{\frac{2}{3}} & \sqrt{\frac{1}{3}} \\
0 & 0 & 0 & 0 & 0 & 0 & 0 & 0 \\
0 & 0 & 0 & 0 & -\sqrt{\frac{2}{3}} & 0 & 0 & 0 \\
0 & 0 & 0 & 0 & \sqrt{\frac{1}{3}} & 0 & 0 & 0
\end{array}\right)
\end{array}$$

b) TM mode

Table 4.1

Matrix elements between basis functions

the wave functions. We need to ensure that $\int \Psi_f^* \Psi_i d^3\mathbf{r} = 1$. Clearly this integral is just the same as the optical matrix element integral but with $Q_{i'jj'} = \delta_{jj'}$ and $\Psi_f = \Psi_i$ = the wave function to be normalised. We thus have

$$|I_L + I_W + I_R|^2 = 1 \tag{4.18}$$

with each I taking the form

$$I = \sum_{iji'j'} C_{iji'j'} \; {}_a^bL_{ii'} \; \delta_{jj'}$$

4.4 TE and TM mode transitions

In a bulk semiconductor, the matrix elements depend, in general, on the angle the electric field vector makes with the crystal axes. It is clear, however, that certain directions are equivalent — the labelling of the axes in a cubic crystal is arbitrary and so an electric field lying in the x direction will give exactly the same transition probability as one lying in the y or z (or the $-x$, $-y$ or $-z$) direction. In a quantum well structure, however, one degree of symmetry is broken, and there are two distinct situations to consider (see figure 4.1).

One possibility is that the electric field vector lies in a direction parallel to the interface planes (i.e. in the (x,y) plane). This configuration is the transverse electric (TE) mode. Alternatively, the electric field vector may lie in the growth (z) direction; this is the transverse magnetic (TM)

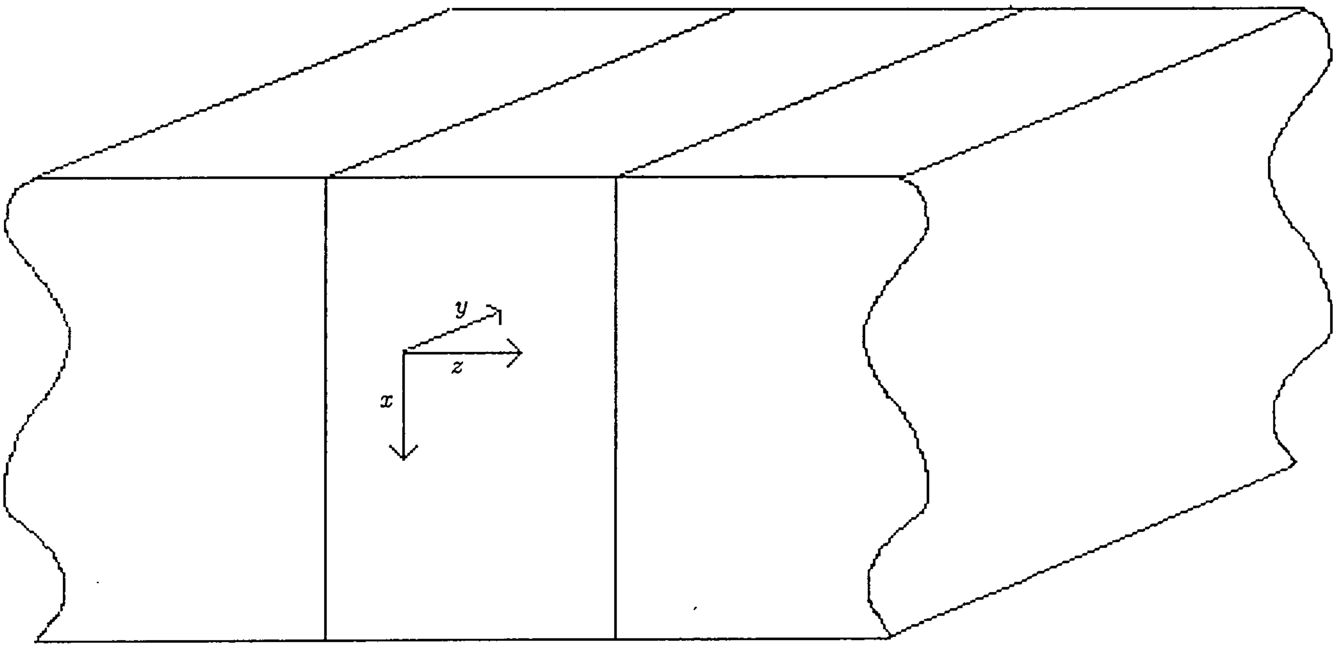

Coordinate system used in discussion of TE and TM modes.

Figure 4.1

mode. This nomenclature is used since the electromagnetic field in the quantum well in one of these modes corresponds to that in the equivalent mode of a planar waveguide. Since the wave vector in the growth direction is quantised, whilst in the in-plane direction is not, the matrix element for a TM mode transition will not in general be the same as that for the equivalent TE mode transition.

For the case of a transition between a bound conduction band state and a bound valence band state at the band edge ($k_{\|} = 0$), the dominant TE mode transition is that between an electron and a heavy ($m_j = \frac{3}{2}$) hole, whilst for the TM mode the light ($m_j = \frac{1}{2}$) hole transition dominates. Several authors [1-4] have investigated the dependence of the matrix elements on the in-plane wave vector using a simple parabolic bandstructure approach. They show that as the in-plane wave vector is increased (moving away from the subband edge), the quantum well optical matrix element for a vertical transition between bound states of the same excitation level n vary as (assuming $k_y = 0$) [4]

$$\begin{array}{llll} \text{TE mode} & : & M^2 = \frac{1}{2}M_0^2\cos^2\theta & \text{c} - \text{hh} \\ & & M^2 = \left(\frac{1}{6}\cos^2\theta + \frac{2}{3}\sin^2\theta\right)M_0^2 & \text{c} - \text{lh} \\ \text{TM mode} & : & M^2 = \frac{1}{2}M_0^2\sin^2\theta & \text{c} - \text{hh} \\ & & M^2 = \left(\frac{1}{6}\sin^2\theta + \frac{2}{3}\cos^2\theta\right)M_0^2 & \text{c} - \text{lh} \end{array} \tag{4.19}$$

where θ is the angle the total wave vector $(k_x\hat{\mathbf{x}} + k_z\hat{\mathbf{z}})$ makes with the z axis, which is given approximately by

$$\cos^2\theta = \frac{E_n}{\epsilon_n}$$

where E_n is the confinement energy of the nth subband at $k_{\|} = 0$ and ϵ_n $(= E_n + \frac{\hbar^2 k_x^2}{2m_n^*})$ is the energy of the state at k_x. Transitions between states with different quantum number n are forbidden.[†] The results (4.19) predicted by a parabolic band model which neglects subband mixing effects are shown in figure 4.2.

4.5 Results from the k.p Model

The wave functions obtained from the **k.p** bandstructure model described in chapter 2 have been used to calculate the optical matrix elements of strained and unstrained quantum wells. Although the general trends outlined in the previous section are observed, the shape of the dependence of the squared matrix element on the in-plane wave vector is modified by the wave function mixing effects described in section 2.7. These effects can also give rise to non-zero matrix elements between pairs of states corresponding to transitions predicted by the simpler models to be forbidden.

[†] More precisely, transitions between states with different quantum number n are forbidden in a quantum well of infinite depth. In a finite well these transitions are allowed but have very small matrix elements.

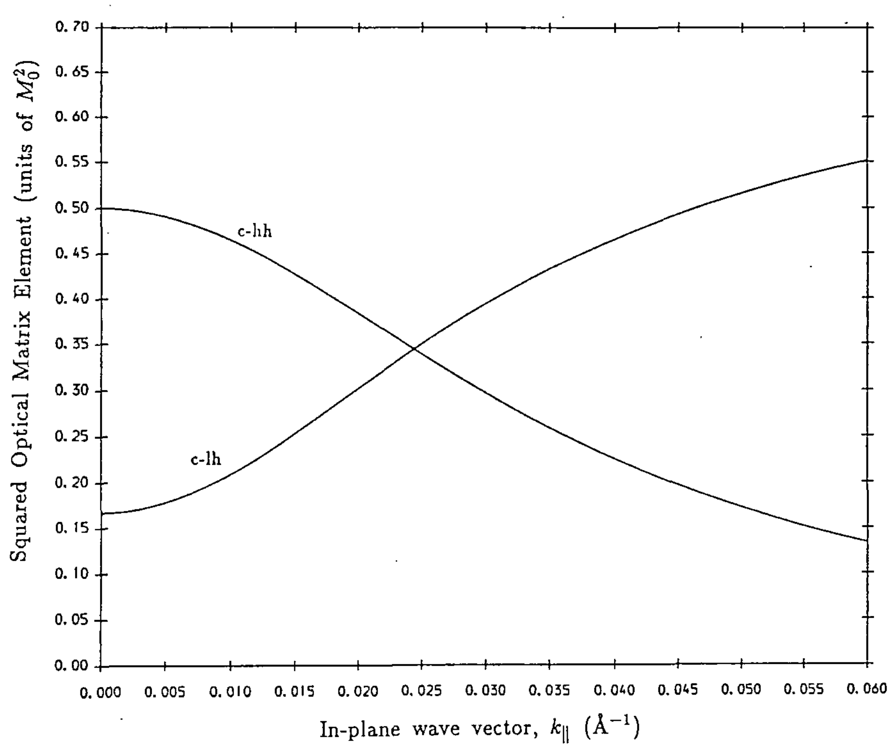

a) TE mode.

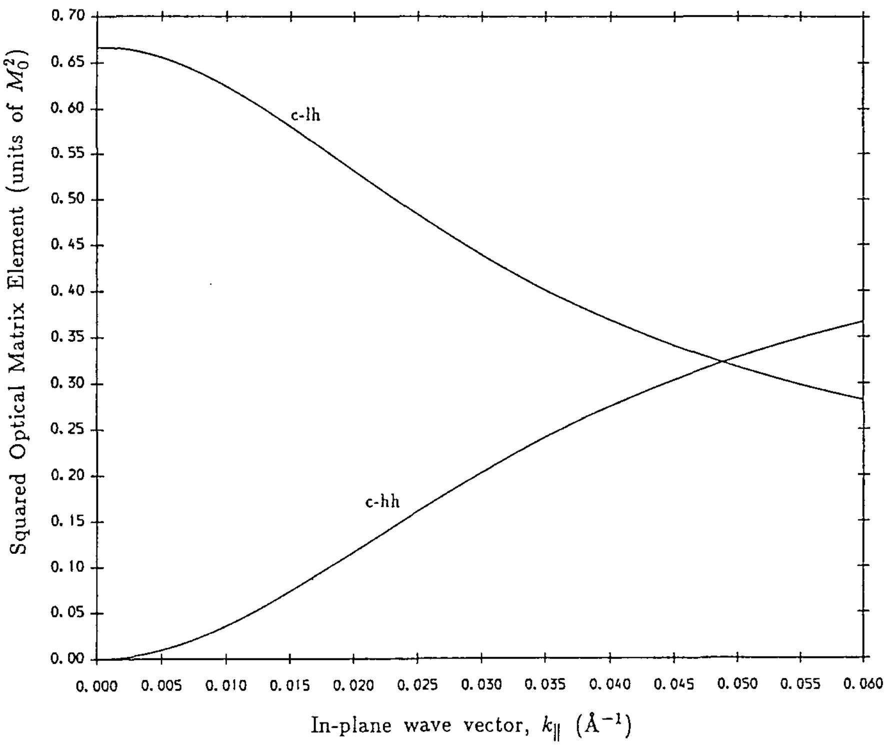

b) TM mode.

Optical matrix elements in the parabolic band model.

Figure 4.2

Figure 4.3 shows the variation of the squared TE and TM mode matrix elements with in-plane wave vector for a 50Å $In_{0.53}Ga_{0.47}As/InP$ quantum well, the bandstructure of which is given in figure 2.4. We follow the usual convention by converting the squared matrix elements into units of eV. All these matrix elements are for transitions between the nth valence subband and the first (and only) conduction subband. The first valence subband states are characteristic of bulk heavy holes (i.e. $m_j = \frac{3}{2}$) at the two dimensional Brillouin zone centre, and hence have a large TE mode matrix element and a zero TM mode matrix element at this point. The second valence subband states are characteristic of bulk light holes ($m_j = \frac{1}{2}$) at the zone centre, and as predicted by the simple model have a large TM mode matrix element, and a squared TE mode matrix element which is about one third of that of the TM mode, which is close to the ratio of 0.25 predicted by the simple model. The matrix elements associated with higher (in hole energy) valence subbands are clearly non-zero however, and become more significant as $k_{\|}$ is increased. These transitions become allowed as a result of the mixing-in of wave function components characteristic of allowed transitions. This effect is most apparent in the large matrix element for the TM mode c-h3 transition (which would be expected to be forbidden since $\Delta n \neq 0$), which arises as a result of mixing between the second and third valence subbands.

Figure 4.4 shows the equivalent results for a 50Å $In_{0.53}Ga_{0.47}As/InP$ quantum well under an artificial biaxial compression of 1% (for the band-

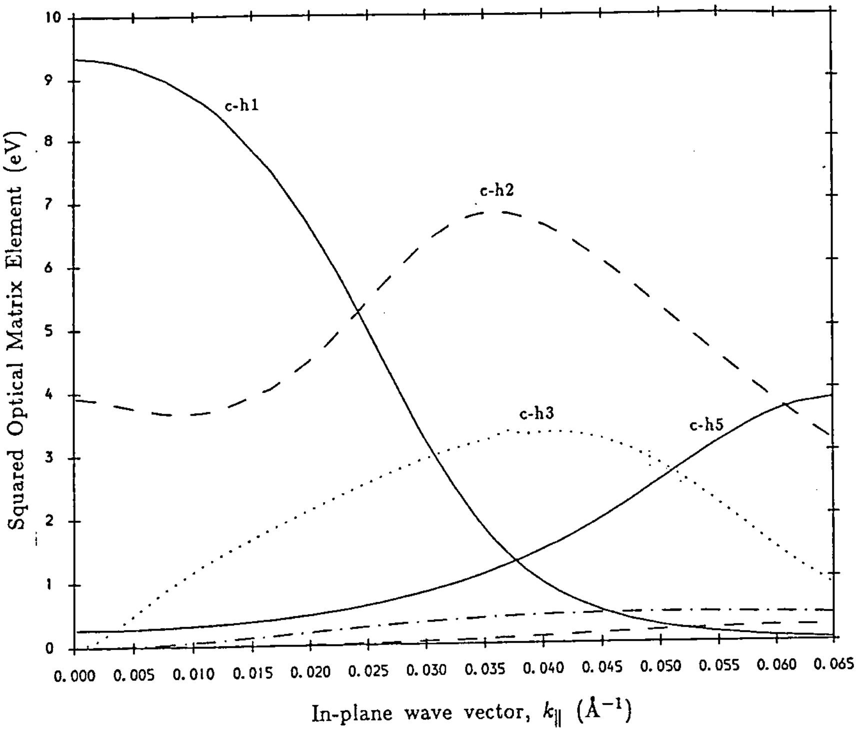

a) TE mode.

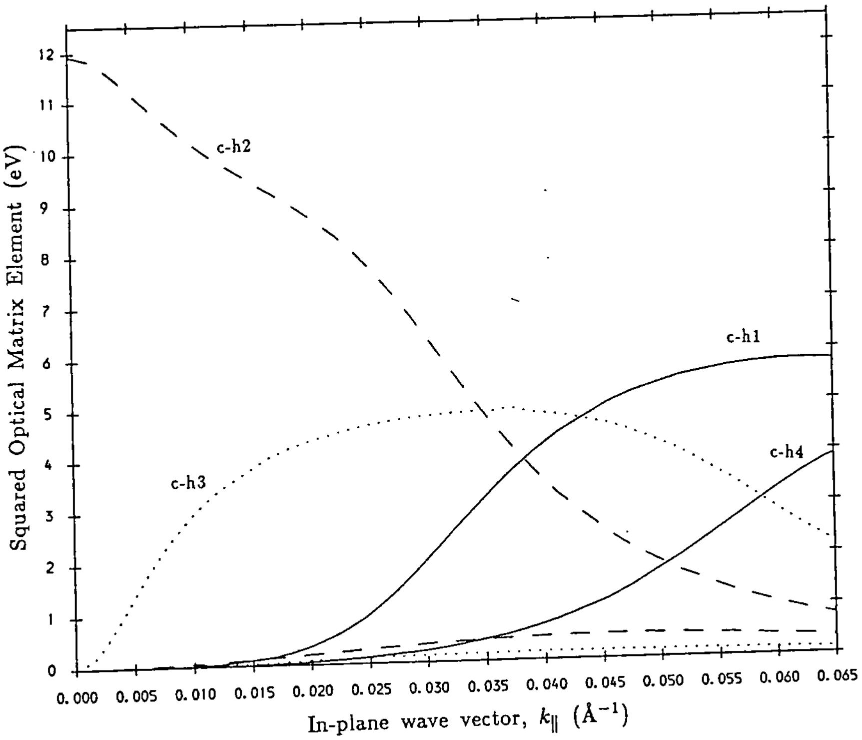

b) TM mode.

Optical matrix elements for a 50Å $In_{0.53}Ga_{0.47}As/InP$ unstrained quantum well.

Figure 4.3

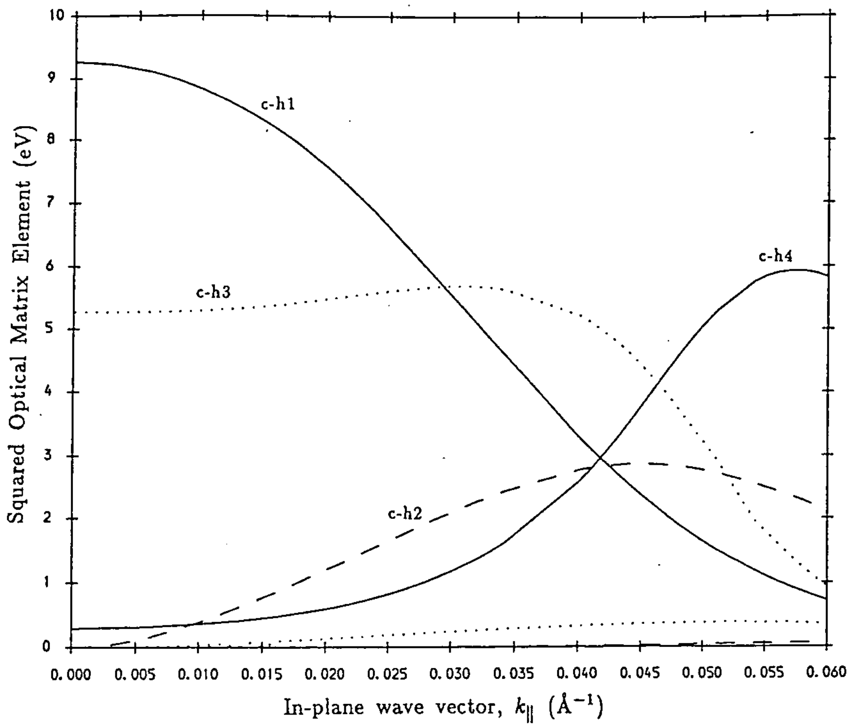

a) TE mode.

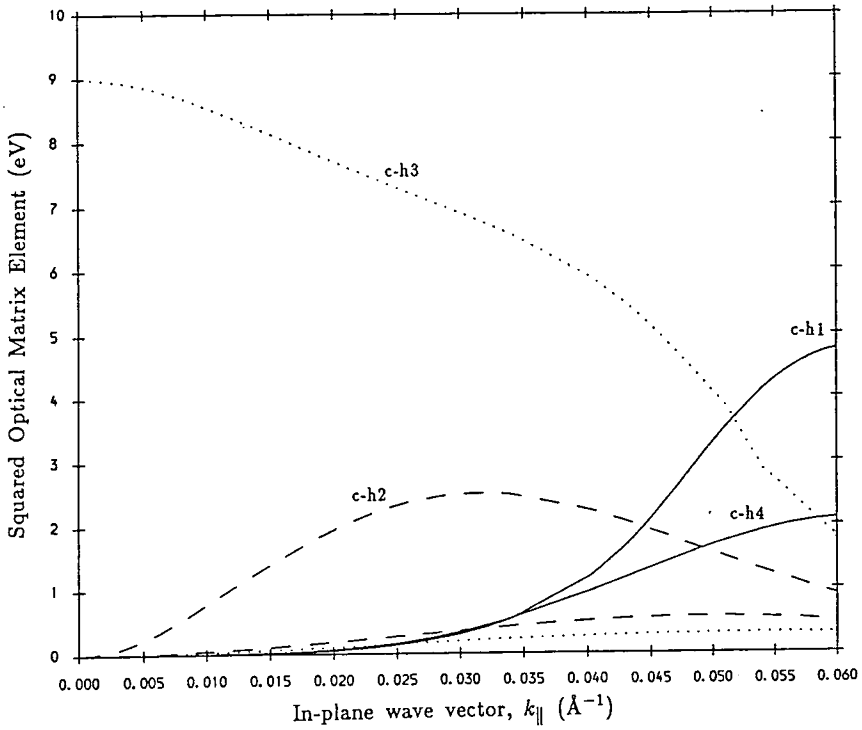

b) TM mode.

Optical matrix elements for a 50Å $In_{0.53}Ga_{0.47}As/InP$ quantum well with 1% artificial biaxial compression.

Figure 4.4

structure of this system refer to figure 3.8. The main effect of the biaxial strain, as discussed in chapter 3, is to raise the hole energy of the $m_j = \frac{1}{2}$ like subbands with respect to the $m_j = \frac{3}{2}$ like subbands, which in turn leads to a reduction in intersubband mixing. Thus the second valence subband is now characteristic of excited $(n = 2)$ bulk 'heavy' $(m_j = \frac{3}{2})$ holes, and the first $m_j = \frac{1}{2}$ 'light' hole subband is now the third valence subband. This is clearly illustrated by the changeover in the behaviour of the optical matrix elements of these two subbands under the influence of strain. It is clear from a comparison of the TM mode matrix elements of the strained and unstrained structures that the matrix elements for states in higher subbands are significantly reduced in the strained structure, which is indicative of the reduction of anticrossing behaviour and mixing of wave function character which results from the raising in energy of the $m_j = \frac{1}{2}$ subbands.

However, such mixing effects are still present to some extent in the strained structure. The strained TE mode matrix elements exhibit one particularly clear example of the effect that wave function mixing can have on the optical matrix elements. Around $k_{\|} = 0.045$ Å^{-1} the c1-h3 matrix element drops off sharply, whilst over the same region of $k_{\|}$ the c1-h4 matrix element increases strongly. This corresponds to a region of marked non-parabolicity and anticrossing behaviour between these two valence subbands in the bandstructure diagram (figure 3.8), and demonstrates the exchange of wave function character described in section 2.7.

It is also interesting to investigate matrix elements involving states in higher conduction subbands. However, the 50Å wells we have so far considered only contain one bound conduction subband, and to obtain matrix elements for c2-hn transitions it is necessary to study a wider quantum well. Figure 4.5 shows the bandstructure of a 100Å unstrained $In_{0.53}Ga_{0.47}As/InP$ quantum well, which has two bound conduction subbands. Only the first seven valence subbands (there are eleven altogether) are considered, since at room temperature or below significant hole populations would not be expected in the higher subbands, except at very high injected carrier densities. Figure 4.6a shows the squared TE mode matrix elements for transitions involving the first conduction subband states, and figure 4.6b shows the corresponding results for transitions involving states in the second conduction subband. Figure 4.7 shows the TM mode results, again with transitions involving states in the first conduction subband in a) and those involving states in the second subband in b).

It is immediately apparent from both the matrix elements and the bandstructure that far more wave function mixing effects are present in the 100Å well than in the 50Å well. This is simply due to the reduced energy separation of the subbands (which, at the subband edges, is approximately inversely proportional to the square of the quantum well width) and is especially evident for the lower (in hole energy) subbands, since these lie closer together than the higher subbands. In particular, the sixth subband, which is characteristic of the first excited $(n = 2)$ $m_j = \frac{1}{2}$ 'light' hole level at the zone centre, hardly mixes with the other subbands at all. This is

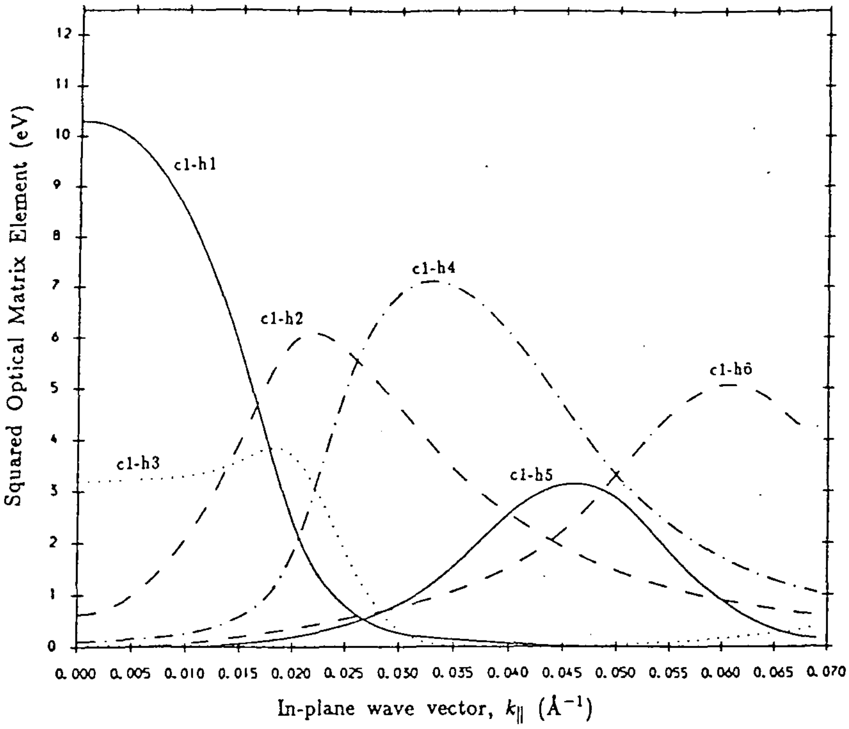

a) Transitions involving first conduction subband.

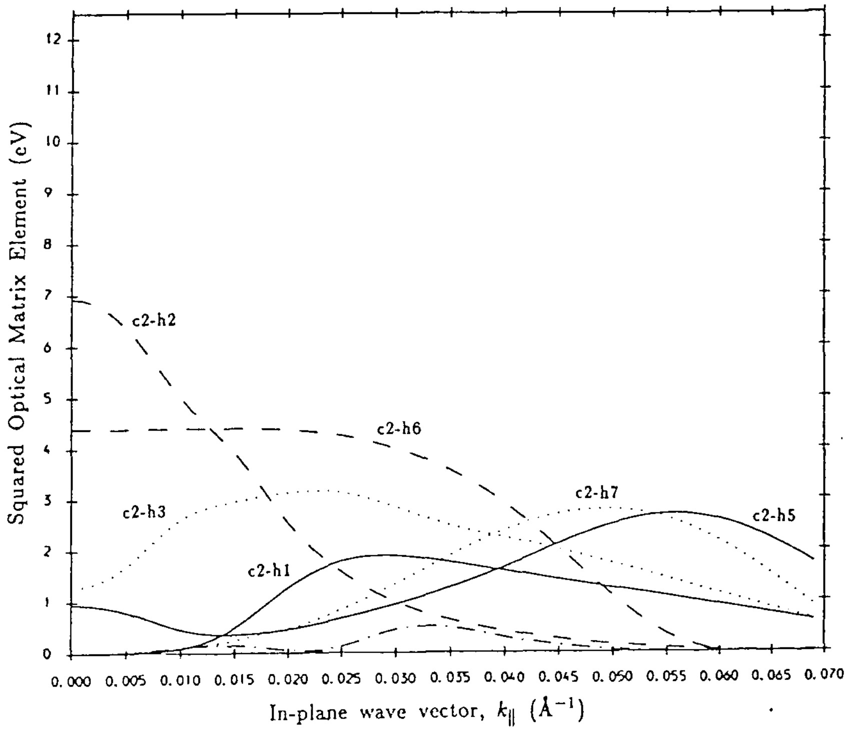

b) Transitions involving second conduction subband.

Optical matrix elements for a 100Å $In_{0.53}Ga_{0.47}As/InP$ unstrained quantum well - TE mode.

Figure 4.6

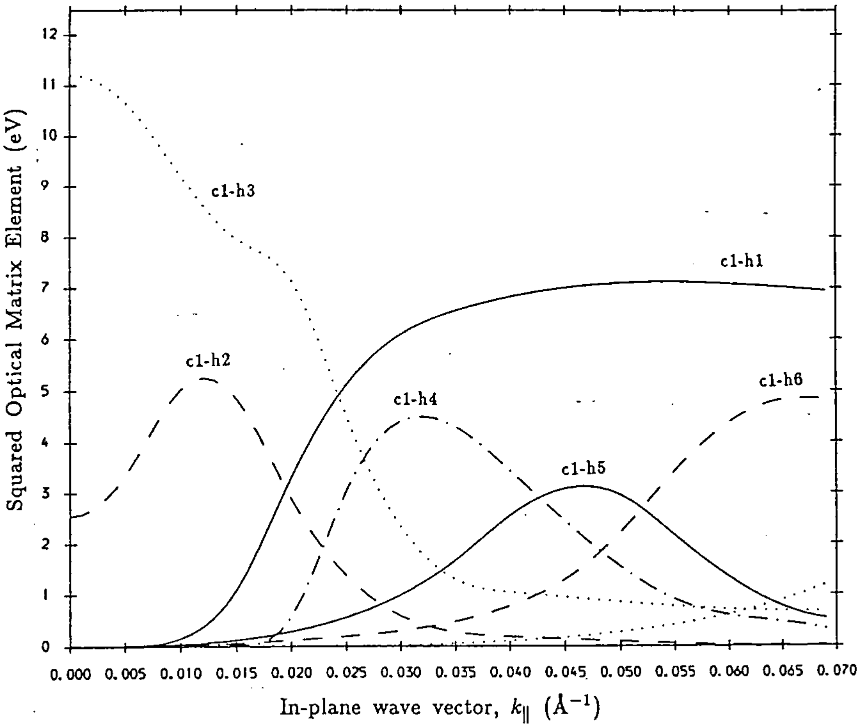

a) Transitions involving first conduction subband.

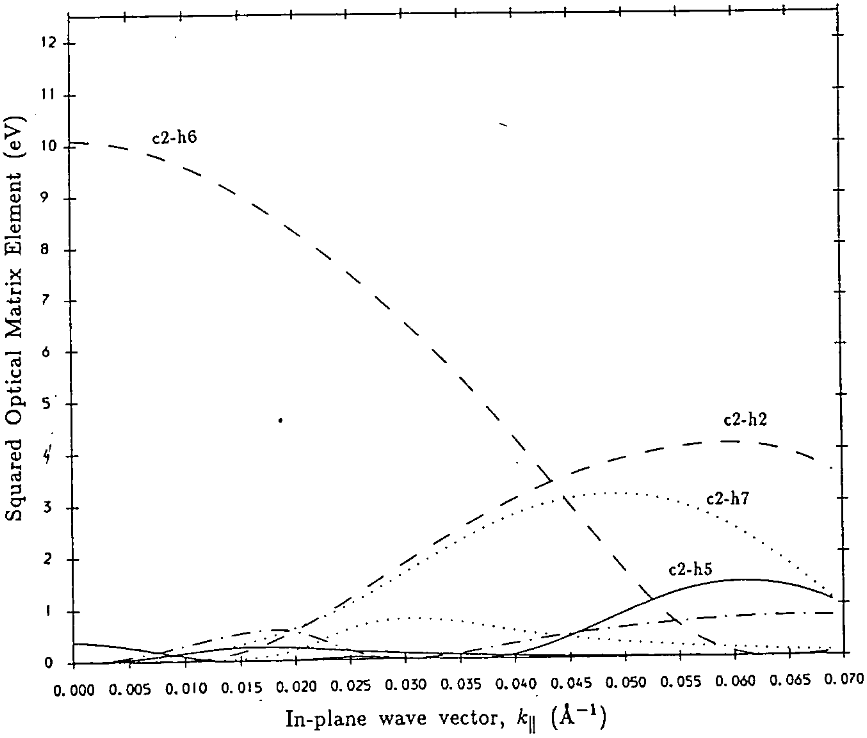

b) Transitions involving second conduction subband.

Optical matrix elements for a 100Å $\text{In}_{0.53}\text{Ga}_{0.47}\text{As/InP}$ unstrained quantum well – TM mode.

Figure 4.7

manifested in the near parabolicity of the dispersion relation of this subband and in the TM mode c2-h6 matrix element following the expected c-lh dependence on $k_{\|}$.

The second and third valence subbands, however, mix strongly even at the centre of the two dimensional Brillouin zone. Their dominant character is 'hh2' ($n = 2$, $m_j = \frac{3}{2}$) and 'lh1' ($n = 1$, $m_j = \frac{1}{2}$) respectively, as is reflected in the large TM mode c1-h3 and TE mode c2-h2 zone centre matrix elements. However, we also observe a large squared matrix element (around 2.5eV) for the c1-h2 TM mode transition, even though this valence band is supposedly of $n = 2$, $m_j = \frac{3}{2}$ character. A simple model which neglect wave function mixing would predict this matrix element to be zero, since the quantum number n is not conserved. Likewise the c2-h3 TE mode matrix element, which might be expected to be zero for the same reason, has a value of just over 1eV.

4.6 Conclusions

The discussion in the previous section of the optical matrix elements obtained from the **k.p** model showed clearly that, whilst broadly following the patterns predicted by a simple model, the matrix elements can be strongly modified by the mixing of wave function character between states in adjacent valence subbands. It is important to include such effects in any realistic description of optical processes in semiconductor quantum wells.

However it is worth noting that these effects may not always be significant since in many cases the mixing is small at the centre of the two dimensional Brillouin zone, where most carriers are to be found, and only dominates at large values of in-plane wave vector, which correspond to transitions 100meV or so above the fundamental absorption edge. For example, in a quantum well laser, which is discussed in detail in the next chapter, it is to be expected that wave function mixing effects will modify the shape of the gain spectrum, but are unlikely to have a significant effect on the threshold properties.

References for Chapter Four

[1] M. Asada, A. Kameyama and Y. Suematsu, IEEE J. Quantum Electron. **QE20**, 745 (1984).

[2] M. Yamanishi and I. Suemene, Jap. J. Appl. Phys. **23**, L35 (1984).

[3] M. Yamada, S. Ogita, M. Yamagishi and K. Tabata, IEEE J. Quantum Electron. **QE21**, 640 (1985).

[4] S. Colak, R. Eppenga and M.F.H. Schuurmans, IEEE J. Quantum Electron. **QE23**, 960 (1987).

[5] Y.C. Chang and J.N. Schulman, Phys. Rev. B **31**, 2069 (1985).

[6] See, for example, S. Gasiorowicz, *Quantum Physics*, Wiley (1974).

[7] E.O. Kane, J. Phys. Chem. Solids **1**, 82 (1956); **1**, 249 (1957).

CHAPTER FIVE

QUANTUM WELL LASER MODELLING

5.1 Introduction

In recent years it has become apparent that semiconductor lasers based on quantum well structures can have considerable advantages over conventional double heterostructure (DH) lasers, such as reduced threshold current [1-4], lower temperature dependence [5-7], a narrower gain spectrum [8], etc. Additionally they offer the ability to tune the lasing wavelength by the appropriate choice of QW width. Such tunability can also be used to improve device performance to some extent; this is especially true in the GaAlAs system, since in this case the alloy composition of the active region and the well width can be chosen independently. Relaxation of the lattice matching condition enables further tailoring of device parameters, and the prospects offered by strained layer lasers for still greater improvements in device performance will be investigated in the next chapter.

The improvement in performance offered by QW lasers is mainly a result of the modified density of states in such a two dimensional structure. This allows a population inversion to be achieved with fewer injected carriers, which are injected into a small volume of active region (the QW itself). In fact, this active layer is often found to be too thin for the various optical losses of the device to be overcome, and it is usually necessary to grow a multiple quantum well (MQW) structure (see figure 5.1) rather than a single quantum well (SQW) in order to enhance the modal gain by increasing the total volume of active material. An alternative (or complementary) approach is to attempt to improve the optical confinement of the emitted beam in addition to the confinement of the carriers. The width of the emitted beam is usually much wider than the width of the quantum well, but a structure can be designed to confine the light over a much narrower region; such a structure is known as a separate confinement heterostructure (SCH). The most promising structure of this type is the graded index separate confinement heterostructure (GRINSCH), in which the composition of the substrate is graded until it reaches that of the barrier (see figure 5.1). Such a device was recently modelled by Chinn *et al* [9]. We consider only the MQW structure in this work, although since the main difference between the MQW and GRINSCH lasers lies in the different optical confinement factor, it would be straightforward to extend this study to GRINSCH structures.

In this chapter the theory of QW laser devices is discussed, and the way in which such a device is modelled is described. The model used includes the effects of realistic bandstructure (see chapter 2) and optical matrix elements (chapter 4), and lifetime broadening effects. It produces gain and spontaneous emission spectra, and can locate the threshold condition of a device, detailing its emission wavelength, current density, linewidth enhancement factor and gainslope at threshold. This model was developed

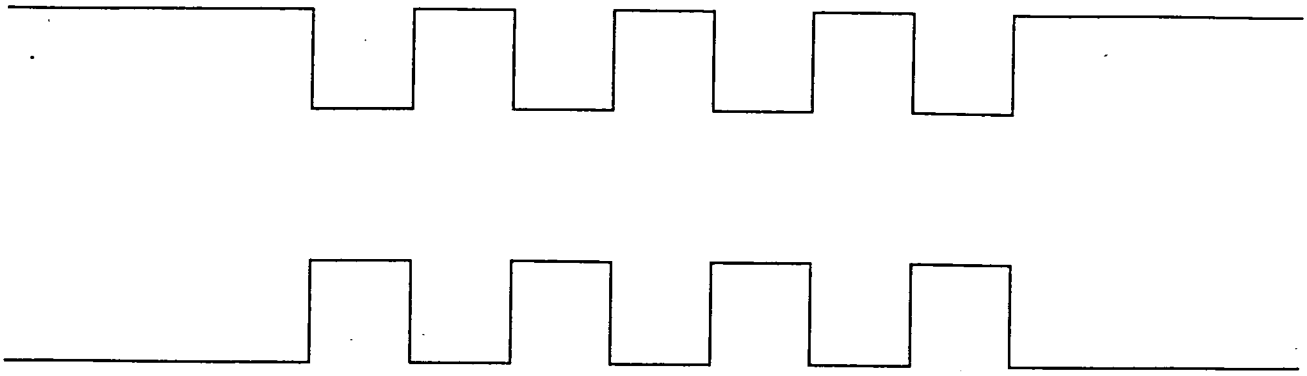

Multiple Quantum Well (MQW)

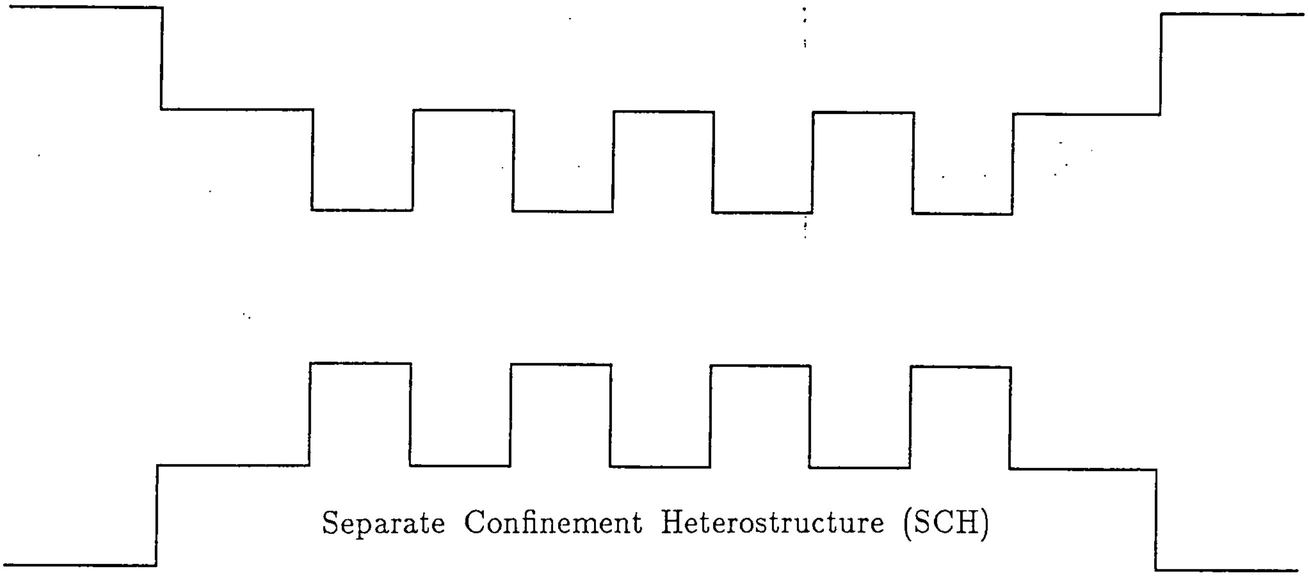

Separate Confinement Heterostructure (SCH)

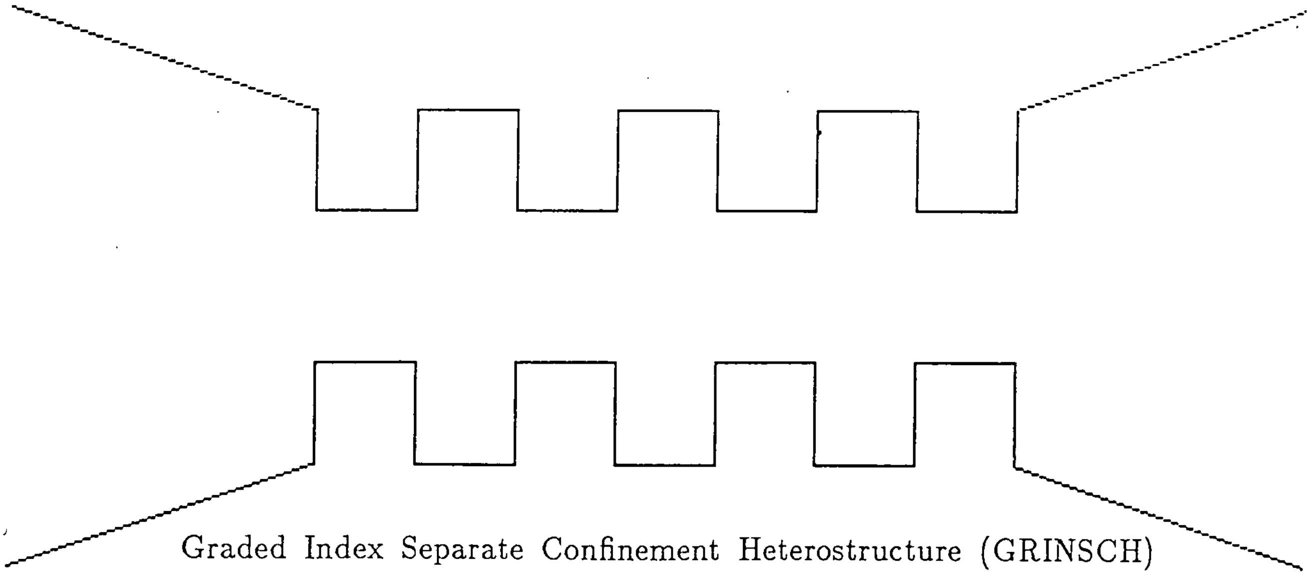

Graded Index Separate Confinement Heterostructure (GRINSCH)

Types of semiconductor laser structures.

Figure 5.1

by the author of this thesis from an existing computer program written by Robbins [10] which calculated the properties of quantum well lasers using a simple parabolic subband approach. The latter has been extensively modified to allow the use of realistic bandstructure and matrix elements, enabling the study of strained layer devices.

Sample results are presented in this chapter for an $In_{0.53}Ga_{0.47}As/InP$ MQW laser device, comparing results obtained from a full **k.p** calculation of the QW states with those from a simple parabolic subband description.

5.2 Absorption and Emission Rates in Semiconductor Lasers

The basic physics of laser operation is well established. The three processes of absorption and spontaneous and stimulated emission can result in the multiplication of photons under certain conditions. The rates of these processes for a two level system are given by [11] :

Absorption $$r_{12}^{a} = B_{12} f_1 (1 - f_2) P(E_{21}) \tag{5.1}$$

Stimulated emission $$r_{21}^{st} = B_{21} f_2 (1 - f_1) P(E_{21}) \tag{5.2}$$

Spontaneous emission $$r_{21}^{sp} = A_{21} f_2 (1 - f_1) \tag{5.3}$$

where A and B are the Einstein coefficients (transition probabilities), f_1 and f_2 are Fermi occupation factors and $P(E_{21})$ is the density of photons of energy E_{21}. In a semiconductor 1 would refer to a state in the valence band and 2 to a state in the conduction band.

It can be shown [11] that

$$B_{12} = B_{21}$$

and

$$A_{21} = \frac{8\pi\mu^3 E_{21}^2}{h^3 c^3} B_{21} \tag{5.4}$$

where μ is the refractive index of the material, h is Planck's constant and c the velocity of light. We can thus combine the absorption and stimulated emission rates into a single rate

$$R_{12}^{\text{abs}} = B_{12}(f_1 - f_2)P(E_{21}) \tag{5.5}$$

The absorption coefficient $\alpha(E_{21})$ is given by the ratio of the absorption rate to the photon flux

$$\alpha(E_{21}) = \frac{R_{12}^{\text{abs}}}{P(E_{21})v_g} = \frac{B_{12}(f_1 - f_2)}{c/\mu} \tag{5.6}$$

where v_g $(= c/\mu)$ is the group velocity of the radiation in the laser material.

From equations (5.3), (5.4) and (5.6) we can express the spontaneous emission rate in terms of the absorption coefficient :

$$r_{21}^{sp} = \frac{8\pi\mu^2 E_{21}^2}{h^3 c^2} \alpha(E_{21}) \frac{f_2(1 - f_1)}{(f_1 - f_2)} \tag{5.7}$$

The Einstein coefficient B_{12} is given by Fermi's Golden Rule :

$$B_{12} = \frac{\pi}{2\hbar} |\langle\psi_1|H'|\psi_2\rangle|^2 \tag{5.8}$$

$$\text{where} \quad H' = -\frac{e}{m}\mathbf{A}.\mathbf{p} \quad \text{(see chapter 4)}$$

$$\text{so} \quad B_{12} = \frac{\pi e^2 \hbar}{m_0^2 \epsilon_0 \mu^2 \hbar\omega} |M|^2 \tag{5.9}$$

where $|M|^2$ is the optical matrix element between states 1 and 2. (See Casey and Panish [11] for further details).

5.3 Interband Absorption and Emission Rates.

In the above discussion the absorption and spontaneous emission rates were given between a *single* valence band state and a *single* conduction band state. Clearly in a semiconductor device there exists a whole range of states which can contribute to the absorption and emission rates, and the expressions obtained must be modified to take account of this. We need to integrate the one state expressions over all possible states, taking into account the density of states. We must only include states which are separated by the appropriate energy ($E_{21} = \hbar\omega$).

Integrating the absorption coefficient (equation (5.6)) over the states of a given pair of subbands of a quantum well, and using equation (5.9) for the transition probability, we obtain an absorption coefficient for the pair given by

$$\alpha_{ij}(\hbar\omega) = \int d\mathbf{k}_{\|} \frac{\pi e^2 \hbar}{m_0^2 \epsilon_0 \mu \hbar\omega c L_z} |M|_{ij}^2 (f_v - f_c)\delta(E_{ij}(\mathbf{k}_{\|}) - \hbar\omega) \tag{5.10}$$

where i and j refer to the conduction and valence subband indices, and E_{ij} is the energy separation of the states. L_z is the quantum well width. Then the absorption coefficient for the quantum well is given by

$$\alpha(\hbar\omega) = \sum_{ij} \alpha_{ij}(\hbar\omega)$$

In laser theory it is usual to give the gain

$$g(\hbar\omega) = -\alpha(\hbar\omega) = -\sum_{ij} \alpha_{ij}(\hbar\omega) \tag{5.11}$$

In chapter 2 we showed that it is reasonable to assume that the bandstructure of a quantum well is isotropic in the (x, y) plane, and introducing this assumption the gain expression becomes :

$$g(\hbar\omega) = \sum_{ij} \int \frac{\pi e^2 \hbar}{m_0^2 \epsilon_0 \mu \hbar\omega c L_z} |M|_{ij}^2 (f_c - f_v)\delta(E_{ij}(k) - \hbar\omega)\frac{4\pi k}{(2\pi)^2} dk \tag{5.12}$$

or
$$g(\hbar\omega) = \sum_{ij} \int \frac{\pi e^2 \hbar}{m_0^2 \epsilon_0 \mu \hbar\omega c L_z} |M|_{ij}^2 (f_c - f_v)\delta(E_{ij}(k) - \hbar\omega)\rho_{ij} dE_{ij} \tag{5.13}$$

where the *joint density of states* ρ_{ij} is given by

$$\rho_{ij} = \frac{k}{\pi} \left| \frac{dk}{dE_{ij}} \right| \tag{5.14}$$

Similarly the spontaneous emission rate is given by

$$r_{sp}(\hbar\omega) = \frac{8\pi^2 e^2 \hbar\omega\mu}{h^2 c^3 m_0^2 \epsilon_0 L_z} \sum_{ij} \int \rho_{ij} f_c (1 - f_v) |M|_{ij}^2 \delta(E_{ij}(k) - \hbar\omega) dE_{ij} \tag{5.15}$$

5.4 Densities of States

Due to the set of discrete energy subbands resulting from the confinement of carriers, the density of states in a quantum well displays a step-like behaviour. This is easily derived from the assumption of parabolic subband dispersion. The number of states per unit area within the range of wave vector from k to $k + dk$ is (assuming isotropic two dimensional bandstructure) given by

$$N(k)dk = 2 \times \left(\frac{1}{2\pi}\right)^2 2\pi k dk$$

where the factor of 2 arises from the spin degeneracy. Hence the density of states per unit area is given by

$$\rho(E)dE = \frac{1}{(2\pi)^2} \frac{4\pi k}{|\partial E/\partial k|} dE = \frac{k}{\pi\, |\partial E/\partial k|} \tag{5.16}$$

For a parabolic subband $E = \frac{\hbar^2 k^2}{2m^*}$, so

$$\rho(E)dE = \frac{k}{\pi \hbar^2 k/m^*} dE = \frac{m^*}{\pi \hbar^2} H(E) dE \tag{5.17}$$

for each subband, with

$$H(E) = \begin{cases} 0, & \text{for } E < \Delta E_0 \\ 1, & \text{for } E \geq \Delta E_0 \end{cases}$$

where ΔE_0 is the subband edge energy.

For a set of subbands, we thus have

$$\rho(E)dE = \sum_i \frac{m_i^*}{\pi \hbar^2} H_i(E) dE \tag{5.18}$$

Similarly the joint density of states is

$$\rho(E)dE = \sum_i \sum_j \frac{m_i^* m_j^*}{m_i^* + m_j^*} H_{ij}(E) \frac{1}{\pi \hbar^2} dE \tag{5.19}$$

where

$$H_{ij}(E) = \begin{cases} 0, & \text{for } E < \Delta E_i + \Delta E_j \\ 1, & \text{for } E \geq \Delta E_i + \Delta E_j \end{cases}$$

with ΔE_i, ΔE_j the band edge energies for subband i, j. The sum over i includes all conduction subbands, and that over j all valence subbands.

It has already been shown in chapter 2, however, that real quantum well subbands can exhibit marked non-parabolicity, due to inter-subband wave function mixing effects. This results in deviations from the simple step-like behaviour of the density of states in the parabolic model, and to obtain accurate results it is necessary to calculate $k/\pi|\partial E/\partial k|$ from the bandstructure. In order to do this, the bandstructure is first fitted to an expansion of cubic splines using a NAG subroutine (E02BAF) — details of the fitting procedure are given in Appendix B. All the calculations which use realistic bandstructure described henceforth utilise this fitting procedure to allow the calculations to be executed on a reasonable timescale. A similar fitting procedure is used to enable the in-plane wave vector dependence of the optical matrix elements to be included.

The valence band density of states is shown in figure 5.2 for a 50Å $In_{0.53}Ga_{0.47}As/InP$ quantum well. (Refer to figure 2.4 for the bandstructure of this structure). The solid line represents the results obtained from a k.p bandstructure calculation and the dashed line shows the step-like behaviour given by a simple parabolic band approach. The effective masses used in the parabolic model were obtained from an approximate fit to the k.p bandstructure, and the subband energies used are taken directly from k.p results. (The effective mass for the parabolic fit was obtained by averaging the effective masses necessary for the subband to pass through each of three calculated points along the band). The threshold energies for the second and fourth subbands differ in the two models since the simple model does

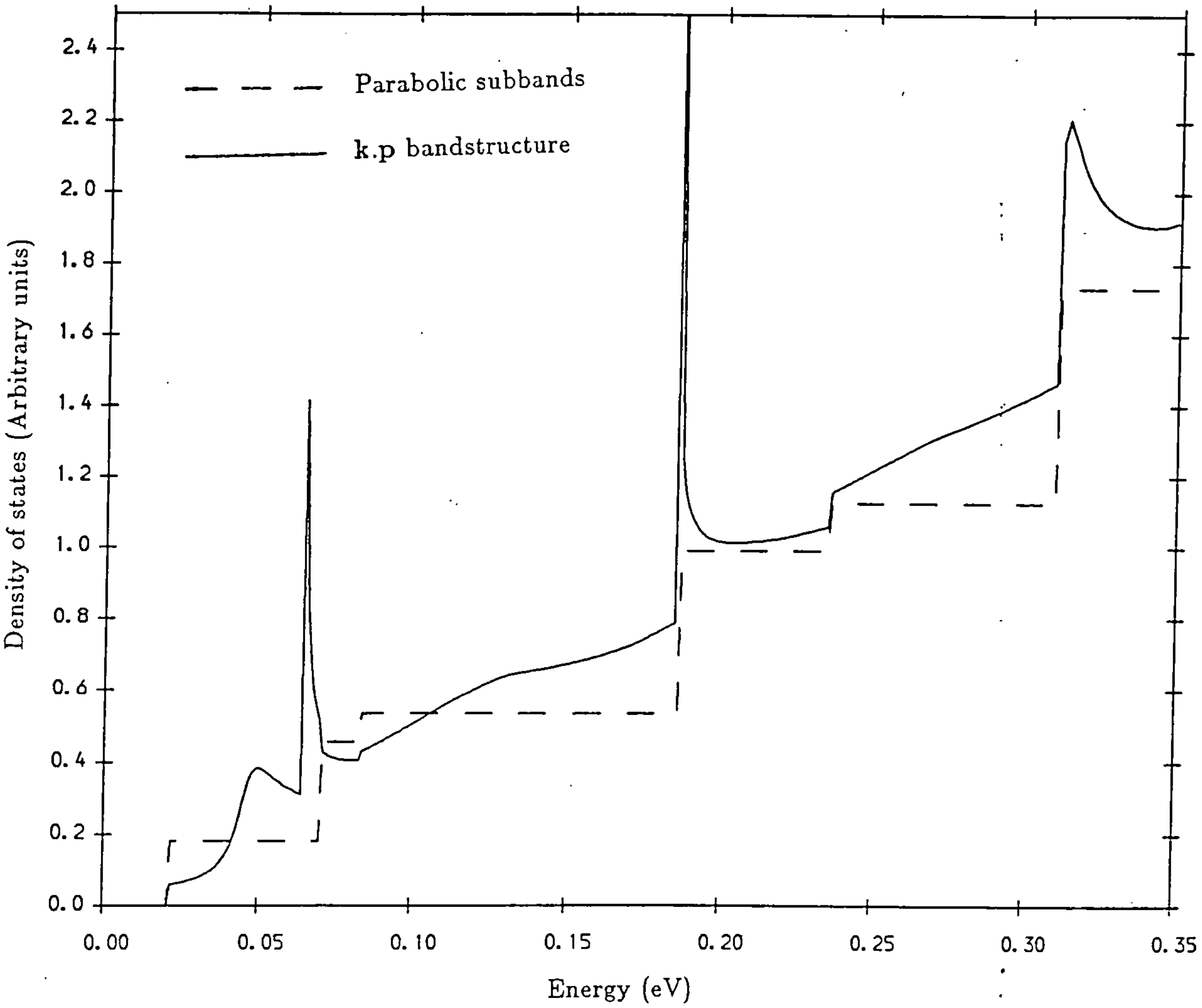

Figure 5.2

Valence band density of states for a 50Å $In_{0.53}Ga_{0.47}As/InP$ quantum well.

not take account of the initial 'electron-like' behaviour of these subbands, which results in the subband minima lying away from the centre of the two dimensional Brillouin zone.

It is clear from figure 5.2 that the density of states obtained using the **k.p** model differs dramatically from the step-like behaviour predicted by the simple model. In particular, singularities occur in the density of states at energies corresponding to the turning points of those subbands which are 'electron-like' close to $k = 0$. It is worth noting that if bulk effective masses had been used in the parabolic band model the discrepancies between the two sets of results would be greater still, suggesting that a realistic description of the quantum well bandstructure is important in the modelling of a laser device.

Figure 5.3 shows the density of states for the conduction band of the same heterostructure. Again the **k.p** results deviate fron those of the simple model, but in this case the difference is less dramatic, and the conduction band density of states fails to reveal the degree of structure which appears in the valence band results. This is to be expected since the conduction subband is close to parabolic (see figure 2.4a).

The joint density of states is illustrated in figure 5.4. Much of the structure observed for the **k.p** results in the valence band density of states is absent from the joint density of states due to the low effective mass of the conduction band. Only the singularity resulting from the turning point in the second valence band remains; the other singularity disappears because

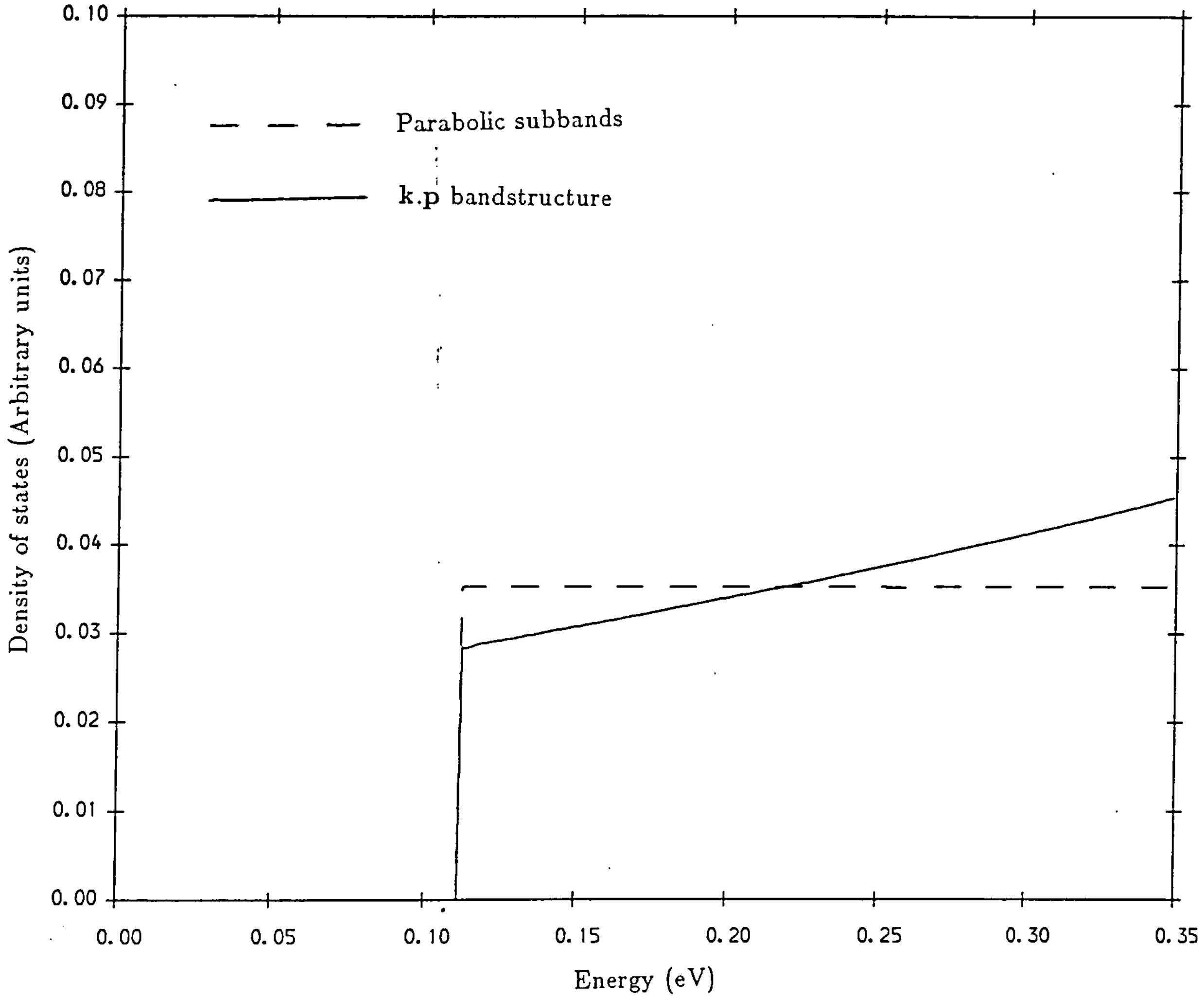

Figure 5.3

Conduction band density of states for a 50Å $In_{0.53}Ga_{0.47}As/InP$ quantum well.

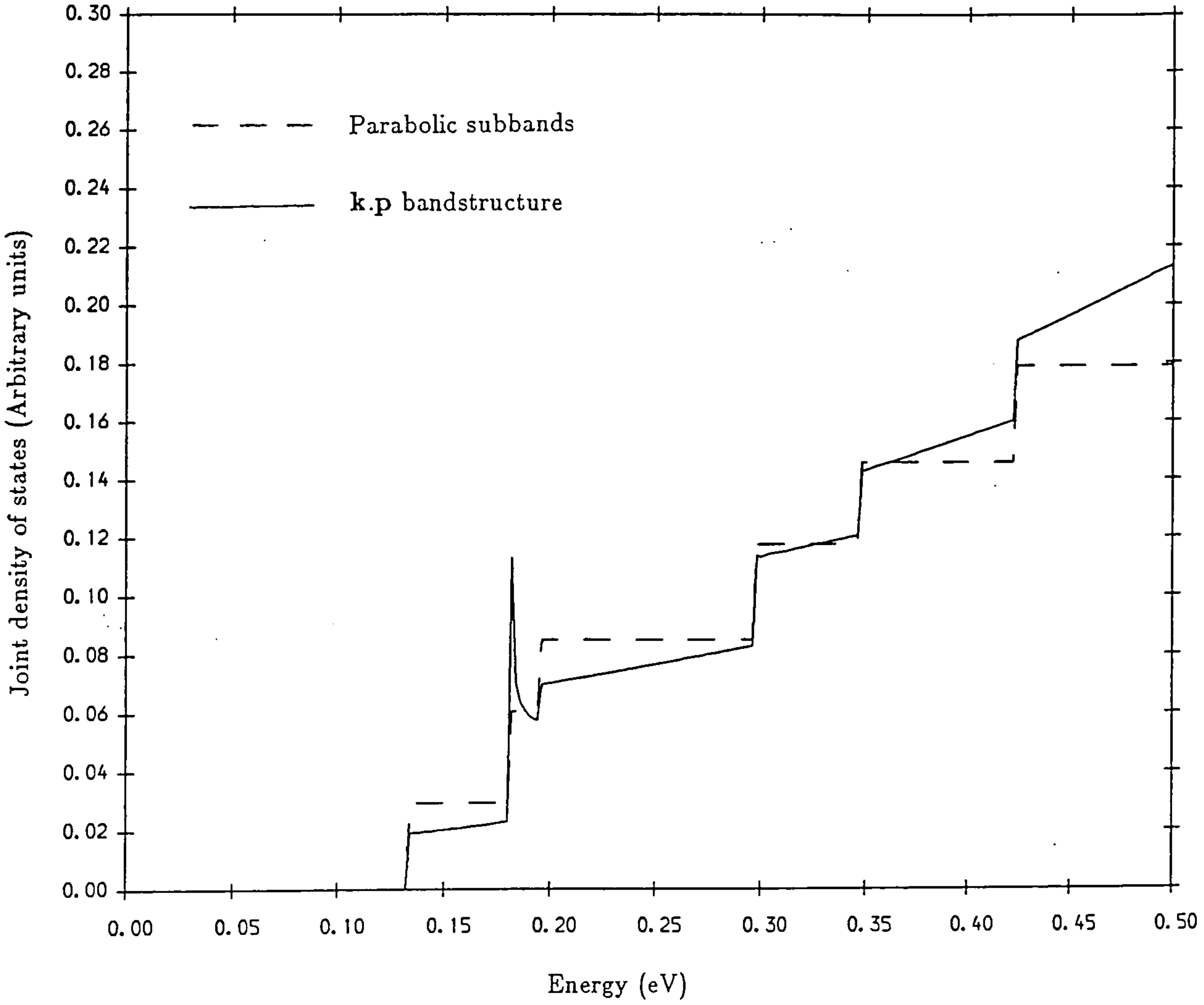

Figure 5.4

Joint density of states for a 50Å $In_{0.53}Ga_{0.47}As/InP$ quantum well.

the conduction band has a lower effective mass close to $k_{\|} = 0$ than the fourth valence band, so the total kinetic energy for this band pair increases with increasing in-plane wave vector, and does not show a turning point.

5.5 Occupation Factors and Quasi-Fermi Levels.

The Fermi occupation factors f_c and f_v appearing in the gain (equation (5.13)) and spontaneous emission (equation (5.15)) rates are given by the usual expressions :

$$f_c(E_c) = \frac{1}{\exp\left[(E_c - F_c)/kT\right] + 1} \tag{5.20}$$

$$f_v(E_v) = \frac{1}{\exp\left[(E_v - F_v)/kT\right] + 1}. \tag{5.21}$$

f_c and f_v are the probabilities that the conduction and valence band levels at E_c and E_v respectively contain an electron. It is important to note that lasers operate under non-equilibrium conditions so the quasi-Fermi levels F_c and F_v will not, in general, be equal. They are calculated from the total number of injected carriers using the conditions

$$n = \frac{1}{L_z}\sum_i \int_{\Delta E_i}^{\infty} f_c(E)\rho_i(E)dE \tag{5.22}$$

$$p = \frac{1}{L_z}\sum_j \int_{-\infty}^{-\Delta E_j} (1 - f_v(E))\rho_j(E)dE \tag{5.23}$$

where n and p are the densities of injected electrons and holes respectively and L_z is the quantum well width. (The charge neutrality condition $n = p$ is used in all our simulations). The sum over i includes all conduction subbands, and that over j includes all valence subbands. In the parabolic band approximation these integrals can be performed analytically to obtain

$$n = \sum_i \frac{m_i^* kT}{\pi \hbar^2 L_z} \ln \left[1 + \exp\left(\frac{F_c - \Delta E_i}{kT} \right) \right] \tag{5.24}$$

$$p = \sum_j \frac{m_j^* kT}{\pi \hbar^2 L_z} \ln \left[1 + \exp\left(\frac{-\Delta E_j - F_v}{kT} \right) \right] \tag{5.24}$$

where ΔE_i (ΔE_j) is the band edge energy of the ith (jth) conduction (valence) subband.

In the full **k.p** calculation the integrals are performed numerically using a NAG subroutine (D01AJF). The integrals are calculated in wave vector space :

$$n = \frac{1}{\pi L_z} \sum_i \int_0^{k_0} \frac{k dk}{1 + \exp\left[(E_i(k) - F_c)/k_B T \right]} \tag{5.26}$$

$$p = \frac{1}{\pi L_z} \sum_j \int_0^{k_0} \frac{k dk}{1 + \exp\left[(F_v - E_j(k))/k_B T \right]} \tag{5.27}$$

The integral is cut-off at an arbitrary wave vector k_0, beyond which the probability of the subband being occupied is assumed to be negligible. In the calculations described the value $k_0 = 0.18\text{Å}^{-1}$ is chosen, which gives virtually zero probability of finding a carrier at the cut-off point, in either the conduction or the valence band.

Figure 5.5 shows the electron and hole quasi Fermi levels (QFLs) as functions of the injected carrier density at 300K. The solid lines are obtained using the full **k.p** bandstructure and the dashed lines from the parabolic approximation to these results described in the last section. As is to be expected, the QFLs move deeper into the subbands as the carrier density

a) Electron quasi Fermi level at 300K.

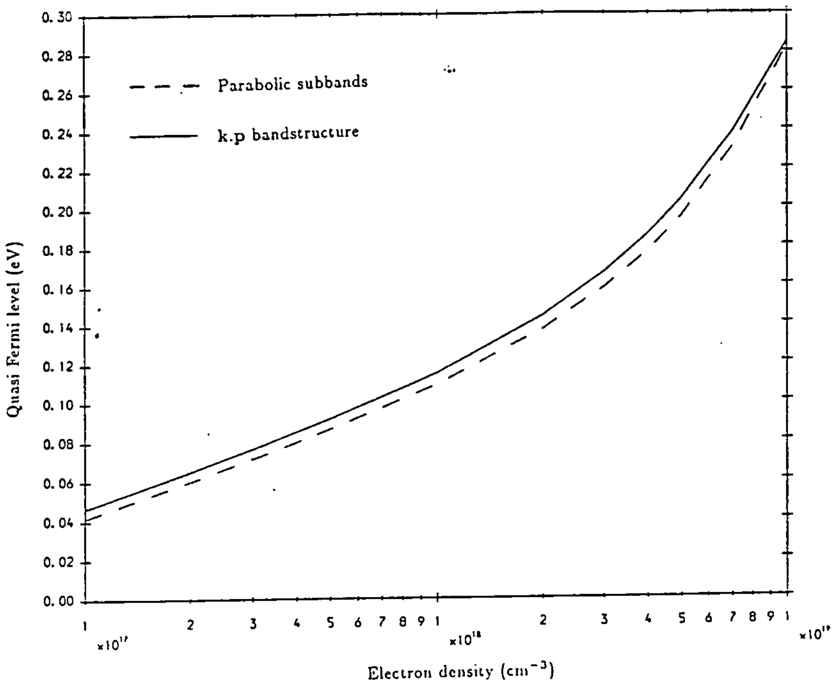

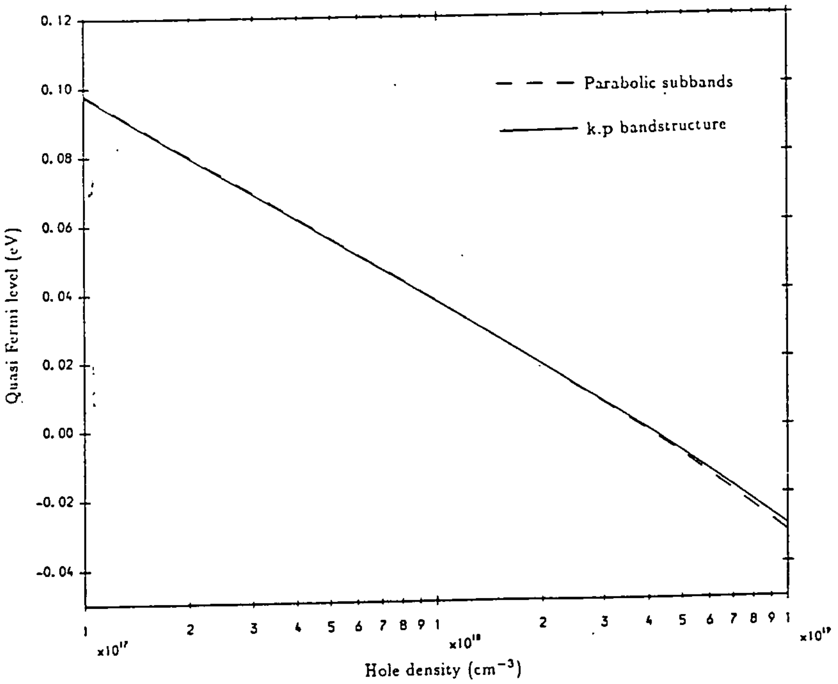

b) Hole quasi Fermi level at 300K.

Figure 5.5

is increased. It is apparent that the non-parabolicity of the subbands has very little effect on the quasi Fermi level, although it should be noted that because the parabolic band results shown here are based on a fit to the **k.p** bandstructure it is to be expected that they will give similar subband occupancies.

Figure 5.6 shows the dependence of the QFLs on temperature for a fixed carrier density ($10^{18}\mathrm{cm}^{-3}$). As the temperature is increased, the mean kinetic energy of the carriers is raised, resulting in the QFLs being lowered in carrier (electron or hole) energy in order to keep the total number of carriers in the bands unchanged.

5.6 Lifetime Broadening Effects.

In the preceding discussion and calculations it has been assumed that only transitions which conserve in-plane momentum are permitted (the so-called *k-selection* condition). It is immediately apparent from experimental gain spectra, however, that this condition is not rigidly upheld in a real device. These spectra do not exhibit the predicted step like structure; rather a series of smoothed peaks is observed, due to a broadening of the spectrum.

The mechanism causing this broadening, and the effect of carrier density and energy on the lifetime associated with the process has been discussed recently by Kucharska and Robbins [12] and by Asada [13]. Both papers consider the broadening resulting from intraband scattering processes,

a) Temperature dependence of electron quasi Fermi level.

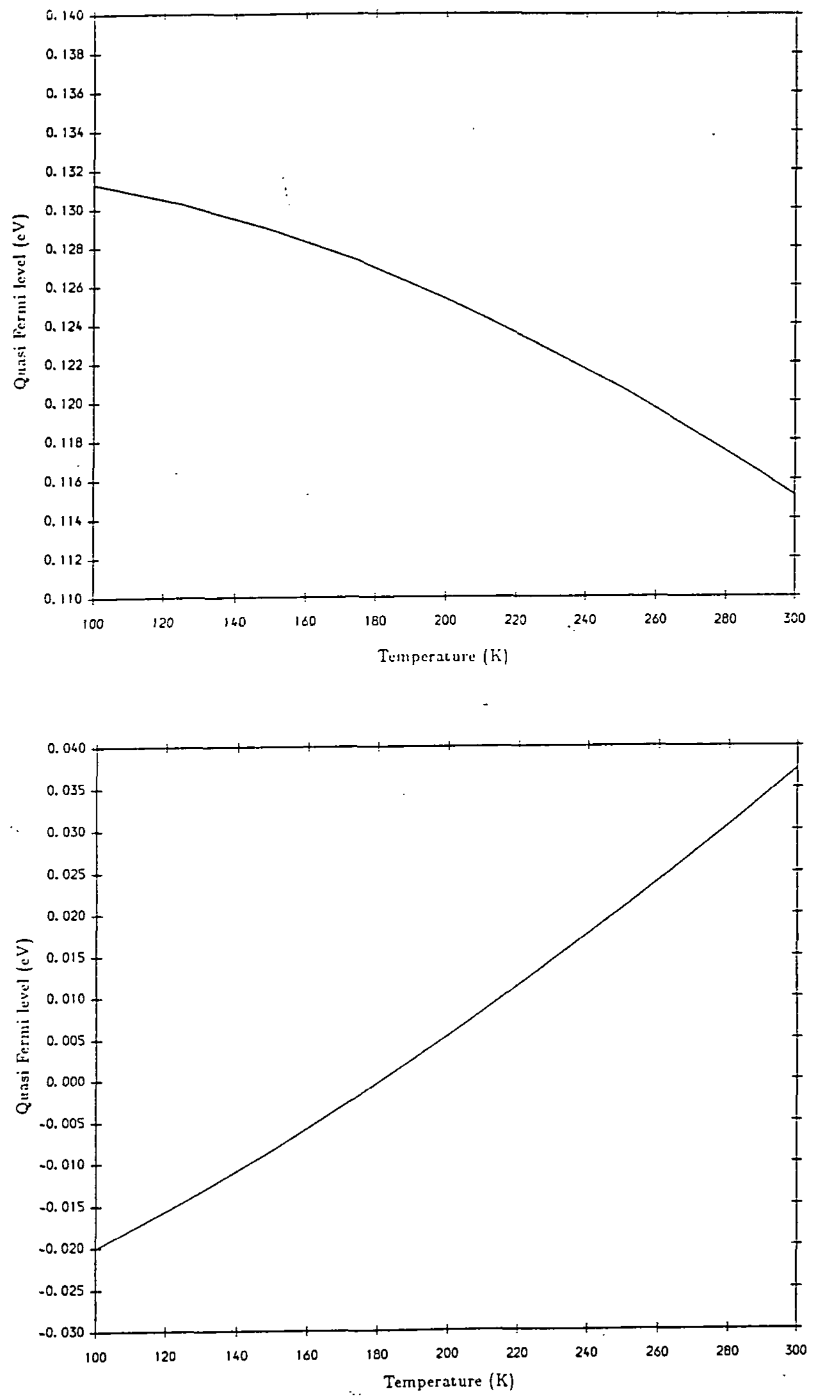

b) Temperature dependence of hole quasi Fermi level.

Figure 5.6

and Asada also includes longitudinal optical phonon scattering. The simplest example of an intraband scattering process is illustrated in figure 5.7. When an electron in the conduction band recombines with a hole in the valence band by the process of stimulated (or spontaneous) emission, the hole which is left behind in the conduction band can be filled by an electron as it undergoes scattering with another electron in the subband. Thus the hole formed by the recombination process has a lifetime associated with it which is determined by the intraband scattering process, and this results in a broadening of the emission spectrum. It is easy to appreciate that this lifetime is dependent on both the density of electrons in the conduction band and on the initial energy of the recombining electron, since these factors affect the probability of finding two further electrons in suitable energy states to fill the resulting hole by an intraband scattering process. The precise form of these dependencies is discussed in detail by both Kucharska and Robbins [12] and Asada [13].

Many authors have included broadening effects in their models of laser gain and spontaneous emission spectra; usually, however, this is done by means of a constant intraband scattering time [14,15]. It is impractical to implement the full descriptions of the works mentioned above [12,13] in our calculations, since this would make them restrictively expensive in computer time, but we do include in our model a broadening energy Γ_{cv} which varies linearly with energy in the region where the intraband scattering is dominant, and which is a material dependent constant for higher energies

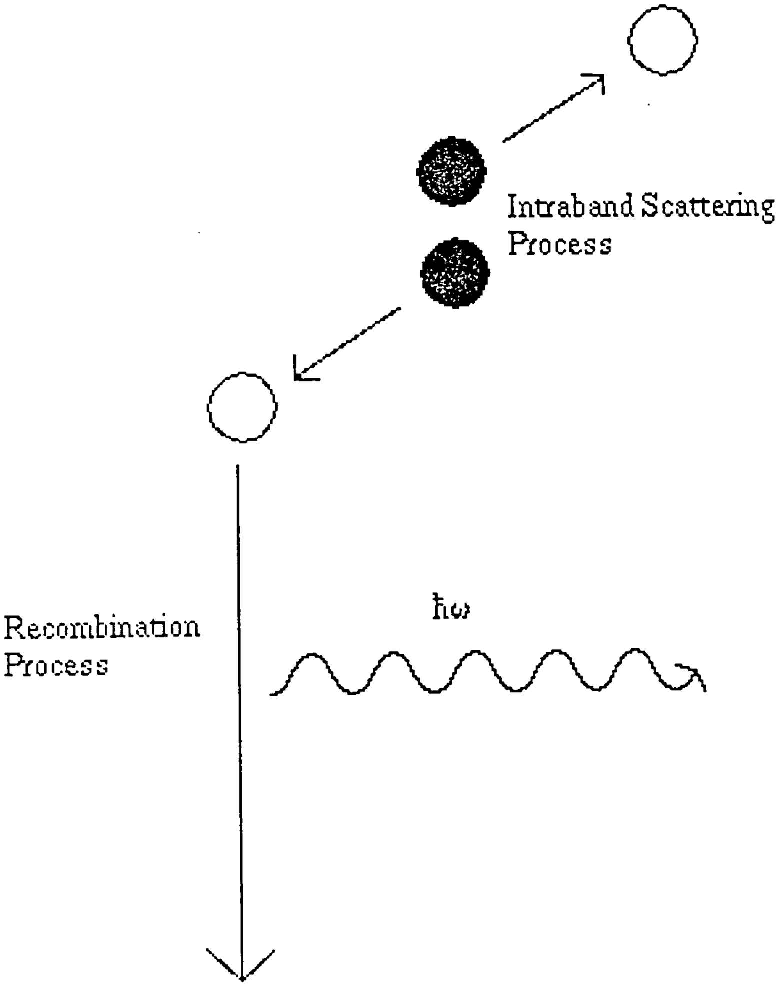

A typical intraband scattering process.

Figure 5.7

(see figure 5.8). This broadening is readily included in the expression for the gain of the laser :

$$g(\hbar\omega) = \sum_{ij} \int dE_{ij} \int_{-\infty}^{\infty} d\epsilon \frac{\rho_{ij} \pi e^2 \hbar}{m_0^2 \varepsilon_0 \mu \hbar \omega c L_z} \left| M \right|_{ij}^2 (f_c - f_v) \frac{L(E_{ij}, \epsilon)}{\pi} \delta(E_{ij}(k) - \hbar\omega) \tag{5.28}$$

where $$L(E_{ij}, \epsilon) = \frac{\Gamma(E_{el})}{(E_{ij} - \hbar\omega - \epsilon)^2 + \Gamma^2(E_{el})} \tag{5.29}$$

with E_{el} = electron kinetic energy

and $$\Gamma = \frac{\hbar}{\tau_{in}}$$

(τ_{in} is the intraband relaxation time).

5.7 Optical Confinement Factor.

So far we have only considered the optical properties of the active region of a quantum well laser device. However, the beam profile of the light emitted by such a device will, in general, be sufficiently broad that the light will propagate not only in the active well and barrier regions, but also in a significant volume of the cladding regions of the device (see figure 5.9). In order to investigate the threshold condition of such a device (see following section), it is necessary to know what proportion of the light propagates within the active region (and experiences a positive net gain), and what proportion propagates within the barrier and cladding regions (and experiences a negative net gain). The important parameter to determine is the ratio of the light intensity within the active layer(s) to the total light

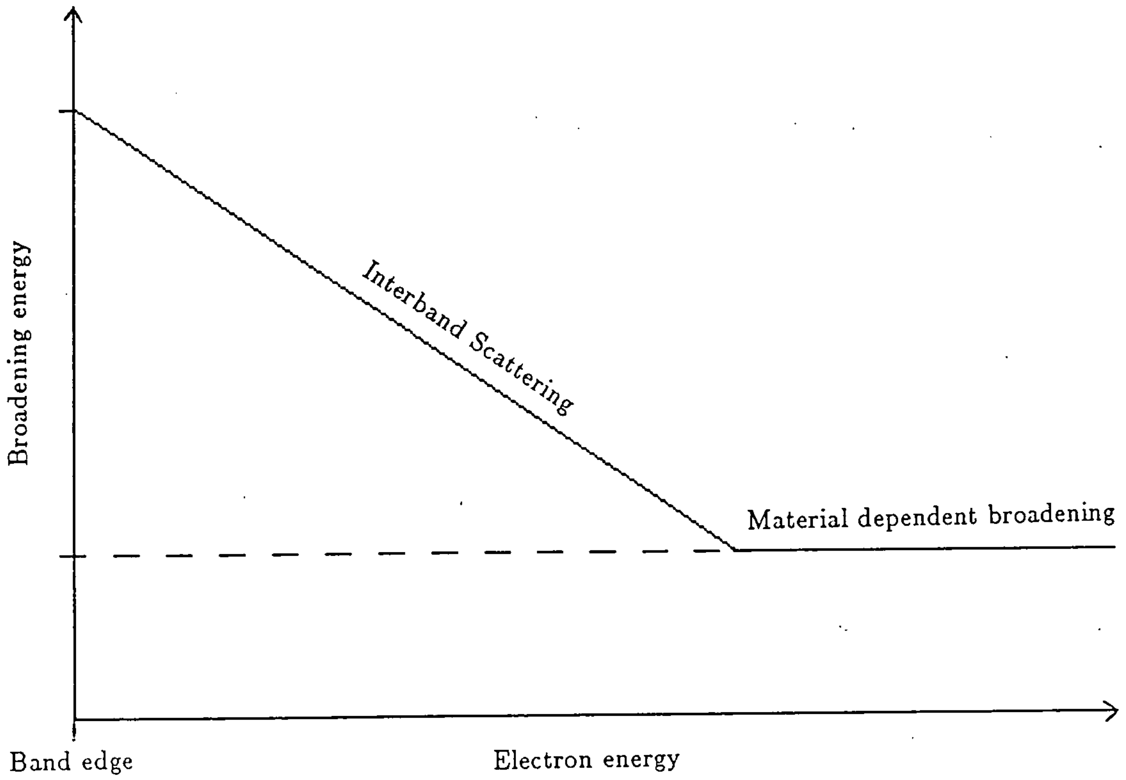

Figure 5.8

The energy dependence of the broadening energy Γ.

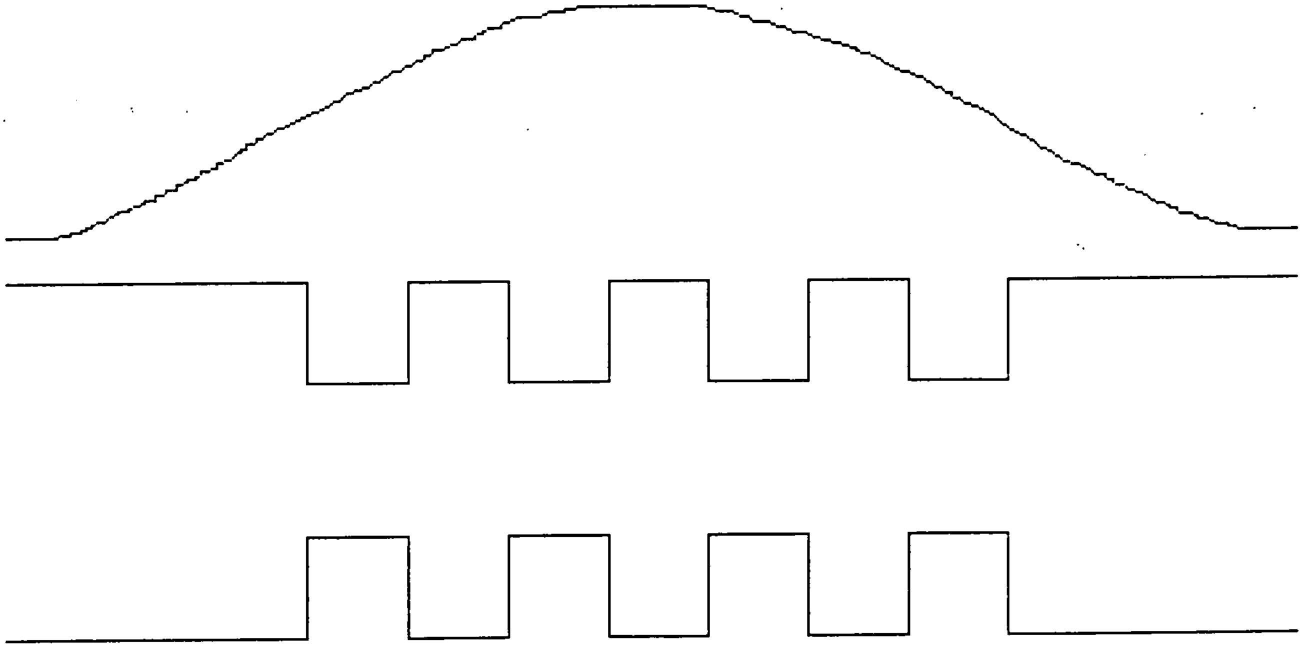

A typical beam profile for an MQW structure.

Figure 5.9

intensity, and is known as the confinement factor, usually denoted by Γ.

Since the light intensity is given by the magnitude of the Poynting vector, which is proportional to the square of the electric field component parallel to the well-barrier interfaces, we obtain

$$\Gamma = \frac{\int_{\mathrm{Wells}} |\mathcal{E}_y|^2 \, dz}{\int_{-\infty}^{\infty} |\mathcal{E}_y|^2 \, dz} \tag{5.30}$$

for light which is propogating in the x direction and confined in the z direction. In general, the determination of Γ requires the calculation of the electric field distribution from the refractive index profile of the device, which is mathematically straightforward but computationally laborious. It has been shown by Streifer *et al* [16] that the transverse electric (TE) mode confinement factor of a multiple quantum well laser can be approximated by treating it as a single quantum well (three layer waveguide) device with the thickness of the active layer region equal to the total thickness, $\bar{t}$, of the wells and barriers, and the refractive index of this region given by the average

$$\bar{n} = \frac{N_W t_W n_W + N_B t_B n_B}{\bar{t}} \tag{5.31}$$

where

$$\bar{t} = N_W t_W + N_B t_B \tag{5.32}$$

They show that this approximation gives results accurate to around 1% or better if the device only supports one TE mode, and to around 4% if the device supports two TE modes.

Using this approximation the confinement factor is simply given by the appropriate three-layer confinement factor weighted by the proportion of the central region which is active :

$$\Gamma = \gamma \frac{N_W t_W}{\bar{t}} \tag{5.33}$$

γ is given by [17]

$$\gamma \simeq \frac{\bar{D}^2}{\bar{D}^2 + 2} \tag{5.34}$$

$$\text{with} \quad \bar{D} = \frac{2\pi \bar{t}}{\lambda_0} \left(\bar{n}^2 - n_c^2 \right)^{\frac{1}{2}} \tag{5.35}$$

where n_c is the refractive index of the cladding region and λ_0 is the free space wavelength of the light.

In figure (5.10) the variation of confinement factor with the number of quantum wells in the structure is shown for three different MQW laser devices. The solid line represents the confinement factor for an $In_{0.53}Ga_{0.47}As/InP$ MQW laser with 50Å wells and 150Å barriers. (The dependence of the confinement factor on the barrier width is small). This is the device structure we shall use to illustrate our model in this chapter. The dashed and dotted lines show the improvement that would be achieved by replacing the cladding InP region (with refractive index 3.19) by a region with refractive index of 3.1 and 2.9 respectively (a so-called separate confinement heterostructure (SCH)). Clearly the structure we are considering is far from optimised with respect to optical confinement, but it will suffice to illustrate the model of laser properties and to evaluate trends. The optimisation of optical confinement and waveguiding properties can be regarded as a separate problem to that of the physics of laser operation, and since the former is well understood, we concentrate our attention in

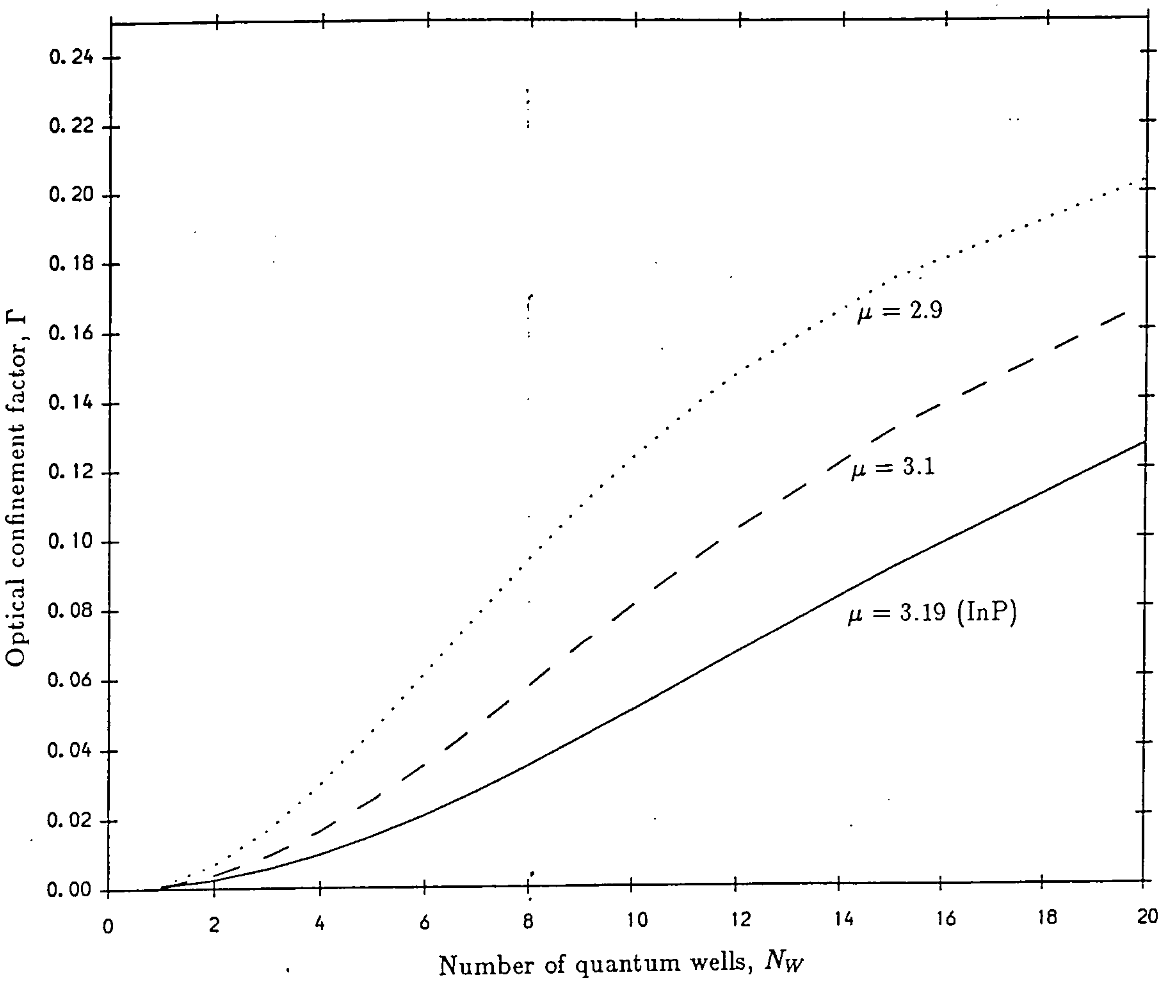

Figure 5.10

Calculated optical confinement factors

this work on the latter problem.

5.8 Threshold Calculations.

As the carrier density within the active region of a semiconductor laser is increased, the gain will be increased faster than the various optical losses (such as intervalence band absorption and light emission through the end facets), and eventually the gain will exceed the losses, resulting in the laser switching on. The properties of the laser in the region of this threshold condition are important factors in determining the usefulness of device. It is important to determine and optimise such properties as the operating wavelength (which depends upon the shape of the gain spectrum at threshold), the threshold current, and the gainslope, $\frac{\partial g}{\partial n}$, which is the rate at which the gain increases with increasing carrier density. The latter parameters determine the power consumption of the device, both at threshold and for a given intensity of the output beam. Clearly it is desirable to make the threshold current as low as possible, and the gainslope as high as possible.

The threshold condition is readily identified from a consideration of gain and loss processes, and is given by [11]

$$\Gamma g_{th} = \Gamma \alpha_a + (1 - \Gamma)\alpha_c + \frac{1}{L}\ln\left(\frac{1}{R}\right) \tag{5.36}$$

where Γ is the optical confinement factor, L the cavity length, R the end facet reflectivity and α_a and α_c the optical losses within the active and cladding/barrier regions respectively. Intervalence band absorption is included in α_a via a simple parameterisation of bulk values from the literature. The threshold condition is located using the NAG routine C05AGF to search for a zero net gain as the carrier density is varied. The threshold current is then obtained by calculating the total current due to spontaneous emission and Auger recombination at the threshold carrier density.

5.9 Results for a 50Å $In_{0.53}Ga_{0.47}As/InP$ MQW laser

To illustrate the capabilities of the laser model we have developed, and to show how the results obtained differ from those obtained using a simple parabolic fit to the **k.p** bandstructure, we present the results of a study of the properties of a 50Å $In_{0.53}Ga_{0.47}As/InP$ multiple quantum well laser. The bandstructure and transverse electric mode matrix elements for a 50Å single quantum well in this material system have already been discussed (in chapters 2 and 4 respectively), and we assume that the barriers are sufficiently wide that the structure acts as a set of N_W independent quantum wells, rather than a short superlattice. The parameters used in these calculations are given in appendix 1.

5.9.1 Gain Spectra

The importance of including realistic bandstructure details in the laser model is illustrated clearly by the gain spectra obtained (see figure 5.11, which shows the gain spectrum of a 50Å $In_{0.53}Ga_{0.47}As/InP$ quantum well with an injected carrier density of $5 \times 10^{18}cm^{-3}$). The use of a parabolic band model overestimates the gain by about a factor of 2 — this confirms that the findings of Colak *et al* [18] for the GaAs/AlGaAs system hold more generally. This arises because of the reduced density of states near to the valence band edge predicted by the full model, and because the optical matrix element for this band edge transition is reduced slightly by intersubband wave function mixing.

The results obtained using a rigid **k**-selection rule show clearly the relative strengths of the transitions between the different subband pairs, which show up as additional steps in the gain spectrum. The transition to the first light hole subband, which has a threshold energy of around 0.93eV, is stronger in the **k.p** model than in the parabolic band model. This is due to the very high density of states of this subband near to the subband edge, which is not included in the simple approach. It is important to notice also that when lifetime broadening effects are included, the peak of the gain spectrum is shifted away from the QW band gap energy, and the peak gain is reduced slightly. For these reasons, it is important to include the broadening in any threshold calculations in order to obtain the

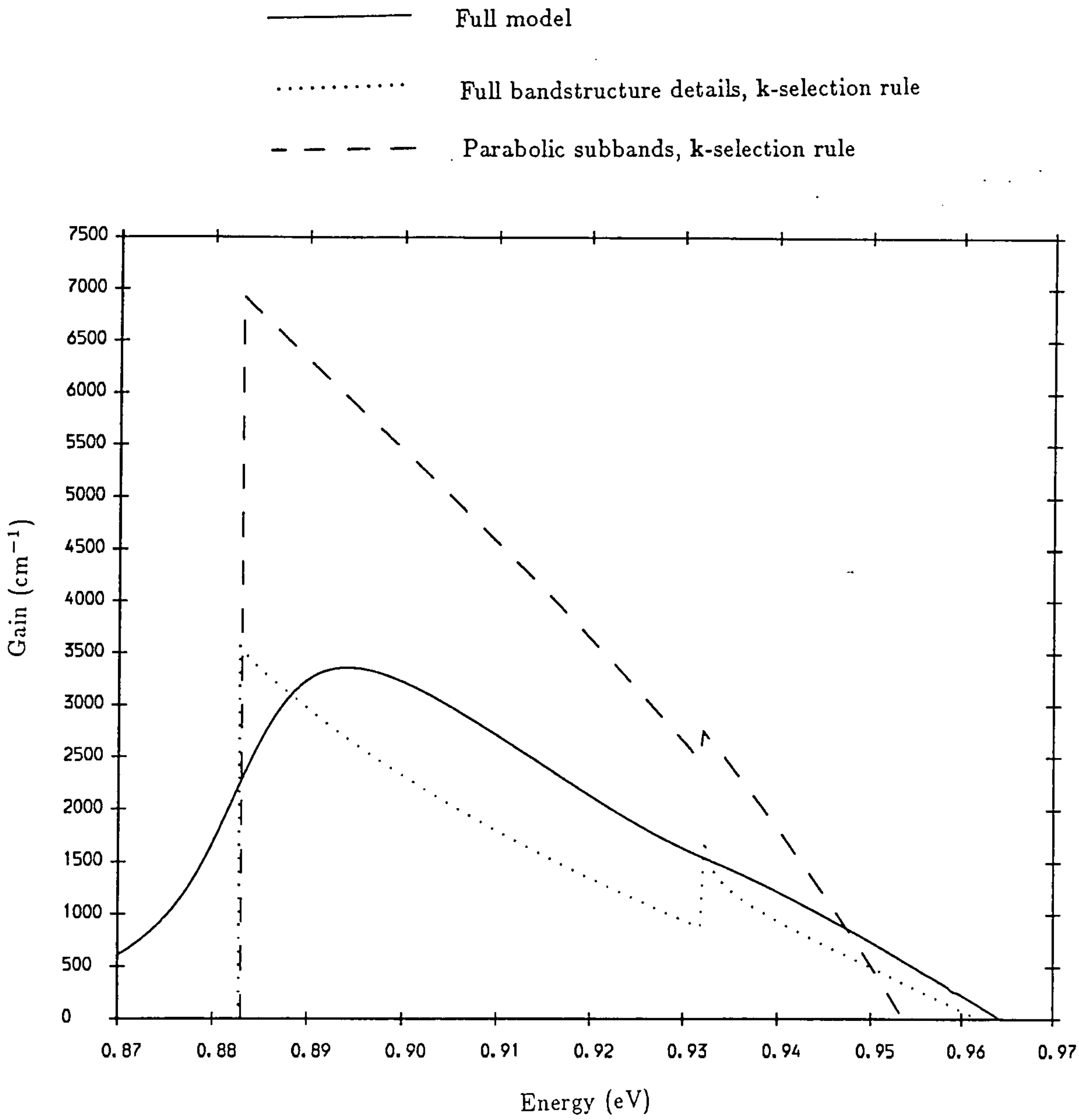

Figure 5.11

Gain spectrum for a 50Å $In_{0.53}Ga_{0.47}As/InP$ quantum well.

correct location of the threshold condition and hence the correct emission wavelength.

Figure 5.12 shows the effect of increasing carrier density on the broadened gain spectrum. Obviously as the number of carriers present increases, the gain increases, but note that the band edge gain increases proportionately more as the carrier density is increased from $3 \times 10^{18}\text{cm}^{-3}$ to $5 \times 10^{18}\text{cm}^{-3}$ than it does when the carrier density is increased beyond $5 \times 10^{18}\text{cm}^{-3}$. This indicates that the first valence subband is very nearly full at $p = 9 \times 10^{18}\text{cm}^{-3}$, resulting in a saturation of the band edge gain. This conclusion is supported by the presence of a 'kink' in the gain spectrum at around 0.93eV in the $p = 9 \times 10^{18}\text{cm}^{-3}$ curve. This corresponds to the transition between the conduction subband and the second valence subband (which has $n = 1$ light hole character), suggesting that at this carrier density any further holes are mainly being injected into the second subband, rather than the first.

5.9.2 Spontaneous Emission

Figure 5.13 shows the spontaneous emission spectrum of a 50Å $In_{0.53}Ga_{0.47}As/InP$ quantum well for an injected carrier density of $5 \times 10^{18}\text{cm}^{-3}$. It is clear that the parabolic band model overestimates the strength of the spontaneous emission at the QW band gap energy, as is the case for the gain spectrum. Again this is due to overestimating the density

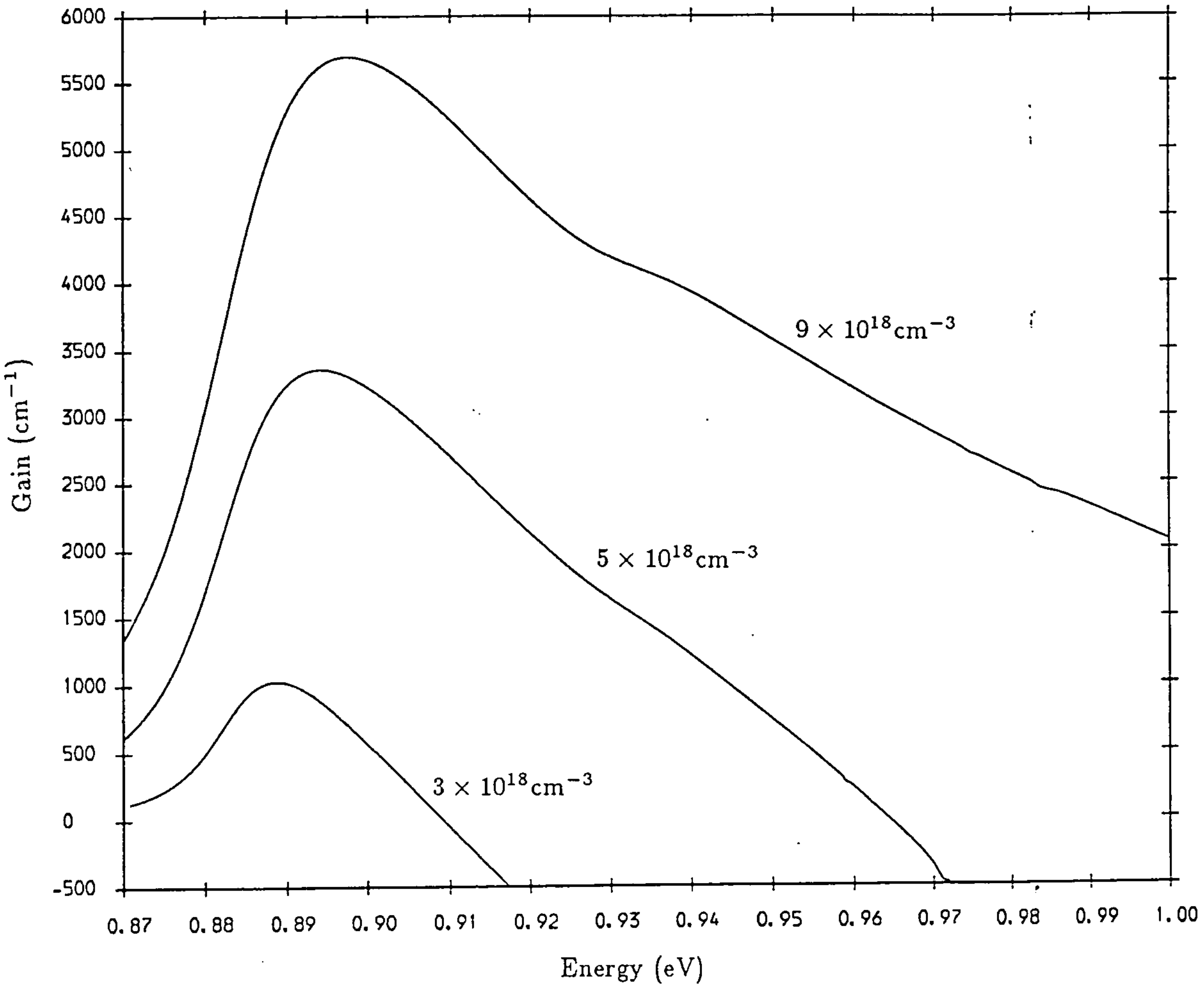

Figure 5.12

Effect of carrier density on gain spectrum.

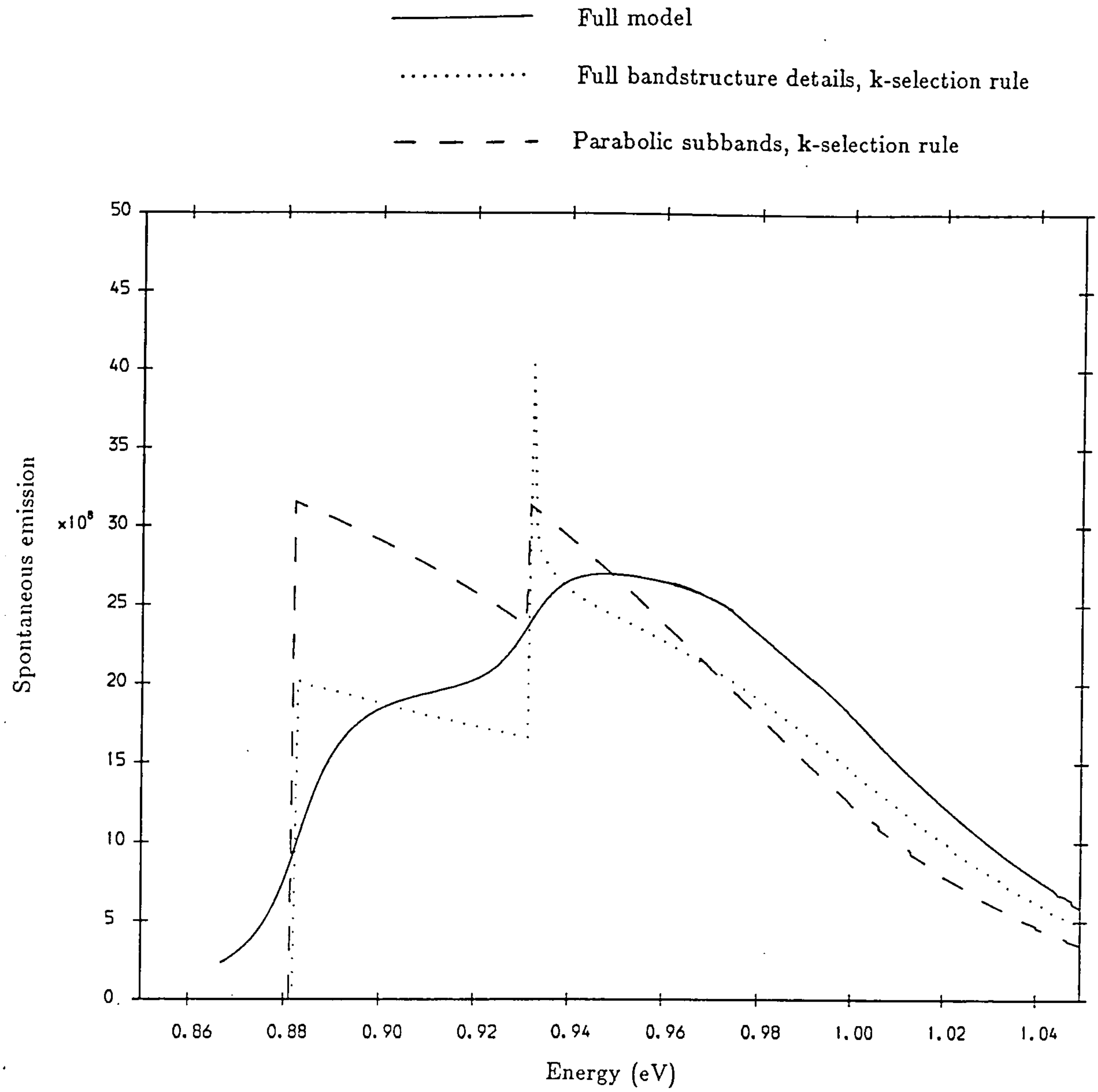

Figure 5.13

Spontaneous emission spectrum for a 50Å $In_{0.53}Ga_{0.47}As/InP$ quantum well.

of states at the valence band edge. On the other hand, the strength of the spontaneous emission at the threshold energy for the transition involving the second valence subband is underestimated by the simple model; this is due to the sharp peak in the density of states at this point predicted by the **k.p** model, corresponding to the electron-like dispersion of this subband near to the centre of the two dimensional Brillouin zone. In fact, this transition can be seen to give rise to a larger spontaneous emission than the band edge transition in the **k.p** model at this carrier density. This becomes more pronounced when broadening effects are included. This effect of the spontaneous emission spectrum being dominated by transitions involving excited subbands is frequently observed experimentally, but rarely predicted by parabolic subband models (except at high carrier densities).

5.9.3 Threshold Calculations

In this section the threshold condition for a 50Å $In_{0.53}Ga_{0.47}As/InP$ MQW laser system is studied as the number of quantum wells in this structure is varied. A cavity length of 250μm and a facet reflectivity of 0.32 are used for these calculations. If insufficient wells are present in the device, then the gain within the active region cannot easily overcome the losses in the outer cladding region of the device. If too many wells are present, there is an element of 'overkill' — once enough wells are included to ensure that threshold is easily achieved, any additional wells draw extra current without significantly enhancing the light output, thus raising the threshold current.

This is well illustrated in figures 5.14 and 5.15, which show the threshold carrier and current densities respectively. The solid lines show the results obtained by including the **k.p** bandstructure and matrix element details; the dashed lines are obtained using a parabolic fit to the **k.p** bandstructure. Both sets of results include lifetime broadening effects. The threshold carrier density reaches a minimum for $N_W \geq 10$ wells (in the full model), and the addition of further wells only marginally reduces the required carrier density. Since the current is proportional to the number of wells, however, the threshold current density is seen to increase for $N_W > 10$; clearly the optimum number of wells for this device is around 8 – 10.

The parabolic subband threshold current results appear to be similar to those obtained using the full model, but shifted with respect to the number of wells. For a small number of wells, the threshold carrier density is high, so the predicted gain at the emission wavelength (for a given carrier density) is much lower in the **k.p** model. The total spontaneous emission predicted by the two models, however, is of the same order, since this process is in this case dominated by transitions involving the highly populated second valence subband, and in this region of the spectrum the spontaneous emission curves obtained by the two models are similar. Hence the predicted threshold carrier density is higher in the full **k.p** model. For a large number of wells, the threshold carrier density is low, so whilst the **k.p** results predict a lower gain, they will also predict a lower spontaneous emission, since the number

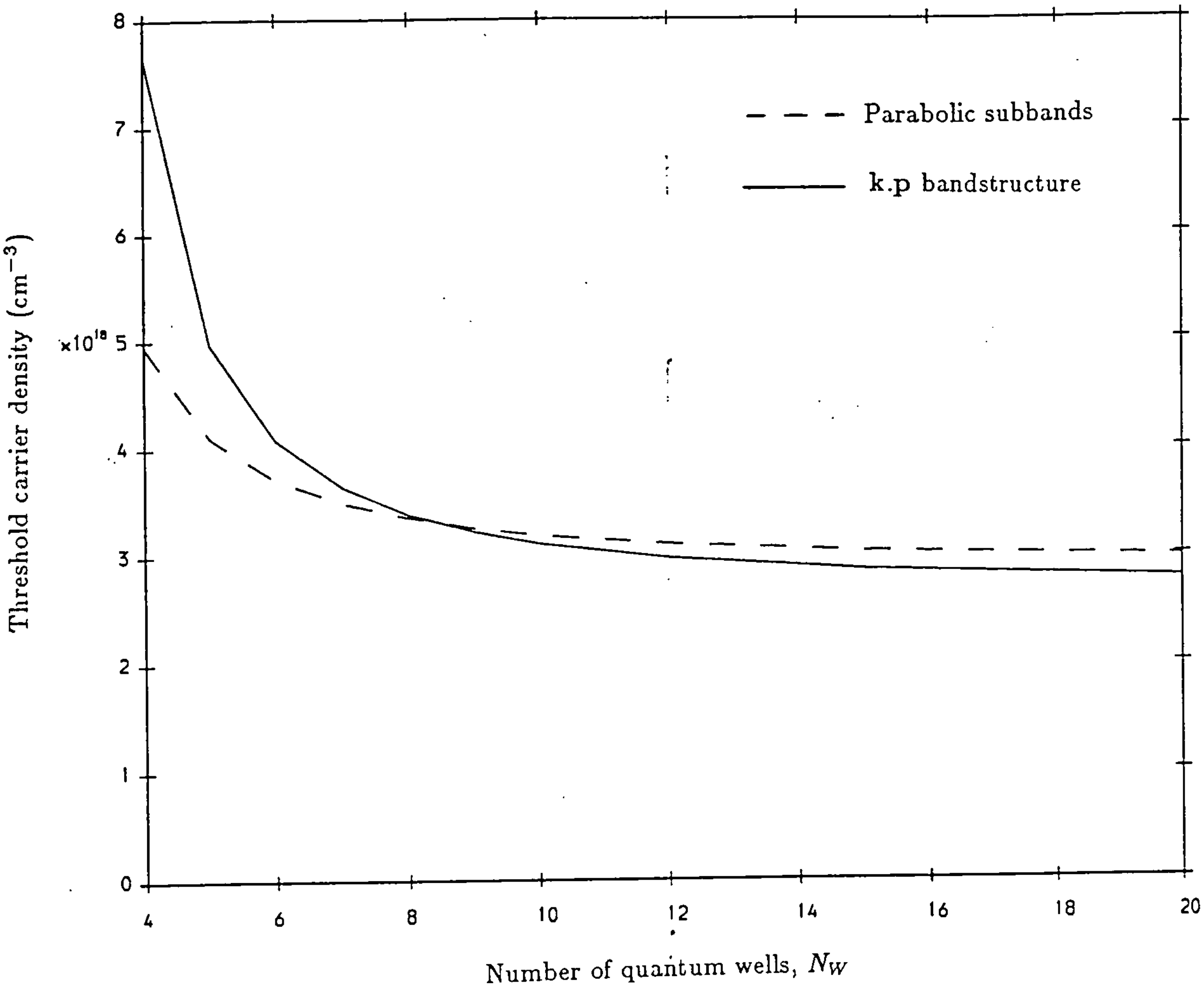

Figure 5.14

Threshold carrier density for a 50Å $In_{0.53}Ga_{0.47}As/InP$ MQW laser.

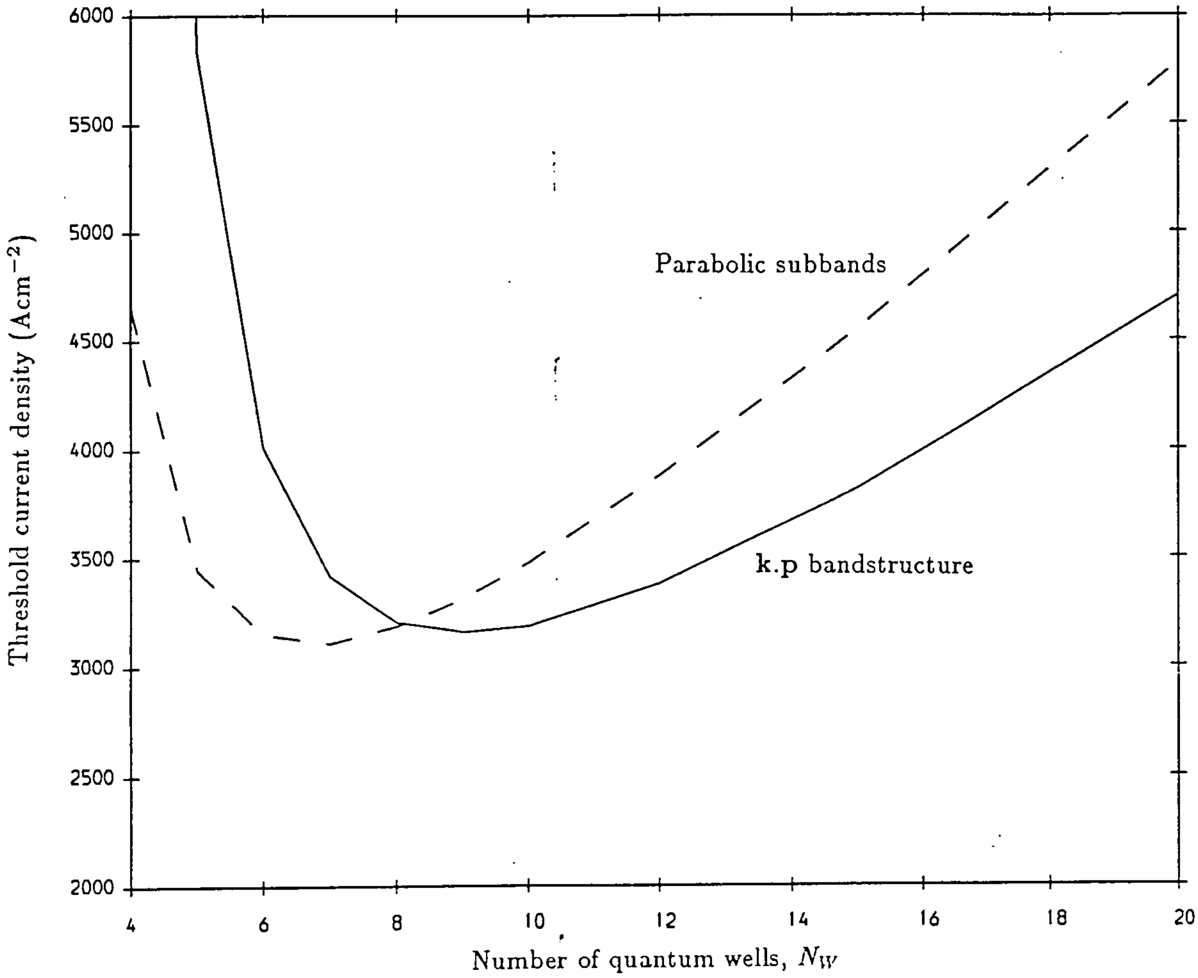

Figure 5.15

Threshold current density for a 50Å $In_{0.53}Ga_{0.47}As/InP$ MQW laser.

of carriers in the dominant second valence subband will be reduced. These effects tend to balance each other, resulting in a slightly lower threshold carrier density (and hence threshold current density) than is obtained using the simple parabolic model.

Figure 5.16 shows the gainslope at threshold of the device (the rate of increase of gain with carrier density). This determines the rate of increase of emitted light intensity with current once the device has reached threshold. The gainslope is lowest where the threshold carrier density is highest, since in this region the gain has started to saturate. The dramatic overestimate of the gainslope given by the simple parabolic subband approach clearly demonstrates the importance of including the full bandstructure and matrix elements in the model of laser performance.

Figure 5.17 shows the variation with number of wells of the lasing energy at threshold — this is the photon energy at which the emitted intensity is the greatest. The results merely reflect the fact that the peak in the gain spectrum shifts to a higher energy as the carrier density is increased (see figure 5.12).

Figure 5.18 illustrates the variation of linewidth enhancement factor, α, with the number of wells in the device. α is a measure of the improvement in the spectral linewidth over the conventional prediction that the linewidth varies inversely with the output power [19]. It can be seen that the predicted linewidth, which is determined by $(1+\alpha^2)$, is smaller in the full model than in the simpler approach.

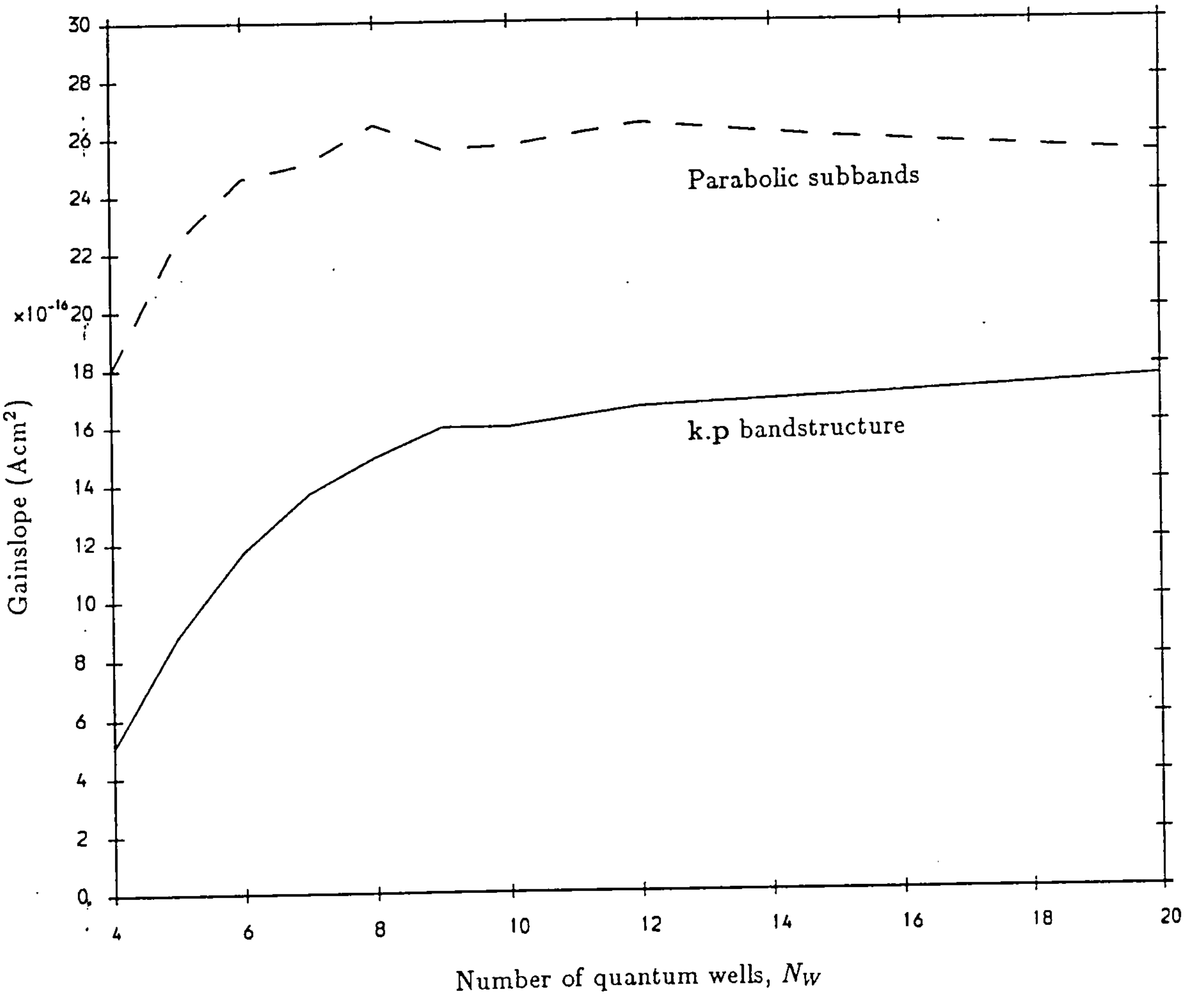

Figure 5.16

Gainslope at threshold for a 50Å $In_{0.53}Ga_{0.47}As/InP$ MQW laser.

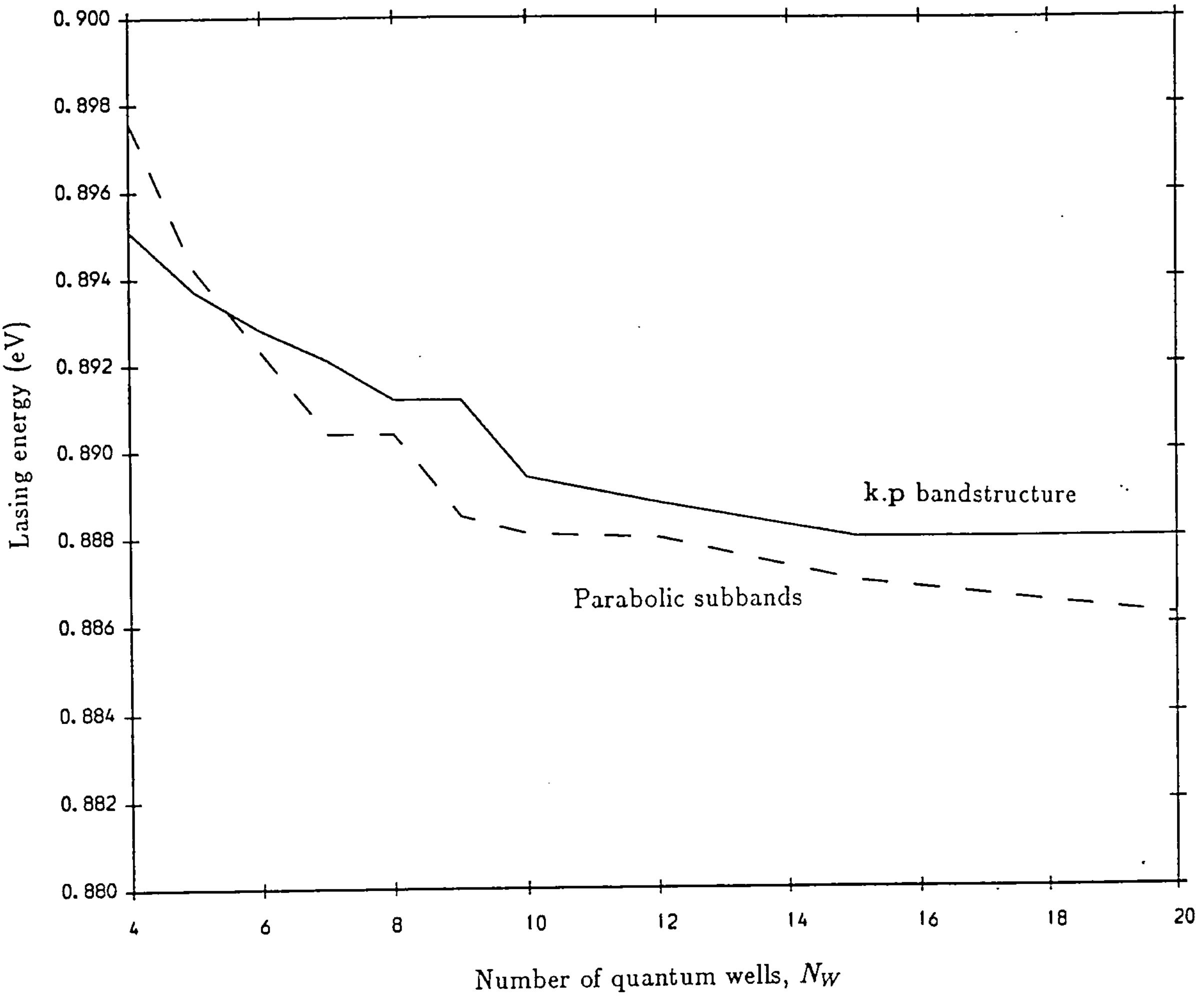

Figure 5.17

Threshold lasing energy for a 50Å $In_{0.53}Ga_{0.47}As/InP$ MQW laser.

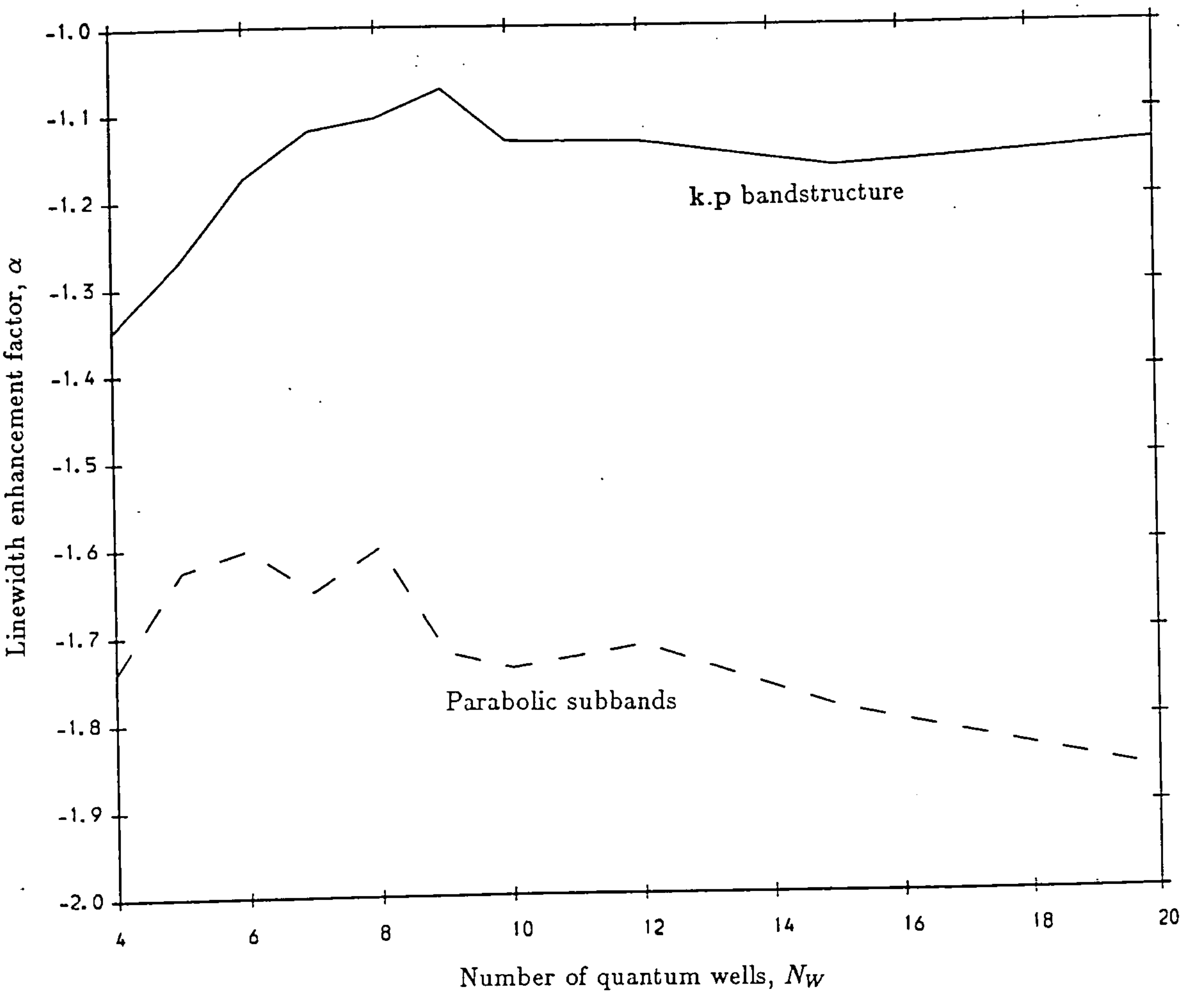

Figure 5.18

Linewidth enhancement factor for a 50Å $In_{0.53}Ga_{0.47}As/InP$ MQW laser.

5.10 Summary and Conclusions

In this chapter we have discussed the physics of the quantum well laser, and outlined the way in which such a device can be modelled. The model which has been developed includes the effects of non-parabolic subband dispersion, matrix elements modified by intersubband wave function mixing, and an energy dependent lifetime broadening. The model enables the calculation of gain and spontaneous emission spectra and threshold properties, and is currently believed to be the most complete model of its kind reported.

We have illustrated the importance of including the full **k**.**p** results and lifetime broadening effects by considering the results obtained for a 50Å $In_{0.53}Ga_{0.47}As/InP$ MQW laser. Although the parabolic model used a fit to the full **k**.**p** results, and is hence a much better model than a more traditional effective mass type approach, it still proved to be incapable of reproducing many of the features of the full model, in particular it overestimates the gain by around a factor of two.

In the next chapter we use the model described here to study the effect of strained layers on laser performance, using the strained layer bandstructure methods discussed in chapter 3.

References for Chapter Five

[1] W.T. Tsang, Appl. Phys. Lett. **40**, 217 (1982).

[2] S.D. Hersee, M. Baldy, P. Assenat, B. de Cremoux and J.P. Duchemin Electron. Lett. **18**, 870 (1982).

[3] R.D. Burnham, W. Streifer, D.R. Scifres, C. Lindström, T.L. Paoli and N. Holonyak, Electron. Lett. **18**, 1095 (1982).

[4] T. Fujii, S. Yamakoshi, K. Nanbu, O. Wada and S. Hiyamizu, J. Vac. Sci. Technol. **2**, 259 (1984).

[5] R. Chin, N. Holonyak Jr., B.A. Vojak, K. Hess, R.D. Dupuis and P.D. Dapkus, Appl. Phys. Lett. **36**, 19 (1980).

[6] K. Hess, B.A. Vojak, N. Holonyak Jr. and R. Chin, Solid State Electronics **23**, 585 (1980).

[7] Y. Arakawa and H. Sakaki, Appl. Phys. Lett. **40**, 939 (1982).

[8] H. Iwamura, T. Saku, T. Ishibashi, K. Otsuka and Y. Horikoshi, Electron. Lett. **19**, 180 (1983).

[9] S.R. Chinn, P.S. Zory and A.R. Reisinger, IEEE J. Quantum Electronics, **QE24**, 2191 (1988).

[10] D.J. Robbins, SPIE **800**, 34 (1987).

[11] H.C. Casey Jr. and M.B. Panish, *Heterostructure Lasers*, Part A : Fundamental Principles, Academic Press, 1978.

[12] A.I. Kucharska and D.J. Robbins, IEEE J. Quantum Electronics **QE26**, 443 (1990).

[13] M. Asada, IEEE J. Quantum Electronics **QE25**, 2019 (1989).

[14] M. Asada, A. Kameyama and Y. Suematsu, IEEE J. Quantum Electronics **QE20**, 745 (1984).

[15] Y. Arakawa and A. Yariv, IEEE J. Quantum Electronics **QE21**, 1666 (1985); **QE22**, 1887 (1986).

[16] W. Streifer, D.R. Scifres and R.D. Burnham, Appl. Optics **18**, 3547 (1979).

[17] D. Botez, IEEE J. Quantum Electronics **QE17**, 178 (1981).

[18] S. Colak, R. Eppenga and M.F.H. Schuurmans, IEEE J. Quantum Electronics **QE23**, 960 (1987).

[19] K. Vahala and A. Yariv, IEEE J. Quantum Electronics **QE18**, 1096 (1982); **QE18**, 1102 (1982).

CHAPTER SIX

STRAINED LAYER QUANTUM WELL LASERS

6.1 Introduction

In an earlier chapter we discussed how the presence of an elastic strain in a lattice mismatched heterostructure can modify the bandstructure, and in particular can lead to a reduction in the effective mass of the lowest valence subband through an increase in the separation of the light and heavy hole subbands. It was suggested independently by Adams [1] and by Yablonovitch and Kane [2] that this effect can be used to lower the threshold current of a multiple quantum well laser by reducing the number of carriers required to achieve population inversion, and offers the prospect of tailoring devices for optimum operation at the desired wavelength by independently varying the strain (through varying the material composition of the well region) and the quantum well width. The lower effective mass of the strained structure is also predicted to lead to reduced Auger recombination and intervalence band absorption losses [1], resulting in not only a reduction in the threshold current and an enhanced efficiency, but also in an improved temperature stability.

Several authors have reported calculations of the threshold current and other device parameters in strained layer laser structures [3-6], and have confirmed that such devices can possess significant advantages over conventional quantum well lasers. Some of these calculations, however, neglect valence subband non-parabolicity and/or energy dependent linewidth broadening effects, both of which were shown in the previous chapter to be significant omissions. There has also been considerable interest in these devices amongst experimental workers, and there have been several recent reports of the successful growth and operation of strained layer lasers [7,8]. The devices grown have, as expected, shown low threshold current, high output power and efficiency and a reduced temperature sensitivity. The InGaAs(P) materials system has generated most interest, with the active regions designed for 1.3μm or 1.55μm operation (these wavelengths correspond to optical fibre transmission windows); devices are usually grown on a GaAs or InP substrate.

In this chapter we investigate the effect of strain on the performance of both 1.3μm and 1.55μm InGaAs/InP multiple quantum well lasers, and include the effects of realistic bandstructure and optical matrix elements and linewidth broadening, using the model described in the previous chapter.

6.2 Design of Strained Layer Structures

The introduction of strain into a quantum well laser requires the alloy composition of the well (or in some materials systems the barrier) to be modified. This has the rather unfortunate effect of changing the bandgap of the active region, and thus altering the wavelength at which the device will operate. In order to overcome this problem, it is necessary to adjust the quantum well width of the device. An estimate of the well width required to preserve the operating wavelength can be obtained from

$$E_\lambda = E_g^0 + E_0^c + E_0^v + \Delta E_g^0 + \Delta E_g^{st} \tag{6.1}$$

$$\text{and} \quad \lambda = \frac{hc}{E_\lambda} \tag{6.2}$$

where E_λ = bandgap of strained QW

E_g^0 = bulk bandgap of unstrained well material

E_0^c = confinement energy of lowest conduction subband

E_0^v = confinement energy of lowest valence subband

ΔE_g^0 = change in bandgap due to change in alloy composition of well material

ΔE_g^{st} = change in bandgap due to strain

h = Planck's constant

c = velocity of light

In practice λ will not correspond exactly to the operating wavelength of the laser, since broadening effects will tend to shift the peak in the gain spectrum to higher energy, but selecting quantum well widths to give the same values of E_λ will enable us to obtain comparable devices, and will eliminate any specifically bandgap dependent effects.

Since E_λ will only be an approximation to the actual emitted photon energy of the device, it is adequate to use simple expressions for the individual terms in equation 6.1. The bulk bandgap of the unstrained well material, E_g^0, is simply the bandgap of $\mathrm{In_{0.53}Ga_{0.47}As}$, 0.75eV. E_0^c and E_0^v are obtained from the effective mass approximation $E_0 = \frac{\hbar^2\pi^2}{2m^*L_z^2}$, where L_z is the quantum well width, and ΔE_g^0 is calculated by assuming a linear bandgap dependence on the indium fraction x of the alloy between the limits $x = 0.53$ ($\mathrm{In_{0.53}Ga_{0.47}As}$, $E_g = 0.75\mathrm{eV}$) and $x = 1.0$ (InAs, $E_g = 0.354\mathrm{eV}$). The change in bandgap caused by the strain is obtained using an empirical fit to the results previously described (chapter 3) which were obtained for a structure with an artificial strain (figure 3.6).

Solving equations 6.1 and 6.2 allows us to obtain the quantum well widths appropriate for 1.3μm and 1.55μm operation of InGaAs/InP devices with indium fractions of 0.53, 0.63 and 0.73. The results are given in figure 6.1. From this graph we obtain well widths of 80Å, 53Å and 43Å for 1.55μm devices, and 40Å, 35Å and 31.5Å for 1.3μm devices for indium fractions of 0.53, 0.63 and 0.73 respectively. These well width estimates are considered sufficiently accurate for the calculations we perform, in which the

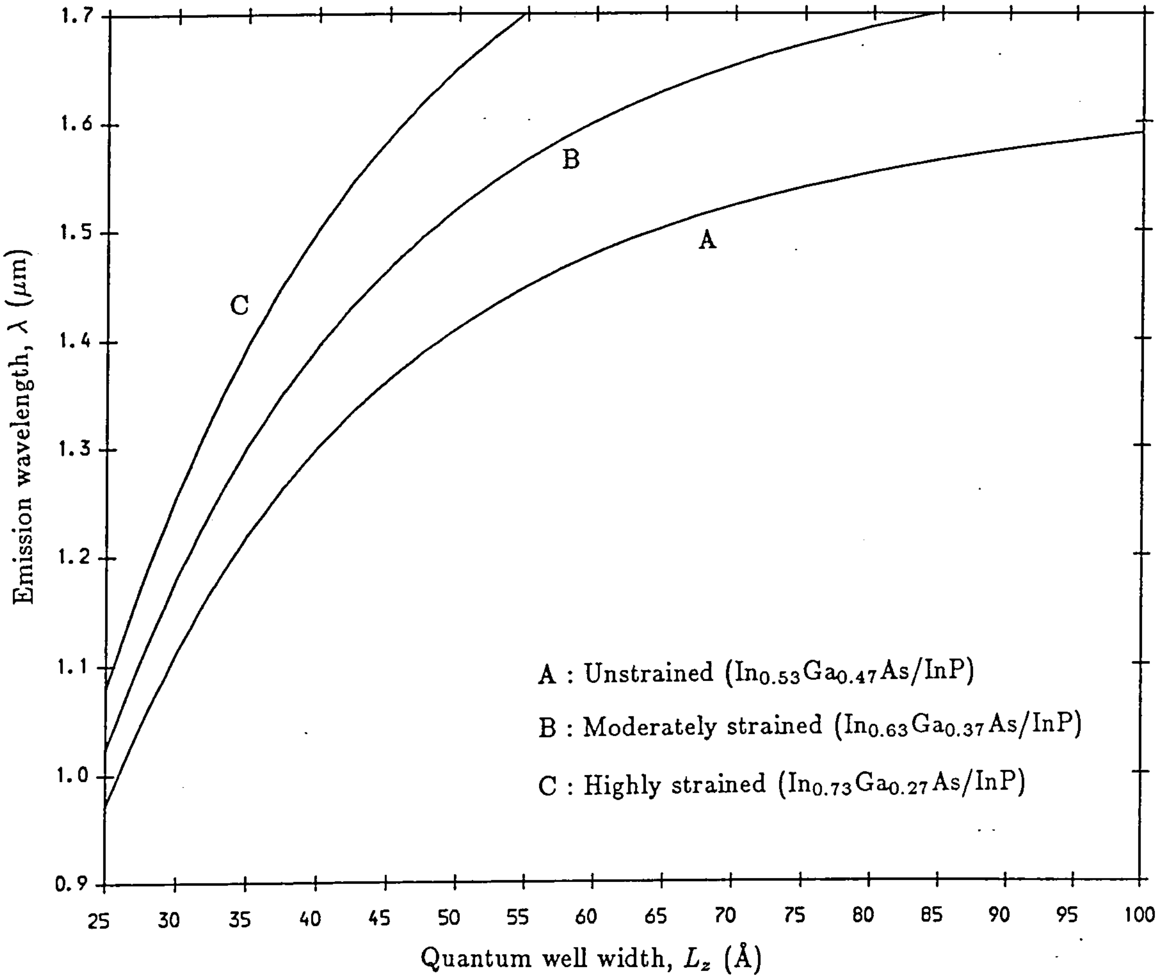

Expected dependence of operating wavelength on quantum well width.

Figure 6.1

main concern is to ensure that the devices will operate close to the required wavelength in order to remove any wavelength dependent effects from the results. If information for the growth of these devices were required, the operating wavelength would be more critcal, and it would be necessary to adjust the well widths used in the model until the peak in the gain spectrum occured at the desired energy. This procedure is straightforward, but extremely time consuming, since each adjustment of the well width requires the calculation of a new set of quantum well bandstructure.

The optical confinement factors of InGaAs/InP MQW lasers are relatively small, and for this reason InGaAlAs (lattice matched to InP and with the aluminium-gallium ratio chosen to give the InP band gap), which gives better optical confinement due to its higher refractive index, is often used as the barrier material instead of InP. However, the effective masses and bandstructure parameters of quaternary materials are not well known, and this introduces an uncertainty into calculations on structures containing InGaAlAs. In fact, the bandstructure of either barrier material does not make much difference to the properties of the bound states of the quantum well, because most of the wave function lies within the well region. Hence we adopt a compromise in this work, whereby the bandstructure of InP is used in the barrier regions, but the refractive index of InGaAlAs is assumed when calculating optical confinement factors. Thus although we refer to all the devices investigated in this chapter as InGaAs/InP devices, they could equally well be considered to be InGaAs/InGaAlAs structures.

6.3 Results for 1.55μm Devices

6.3.1 Bandstructure and Optical Matrix Elements

The effects of strain on the bandstructure of a quantum well were discussed in detail in chapter 3. It was shown that whilst the conduction band remains largely unaffected by the strain (apart from a shift in energy of the whole bandstructure), the valence band is modified by the shifting of the $m_j = \frac{1}{2}$ 'light' holes to higher hole energies relative to the $m_j = \frac{3}{2}$ 'heavy' holes as the strain increases. This reduces the influence of intersubband wave function mixing on the first valence subband, and can reduce the effective mass of this subband. In the structures considered in this chapter, the effect is enhanced by the increased separation of the subbands caused by the reduced quantum well width used in the strained structures.

The bandstructure of the three devices is shown in figure 6.2.† The only noticeable difference between the conduction band results is the presence of an additional bound subband in the unstrained ($In_{0.53}Ga_{0.47}As/InP$) device, due to the wider wells (80Å) chosen for this structure. Note that the energy scale in each case starts at the bulk conduction band edge of the

---

† The kinks in the bandstructure at large in-plane wave vector are not real effects — the diagrams illustrate the bandstructure as fitted to a cubic spline expansion, as described in Appendix 2, and the cubic spline fit is replaced by a simple parabola outside of the range of calculated points. This gives rise to a small discontinuity in the derivative of the dispersion relation.

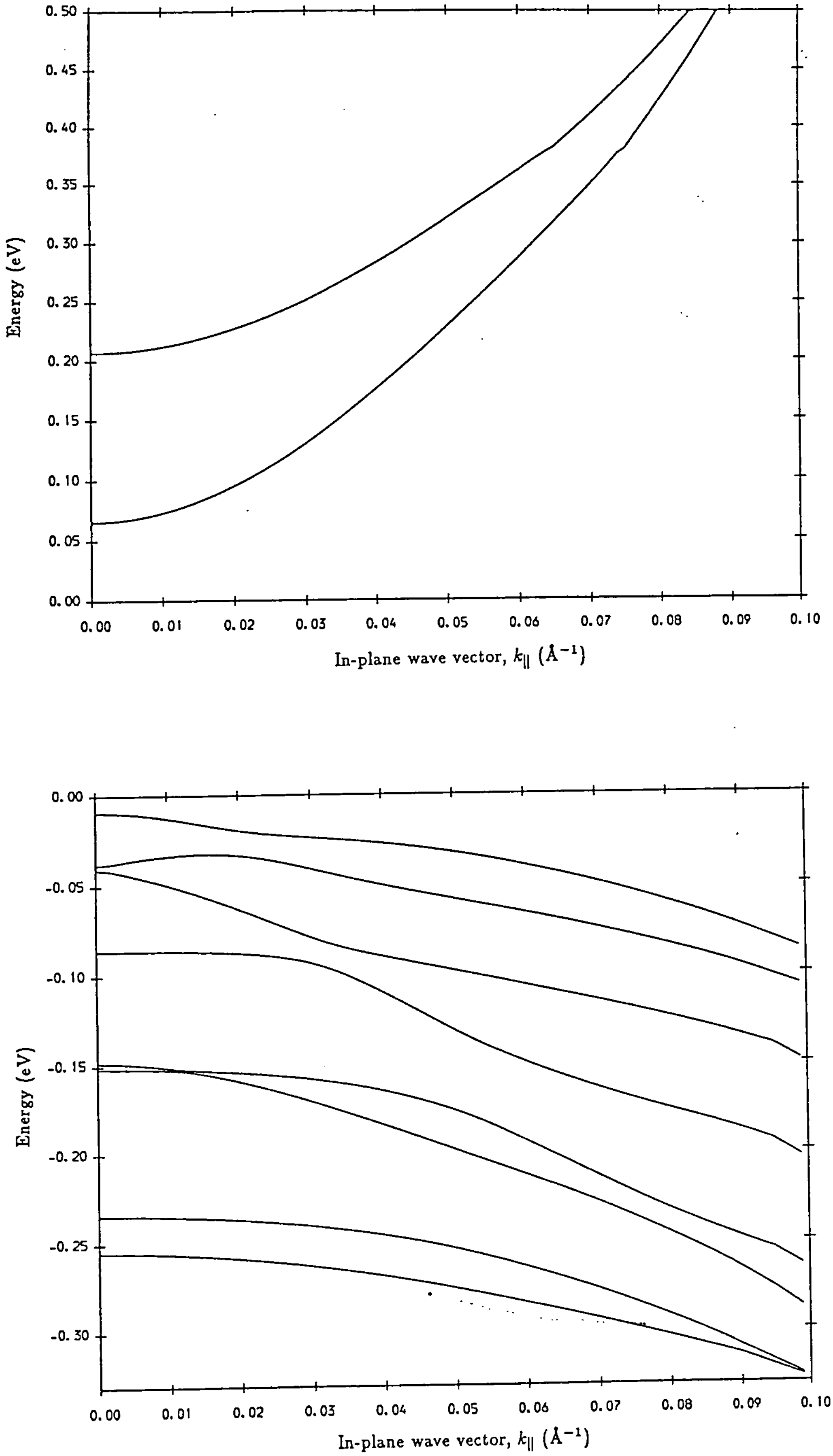

Unstrained

Bandstructure of 80Å $In_{0.53}Ga_{0.47}As/InP$ quantum well.

Figure 6.2a

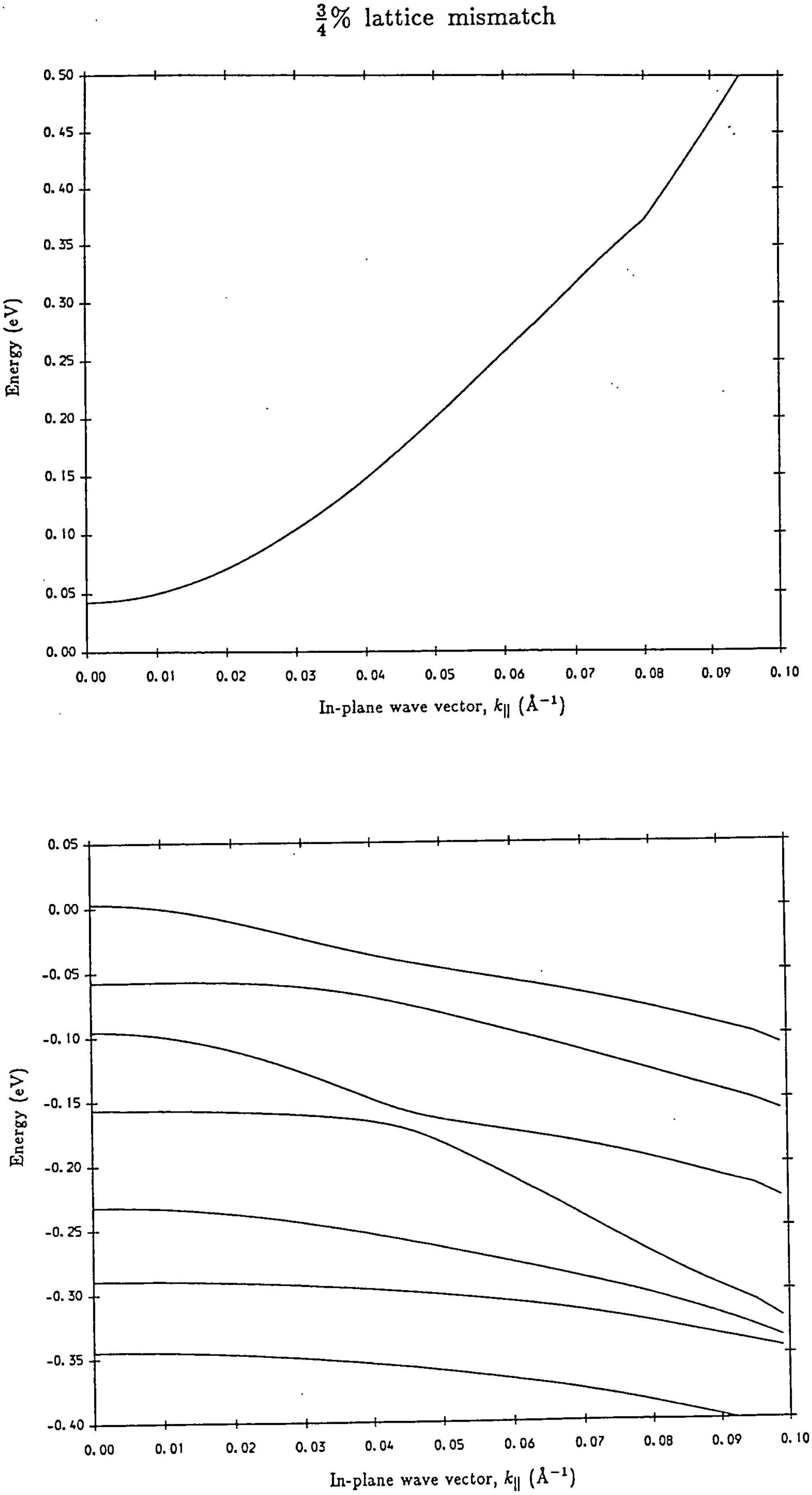

$\frac{3}{4}\%$ lattice mismatch

Bandstructure of 53Å $In_{0.63}Ga_{0.37}As/InP$ quantum well.

Figure 6.2b

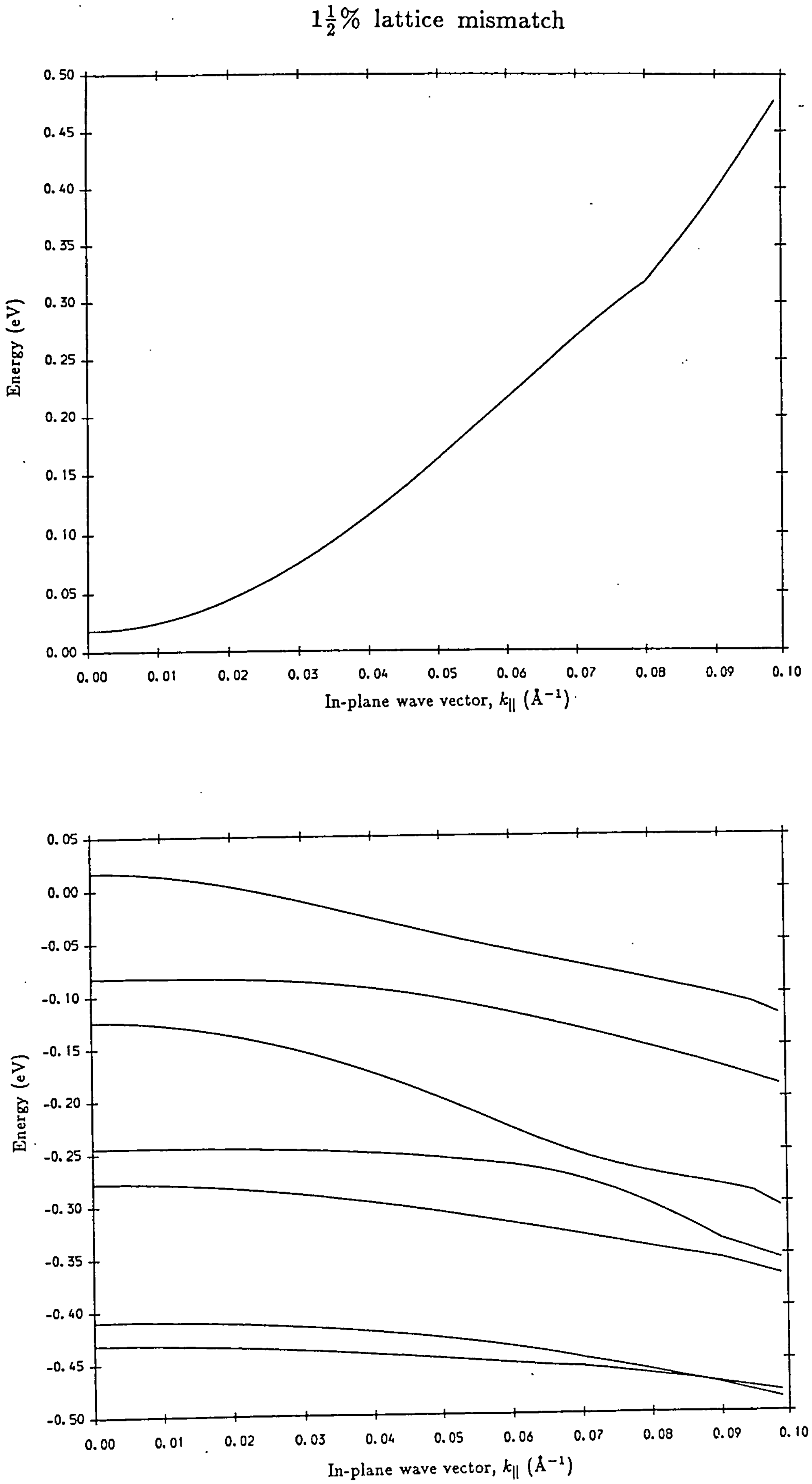

$1\frac{1}{2}\%$ lattice mismatch

Bandstructure of 43Å $In_{0.73}Ga_{0.27}As/InP$ quantum well.

Figure 6.2c

well material. The valence bandstructure, on the other hand, is markedly modified by the strain and by the reduced quantum well width. The expected reduction of wave function mixing and associated lowering of the effective mass of the lowest (in hole energy) subband can be seen when the unstrained and strained (with the well region under a biaxial compression) structures are compared closely. It is interesting to note, however, that most of the reduction in effective mass appears in this case to result from the presence of a moderate degree of strain ($\frac{3}{4}$% mismatch in lattice constant). The difference in effective mass of the first valence subband between the $In_{0.63}Ga_{0.37}As/InP$ ($\frac{3}{4}$% mismatch) and $In_{0.73}Ga_{0.27}As/InP$ ($1\frac{1}{2}$% mismatch) is small.

The removal of wave function mixing is also manifested in the optical matrix elements, which are shown in figure 6.3 for the transverse electric mode for transitions between the (first) conduction subband and the first five valence subbands. In the unstrained device all these transitions have an appreciable optical matrix element over a wide range of in-plane wave vector, but the strained devices follow the $\Delta n = 0$ selection rule far more closely, especially the $In_{0.73}Ga_{0.27}As/InP$ quantum well.

6.3.2 Gain and Spontaneous Emission

The reduction of the effective mass of the lowest valence subband observed in the strained quantum wells, coupled with the increased subband separation resulting from the narrower well widths used in the strained

Unstrained

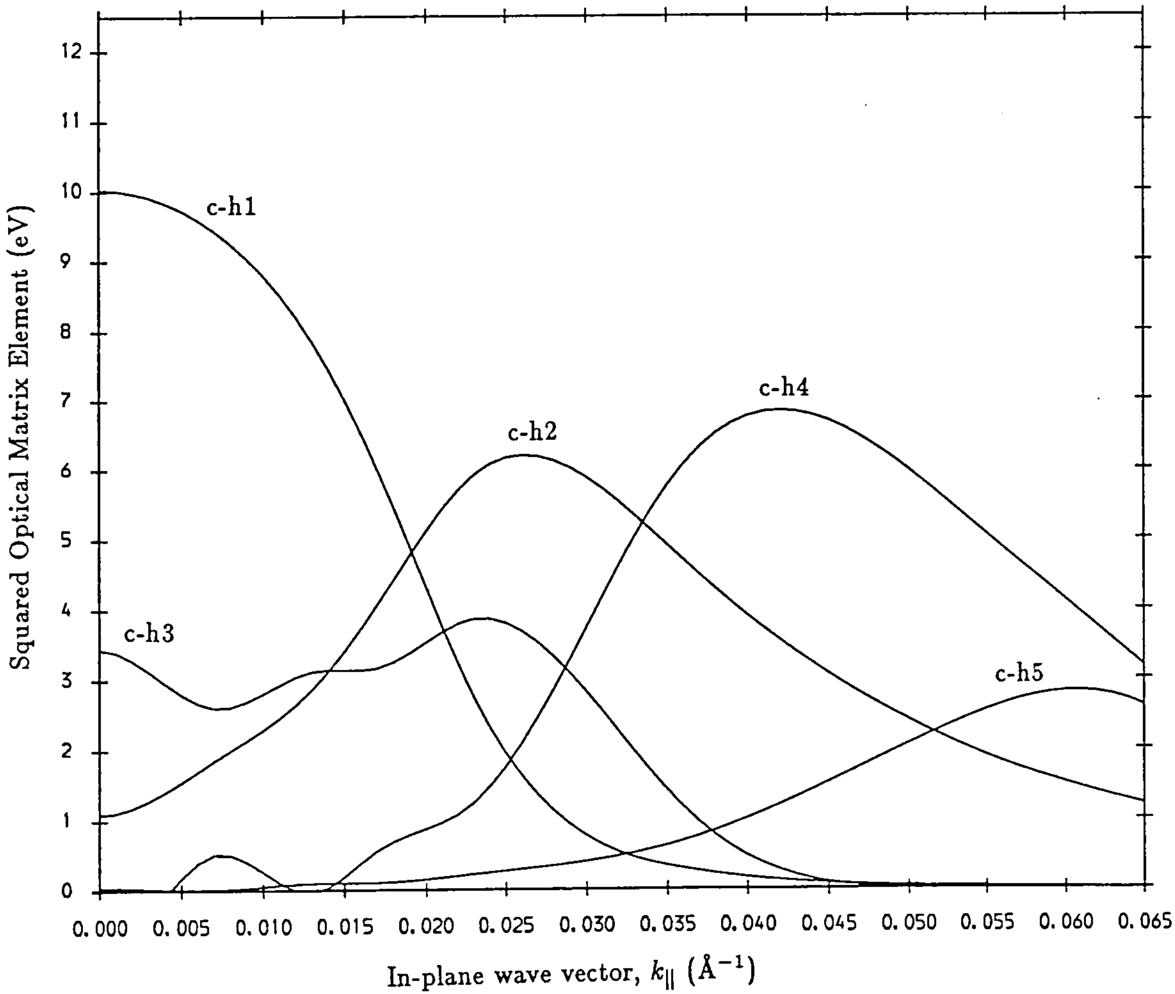

Optical matrix elements of 80Å $In_{0.53}Ga_{0.47}As/InP$ quantum well.

Figure 6.3a

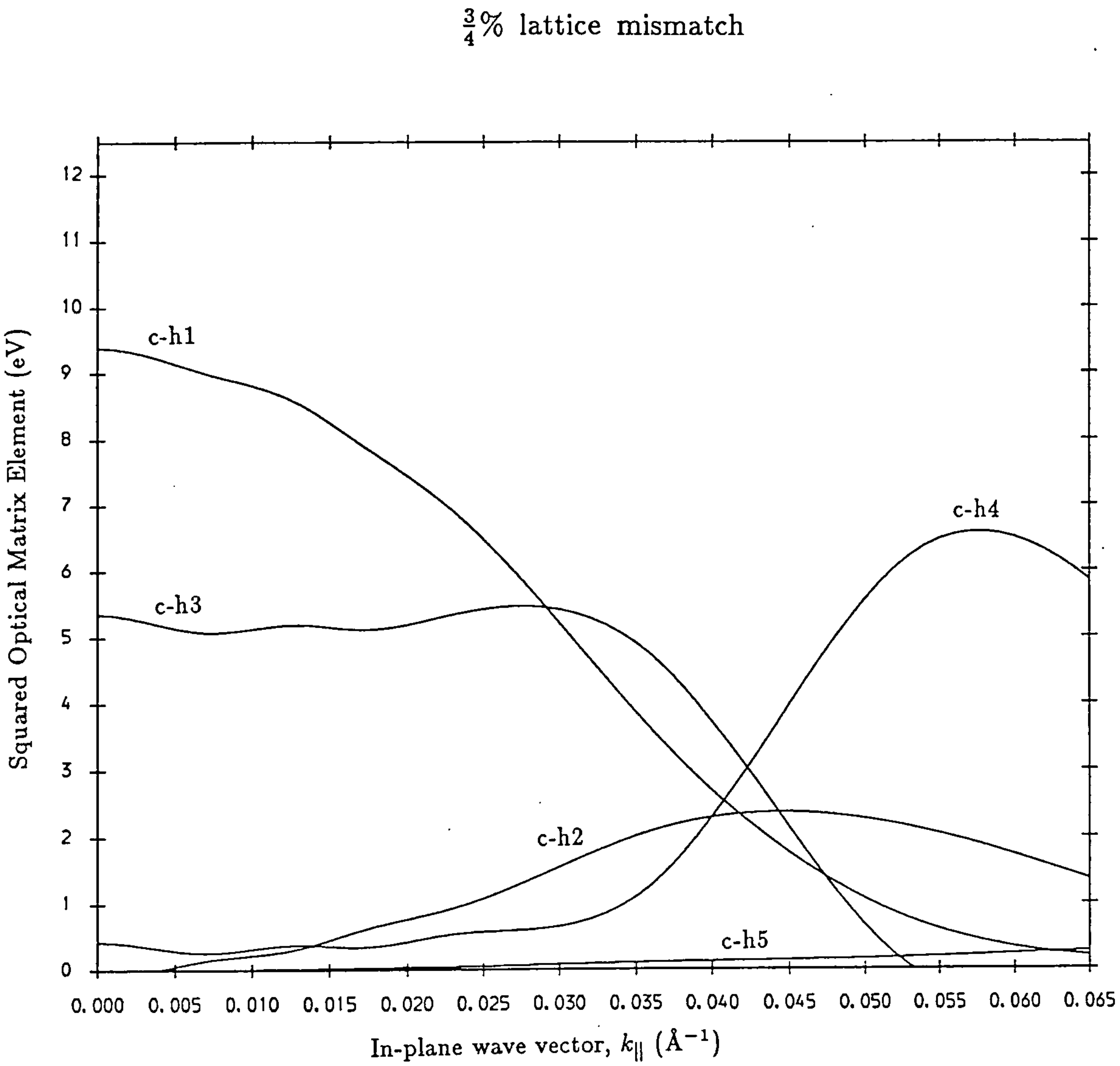

$\frac{3}{4}$% lattice mismatch

Optical matrix elements of 53Å $In_{0.63}Ga_{0.37}As/InP$ quantum well.

Figure 6.3b

$1\frac{1}{2}\%$ lattice mismatch

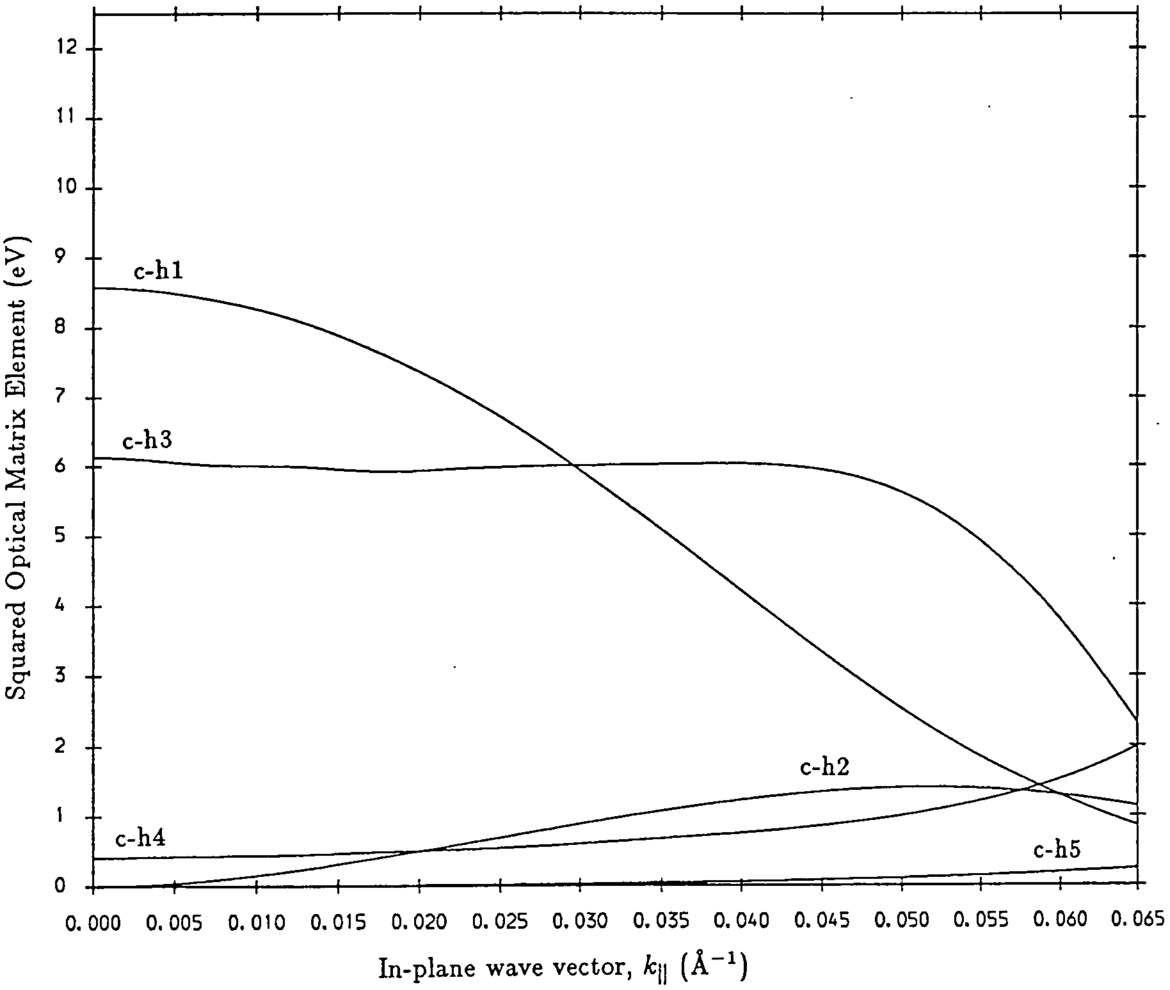

Optical matrix elements of 43Å $In_{0.73}Ga_{0.27}As/InP$ quantum well.

Figure 6.3c

structures makes it easier for the carrier population to be inverted in the strained devices. For a given injected carrier density, a higher proportion of the injected holes will occupy states close to the valence band edge in the strained devices, resulting in higher gain around the band gap energy. This is illustrated in figure 6.4, which shows the peak gain achieved as a function of the injected carrier density for each of the three 1.55μm devices. For hole densities $p \geq 3 \times 10^{18}\mathrm{cm}^{-3}$, it is clear that the peak gain increases significantly with strain in the range considered. However, for hole densities between 2 and $3 \times 10^{18}\mathrm{cm}^{-3}$ the two strained devices are predicted to have similar peak gains. In the next section we discuss the impact of this result on the threshold properties of the device.

Figure 6.5 shows the spontaneous emission current density as a function of injected carrier density for MQW devices containing six quantum wells. The strained devices show a reduced spontaneous emission current, which is not surprising since these devices have reduced well widths and hence a smaller volume of active material. However, this factor cannot account for all of the observed reduction in spontaneous emission and it appears that the strained devices exhibit an intrinsic reduction of this loss mechanism.

Spontaneous emission is just one of the processes responsible for the device current; Auger recombination is also included in the device model (see chapter 5), although the current arising from that is not calculated with reference to the bandstructure of the device, and will be unaffected

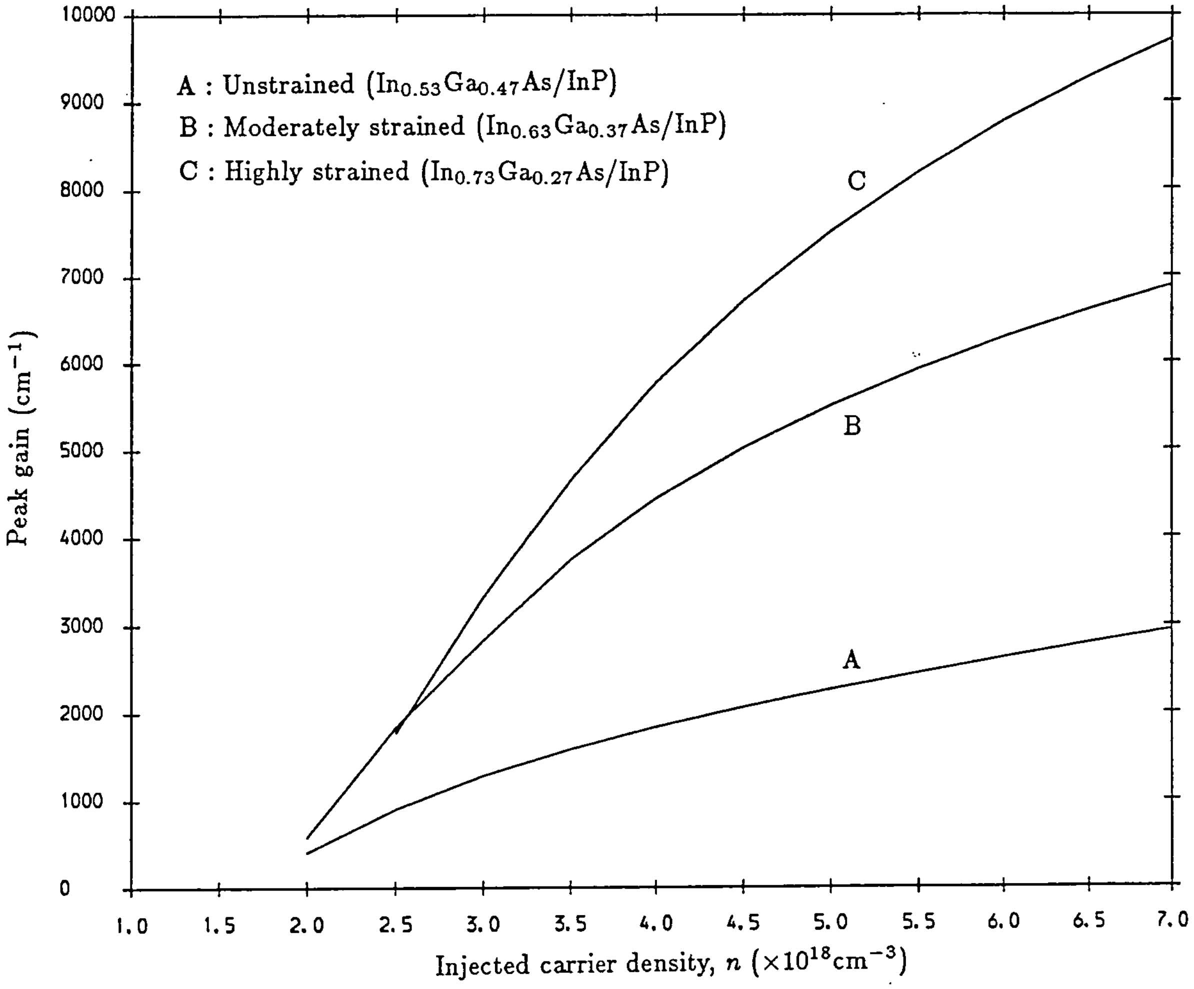

Peak gain dependence on injected carrier density for 1.55μm devices.

Figure 6.4

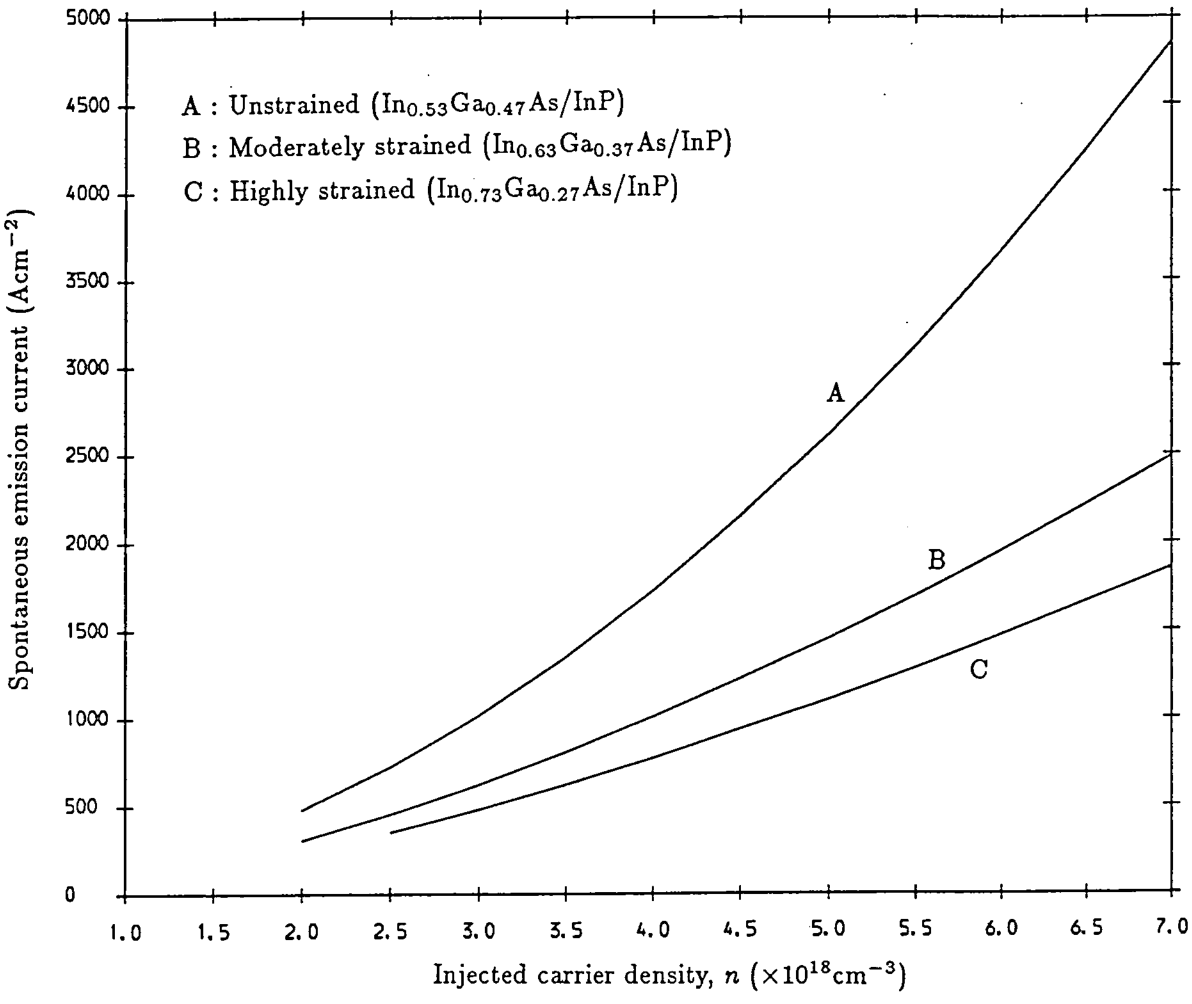

Spontaneous emission current versus injected carrier density

for 1.55μm devices.

Figure 6.5

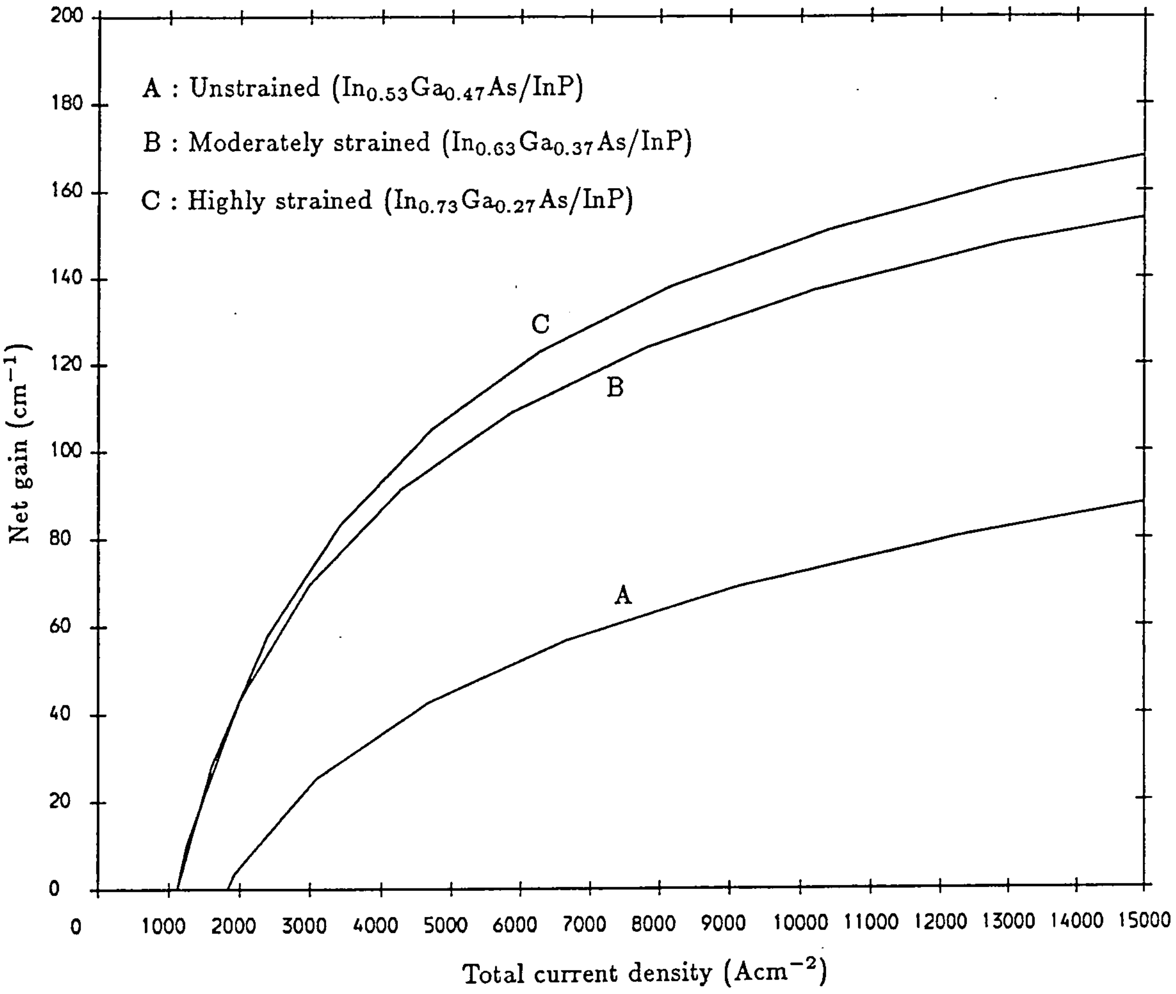

Net gain versus total current for 1.55μm devices.

Figure 6.6

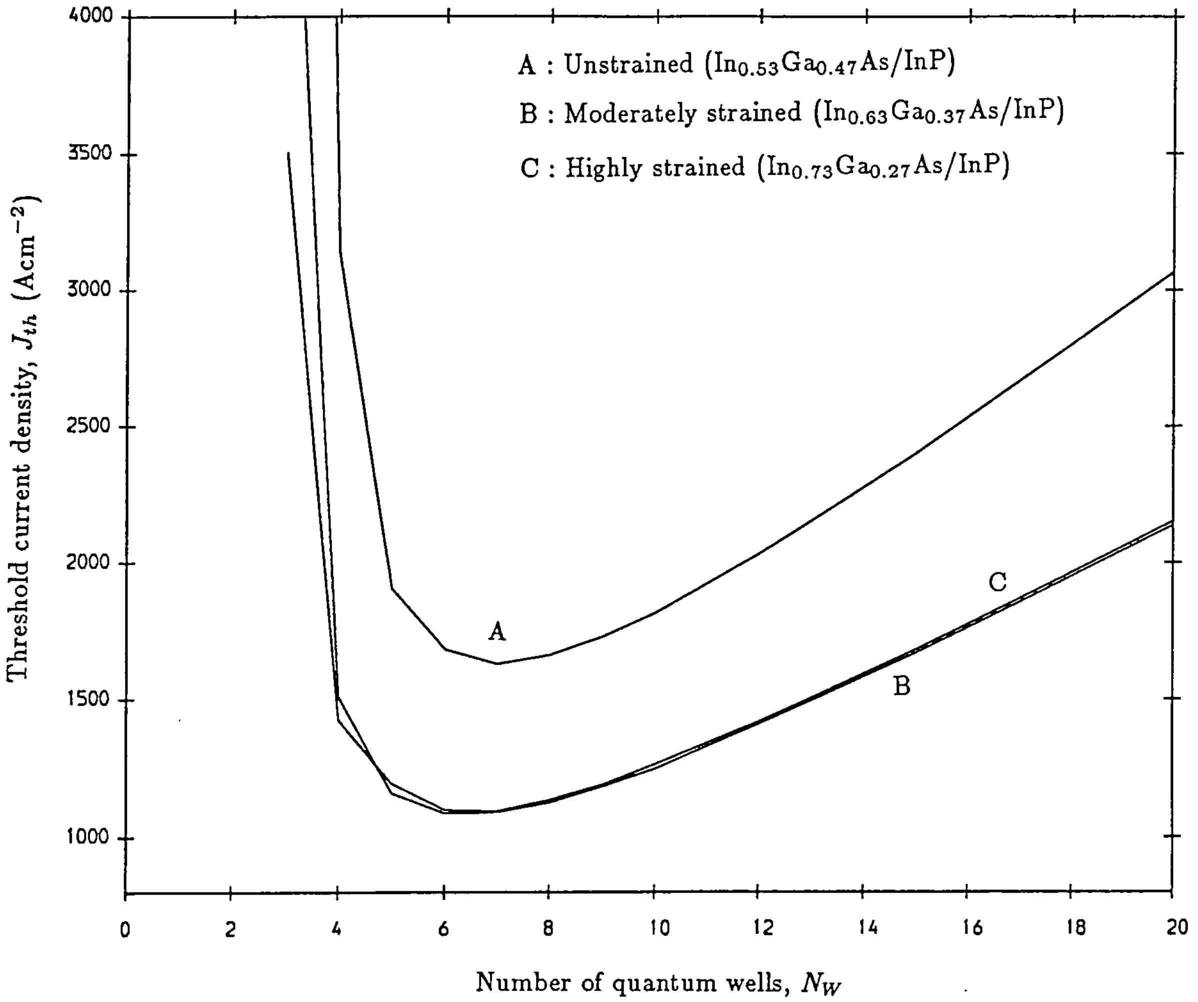

Threshold current density as a function of the number of quantum wells for 1.55μm devices.

Figure 6.7

6.8). Again, this can be seen from figure 6.4, which shows that the gain increases faster with increasing injected carrier density as the amount of strain in the structure is raised. The most highly strained structure shows a threefold increase in the gainslope at threshold.

The linewidth enhancement factor, plotted as a function of the number of quantum wells in figure 6.9, is found to be very low (in absolute value) in the strained devices, lying in the range -0.9 to -1.0, compared with a value of -1.4 to -1.5 for the unstrained structure. This result is in good agreement with the recent experimental findings of Dutta *et al* [9]. The reader should recall that even the unstrained value is much lower than the value of around -2 predicted for unstrained devices by parabolic subband models (see chapter 5). However, once again it appears that most of the improvement offered by the strained devices can be achieved with a moderate degree of strain.

The temperature dependence of the threshold current in the three devices has also been investigated, and the results are given in figure 6.10. It should be noted that the Auger recombination and intervalence band absorption (IVBA) rates in this calculation use parameters characteristic of an unstrained device for all three structures, and any possible reduction in these processes arising from the strain is neglected. Even omitting this factor, we still find the value of T_0 (where $J(T) = J_0 \exp(T/T_0)$) for structures containing 6 quantum wells is increased from 96K in the unstrained device to 100K in the moderately strained device and 109K in the highly strained

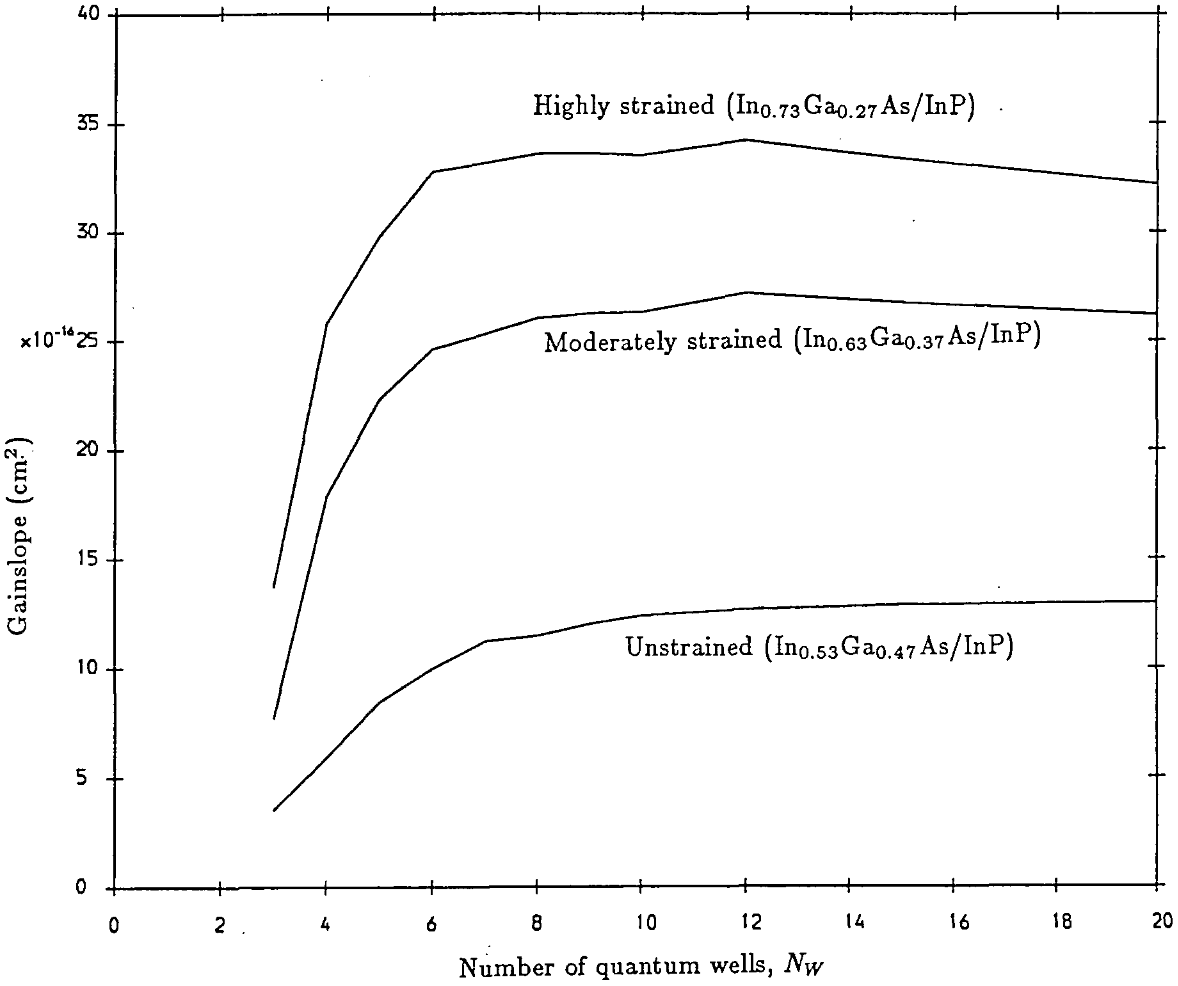

Gainslope of 1.55μm devices.

Figure 6.8

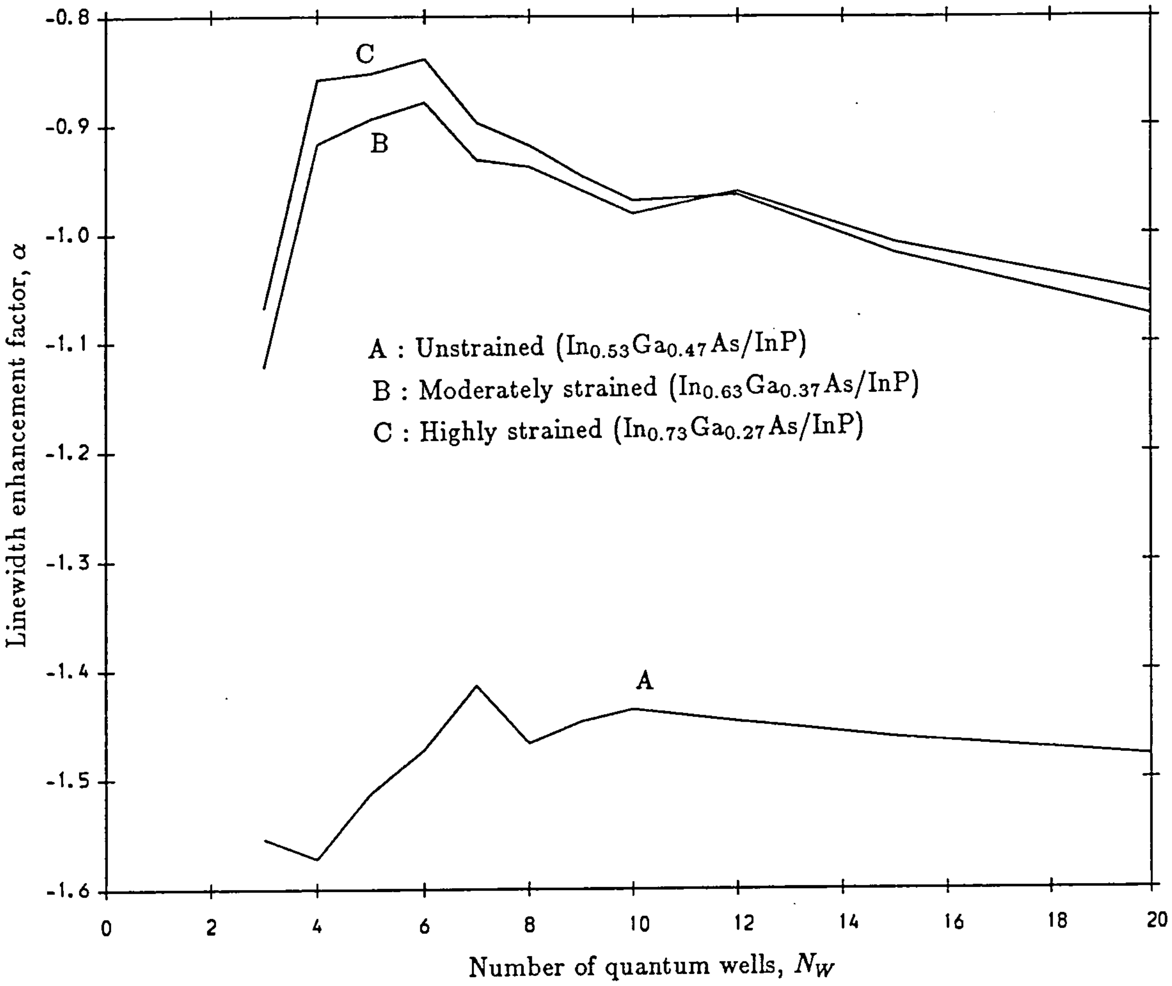

Linewidth enhancement factor of 1.55μm devices.

Figure 6.9

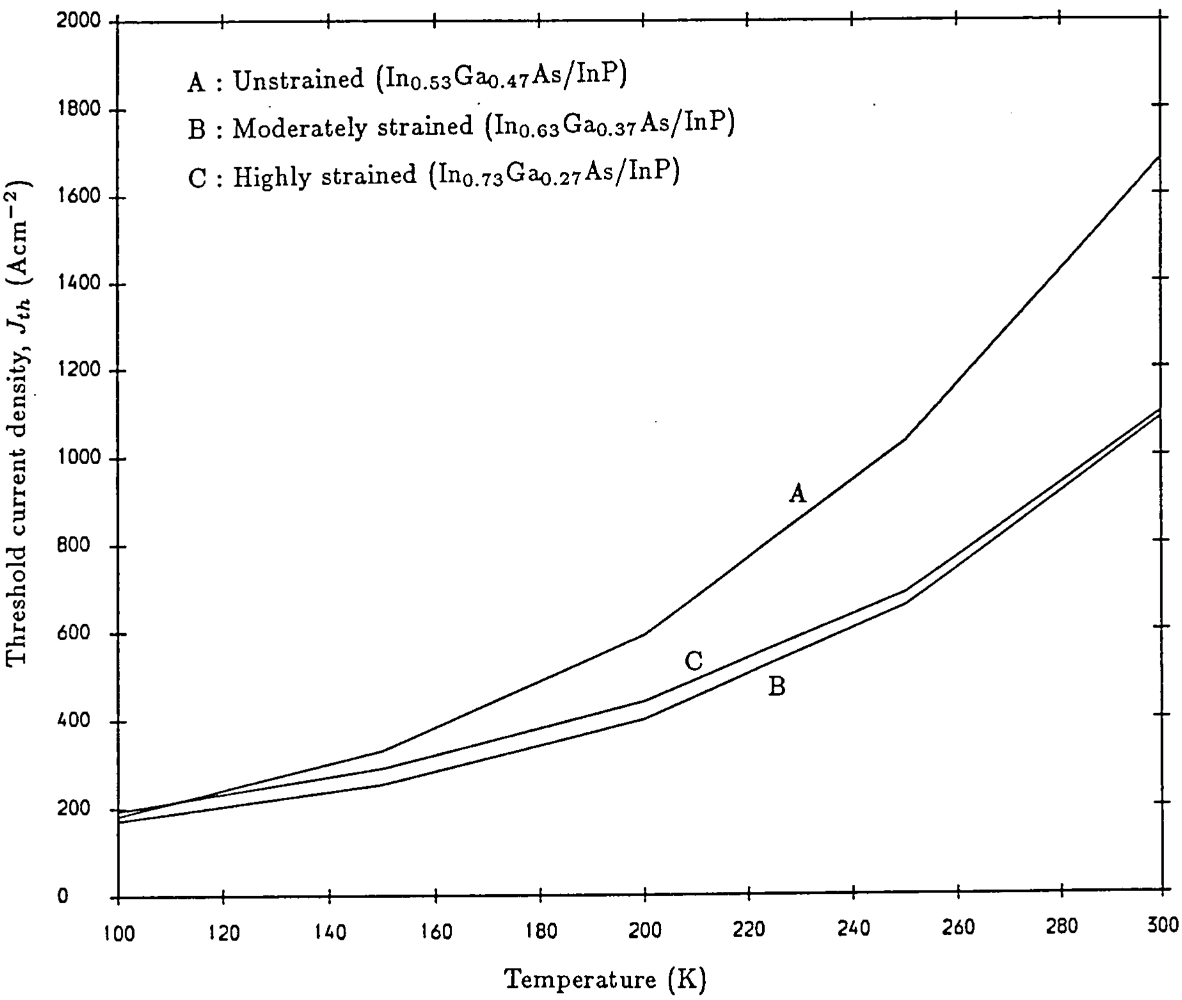

Temperature dependence of threshold current for 1.55μm devices.

Figure 6.10

device, for temperatures in the range 200K to 300K. It thus appears that the strained devices offer an intrinsic improvement in T_0 additional to that expected to result from changes in Auger and IVBA coefficients.

6.4 Results for 1.3μm Devices

6.4.1 Bandstructure and Optical Matrix Elements

The well widths of the MQW structures needed for 1.3μm operation are significantly smaller than those required for 1.55μm. This results in an increased separation of the confined valence subbands, and a reduction in their number. This is especially true of the unstrained structure (see figure 6.11a and compare with figure 6.2a), which has a well width of 40Å in the 1.3μm devices and 80Å in the 1.55μm devices. The strained structures (figure 6.11 b,c), most notably the $In_{0.63}Ga_{0.37}As/InP$ well, have the interesting feature that the second and third valence subbands lie very close together (this is also true of the fourth and fifth subbands, but these bands are not highly populated for the carrier densities we consider). This results in a large amount of mixing of wave function character between states in the subbands. The mixing does not affect the first subband which, as was found for the 1.55μm wells, exhibits a reduction in effective mass as the strain in the structure is increased. Again this reduction can be achieved with only a moderate degree of strain, although the slight reduction in the mixing between states in the second and third subbands in

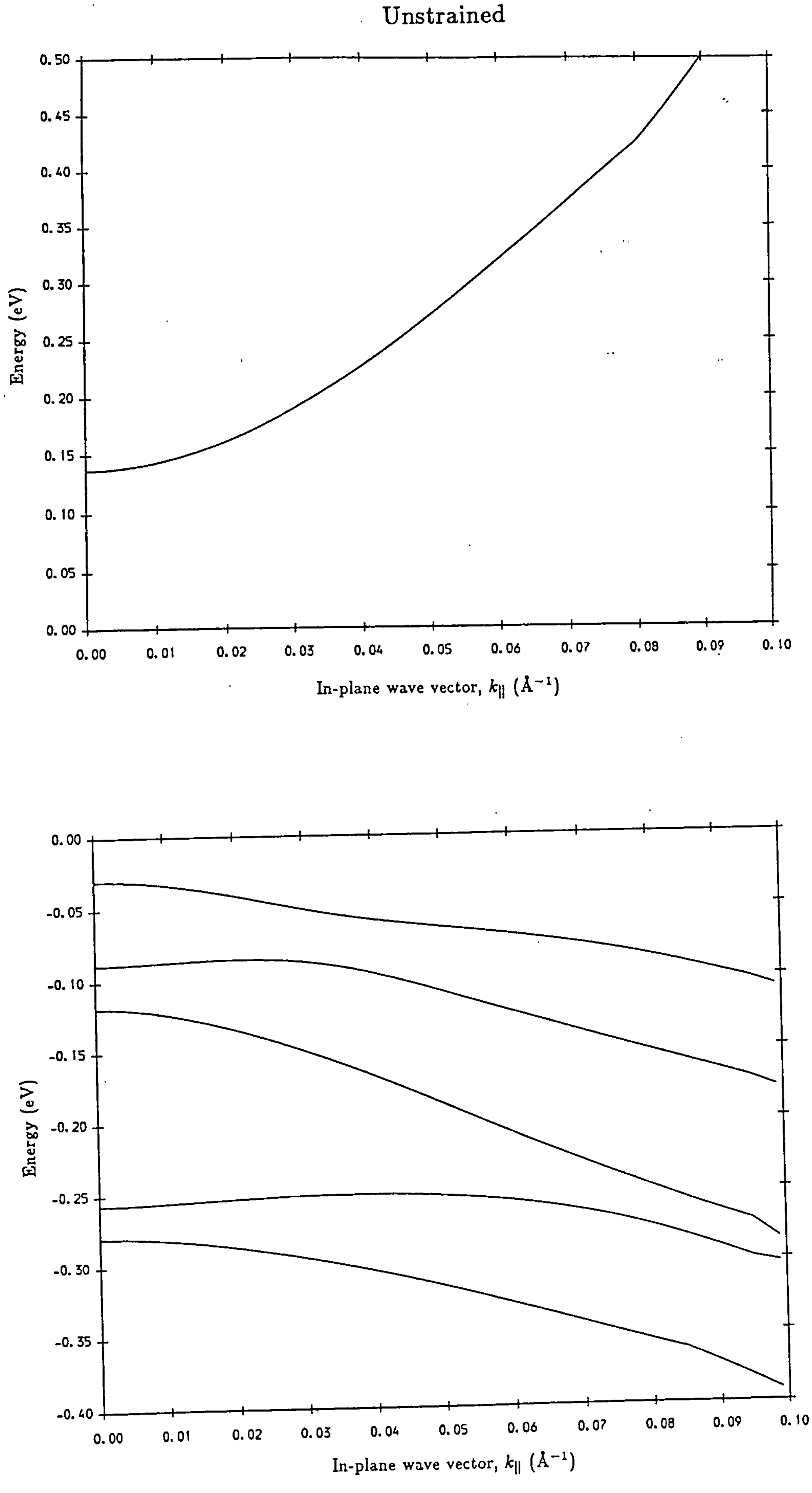

Bandstructure of 40Å $In_{0.53}Ga_{0.47}As/InP$ quantum well.

Figure 6.11a

$\frac{3}{4}$% lattice mismatch

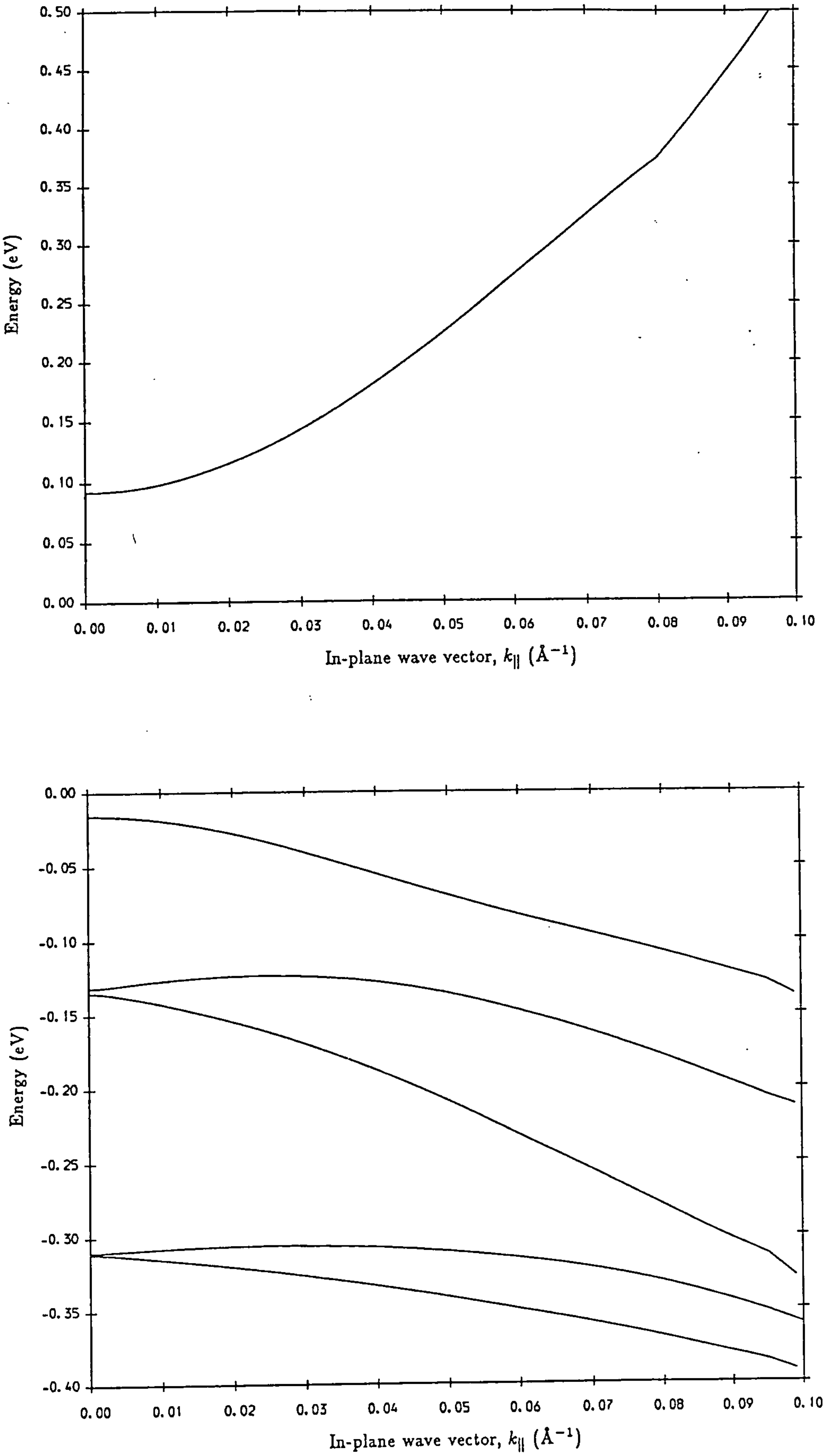

Bandstructure of 35Å $In_{0.63}Ga_{0.37}As$/InP quantum well.

Figure 6.11b

$1\frac{1}{2}\%$ lattice mismatch

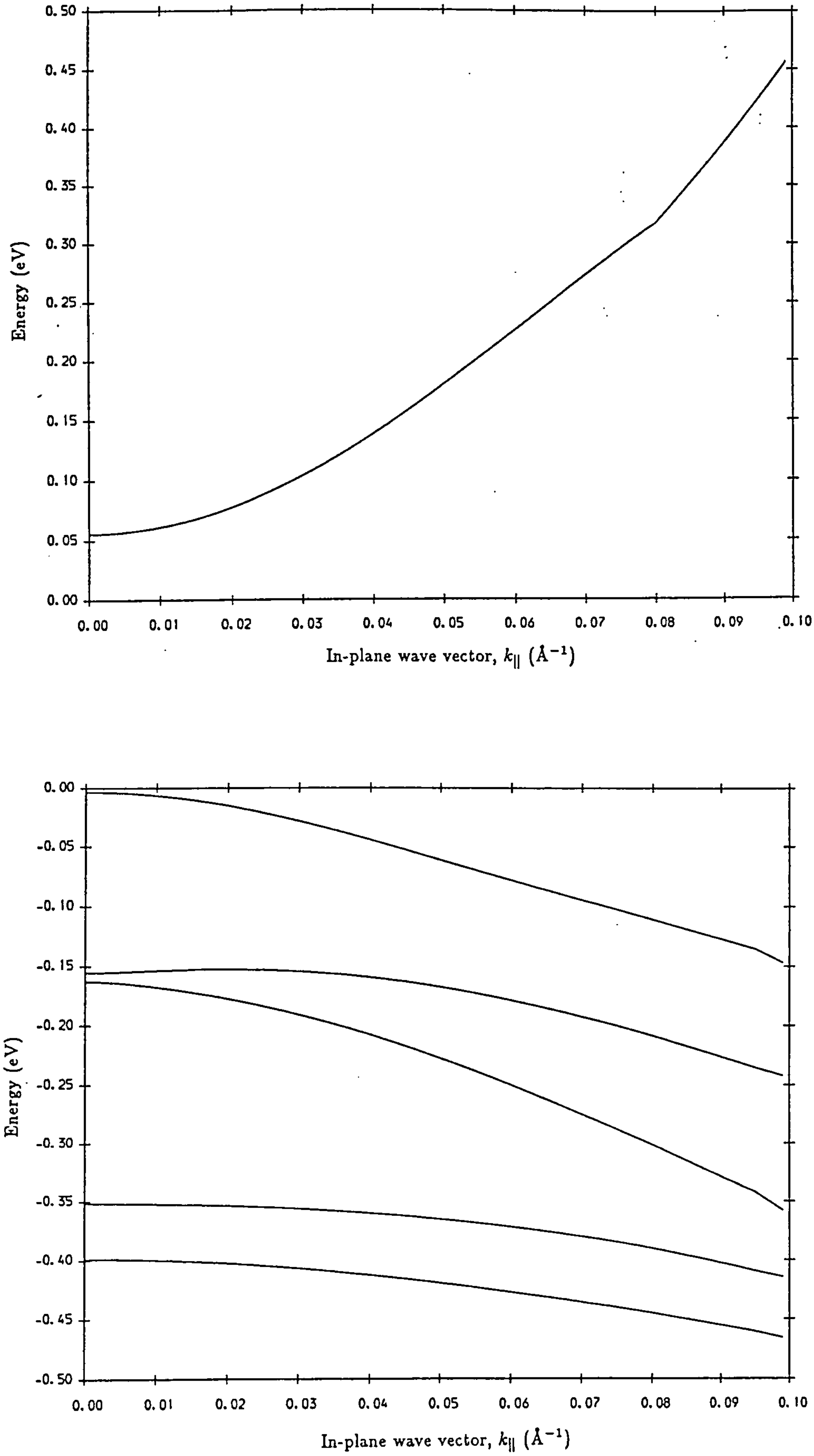

Bandstructure of 31.5Å $In_{0.73}Ga_{0.27}As/InP$ quantum well.

Figure 6.11c

the $In_{0.73}Ga_{0.27}As/InP$ device compared with the $In_{0.63}Ga_{0.37}As/InP$ device does result in the former structure maintaining the reduction in the effective mass of the ground state subband over a larger range of in-plane wave vector than the latter.

The TE mode optical matrix elements of these structures are shown in figure 6.12. In all three quantum wells the overall degree of mixing evident is less than that in the 1.55μm devices, although the strong mixing between the second and third subbands in the two strained 1.3μm structures results in the c1-lh1 oscillator strength being distributed between these two subbands in these devices.

6.4.2 Gain and Spontaneous Emission

The peak net gain of the three 1.3μm devices is shown as a function of injected carrier density in figure 6.13. In this case, the improvement offered by the highly strained $In_{0.73}Ga_{0.27}As/InP$ wells over the moderately strained $In_{0.63}Ga_{0.37}As/InP$ structures is less significant than for the 1.55μm devices. The peak gain is lower in the more highly strained device for injected carrier densities below about $4 \times 10^{18}\text{cm}^{-3}$. The strained structures again show a much higher peak gain than the lattice matched device, although the latter shows a considerably higher gain than the unstrained 1.55μm device due to the increased valence subband separation resulting from the reduced quantum well width. The spontaneous emission current, given in figure 6.14, is very similar in all three devices. The slight difference

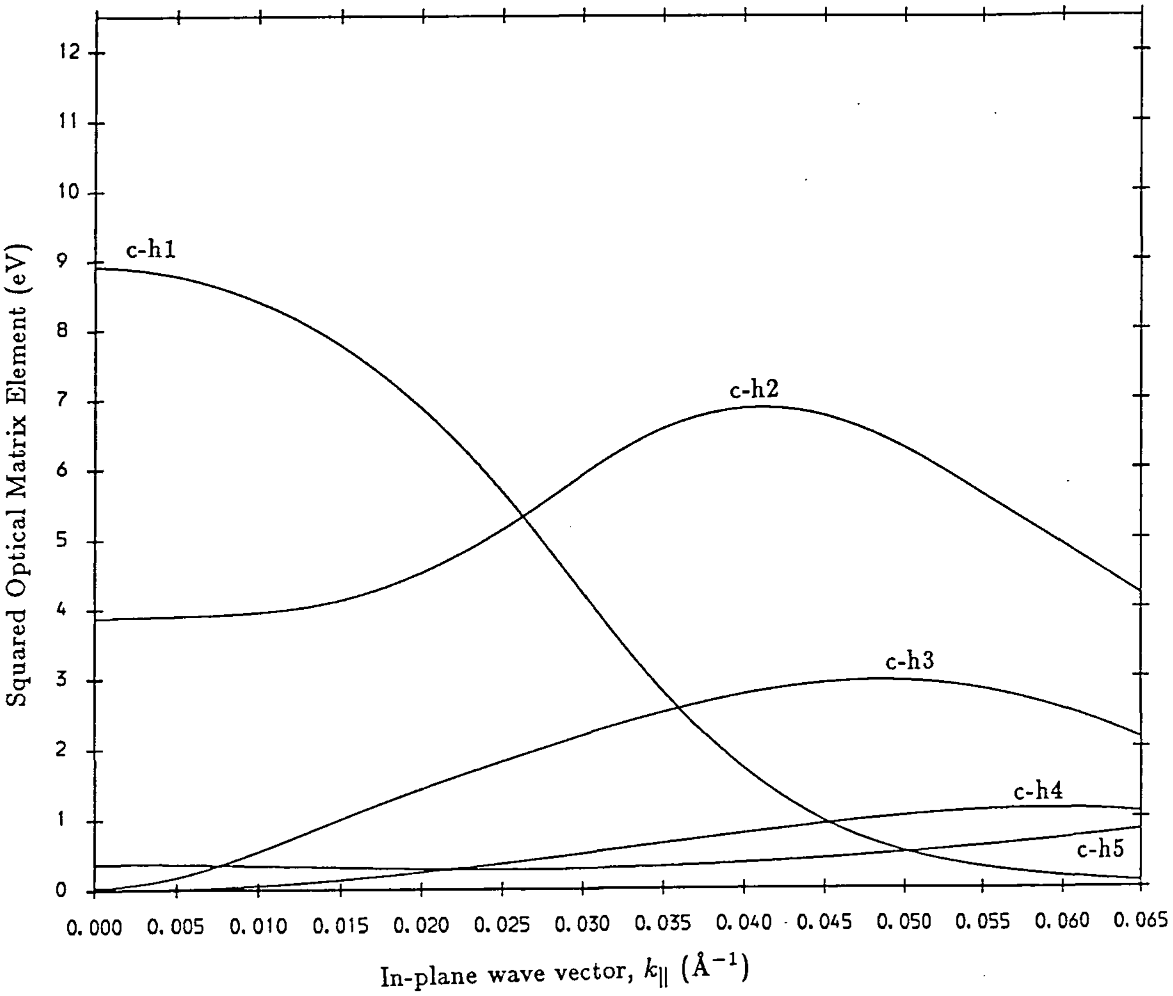

Optical matrix elements of 40Å $In_{0.53}Ga_{0.47}As$/InP quantum well.

Figure 6.12a

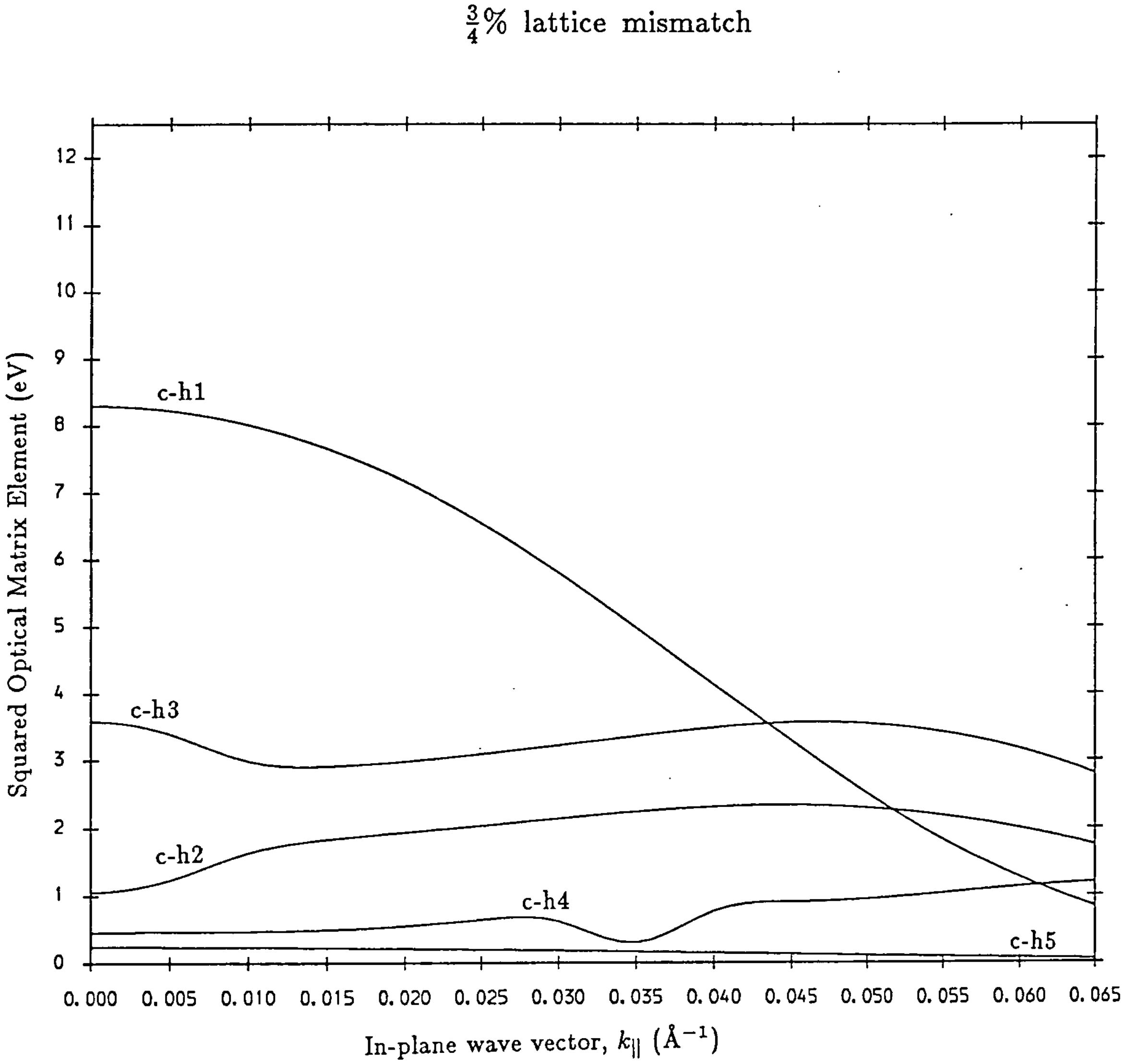

Optical matrix elements of 35Å $In_{0.63}Ga_{0.37}As/InP$ quantum well.

Figure 6.12b

$1\frac{1}{2}\%$ lattice mismatch

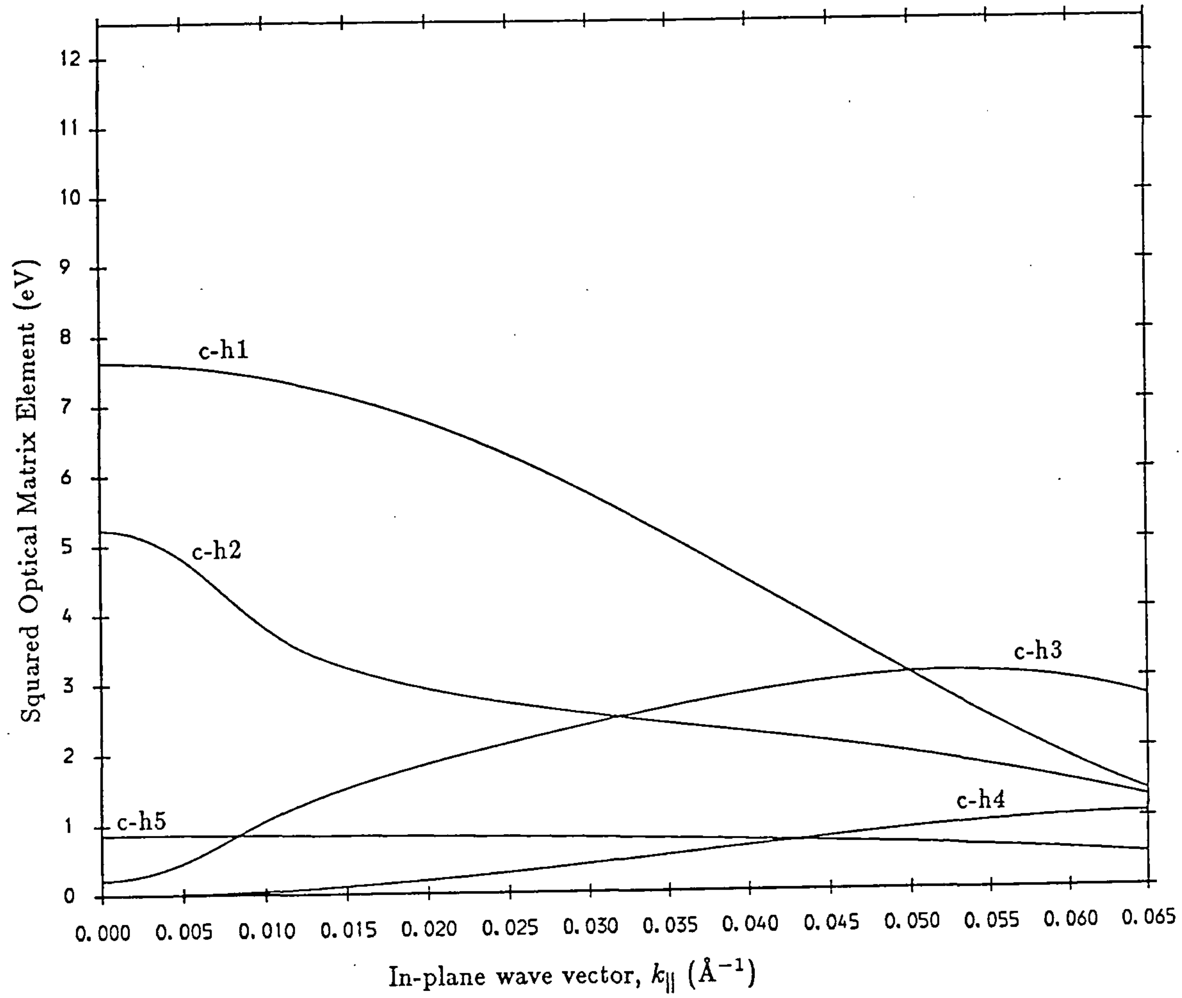

Optical matrix elements of 31.5Å $In_{0.73}Ga_{0.27}As/InP$ quantum well.

Figure 6.12c

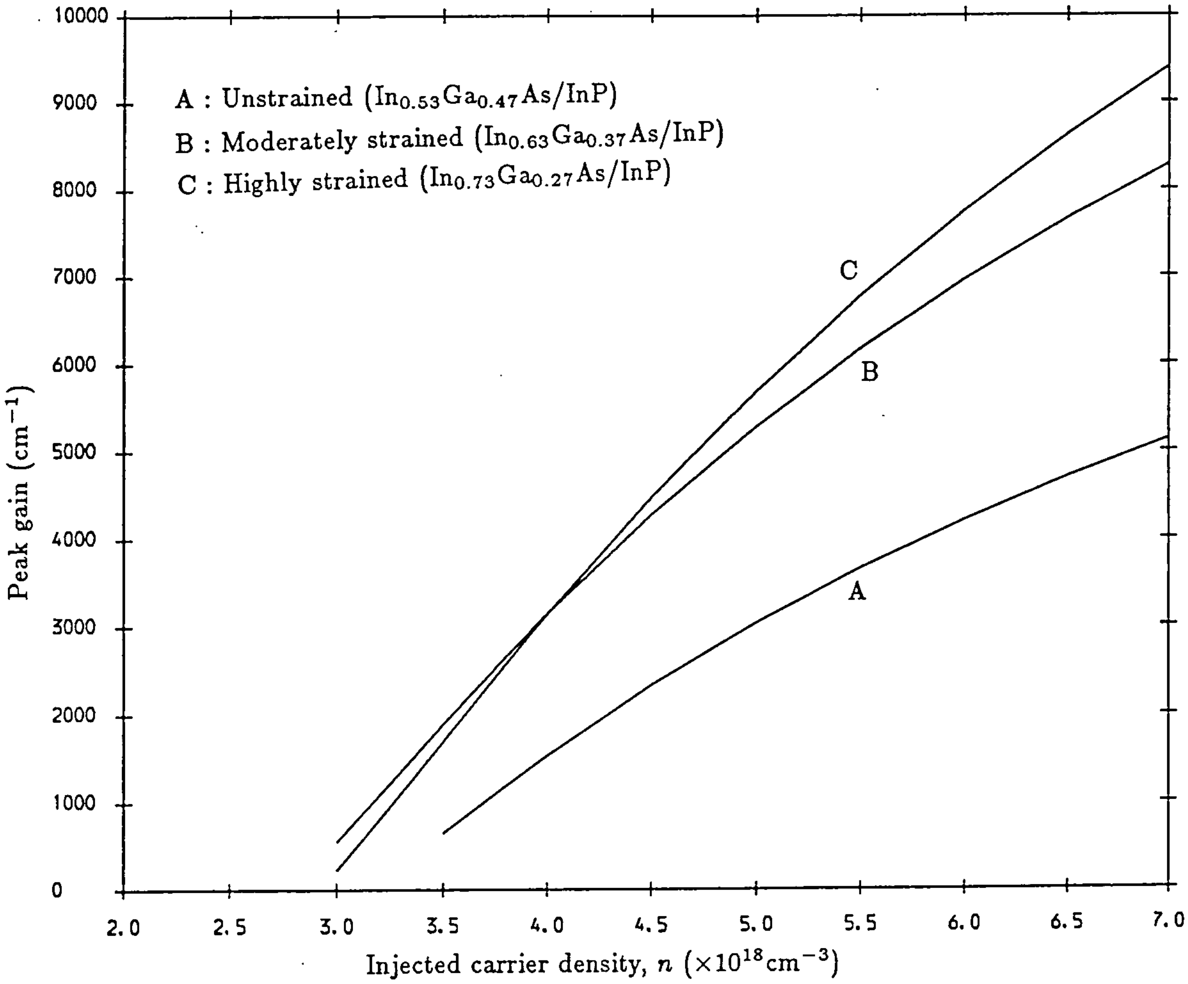

Peak gain dependence on injected carrier density for 1.3μm devices.

Figure 6.13

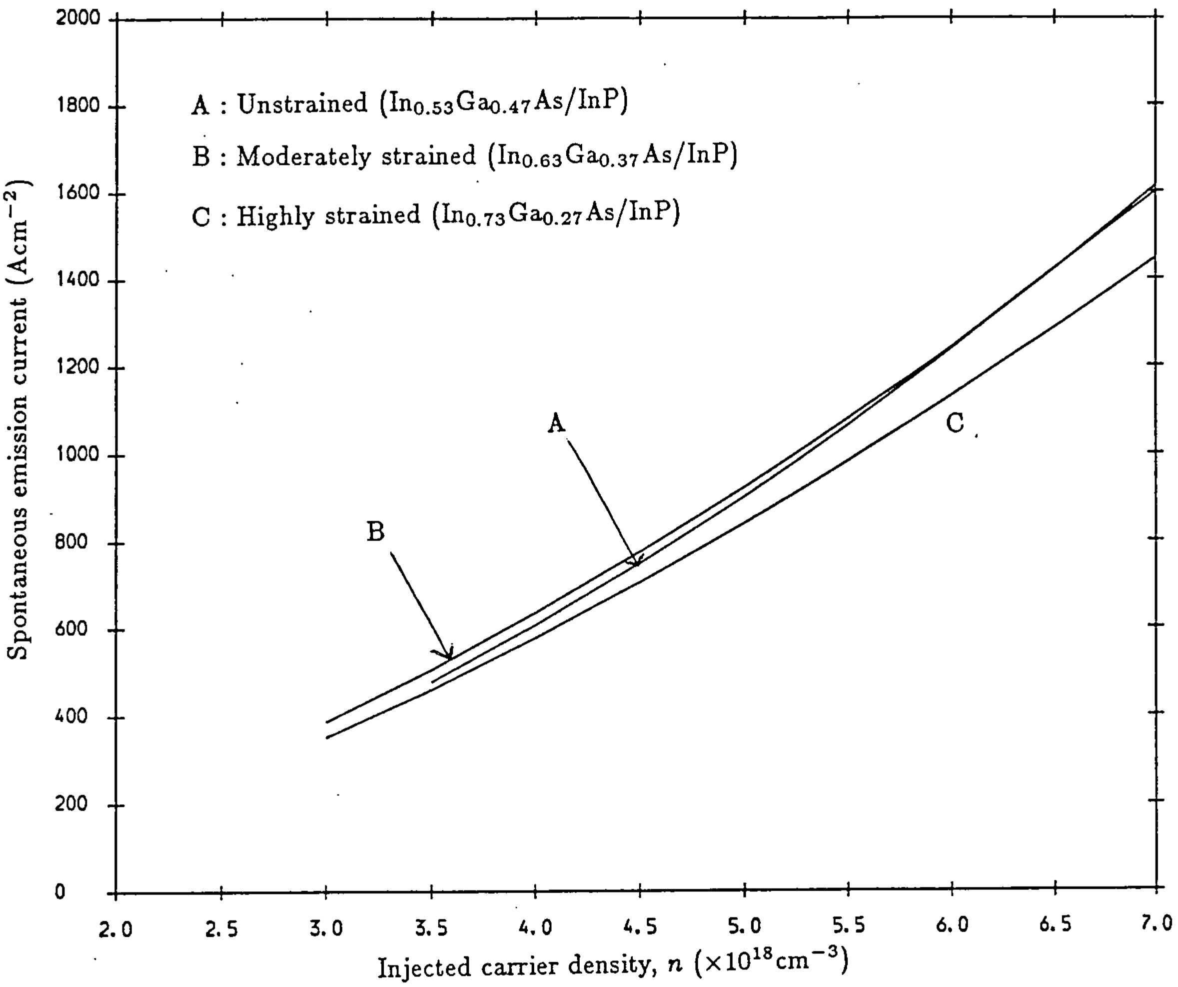

Spontaneous emission current versus injected carrier density

for 1.3μm devices.

Figure 6.14

seen is mainly due to the different well widths of the devices, rather than the strain.

The net gain obtained for a given total current density is shown in figure 6.15. The net gain is highest in the $\frac{3}{4}\%$ lattice mismatched $In_{0.63}Ga_{0.37}As/InP$ device. The lower optical confinement factor of the $1\frac{1}{2}\%$ mismatched $In_{0.73}Ga_{0.27}As/InP$ device results in this structure having a slightly lower net gain, but both of the strained devices have around twice the net gain of the unstrained device for a given current. As we discussed for the $1.55\mu m$ structures, this arises from the reduced effective mass at the valence band edge, which results in a higher proportion of the injected holes occupying states around this point.

6.4.3 Threshold Properties

The threshold properties of the $1.3\mu m$ devices show a strain dependence which is qualitatively similar to that of the $1.55\mu m$ lasers. The threshold currents (figure 6.16) are all considerably higher in the $1.3\mu m$ devices due to the reduced optical confinement resulting from the narrower quantum well widths used in these structures, but again the unstrained device shows a much higher threshold current density than either of the strained structures. The moderately strained ($\frac{3}{4}\%$ lattice mismatch) device has a slightly lower threshold current than the highly strained ($1\frac{1}{2}\%$ mismatch) device, which reflects the fact that the latter device has a lower net gain than the former for injected carrier densities less than about $4 \times 10^{18} cm^{-3}$, as

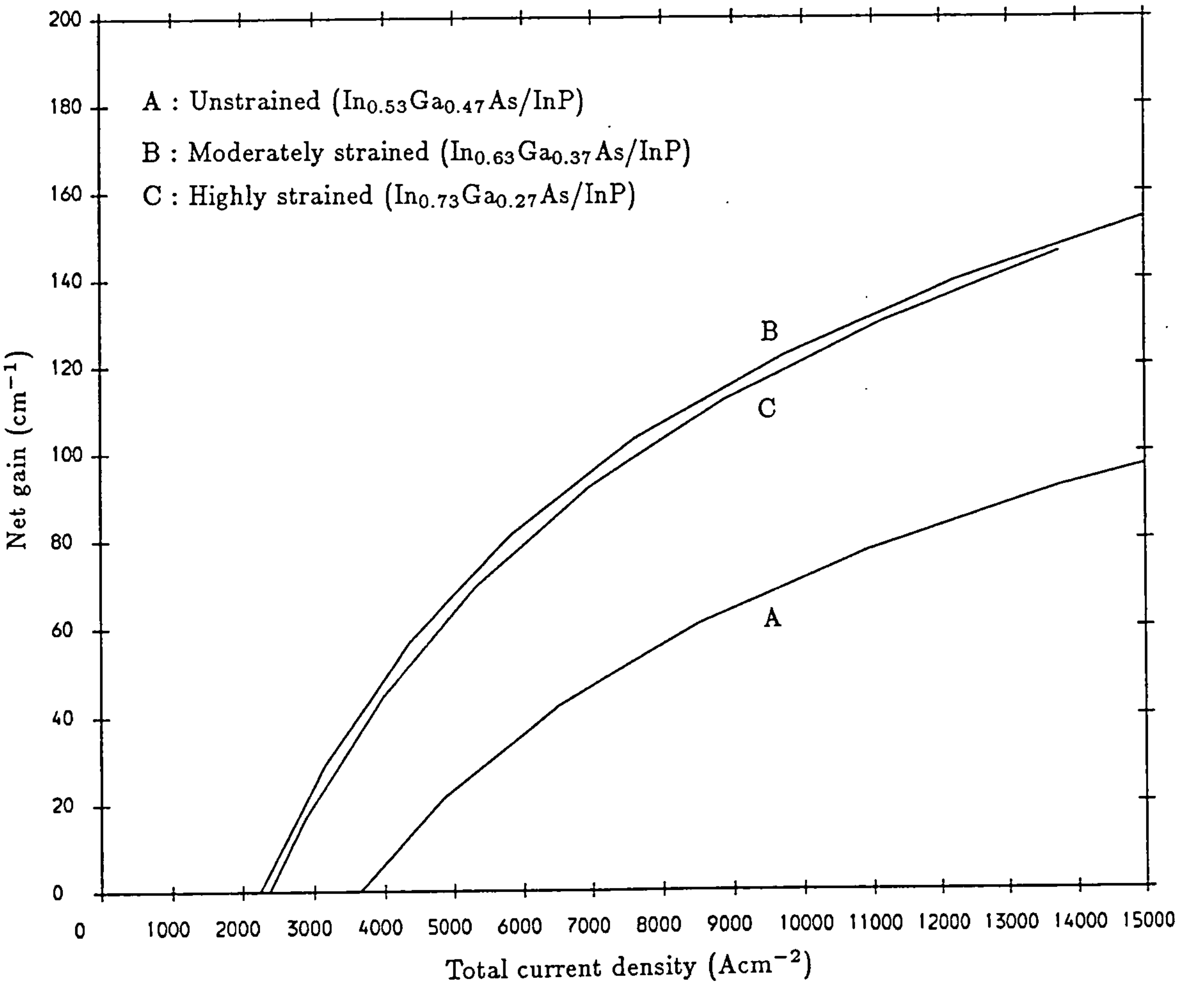

Net gain versus total current for 1.3μm devices.

Figure 6.15

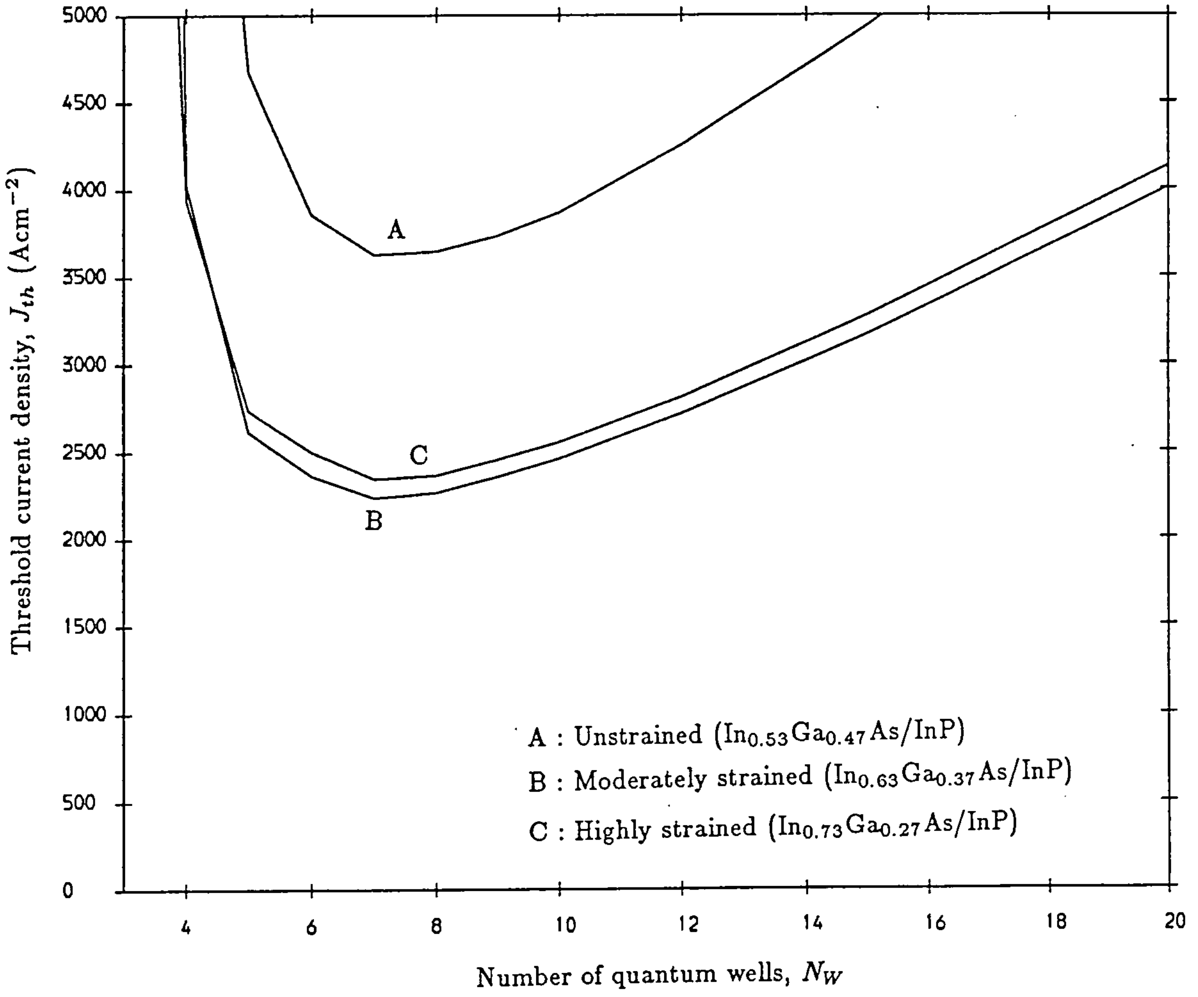

Threshold current density as a function of the number of quantum wells for 1.3μm devices.

Figure 6.16

shown in figure 6.13. That figure also showed that the gain increases more rapidly with increasing carrier density in the highly strained structure, and this is confirmed by examining the gainslope at threshold shown in figure 6.17. The gainslope of the lattice matched device is considerably lower than that of either of the strained structures.

The linewidth enhancement factor of the 1.3μm lasers is also improved by the strain, as demonstrated by figure 6.18, but this improvement is not so marked as it is in the 1.55μm devices. This is because the enhancement factor of the unstrained device is lower (in absolute value) in the 1.3μm structure than in the wide well 1.55μm device, which reduces the scope for improvement in the former device. The enhancement factor of the strained devices is largely unaffected by the reduction in well width required to change the operating wavelength.

The variation of the threshold current with temperature is shown in figure 6.19. The two strained devices both show a reduced temperature dependence ($T_0 = 103$K for the $In_{0.73}Ga_{0.27}As/InP$ device and $T_0 = 97$K for the $In_{0.63}Ga_{0.37}As/InP$ device) compared with the lattice matched device ($T_0 = 82$K). Again it must be noted that the effect of strain on the intervalence band absorption and Auger recombination coefficients has not been included in this calculation, so the actual improvement in temperature stability offered by strain is likely to be even greater.

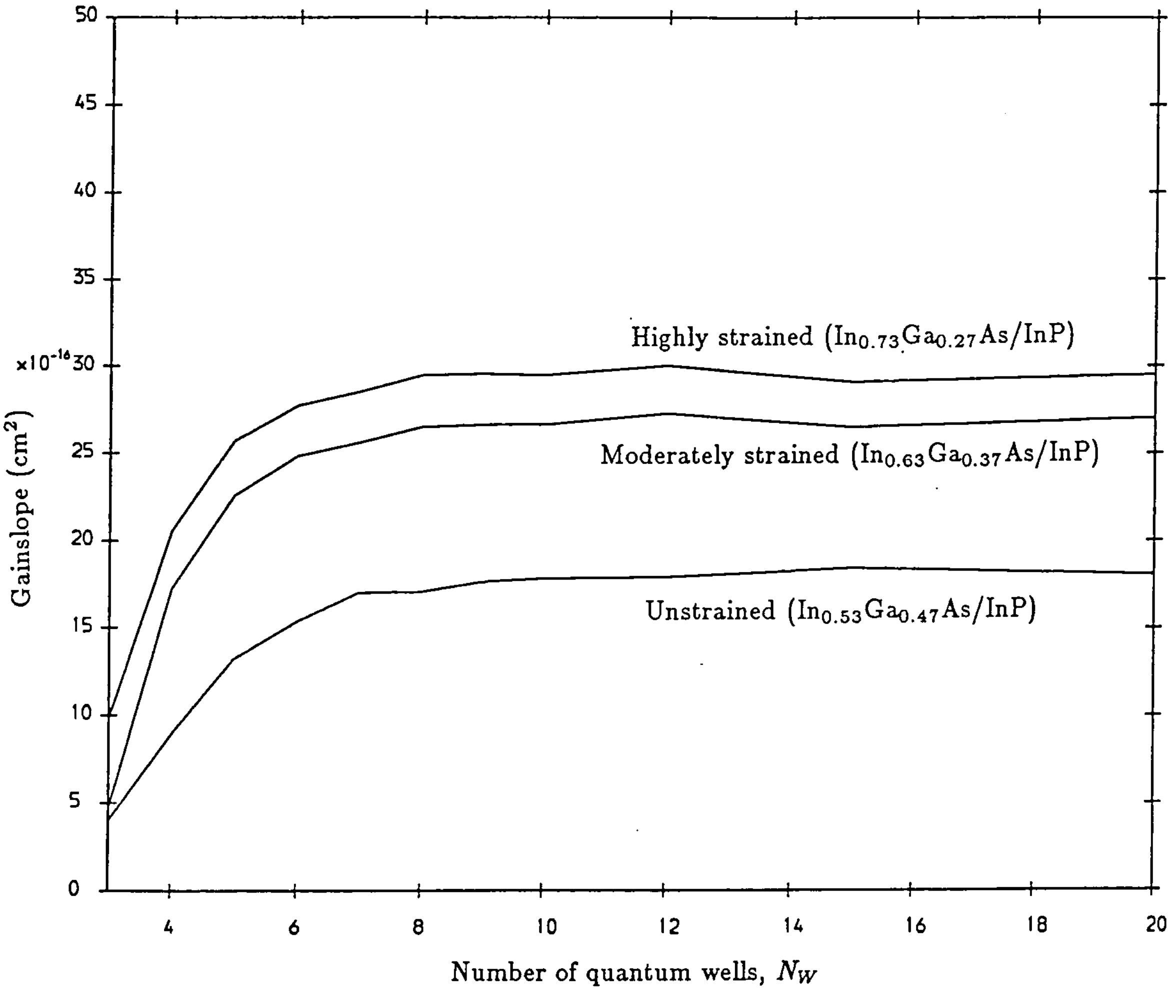

Gainslope of 1.3μm devices.

Figure 6.17

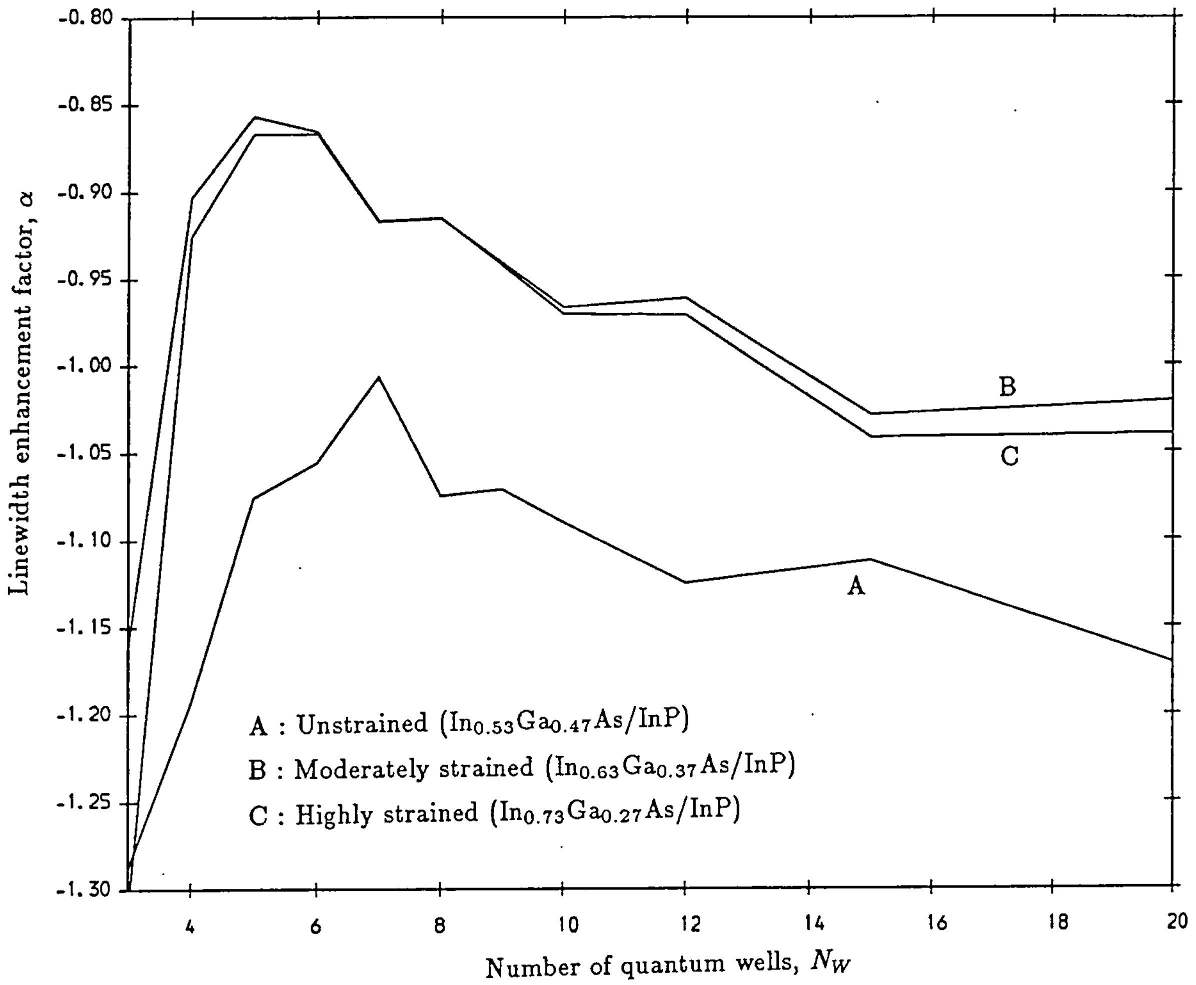

Linewidth enhancement factor of 1.3μm devices.

Figure 6.18

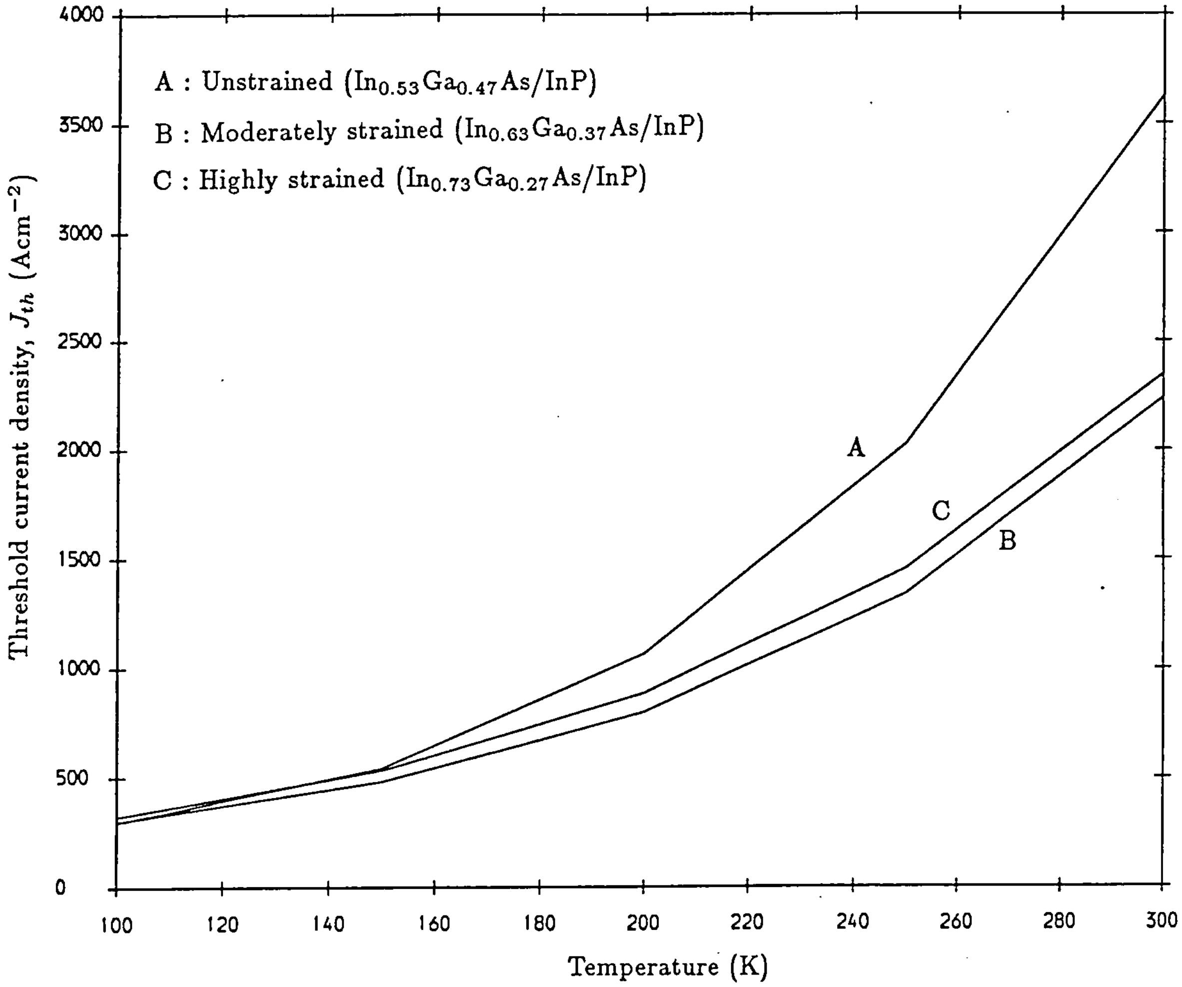

Temperature dependence of threshold current for 1.3μm devices.

Figure 6.19

6.5 Conclusions

The results presented in this chapter demonstrate that the use of a lattice mismatched quantum well structure can enhance the performance of multiple quantum well lasers, confirming the suggestions of Adams [1] and Yablonovitch and Kane [2] and the findings of several authors using less complete models. The results obtained show that such strained layer devices can have numerous advantages over conventional MQW lasers including a reduction in the threshold current density and its temperature dependence, a reduction in the absolute value of the linewidth enhancement factor, and an increase in the gainslope. Indeed, no property investigated here has been found to be affected detrimentally by the strain.

It has been quite widely believed that the enhancement in performance of a laser will increase with increasing strain. This work has shown that, at least for the devices considered here, this is clearly not the case. Whilst the current requirements at high output levels of the 1.55μm devices may show a monotonic reduction with increasing strain (this appears not to be the case for the 1.3μm devices), this effect is certainly not linear, with the reduction in current becoming proportionately less at higher levels of strain. For both the 1.55μm and 1.3μm devices investigated in this chapter, most of the enhancement in overall laser performance can be achieved with moderate amounts of strain ($\frac{3}{4}$% mismatch in lattice constant) present in the structure.

The reason for this can be seen from the quantum well bandstructure. Only a moderate amount of strain is necessary to shift the first $m_j = \frac{1}{2}$ 'light' hole subband to a sufficiently high hole energy that wave function mixing between states in this subband and states in the first $m_j = \frac{3}{2}$ 'heavy' hole subband is eliminated, resulting in a reduction in the effective mass of the ground subband. This increases the proportion of carriers at the valence band edge, and thus enhances the gain. The reduction in quantum well width necessitated by the strain also plays a role by increasing the separation of the $m_j = \frac{3}{2}$ subbands, but this advantage is countered by the reduced optical confinement factor of devices with narrow quantum wells. The reduced optical confinement is one reason why further increases in the level of strain are less effective in giving greater device performance. Another reason is the fact that once the $m_j = \frac{1}{2}$ subband has moved to a sufficiently high hole energy that it no longer mixes at all with the first $m_j = \frac{3}{2}$ subband, any further movement has no effect on the effective mass of the ground subband.

Comparison of the performance of the unstrained 1.55μm and 1.3μm devices confirms that merely reducing the quantum well width does not give a better device — clearly the strain is the most important factor in explaining the improved characteristics of the $In_{0.63}Ga_{0.37}As/InP$ and $In_{0.73}Ga_{0.27}As/InP$ devices.

The fact that enhanced laser performance can be achieved with only a moderate degree of strain becomes important when the critical thickness of the strained epilayers is considered. The 1.55μm laser requires at least 5 quantum wells to be present in the device if a low threshold current is to be achieved. This corresponds to a total strain (lattice mismatch × total strained layer thickness) of around 200Å% for the $In_{0.63}Ga_{0.37}As/InP$ device, but well over 300Å% for the $In_{0.73}Ga_{0.27}As/InP$ structure. A device with a total strain of 200Å% is likely to be possible, but the prospects of growing reliable devices with over 300Å% strain are less promising.

References for Chapter Six

[1] A.R. Adams, Electron. Lett. **22**, 249 (1986).

[2] E. Yablonovitch and E.O. Kane, IEEE J. Lightwave Tech. **LT4**, 504 (1986).

[3] K.C. Heasman, E.P. O'Reilly, G.P. Witchlow, W. Batty and A.R. Adams, SPIE **800**, 50 (1987).

[4] A. Ghiti, W. Batty, U. Ekenberg and E.P. O'Reilly, SPIE **861**, 96 (1987).

[5] A. Ghiti, E.P. O'Reilly and A.R. Adams, Electron. Lett. **25**, 821 (1989).

[6] T.C. Chong and C.G. Fonstad, IEEE J. Quantum Electronics **QE25**, 171 (1989).

[7] P.J.A. Thijs and T. Van Dongen, Electron. Lett. **25**, 1735 (1989).

[8] U. Koren, M. Oron, M.G. Young, B.I. Miller, J.L. de Miguel, G. Raybon and M. Chien, Electron. Lett. **26**, 465 (1990).

[9] N.K. Dutta, J. Wynn, D.L. Sivco and A.Y. Cho, Appl. Phys. Lett. **56**, 2293 (1990).

CHAPTER SEVEN

INTERVALENCE BAND ABSORPTION IN STRAINED QUANTUM WELLS

7.1 Introduction

In previous chapters of this thesis we described a method for obtaining quantum well bandstructure and wave functions in unstrained (chapter 2) and strained (chapter 3) systems. The results obtained for the bound states of the quantum well were then applied to a study of gain and spontaneous emission processes in quantum well lasers (chapters 5 and 6). It was also shown in chapter 2 that unbound states of the quantum well can be calculated using the same method. In this chapter the contribution of these unbound states to intervalence band absorption (IVBA) in strained and lattice matched quantum wells is investigated.

7.2 The Intervalence Band Absorption Process

Intervalence band absorption is the main optical loss mechanism in semiconductor lasers, and it has been suggested that it is partly or largely responsible for the temperature dependence of the threshold current of these devices [1-4], although this assertion has since been questionned by a variety of authors, most of whom suggest that Auger recombination is the main cause [5-8]. The IVBA process involves the absorption of light with the excitation of an electron from a deep valence band state to an unoccupied level nearer to the valence band edge. Clearly this process requires the initial presence of a hole in the final state which is therefore usually close to the valence band edge.

In a conventional double heterostructure (DH) laser, the main contribution to IVBA arises from transitions from the spin-orbit split-off band to the heavy hole band, as shown in figure 7.1 [8]. A smaller contribution also arises from transitions to states in the light hole band. In a quantum well laser, however, there are two distinct types of process which can occur. The bound-bound transition, shown as A in figure 7.2, in which an electron in a *bound* spin split-off subband[†] is excited into a *bound* light or heavy hole subband will tend to dominate in structures where the band gap E_g and the spin-orbit splitting energy Δ are comparable. In InGaAs devices suitable for operation in the 1.3μm to 1.55μm range, however, the band gap is 2-3 times the spin-orbit splitting. In such systems the bound-bound transitions can only occur (neglecting phonon assisted transitions) between states with very large in-plane wave vector where few holes reside. However,

---

[†] The spin split-off states experience a confining potential due to the different spin orbit splitting energy Δ and valence band offset ΔE_v of the well and barrier materials in the same way as electrons and light and heavy holes are confined by the band edge potential. In general the depth of the spin split-off well will differ from that confining the other holes.

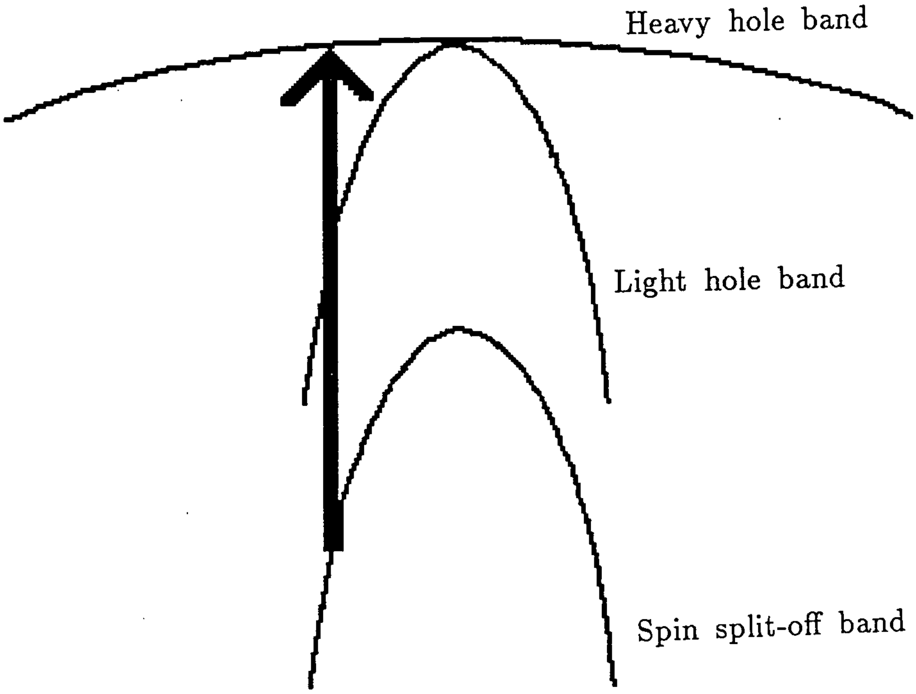

The dominant IVBA process in bulk materials.

Figure 7.1

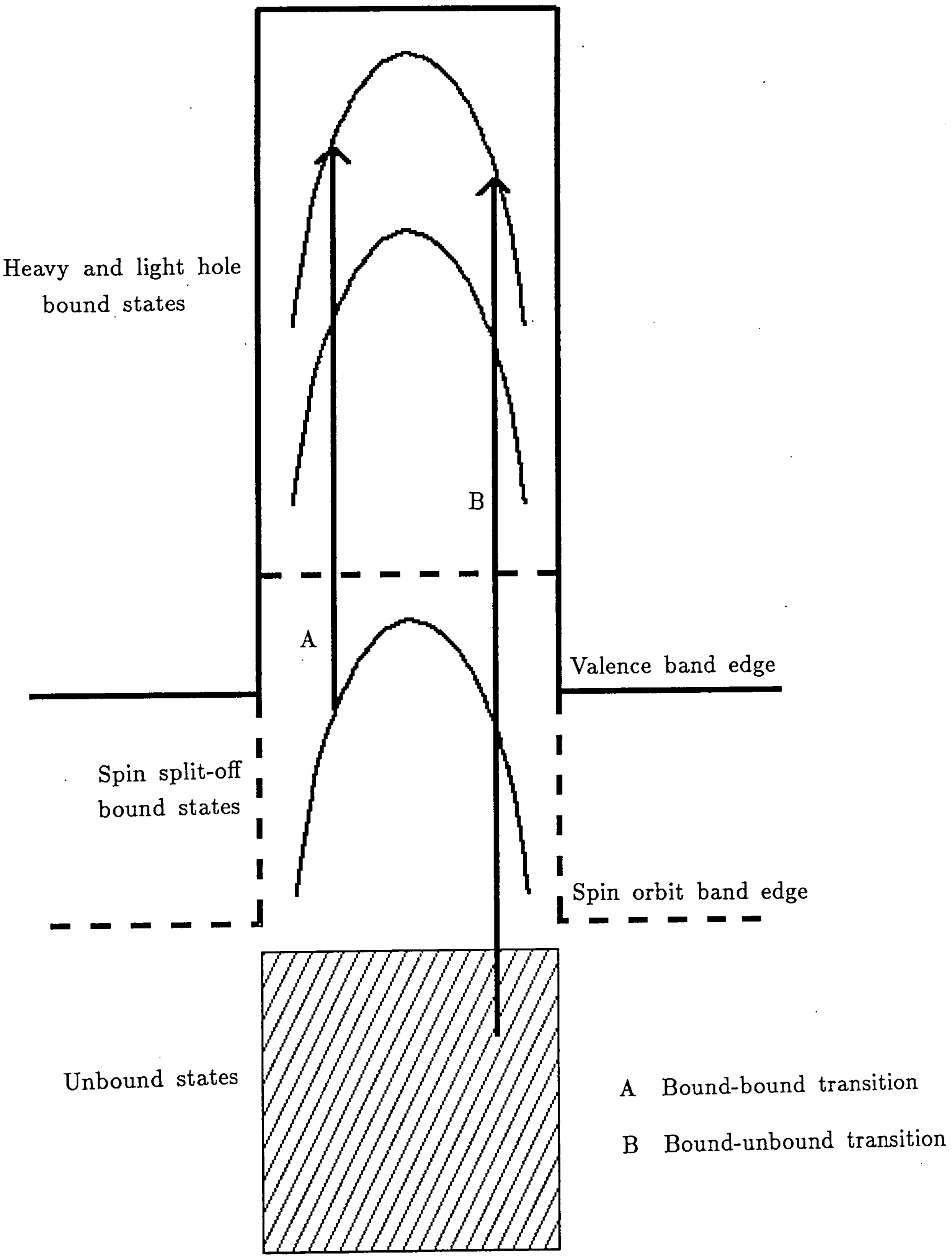

The bound-bound (A) and bound-unbound (B) IVBA processes in a quantum well.

Figure 7.2

the bound-unbound process, shown as B in figure 7.2, which can occur even at zero in-plane wave vector, could be important.

Calculations of IVBA in bulk materials, and of bound-bound processes in (unstrained) quantum wells have been carried out using approaches of varying sophistication [8-11], but to the author's knowledge there have previously been no reports of calculations of bound-unbound absorption rates. The bound-bound IVBA rate is straightforward to calculate using the **k**.**p** model described in chapter 2. Essentially the procedure to be followed is similar to that used to obtain gain and spontaneous emission spectra described in chapter 5, the only significant difference being that both of the subbands involved have the same type of curvature. The bound-unbound absorption process is somewhat different because transitions of a given energy can occur to all the states occupied by holes in a given bound subband, even when the **k**-selection rule is strictly applied. In contrast the bound-bound transitions occur only for wave vectors on a closed curve in the two dimensional wave vector space for which the intersubband energy separation is the appropriate value. For this reason a new set of unbound wave functions and optical matrix elements must be calculated each time the transition energy is changed, which means that a large processing time is required to obtain a spectrum containing points at more than a few different wavelengths. It is somewhat easier to adjust the temperature or hole density in the calculation at a given wavelength, and in this thesis we concentrate on the influence of these parameters on the IVBA rate, with only a brief investigation of the wavelength dependence.

7.3 Theory of Bound-Unbound IVBA Processes

The absorption rate for intervalence band transitions is obtained in the same way as that for the fundamental absorption as described in chapter 5, and for the bound-unbound process is given by (cf. equation 5.10)

$$\alpha = \frac{\pi e^2 \hbar}{m_0^2 \epsilon_0 \mu \hbar \omega c L_z} \int |M|_{UB}^2 (f_B - f_U) \delta(E_B - E_U - \hbar\omega) \mathrm{d}^3\mathbf{k} \qquad (7.1)$$

f_B and f_U now represent the probability of the bound and unbound states respectively being occupied by a *hole.* $|M|_{UB}^2$ is the optical matrix element (averaged over TE and TM modes) between the initial unbound and final bound states.

The delta function can be transformed in the standard manner to facilitate the integral over wave vector

$$\int \delta(E_B - E_U - \hbar\omega) = \sum_{n_B} \int \sum_{k_{\mathrm{root}}} \frac{\delta(k_z - k_{\mathrm{root}})}{\left|\frac{dE_U}{dk_z}\right|_{k_z}} \qquad (7.2)$$

The k_{root} are the values of the z component of the wave vector of the unbound states which are the roots of the delta function for a given in-plane wave vector $k_{\|}$. n_B represents the bound subband index.

For a given transition energy $\hbar\omega$ the unbound states corresponding to the roots of the delta function lie on a 'quasi-subband' which has the same dispersion with $k_{\|}$ as the bound subband but displaced by an energy

$\hbar\omega$, as shown in figure 7.3. The roots can be categorised according to the nature in the barrier material of the corresponding unbound state. Hence the sum over the roots includes unbound light and heavy hole states and (at energies above the top of the spin split-off well) spin split-off holes. At any energy the z dependence of the unbound state wave functions exist with both even or odd parity and for each of these two spin states are possible. The absorption rate is obtained by carrying out the integration over wave vector :

$$\alpha = \frac{\pi e^2 \hbar}{m_0^2 \epsilon_0 \mu \hbar \omega c L_z} \sum_{n_B} \int (f_B - f_U) \sum_{\substack{\mathrm{hh} \\ \mathrm{lh} \\ \mathrm{so}}} \sum_{\substack{\mathrm{odd} \\ \mathrm{even}}} \sum_{\mathrm{spin}} |M|_{UB}^2 \frac{2\pi k_\parallel}{\left|\frac{dE_U}{dk_z}\right|_{k_z}} dk_\parallel \tag{7.3}$$

$|dE_U/dk_z|^{-1}$ is actually proportional to the density of unbound states at a given $k_\parallel$. This density of states is determined by the behaviour of the wave function in the barrier region, and is obtained from the bulk bandstructure of the barrier with in-plane wave vector $k_\parallel$. The integral in (7.3) is evaluated numerically using the trapezium rule, calculating the integrand at 20 points along the subband from $k_\parallel = 0$ to $k_\parallel = 0.1\text{Å}^{-1}$ for each bound subband.

7.4 Results and Discussion

Intervalence band absorption rates have been calculated over a range of carrier densities and temperatures for each of the six devices described in the previous chapter, namely InGaAs/InP quantum wells suitable for 1.3μm

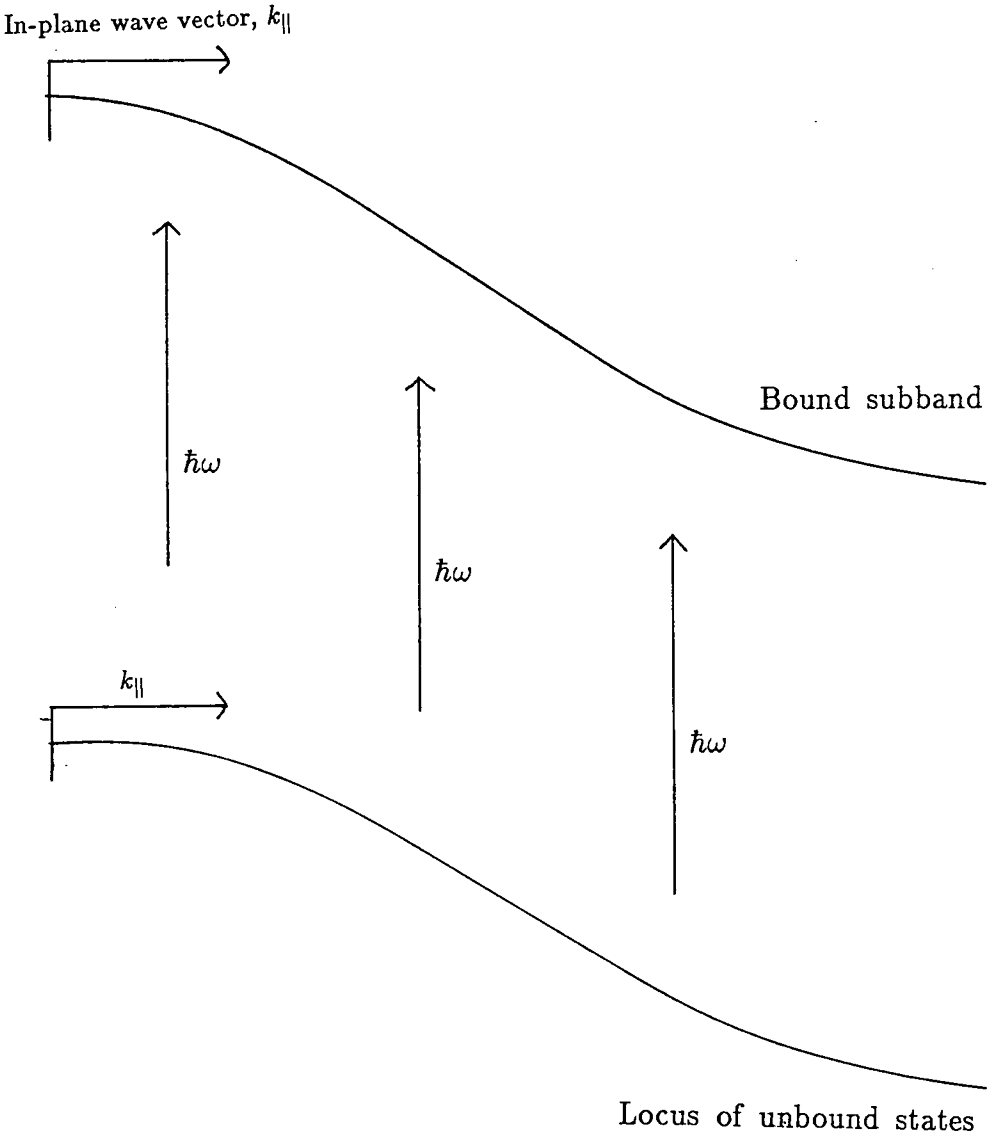

The bound-unbound state pairs giving rise to absorption at a given wavelength.

Figure 7.3

and 1.55μm laser operation with 0%, $\frac{3}{4}$% and $1\frac{1}{2}$% mismatch in lattice constant between the well and barrier materials.

Figure 7.4 shows the temperature variation of the bound-unbound IVBA coefficient for the 1.55μm devices for transitions at the band gap energy with a hole density of 2×10^{18}cm^{-3}. The overall magnitude of all the absorption coefficients are considerably smaller than those obtained for calculations of bound-bound IVBA rates [11]. This is because the bound-bound process is dominated by transitions form an $n = 1$ spin split-off subband to an $n = 1$ heavy or light hole subband. The overlap between the envelopes of two $n = 1$ states is considerably larger than the overlap between an $n = 1$ state and an unbound state which has several nodes.

The unstrained and moderately strained devices show only a small increase in IVBA as the temperature is increased. The highly strained device shows a higher temperature dependence, although even for this structure the absorption only increases by a factor of 3 over the range of temperatures considered (100K to 400K), which is considerably less than that predicted for bulk InGaAs [8]. Figure 7.5 shows the effect of temperature on the bound-unbound absorption rate at the band gap energy for the 1.3μm devices, at the same hole concentration as above. All of these devices have IVBA coefficients which are largely unaffected by temperature.

The small temperature dependences observed arise because the redistribution of carriers within the subbands as the temperature changes does not greatly modify the absorption. For the bound-bound (and bulk) tran-

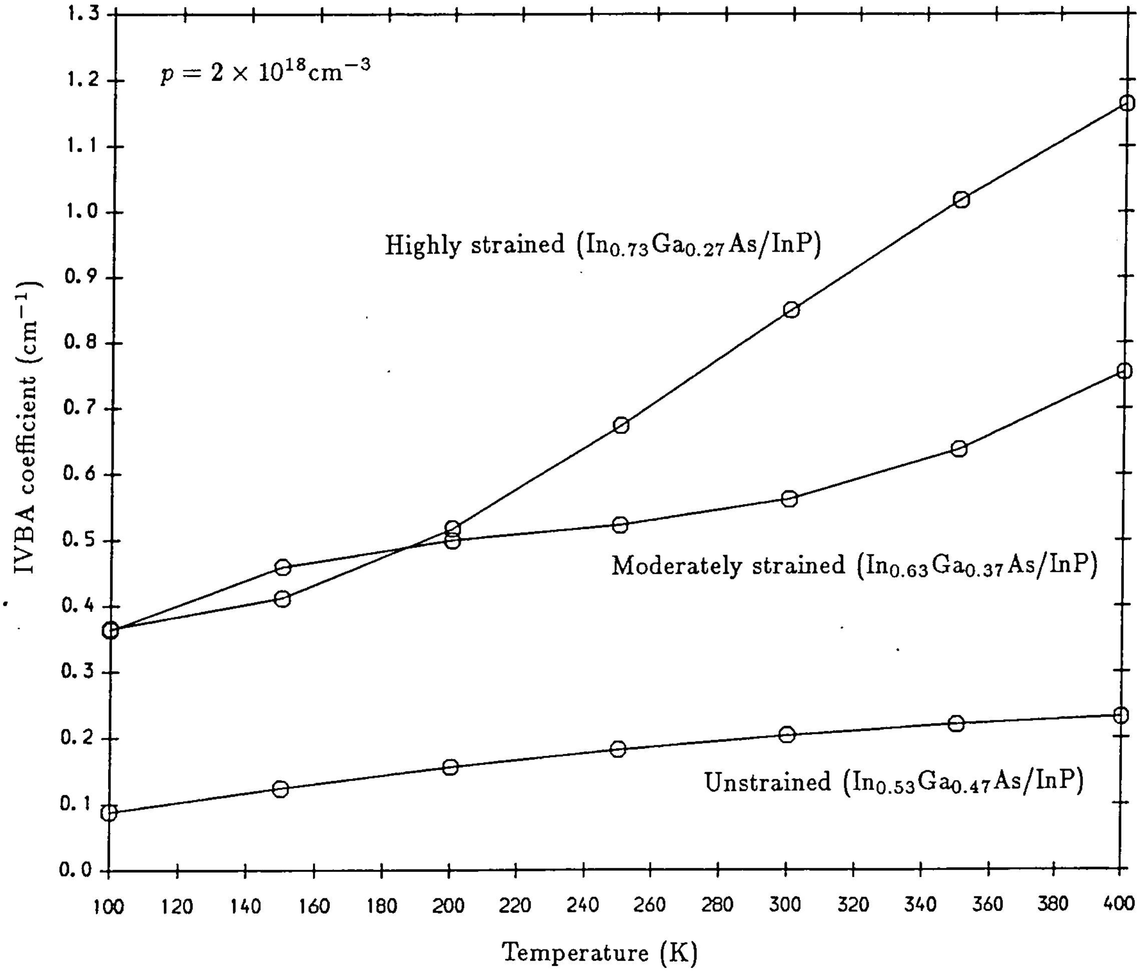

Temperature variation of bound-unbound IVBA in 1.55μm laser devices.

Figure 7.4

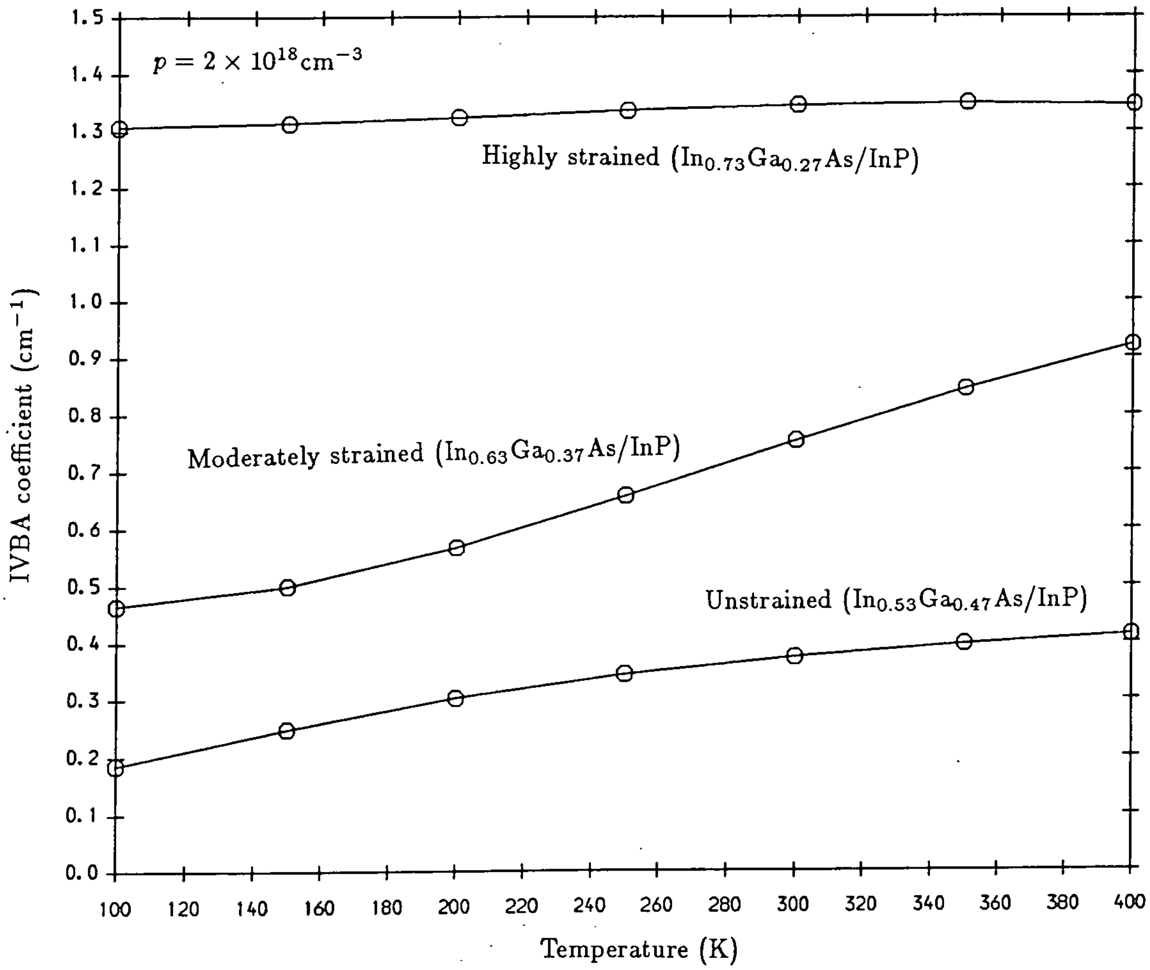

Temperature variation of bound-unbound IVBA in 1.3μm laser devices.

Figure 7.5

sitions, moving a hole along a subband will change the possible transition energies associated with that carrier, and hence modify the spectrum. On the other hand, for the bound-unbound process, transitions of a given energy are possible into *all* states of the bound subband, as long as the energy is sufficient to allow bound-unbound transitions. The effect of temperature on the bound-unbound absorption rate is thus dominated by the effect of exciting holes into higher subbands. This will increase the overlap between the bound and unbound wave functions and hence enhance the optical matrix element.

The dependence of the absorption coefficient on the hole density is shown in figure 7.6 for the 1.55μm structures and in figure 7.7 for the 1.3μm devices. The IVBA rate is found to increase linearly with hole concentration, which is the same result as has been obtained for both bulk materials [8] and for the bound-bound quantum well rate in the GaAs/AlGaAs system [11].

The bound-unbound absorption spectrum has been investigated for the 1.3μm devices. (The large requirements of CPU time (3500s per point on the spectrum per device) made this calculation possible for only one set of devices). The results are shown in figure 7.8. For the unstrained and moderately strained devices the absorption increases with increasing wavelength. This result is to be expected since as the transition energy decreases the number of nodes in the wave function of the unbound state will decrease, resulting in an increased overlap between the bound and

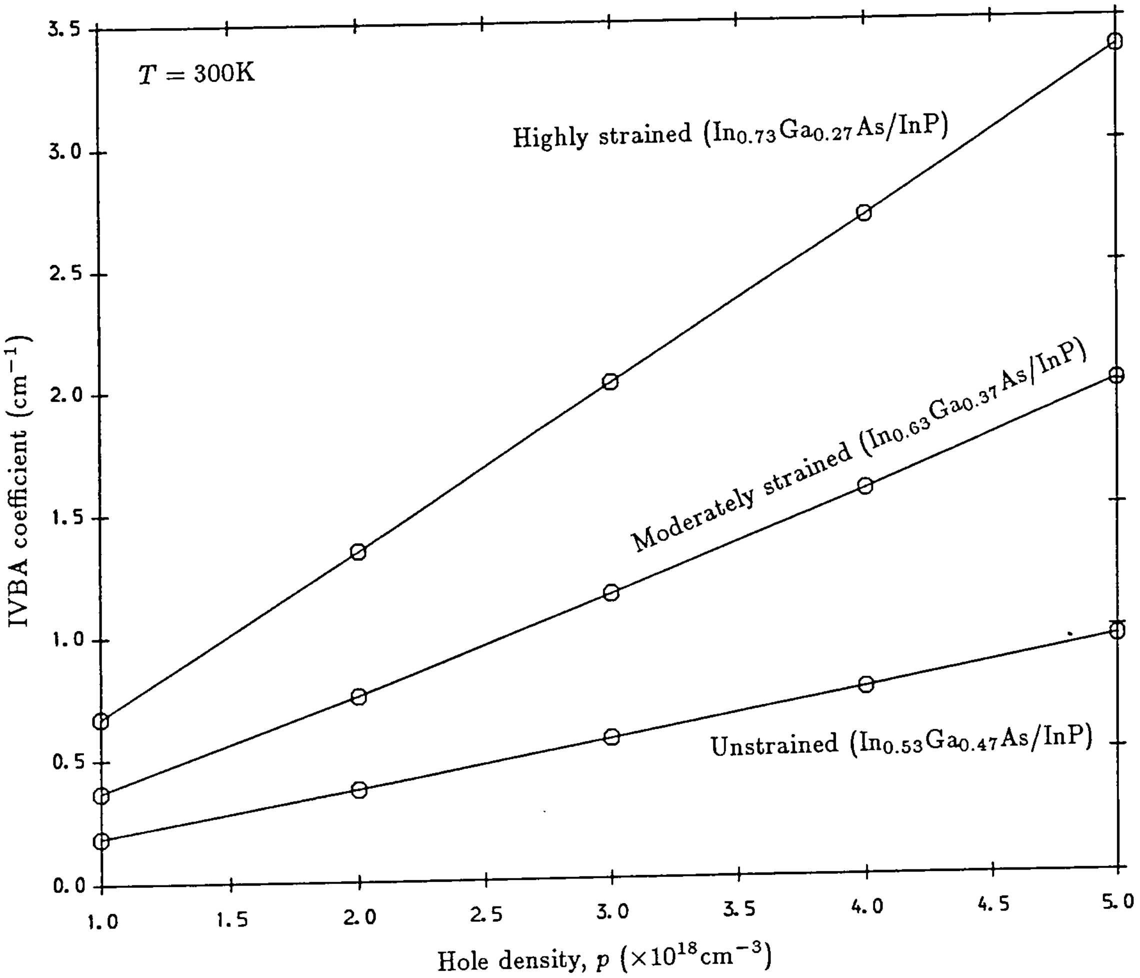

Dependence of bound-unbound IVBA on hole concentration in 1.55μm laser devices.

Figure 7.6

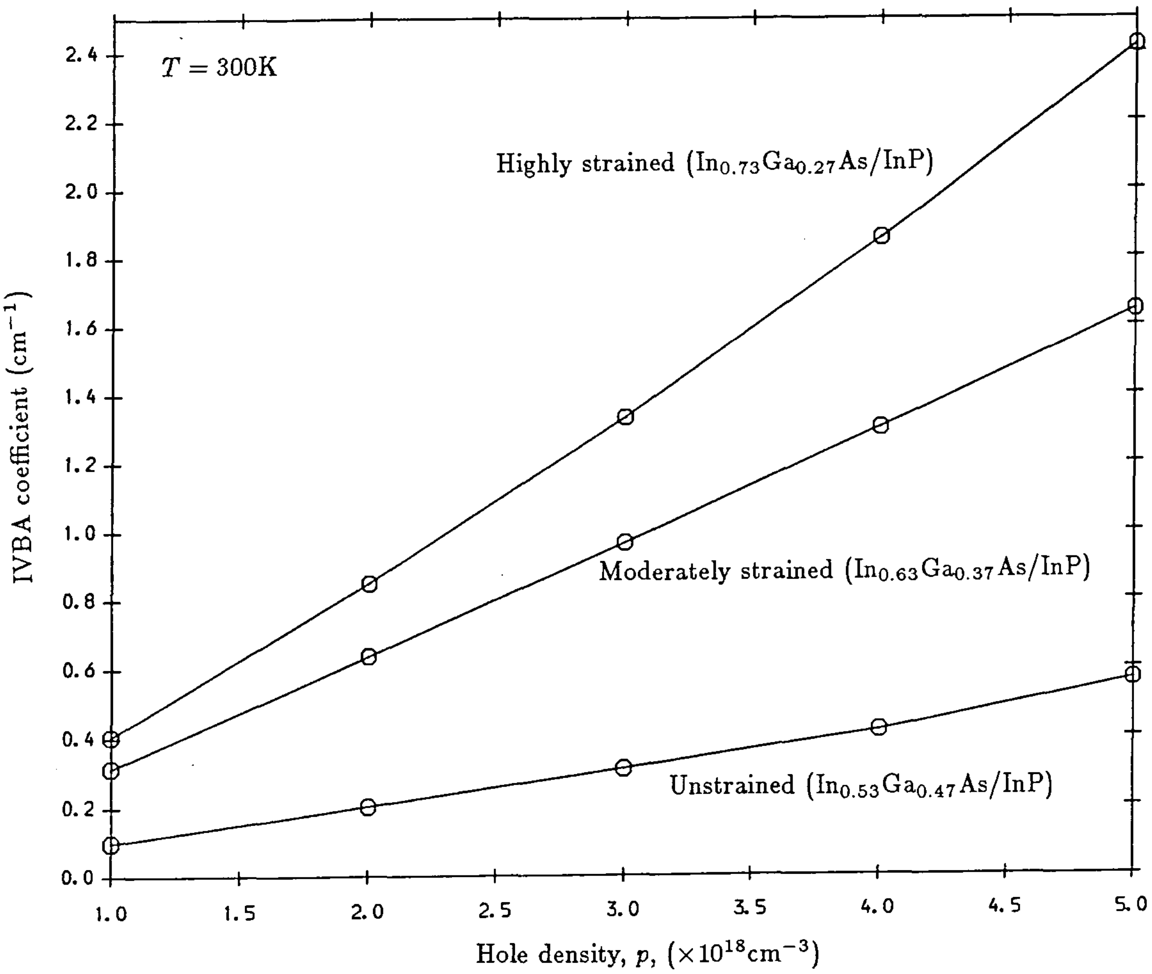

Dependence of bound-unbound IVBA on hole concentration in 1.3μm laser devices.

Figure 7.7

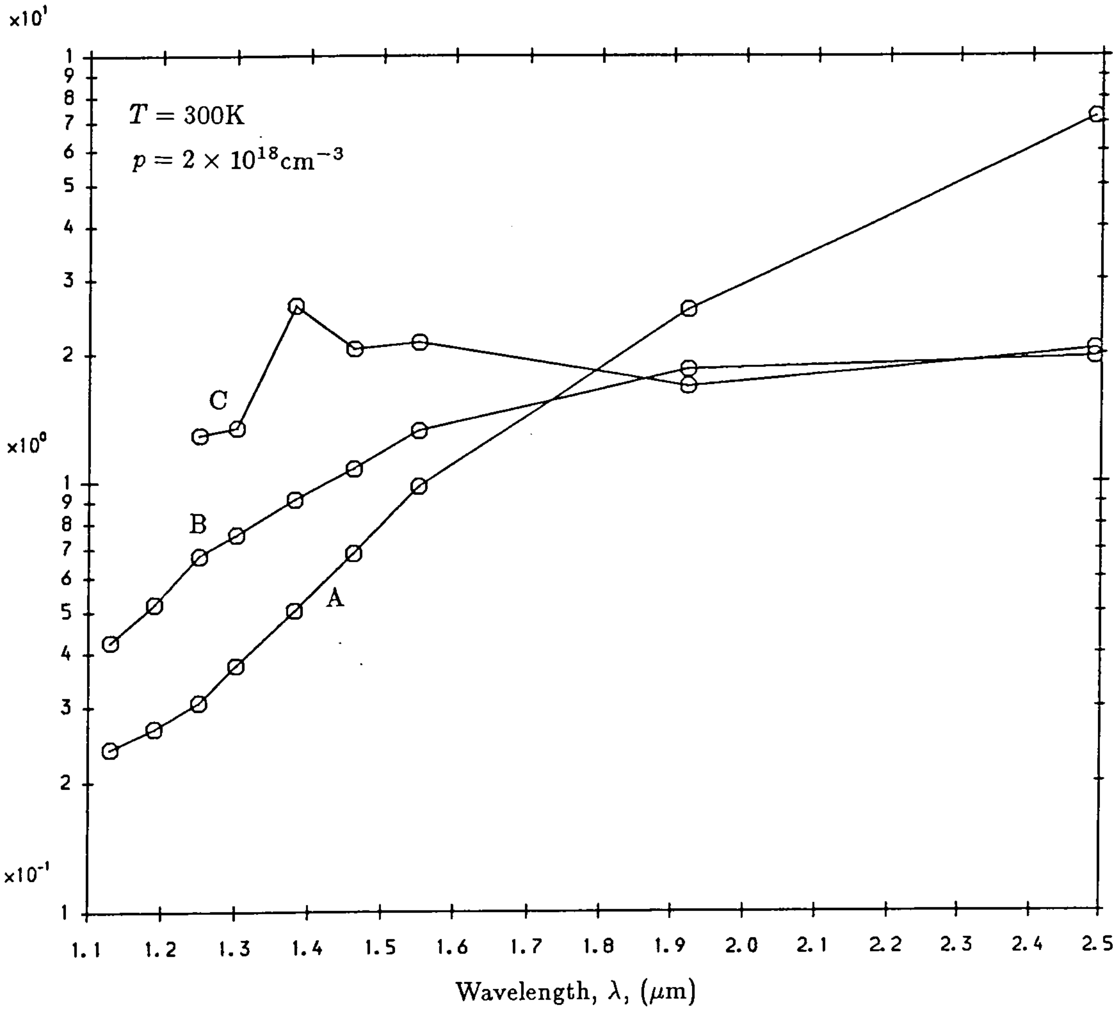

Bound-unbound IVBA spectrum of 1.3μm laser devices.

Figure 7.8

unbound state wave functions and leading to a larger optical matrix element. This effect is masked in the highly strained structure because the threshold wavelength for the onset of unbound spin split-off states (i.e. the wavelength corresponding to the energy of the top of the spin split-off potential well) occurs at around 2.3μm at the zone centre, and at around 1.5μm at $k_{\|} = 0.1\text{Å}^{-1}$. This is illustrated in figure 7.9, which demonstrates the variation with in-plane wave vector of the spin split-off potential well, with the locus of unbound states appropriate to the 1.3μm transition to the ground state bound subband given for comparison. As the wavelength increases, the transition energy decreases and the locus of unbound states will enter the spin split-off well. This makes it clear that the decrease in IVBA from 1.55μm to 1.92μm for this device results from the fact that the unbound spin split-off states which can be involved in transitions to the ground state bound subband only exist near to the zone centre when the transition energy corresponds to a wavelength of 1.92μm. Away from the zone centre, the required initial energy for such transitions lies within the spin-orbit potential well and processes involving spin-orbit unbound states are not possible. Transitions involving *bound* spin split-off states might be possible at certain energies in addition to transitions involving light and heavy hole *unbound* states. This effect is also responsible for the flattening of the curve for the moderately strained structure for $\lambda > 2\mu$m, but does not occur in the unstrained structure in the wavelength range considered due to the different line-up of the bulk subband edges in this structure.

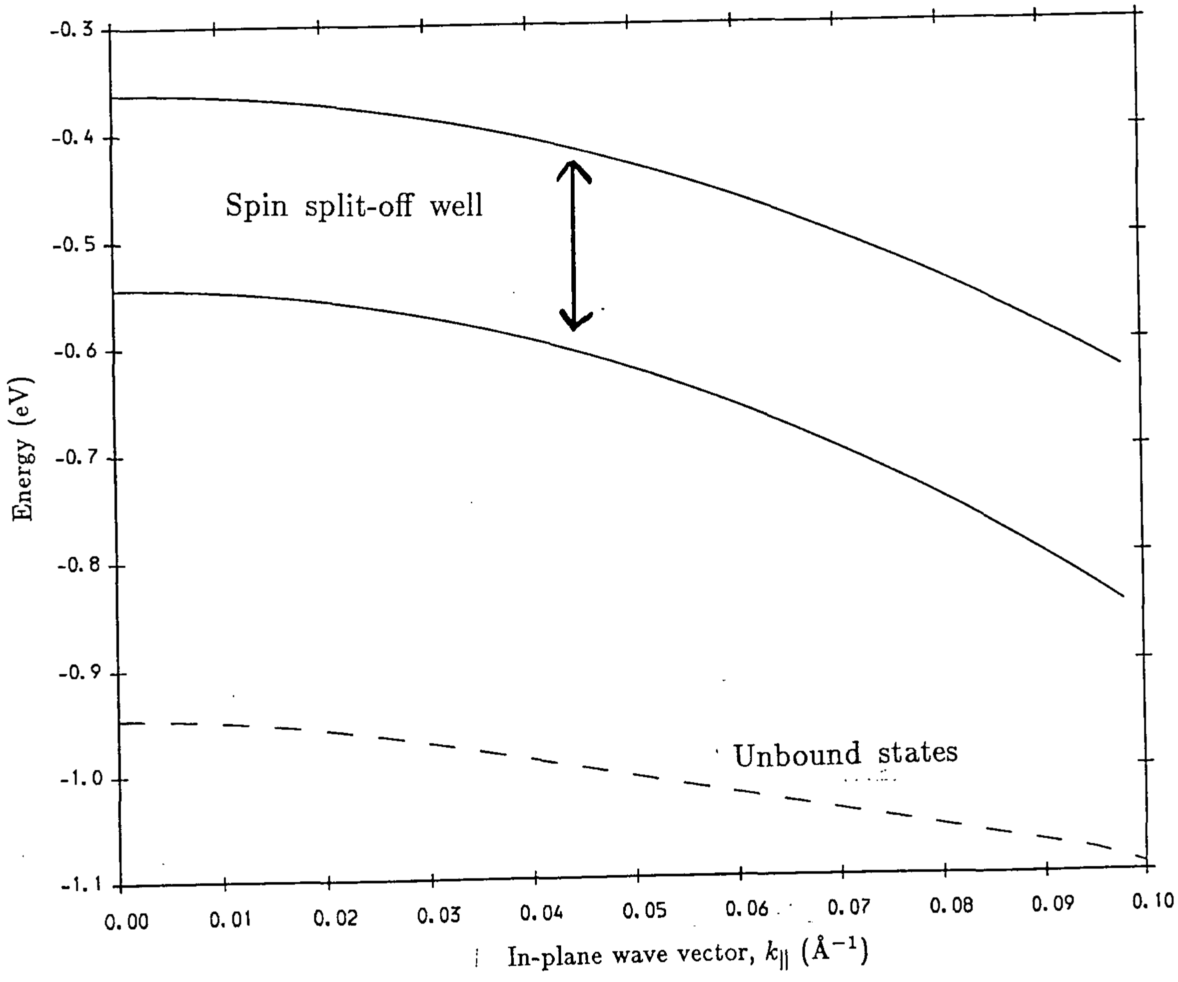

Variation of spin split-off well with in-plane wave vector.

Figure 7.9

The peak in the highly strained spectrum at $\lambda = 1.38\mu$m may arise from a spin split-off resonance feature. This can occur if the locus of unbound states coincides with the position at which a bound spin split-off subband would lie if the potential well were sufficiently deep. When this happens, the overlap between the bound and unbound wave functions will be considerable enhanced, leading to increased absorption.

The effect of strain on the IVBA coefficients appears to be dominated by the decreased well width and modified spin split-off band line up of the strained structures. The reduced well width enhances the bound-unbound matrix element by reducing the number of nodes in the unbound matrix element at a given energy.

7.5 Summary

In this chapter we have shown how the unbound states of the quantum well obtained from the **k.p** model described in chapters 2 and 3 can be used to calculate bound-unbound intervalence band absorption rates in strained and lattice matched systems. The absorption coefficient for bound-unbound transitions is considerably smaller than for bound-bound or bulk transitions, which suggests that structures such as those considered here in which bound-bound transitions do not occur at the band gap energy should have negligible intervalence band absorption at this energy. The temperature dependence of bound-unbound IVBA is generally small, and absorption increases linearly with hole concentration.

References for Chapter Seven

[1] A.R. Adams, M. Asada, Y. Suematsu and S. Arai, Jap. J. Appl. Phys. **19**, L621 (1980).

[2] S.Arai, IEEE J. Quantum Electronics **QE17**, 611 (1981).

[3] A. Mozer, K.M. Romanek, O. Hildebrand, W. Schmid and M.H. Pilkuhn, IEEE J. Quantum Electronics **QE19**, 913 (1983).

[4] A.R. Adams, K.C. Heasman and J. Hilton, Semicond. Sci. Technol. **2**, 761 (1987).

[5] A. Sugimura, IEEE J. Quantum Electronics **QE17**, 627 (1981); Appl. Phys. Lett. **39**, 21 (1981).

[6] N.K. Dutta, J. Appl. Phys. **54**, 1236 (1983).

[7] C.H. Henry, R.A. Logan, F.R. Merrit and J.P. Luongo, IEEE J. Quantum Electronics **QE19**,947 (1983).

[8] G.N. Childs, S.Brand and R.A. Abram, Semicond. Sci. Technol. **1**, 116 (1986).

[9] M. Asada, A. Kameyama and Y. Suematsu, IEEE J. Quantum Electronics **QE20**,745 (1984).

[10]M. Takeshima, Jap. J. Appl. Phys. **23**, 428 (1984); J. Appl. Phys. **56**, 49 (1984); J. Appl. Phys. **56**, 691 (1984).

[11]G.N. Childs, Ph. D. Thesis, University of Durham (1987).

8 CONCLUSION

8.1 Summary

The aim of this work has been to investigate the effect of strain on the bandstructure and optical properties of quantum wells. Particular emphasis has been given to the properties of strained layer multiple quantum well lasers.

In chapter 2 it was shown that the **k.p** method used within the envelope function framework provides an efficient means of obtaining the bandstructure and wave functions of a quantum well. This model forms the starting point for all of the work described in this thesis. It includes an explicit description of the conduction and valence subbands, together with spin effects. The bandstructure and wave functions obtained from the model are strongly influenced by intersubband mixing effects, resulting in anticrossing behaviour between adjacent subbands. The method also enables the unbound states of the conduction and valence band wells to be obtained.

Chapter 3 described the inclusion of strain effects into the bandstructure model. The effects of artificial biaxial compression and tension on the bandstructure of an $In_{0.53}Ga_{0.47}As/InP$ quantum well were investigated, and it was shown how strain changes the relative positions of the $m_j = \frac{1}{2}$ and $m_j = \frac{3}{2}$ subbands. In particular, it was shown that a biaxial compression can be used to shift the $m_j = \frac{1}{2}$ subbands to higher hole energy, causing a reduction in intersubband mixing effects and resulting in a lowering of the in-plane effective mass of the ground state subband.

In chapter 4 the transverse electric mode optical matrix elements between bound conduction and valence band states were calculated for both unstrained and strained quantum wells. The wave function mixing which occurs in the unstrained quantum well strongly modifies the matrix elements, causing some transitions to have appreciable matrix elements when they are expected from simple selection rules to be forbidden. Conversely, some transitions which are expected to be strong turn out to be considerably diminished. The reduction of mixing in the strained structures can be clearly seen in the matrix elements.

Chapter 5 showed how gain and spontaneous emission spectra, together with a range of threshold properties, of a quantum well laser can be calculated from the **k.p** bandstructure and optical matrix elements. The model developed also includes lifetime broadening effects through an energy dependent Lorentzian function. The importance of including a realistic description of the subband dispersion and the optical matrix elements was demonstrated by comparing results obtained from the full model with results obtained using a parabolic fit to the bandstructure and simple selection rules. In chapter 6 the model was used to compare the properties of strained and unstrained InGaAs/InP quantum well lasers, for operation at 1.3μm and 1.55μm. The strained devices exhibit a number of advantages, such as reduced threshold current and linewidth enhancement factor, and improved gainslope and temperature stability. Most of the enhancement in these devices could be obtained using only a moderate degree of strain ($\frac{3}{4}$% lattice mismatch). The improved performance offered by the strained layer lasers is largely attributed to the reduced effective mass of the first valence subband.

In chapter 7 the bound-unbound intervalence band absorption rate in the lasers studied in chapter 6 was investigated. In all cases the IVBA coefficent for the bound-unbound process was found to be small ($< 2\mathrm{cm}^{-1}$, compared with typical values in the bulk of around $30\mathrm{cm}^{-1}$ [1]), which is a consequence of the very small overlap of the bound and unbound state wave functions at the transition energies considered. The absorption coefficient is found to increase linearly with increasing hole concentration and to vary only slowly with temperature for all of the devices considered.

8.2 Suggestions for Further Work

The work in this thesis has concentrated on applying the bandstructure model described in chapters 2 and 3 to a study of the properties of strained layer quantum well lasers. Whilst the laser model itself would not stand any increased sophistication since it already requires substantial processing time to calculate broadened spectra and threshold properties, several important processes which are important in such structures have merely been parameterised using unstrained results from the literature. In particular, Auger recombination and intervalence band absorption are only included in a simplistic fashion and improvements are desirable. With the intention of providing better descriptions of such processes, a start has been made in this work to investigate IVBA in strained materials, but the bound-bound processes have not been considered. Whilst this omission is not important in the particular devices considered in this thesis, this is certainly an area where there is a need for further calculations. An investigation of bound-bound IVBA in strained quantum wells would require little further effort, since the bound spin split-off states can be calculated using the **k**.**p** model with an appropriate modification of the boundary conditions, and the matrix elements can be obtained as described previously.

Also of importance in quantum well lasers is Auger recombination [2]. The **k**.**p** strained quantum well model could be used to extend the recent work of Taylor *et al* [3] to strained layer structures. Such work is particularly important since the reduced IVBA coefficients obtained in chapter 7 suggest that Auger recombination is likely to be the dominant loss mechanism in InGaAs/InP strained quantum well lasers in the 1.3μm to 1.55μm range.

The models described in this work could also be applied to a study of semiconductor optical amplifiers. These devices have always suffered from the large difference between the TE mode and TM mode gain in a quantum well. It has been suggested recently that the use of a quantum well under biaxial tension can overcome this difficulty by enhancing the TM mode gain, allowing this structure to be used as a polarisation insensitive amplifier [4].

It has already been mentioned that bandstructure obtained from the model described in chapter 2 has been used in a Monte Carlo calculation to study hole relaxation in GaAs quantum wells [5,6]. The availability of strained bandstructure would allow a thorough investigation of the transport properties of devices such as InGaAs/GaAs pseudomorphic high electron mobility transistors (HEMTs) and similar structures in which the strain can be used to produce high mobility holes.

References for Chapter Eight

[1] G.N. Childs, S. Brand and R.A. Abram, Semicond. Sci. Technol. **1**, 116 (1986).

[2] A.R. Beattie and P.T. Landsberg, Proc. R. Soc. A **249**, 16 (1958)

[3] R.I. Taylor, R.A. Abram, M.G. Burt and C. Smith, Semicon. Sci. Technol. **5**, 90 (1990).

[4] K. Magari, M. Okamoto, H. Yasaka, K. Sato, Y. Noguchi and O. Mikami, IEEE Topical Meeting on Optical Amplifiers and their Applications, Monterrey 1990.

[5] R.W. Kelsall, R.I. Taylor, A.C.G. Wood and R.A. Abram, Superlattices and Microstructures **5**, 207 (1989).

[6] R.W. Kelsall, R.I. Taylor, A.C.G. Wood and R.A. Abram, Semicond. Sci. Technol. **5**, 877 (1990).

APPENDIX A

Parameters used in the Calculations

a) Bandstructure Calculations :

	$In_{0.53}Ga_{0.47}As$	$In_{0.63}Ga_{0.37}As$	$In_{0.73}Ga_{0.27}As$	InP
E_g (eV)	0.75	0.643	0.535	1.351
Δ (eV)	0.356	0.359	0.362	0.11
s	-1.86	-8.37	-8.38	-1.34
γ_1	1.28	-1.34	-1.65	0.036
γ_2	-0.438	-1.77	-1.94	-0.751
γ_3	-0.193	-1.50	-1.66	-0.751
E_p (eV)	22.09	25.83	23.91	19.89
ΔE_v (with InP)	0.32	0.377	0.434	
m	1.70	1.70	1.70	
c	-6.93	-6.93	-6.93	
l	-3.40	-3.40	-3.40	

The parameters were derived from effective masses taken from Landolt-Börnstein Vol. 17 *Semiconductors*, Subvolume a, ed. O. Madelung, Springer-Verlag (1982). Where necessary, a linear interpolation between values for InAs and GaAs was used.

b) Laser calculations :

Cavity length	250μm
Facet reflectivity	0.32
IVBA coefficient	40cm^{-1} at $n = 10^{18}\text{cm}^{-3}$
Auger coefficient	$10^{28}\text{cm}^{-6}\text{s}^{-1}$
Mirror plus cavity loss	45cm^{-1}
Broadening	$\Delta E = 8\text{meV} - 0.107E_{el}$
Background broadening	1meV

(D.J. Robbins, private communication)

APPENDIX B

Bandstructure Fitting Procedure

The quantum well bandstructure calculations described in chapter 2, whilst fairly efficient as regards computer time, are too complex to be carried out from within a laser modelling or intervalence band absorption (IVBA) calculation. To overcome this difficulty, all the bandstructure obtained from the **k.p** model is fitted to a cubic spline expansion, and decoded as required by the laser and IVBA calculations, using NAG library routines (E02BAF and E02BBF).

Rather than fit the energy as a function of in-plane wave vector, a function which is, in principal, more slowly varying is chosen, in the hope of maximising the accuracy of the fit. This is done by removing the $k_{\|}^2$ dependence of the energy by writing the dispersion relation for each subband in the form

$$E_i(k_{\|}) = g_i(k_{\|}) \frac{\hbar^2 k_{\|}^2}{2m_i^*} \qquad (A2.1)$$

and fitting the 'non-parabolicity correction factors ' g_i to the cubic spline representation. This approach allows the results of the full calculation to be easily compared with those of a simple parabolic band model, which are obtained by simply setting $g_i(k_{\|}) = 1$ for all $k_{\|}$. g_i is set to 1 for wave vectors beyond the range of calculated values.

It should be noted that although the effective masses of the subbands are used in calculating the cubic spline fits, we are free to use any value of m^* in the fitting procedures, provided that the same value is used to decode the fit. As this parameter is somewhat arbitrary, and included only for the purpose of normalising the g_i to unity, the effective masses used in the calculations described in this thesis are approximate values obtained by inspection of 3 or 4 points along each subband.

The joint density of states is readily obtained from the fit using

$$\text{JDOS} \quad \propto \left[\frac{2g_c + k_{\|}g'_c}{2m^*_c} + \frac{2g_v + k_{\|}g'_v}{2m^*_v}\right]^{-1} \tag{A2.2}$$

for a given conduction (c) and valence (v) subband pair. g' is the derivative $dg/dk_{\|}$. It can be seen that the parabolic subband result

$$\text{JDOS} \quad \propto \frac{m^*_c m^*_v}{m^*_c + m^*_v} \tag{A2.3}$$

is obtained from (A2.2) by setting $g = 1$ and $g' = 0$, as expected.

The matrix elements are also fitted to a cubic spline representation for use in the laser model; in this case the cubic splines are fitted directly to the squared optical matrix element.